

①

AD-A227 609

August 1989

Thesis/Dissertation

Radar Analysis of a Tamex Frontal System

Alan D. Robinson

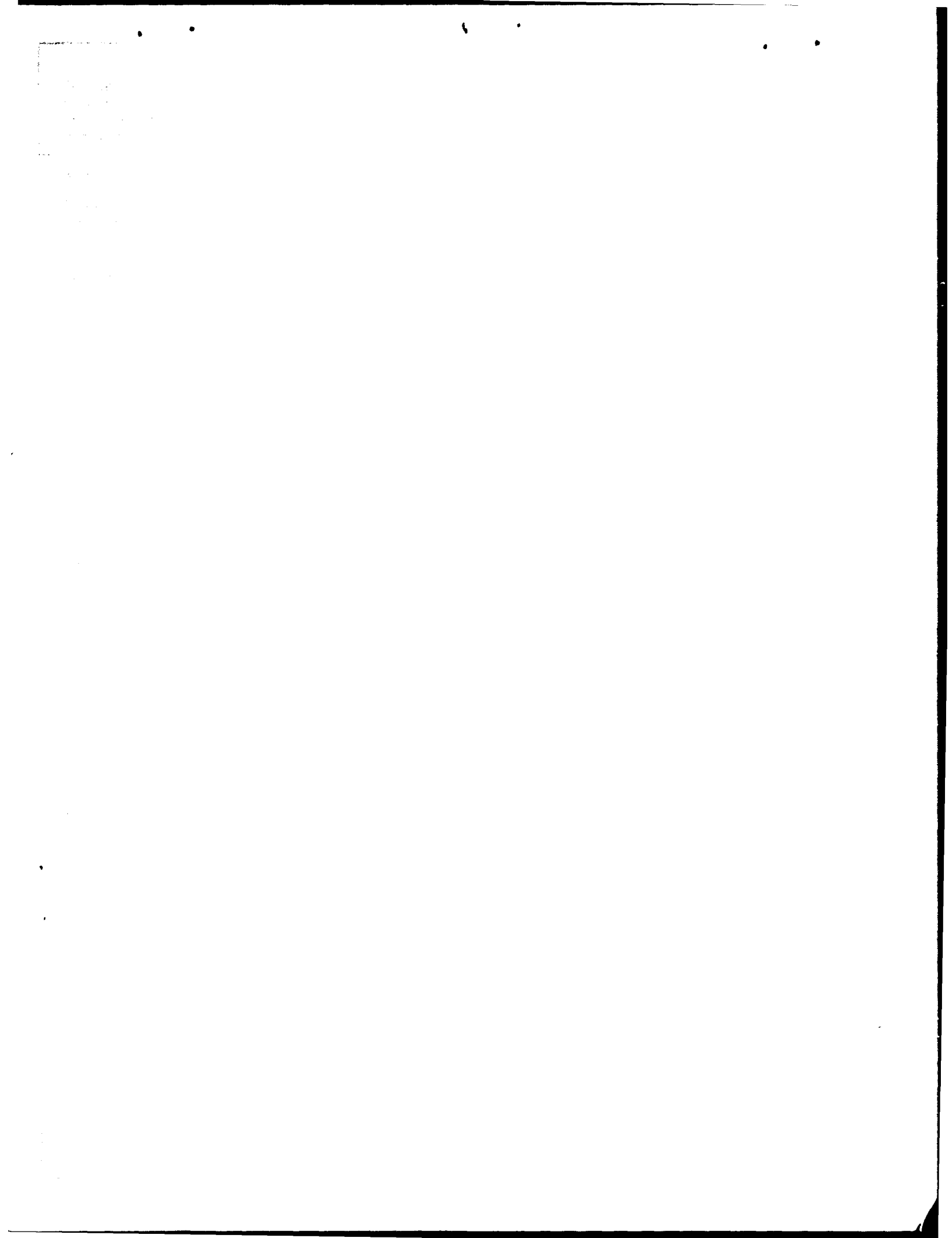
AFIT Student at: Florida State University

AFIT/CI/CIA -90-073

AFIT/CI  
Wright-Patterson AFB OH 45433

Approved for Public Release IAW AFR 190-1  
Distribution Unlimited  
ERNEST A. HAYGOOD, 1st Lt, USAF  
Executive Officer, Civilian Institution Programs

DTIC  
ELECTE  
OCT 23 1990  
S B D  
*CD*



THE FLORIDA STATE UNIVERSITY  
COLLEGE OF ARTS AND SCIENCES

RADAR ANALYSIS OF A  
TAMEX FRONTAL SYSTEM

By  
Alan D. Robinson

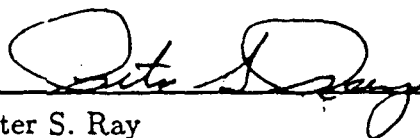
A Thesis submitted to the  
Department of Meteorology  
in partial fulfillment of the  
requirements for the degree of  
**Master of Science**

Degree Awarded:

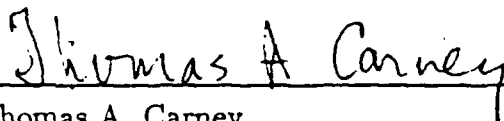
Fall Semester, 1989

90 16 22 197

The members of the Committee approve the thesis of Alan D. Robinson defended on August 23, 1989.



Peter S. Ray  
Professor Directing Thesis



Thomas A. Carney  
Committee Member



Noel E. LaSeur  
Committee member

This work is dedicated with love to my parents Mr. and Mrs. William H. Robinson, Jr., who have always been there when I needed them. It is also dedicated to Susan Michelle Peterson, who has been the best friend anyone could ever hope to have, and to my co-workers Terence Given and Patrick Moore, whose assistance was invaluable to the completion of this work. Finally, it is dedicated to Christopher Fenton Keohan, who during the course of my research became critically ill and was three times hospitalized for major operations, allowing me time to steal his desk.



|                      |  |
|----------------------|--|
| <b>Accession For</b> |  |
| NTIS GRA&I           | <input checked="checked" type="checkbox"/> |
| DTIC TAB             | <input type="checkbox"/>                   |
| Unannounced          | <input type="checkbox"/>                   |
| Justification        |  |
| By                   |  |
| Distribution/        |  |
| Availability Codes   |  |
| Dist                 | Avail and/or Special                       |
| A-1                  |  |

## ACKNOWLEDGEMENTS

I would like to express my deepest thanks to my major professor, Dr. Peter S. Ray, for his knowledge, guidance, and support during the course of this work. Many thanks are given to the other members of my committee, Dr. Thomas Carney and Dr. Noel LaSeur. Finally, I wish to acknowledge the United States Air Force for allowing me to participate in this program.

## TABLE OF CONTENTS

|   |       |
|---|-------|
| <b>List of Figures</b> . . . . .                                | v     |
| <b>List of Symbols</b> . . . . .                                | xviii |
| <b>Chapter 1. Introduction</b> . . . . .                        | 1     |
| 1.1. The TAMEX Experiment . . . . .                             | 1     |
| 1.1.1. Geography . . . . .                                      | 2     |
| 1.1.2. Synoptic Setting . . . . .                               | 4     |
| 1.2. Tropical Mesoscale Convective Life Cycle . . . . .         | 13    |
| 1.2.1. The Formative Stage . . . . .                            | 16    |
| 1.2.2. The Intensifying Stage . . . . .                         | 18    |
| 1.2.3. The Mature Stage . . . . .                               | 18    |
| 1.2.4. The Dissipating Stage . . . . .                          | 19    |
| 1.3. Echo Scales and Sizes . . . . .                            | 19    |
| 1.4. Echo Morphology . . . . .                                  | 21    |
| 1.5. Flow Patterns, Convergent and Divergent Patterns . . . . . | 24    |
| 1.6. Storm Movement . . . . .                                   | 35    |
| 1.7. Mid-Latitude and Tropical Comparison . . . . .             | 37    |
| <b>Chapter 2. Methodology</b> . . . . .                         | 39    |
| 2.1. Doppler Radar Analyses . . . . .                           | 39    |
| 2.1.1. Dual-Doppler Analysis . . . . .                          | 39    |
| 2.2. Errors . . . . .   | 43    |
| 2.3. Velocity Azimuth Display . . . . .                         | 46    |
| <b>Chapter 3. Analysis</b> . . . . .                            | 49    |
| 3.1. Dual-Doppler Analysis . . . . .                            | 49    |
| 3.2. RHI Analysis . . . . .                                     | 149   |
| 3.3. VAD Analysis . . . . .                                     | 153   |

|   |     |
|---|-----|
| <b>Chapter 4. Conclusions</b> . . . . . | 179 |
| 4.1. Conclusions . . . . .              | 179 |
| <b>References</b> . . . . .             | 182 |
| <b>Appendix A.</b> . . . . .            | 185 |
| <b>Appendix B.</b> . . . . .            | 190 |
| <b>Appendix C.</b> . . . . .            | 193 |
| <b>Appendix D.</b> . . . . .            | 196 |

## LIST OF FIGURES

- Fig. 1. Doppler radar network for TAMEX. Cross-hatched areas denote elevations greater than 250 m, and stippled areas denote elevations above 1000 m. From Cunning (1988).
- Fig. 2. Synoptic scale surface analysis for TAMEX on 7 June. From Cunning (1988).
- Fig. 3. Synoptic scale upper air analysis for TAMEX on 7 June. From Cunning (1988).
- Fig. 4. Sea-level pressure with 1-mb contour intervals. Station model symbols have conventional meanings at 0600 LST for 8 June. From Trier *et al.* (1989).
- Fig. 5. Synoptic scale upper air analysis for TAMEX on 8 June. From Cunning (1988).
- Fig. 6. Sea-level pressure with 1-mb contour intervals. Station model symbols have conventional meanings at 1200 LST for 8 June. From Trier *et al.* (1989).
- Fig. 7. Sea-level pressure with 1-mb contour intervals. Station model symbols have conventional meanings at 1800 LST for 8 June. From Trier *et al.* (1989).
- Fig. 8. Synoptic scale surface analysis for TAMEX on 9 June. From Cunning (1988).
- Fig. 9a. Dual-Doppler analysis of reflectivities and horizontal velocities for 082029, at the surface. The length scale for the vectors is given in the lower right-hand corner. The reflectivity gray scale is given on the right side of the figure. Radar positions and the coastline of Taiwan are also given.
- Fig. 9b. Dual-Doppler analysis of reflectivities and horizontal velocities for 082029, at 1.0 km above the ground. The length scale for the vectors is given in the lower right-hand corner. The reflectivity gray scale is given on the right side of the figure. Radar positions and the coastline of Taiwan are also given.
- Fig. 9c. Dual-Doppler analysis of reflectivities and horizontal velocities for 082029, at 2.0 km above the ground. The length scale for the vectors is given in the lower right-hand corner. The reflectivity gray scale is given on the right side of the figure. Radar positions and the coastline of Taiwan are also given.

- Fig. 9d. Dual-Doppler analysis of reflectivities and horizontal velocities for 082029, at 3.0 km above the ground. The length scale for the vectors is given in the lower right-hand corner. The reflectivity gray scale is given on the right side of the figure. Radar positions and the coastline of Taiwan are also given.
- Fig. 9e. Dual-Doppler analysis of reflectivities and horizontal velocities for 082029, at 4.0 km above the ground. The length scale for the vectors is given in the lower right-hand corner. The reflectivity gray scale is given on the right side of the figure. Radar positions and the coastline of Taiwan are also given.
- Fig. 9f. Dual-Doppler analysis of reflectivities and horizontal velocities for 082029, at 5.0 km above the ground. The length scale for the vectors is given in the lower right-hand corner. The reflectivity gray scale is given on the right side of the figure. Radar positions and the coastline of Taiwan are also given.
- Fig. 9g. Dual-Doppler analysis of reflectivities and horizontal velocities for 082029, at 6.0 km above the ground. The length scale for the vectors is given in the lower right-hand corner. The reflectivity gray scale is given on the right side of the figure. Radar positions and the coastline of Taiwan are also given.
- Fig. 10a. Dual-Doppler analysis of reflectivities and horizontal velocities for 083559 at the surface. The length scale for the vectors is given in the lower right-hand corner. The reflectivity gray scale is given on the right side of the figure. Radar positions and the coastline of Taiwan are also given.
- Fig. 10b. Dual-Doppler analysis of reflectivities and horizontal velocities for 083559, at 1.0 km above the ground. The length scale for the vectors is given in the lower right-hand corner. The reflectivity gray scale is given on the right side of the figure. Radar positions and the coastline of Taiwan are also given.
- Fig. 10c. Dual-Doppler analysis of reflectivities and horizontal velocities for 083559, at 2.0 km above the ground. The length scale for the vectors is given in the lower right-hand corner. The reflectivity gray scale is given on the right side of the figure. Radar positions and the coastline of Taiwan are also given.
- Fig. 10d. Dual-Doppler analysis of reflectivities and horizontal velocities for 083559, at 3.0 km above the ground. The length scale for the vectors is given in the lower right-hand corner. The reflectivity gray scale is given on the right side of the figure. Radar positions and the coastline of Taiwan are also given.
- Fig. 10e. Dual-Doppler analysis of reflectivities and horizontal velocities for 083559, at 4.0 km above the ground. The length scale for the vectors is given in the lower right-hand corner. The reflectivity gray scale is given on the right side of the figure. Radar positions and the coastline of Taiwan are also given.

- Fig. 10f. Dual-Doppler analysis of reflectivities and horizontal velocities for 083559, at 5.0 km above the ground. The length scale for the vectors is given in the lower right-hand corner. The reflectivity gray scale is given on the right side of the figure. Radar positions and the coastline of Taiwan are also given.
- Fig. 10g. Dual-Doppler analysis of reflectivities and horizontal velocities for 083559, at 6.0 km above the ground. The length scale for the vectors is given in the lower right-hand corner. The reflectivity gray scale is given on the right side of the figure. Radar positions and the coastline of Taiwan are also given.
- Fig. 10h. Dual-Doppler analysis of reflectivities and horizontal velocities for 083559, at 7.0 km above the ground. The length scale for the vectors is given in the lower right-hand corner. The reflectivity gray scale is given on the right side of the figure. Radar positions and the coastline of Taiwan are also given.
- Fig. 11a. Dual-Doppler analysis of reflectivities and horizontal velocities for 085133, at the ground. The length scale for the vectors is given in the lower right-hand corner. The reflectivity gray scale is given on the right side of the figure. Radar positions and the coastline of Taiwan are also given.
- Fig. 11b. Dual-Doppler analysis of reflectivities and horizontal velocities for 085133, at 1.0 km above the ground. The length scale for the vectors is given in the lower right-hand corner. The reflectivity gray scale is given on the right side of the figure. Radar positions and the coastline of Taiwan are also given.
- Fig. 11c. Dual-Doppler analysis of reflectivities and horizontal velocities for 085133, at 2.0 km above the ground. The length scale for the vectors is given in the lower right-hand corner. The reflectivity gray scale is given on the right side of the figure. Radar positions and the coastline of Taiwan are also given.
- Fig. 11d. Dual-Doppler analysis of reflectivities and horizontal velocities for 085133, at 3.0 km above the ground. The length scale for the vectors is given in the lower right-hand corner. The reflectivity gray scale is given on the right side of the figure. Radar positions and the coastline of Taiwan are also given.
- Fig. 11e. Dual-Doppler analysis of reflectivities and horizontal velocities for 085133, at 4.0 km above the ground. The length scale for the vectors is given in the lower right-hand corner. The reflectivity gray scale is given on the right side of the figure. Radar positions and the coastline of Taiwan are also given.
- Fig. 11f. Dual-Doppler analysis of reflectivities and horizontal velocities for 085133, at 5.0 km above the ground. The length scale for the vectors is given in the lower right-hand corner. The reflectivity gray scale is given on the right side of the figure. Radar positions and the coastline of Taiwan are also given.

- Fig. 11g. Dual-Doppler analysis of reflectivities and horizontal velocities for 085133, at 6.0 km above the ground. The length scale for the vectors is given in the lower right-hand corner. The reflectivity gray scale is given on the right side of the figure. Radar positions and the coastline of Taiwan are also given.
- Fig. 11h. Dual-Doppler analysis of reflectivities and horizontal velocities for 085133, at 7.0 km above the ground. The length scale for the vectors is given in the lower right-hand corner. The reflectivity gray scale is given on the right side of the figure. Radar positions and the coastline of Taiwan are also given.
- Fig. 12a. Dual-Doppler analysis of reflectivities and horizontal velocities for 090524, at the ground. The length scale for the vectors is given in the lower right-hand corner. The reflectivity gray scale is given on the right side of the figure. Radar positions and the coastline of Taiwan are also given.
- Fig. 12b. Dual-Doppler analysis of reflectivities and horizontal velocities for 090524, at 1.0 km above the ground. The length scale for the vectors is given in the lower right-hand corner. The reflectivity gray scale is given on the right side of the figure. Radar positions and the coastline of Taiwan are also given.
- Fig. 12c. Dual-Doppler analysis of reflectivities and horizontal velocities for 090524, at 2.0 km above the ground. The length scale for the vectors is given in the lower right-hand corner. The reflectivity gray scale is given on the right side of the figure. Radar positions and the coastline of Taiwan are also given.
- Fig. 12d. Dual-Doppler analysis of reflectivities and horizontal velocities for 090524, at 3.0 km above the ground. The length scale for the vectors is given in the lower right-hand corner. The reflectivity gray scale is given on the right side of the figure. Radar positions and the coastline of Taiwan are also given.
- Fig. 12e. Dual-Doppler analysis of reflectivities and horizontal velocities for 090524, at 4.0 km above the ground. The length scale for the vectors is given in the lower right-hand corner. The reflectivity gray scale is given on the right side of the figure. Radar positions and the coastline of Taiwan are also given.
- Fig. 12f. Dual-Doppler analysis of reflectivities and horizontal velocities for 090524, at 5.0 km above the ground. The length scale for the vectors is given in the lower right-hand corner. The reflectivity gray scale is given on the right side of the figure. Radar positions and the coastline of Taiwan are also given.
- Fig. 12g. Dual-Doppler analysis of reflectivities and horizontal velocities for 090524, at 6.0 km above the ground. The length scale for the vectors is given in the lower right-hand corner. The reflectivity gray scale is given on the right side of the figure. Radar positions and the coastline of Taiwan are also given.

- Fig. 12h. Dual-Doppler analysis of reflectivities and horizontal velocities for 090524, at 7.0 km above the ground. The length scale for the vectors is given in the lower right-hand corner. The reflectivity gray scale is given on the right side of the figure. Radar positions and the coastline of Taiwan are also given.
- Fig. 13a. Dual-Doppler analysis of reflectivities and horizontal velocities for 095308, at the ground. The length scale for the vectors is given in the lower right-hand corner. The reflectivity gray scale is given on the right side of the figure. Radar positions and the coastline of Taiwan are also given.
- Fig. 13b. Dual-Doppler analysis of reflectivities and horizontal velocities for 095308, at 1.0 km above the ground. The length scale for the vectors is given in the lower right-hand corner. The reflectivity gray scale is given on the right side of the figure. Radar positions and the coastline of Taiwan are also given.
- Fig. 13c. Dual-Doppler analysis of reflectivities and horizontal velocities for 095308, at 2.0 km above the ground. The length scale for the vectors is given in the lower right-hand corner. The reflectivity gray scale is given on the right side of the figure. Radar positions and the coastline of Taiwan are also given.
- Fig. 13d. Dual-Doppler analysis of reflectivities and horizontal velocities for 095308, at 3.0 km above the ground. The length scale for the vectors is given in the lower right-hand corner. The reflectivity gray scale is given on the right side of the figure. Radar positions and the coastline of Taiwan are also given.
- Fig. 13e. Dual-Doppler analysis of reflectivities and horizontal velocities for 095308, at 4.0 km above the ground. The length scale for the vectors is given in the lower right-hand corner. The reflectivity gray scale is given on the right side of the figure. Radar positions and the coastline of Taiwan are also given.
- Fig. 13f. Dual-Doppler analysis of reflectivities and horizontal velocities for 095308, at 5.0 km above the ground. The length scale for the vectors is given in the lower right-hand corner. The reflectivity gray scale is given on the right side of the figure. Radar positions and the coastline of Taiwan are also given.
- Fig. 13g. Dual-Doppler analysis of reflectivities and horizontal velocities for 095308, at 6.0 km above the ground. The length scale for the vectors is given in the lower right-hand corner. The reflectivity gray scale is given on the right side of the figure. Radar positions and the coastline of Taiwan are also given.
- Fig. 13h. Dual-Doppler analysis of reflectivities and horizontal velocities for 095308, at 7.0 km above the ground. The length scale for the vectors is given in the lower right-hand corner. The reflectivity gray scale is given on the right side of the figure. Radar positions and the coastline of Taiwan are also given.

- Fig. 14a. Dual-Doppler analysis of reflectivities and horizontal velocities for 105232, at the ground. The length scale for the vectors is given in the lower right-hand corner. The reflectivity gray scale is given on the right side of the figure. Radar positions and the coastline of Taiwan are also given.
- Fig. 14b. Dual-Doppler analysis of reflectivities and horizontal velocities for 105232, at 1.0 km above the ground. The length scale for the vectors is given in the lower right-hand corner. The reflectivity gray scale is given on the right side of the figure. Radar positions and the coastline of Taiwan are also given.
- Fig. 14c. Dual-Doppler analysis of reflectivities and horizontal velocities for 105232, at 2.0 km above the ground. The length scale for the vectors is given in the lower right-hand corner. The reflectivity gray scale is given on the right side of the figure. Radar positions and the coastline of Taiwan are also given.
- Fig. 14d. Dual-Doppler analysis of reflectivities and horizontal velocities for 105232, at 3.0 km above the ground. The length scale for the vectors is given in the lower right-hand corner. The reflectivity gray scale is given on the right side of the figure. Radar positions and the coastline of Taiwan are also given.
- Fig. 14e. Dual-Doppler analysis of reflectivities and horizontal velocities for 105232, at 4.0 km above the ground. The length scale for the vectors is given in the lower right-hand corner. The reflectivity gray scale is given on the right side of the figure. Radar positions and the coastline of Taiwan are also given.
- Fig. 14f. Dual-Doppler analysis of reflectivities and horizontal velocities for 105232, at 5.0 km above the ground. The length scale for the vectors is given in the lower right-hand corner. The reflectivity gray scale is given on the right side of the figure. Radar positions and the coastline of Taiwan are also given.
- Fig. 14g. Dual-Doppler analysis of reflectivities and horizontal velocities for 105232, at 6.0 km above the ground. The length scale for the vectors is given in the lower right-hand corner. The reflectivity gray scale is given on the right side of the figure. Radar positions and the coastline of Taiwan are also given.
- Fig. 15a. Dual-Doppler analysis of reflectivities and horizontal velocities for 113232, at the ground. The length scale for the vectors is given in the lower right-hand corner. The reflectivity gray scale is given on the right side of the figure. Radar positions and the coastline of Taiwan are also given. Frontal position is indicated by the heavy dashed line.

- Fig. 15b. Dual-Doppler analysis of reflectivities and horizontal velocities for 113232, at 1.0 km above the ground. The length scale for the vectors is given in the lower right-hand corner. The reflectivity gray scale is given on the right side of the figure. Radar positions and the coastline of Taiwan are also given. Frontal position is indicated by the heavy dashed line.
- Fig. 15c. Dual-Doppler analysis of reflectivities and horizontal velocities for 113232, at 2.0 km above the ground. The length scale for the vectors is given in the lower right-hand corner. The reflectivity gray scale is given on the right side of the figure. Radar positions and the coastline of Taiwan are also given.
- Fig. 15d. Dual-Doppler analysis of reflectivities and horizontal velocities for 113232, at 3.0 km above the ground. The length scale for the vectors is given in the lower right-hand corner. The reflectivity gray scale is given on the right side of the figure. Radar positions and the coastline of Taiwan are also given.
- Fig. 15e. Dual-Doppler analysis of reflectivities and horizontal velocities for 113232, at 4.0 km above the ground. The length scale for the vectors is given in the lower right-hand corner. The reflectivity gray scale is given on the right side of the figure. Radar positions and the coastline of Taiwan are also given.
- Fig. 15f. Dual-Doppler analysis of reflectivities and horizontal velocities for 113232, at 5.0 km above the ground. The length scale for the vectors is given in the lower right-hand corner. The reflectivity gray scale is given on the right side of the figure. Radar positions and the coastline of Taiwan are also given.
- Fig. 15g. Dual-Doppler analysis of reflectivities and horizontal velocities for 113232, at 6.0 km above the ground. The length scale for the vectors is given in the lower right-hand corner. The reflectivity gray scale is given on the right side of the figure. Radar positions and the coastline of Taiwan are also given.
- Fig. 15h. Dual-Doppler analysis of reflectivities and horizontal velocities for 113232, at 7.0 km above the ground. The length scale for the vectors is given in the lower right-hand corner. The reflectivity gray scale is given on the right side of the figure. Radar positions and the coastline of Taiwan are also given.
- Fig. 15i. Dual-Doppler analysis of reflectivities and horizontal velocities for 113232, at 8.0 km above the ground. The length scale for the vectors is given in the lower right-hand corner. The reflectivity gray scale is given on the right side of the figure. Radar positions and the coastline of Taiwan are also given.

- Fig. 16a. Dual-Doppler analysis of reflectivities and horizontal velocities for 115142, at the ground. The length scale for the vectors is given in the lower right-hand corner. The reflectivity gray scale is given on the right side of the figure. Radar positions and the coastline of Taiwan are also given. Frontal position is indicated by the heavy dashed line.
- Fig. 16b. Dual-Doppler analysis of reflectivities and horizontal velocities for 115142, at 1.0 km above the ground. The length scale for the vectors is given in the lower right-hand corner. The reflectivity gray scale is given on the right side of the figure. Radar positions and the coastline of Taiwan are also given. Frontal position is indicated by the heavy dashed line.
- Fig. 16c. Dual-Doppler analysis of reflectivities and horizontal velocities for 115142, at 2.0 km above the ground. The length scale for the vectors is given in the lower right-hand corner. The reflectivity gray scale is given on the right side of the figure. Radar positions and the coastline of Taiwan are also given.
- Fig. 16d. Dual-Doppler analysis of reflectivities and horizontal velocities for 115142, at 3.0 km above the ground. The length scale for the vectors is given in the lower right-hand corner. The reflectivity gray scale is given on the right side of the figure. Radar positions and the coastline of Taiwan are also given.
- Fig. 16e. Dual-Doppler analysis of reflectivities and horizontal velocities for 115142, at 4.0 km above the ground. The length scale for the vectors is given in the lower right-hand corner. The reflectivity gray scale is given on the right side of the figure. Radar positions and the coastline of Taiwan are also given.
- Fig. 16f. Dual-Doppler analysis of reflectivities and horizontal velocities for 115142, at 5.0 km above the ground. The length scale for the vectors is given in the lower right-hand corner. The reflectivity gray scale is given on the right side of the figure. Radar positions and the coastline of Taiwan are also given.
- Fig. 16g. Dual-Doppler analysis of reflectivities and horizontal velocities for 115142, at 6.0 km above the ground. The length scale for the vectors is given in the lower right-hand corner. The reflectivity gray scale is given on the right side of the figure. Radar positions and the coastline of Taiwan are also given.
- Fig. 16h. Dual-Doppler analysis of reflectivities and horizontal velocities for 115142, at 7.0 km above the ground. The length scale for the vectors is given in the lower right-hand corner. The reflectivity gray scale is given on the right side of the figure. Radar positions and the coastline of Taiwan are also given.

- Fig. 17a. Dual-Doppler analysis of reflectivities and horizontal velocities for 1123013, at the ground. The length scale for the vectors is given in the lower right-hand corner. The reflectivity gray scale is given on the right side of the figure. Radar positions and the coastline of Taiwan are also given. Frontal position is indicated by the heavy dashed line.
- Fig. 17b. Dual-Doppler analysis of reflectivities and horizontal velocities for 123013, at 1.0 km above the ground. The length scale for the vectors is given in the lower right-hand corner. The reflectivity gray scale is given on the right side of the figure. Radar positions and the coastline of Taiwan are also given. Frontal position is indicated by the heavy dashed line. Cross-sectional plot given in Figure 19 is denoted by line A-B.
- Fig. 17c. Dual-Doppler analysis of reflectivities and horizontal velocities for 123013, at 2.0 km above the ground. The length scale for the vectors is given in the lower right-hand corner. The reflectivity gray scale is given on the right side of the figure. Radar positions and the coastline of Taiwan are also given.
- Fig. 17d. Dual-Doppler analysis of reflectivities and horizontal velocities for 123013, at 3.0 km above the ground. The length scale for the vectors is given in the lower right-hand corner. The reflectivity gray scale is given on the right side of the figure. Radar positions and the coastline of Taiwan are also given.
- Fig. 17e. Dual-Doppler analysis of reflectivities and horizontal velocities for 123013, at 4.0 km above the ground. The length scale for the vectors is given in the lower right-hand corner. The reflectivity gray scale is given on the right side of the figure. Radar positions and the coastline of Taiwan are also given.
- Fig. 17f. Dual-Doppler analysis of reflectivities and horizontal velocities for 123013, at 5.0 km above the ground. The length scale for the vectors is given in the lower right-hand corner. The reflectivity gray scale is given on the right side of the figure. Radar positions and the coastline of Taiwan are also given.
- Fig. 17g. Dual-Doppler analysis of reflectivities and horizontal velocities for 123013, at 6.0 km above the ground. The length scale for the vectors is given in the lower right-hand corner. The reflectivity gray scale is given on the right side of the figure. Radar positions and the coastline of Taiwan are also given.
- Fig. 17h. Dual-Doppler analysis of reflectivities and horizontal velocities for 123013, at 7.0 km above the ground. The length scale for the vectors is given in the lower right-hand corner. The reflectivity gray scale is given on the right side of the figure. Radar positions and the coastline of Taiwan are also given.

- Fig. 17i. Dual-Doppler analysis of reflectivities and horizontal velocities for 123013, at 8.0 km above the ground. The length scale for the vectors is given in the lower right-hand corner. The reflectivity gray scale is given on the right side of the figure. Radar positions and the coastline of Taiwan are also given.
- Fig. 18. Vertical cross-section of reflectivity and wind. View is toward the WNW along the cross-section (A-B) indicated in Fig. 17b.
- Fig. 19a. Dual-Doppler analysis of reflectivities and horizontal velocities for 124924, at the ground. The length scale for the vectors is given in the lower right-hand corner. The reflectivity gray scale is given on the right side of the figure. Radar positions and the coastline of Taiwan are also given. Frontal position is indicated by the heavy dashed line.
- Fig. 19b. Dual-Doppler analysis of reflectivities and horizontal velocities for 124924, at 1.0 km above the ground. The length scale for the vectors is given in the lower right-hand corner. The reflectivity gray scale is given on the right side of the figure. Radar positions and the coastline of Taiwan are also given. Frontal position is indicated by the heavy dashed line. Line A-B depicts the position of the cross-sectional plot depicted in Fig. 21.
- Fig. 19c. Dual-Doppler analysis of reflectivities and horizontal velocities for 124924, at 2.0 km above the ground. The length scale for the vectors is given in the lower right-hand corner. The reflectivity gray scale is given on the right side of the figure. Radar positions and the coastline of Taiwan are also given.
- Fig. 19d. Dual-Doppler analysis of reflectivities and horizontal velocities for 124924, at 3.0 km above the ground. The length scale for the vectors is given in the lower right-hand corner. The reflectivity gray scale is given on the right side of the figure. Radar positions and the coastline of Taiwan are also given.
- Fig. 19e. Dual-Doppler analysis of reflectivities and horizontal velocities for 124924, at 4.0 km above the ground. The length scale for the vectors is given in the lower right-hand corner. The reflectivity gray scale is given on the right side of the figure. Radar positions and the coastline of Taiwan are also given.
- Fig. 19f. Dual-Doppler analysis of reflectivities and horizontal velocities for 124924, at 5.0 km above the ground. The length scale for the vectors is given in the lower right-hand corner. The reflectivity gray scale is given on the right side of the figure. Radar positions and the coastline of Taiwan are also given.

- Fig. 19g. Dual-Doppler analysis of reflectivities and horizontal velocities for 124924, at 6.0 km above the ground. The length scale for the vectors is given in the lower right-hand corner. The reflectivity gray scale is given on the right side of the figure. Radar positions and the coastline of Taiwan are also given.
- Fig. 19h. Dual-Doppler analysis of reflectivities and horizontal velocities for 124913, at 7.0 km above the ground. The length scale for the vectors is given in the lower right-hand corner. The reflectivity gray scale is given on the right side of the figure. Radar positions and the coastline of Taiwan are also given.
- Fig. 20. Vertical cross-section of reflectivity and wind. View is toward the WNW along the cross-section (A-B) indicated in Fig. 19b.
- Fig. 21a. Dual-Doppler analysis of reflectivities and horizontal velocities for 132902, at the ground. The length scale for the vectors is given in the lower right-hand corner. The reflectivity gray scale is given on the right side of the figure. Radar positions and the coastline of Taiwan are also given. Frontal position is indicated by the heavy dashed line.
- Fig. 21b. Dual-Doppler analysis of reflectivities and horizontal velocities for 132902, at 1.0 km above the ground. The length scale for the vectors is given in the lower right-hand corner. The reflectivity gray scale is given on the right side of the figure. Radar positions and the coastline of Taiwan are also given. Frontal position is indicated by the heavy dashed line. Line A-B denotes the position of the cross-sectional plot in Fig. 22.
- Fig. 21c. Dual-Doppler analysis of reflectivities and horizontal velocities for 132902, at 2.0 km above the ground. The length scale for the vectors is given in the lower right-hand corner. The reflectivity gray scale is given on the right side of the figure. Radar positions and the coastline of Taiwan are also given.
- Fig. 22. Vertical cross-section of reflectivity and wind. View is toward the WNW along the cross-section (A-B) indicated in Fig. 21b.
- Fig. 23. Dual-Doppler analysis of reflectivities and horizontal velocities for 140905, at 1.0 km above the ground. The length scale for the vectors is given in the lower right-hand corner. The reflectivity gray scale is given on the right side of the figure. Radar positions and the coastline of Taiwan are also given. Frontal position is indicated by the heavy dashed line.
- Fig. 24. RHI scan of reflectivity and radial velocity from the NCAR CP-4. (a) is reflectivity and (b) is radial velocity, both at 10 degrees azimuth at 110039 LST. Scales are given at the bottom of each figure.

- Fig. 25. RHI scan of reflectivity and radial velocity from the NCAR CP-4. (a) is reflectivity and (b) radial velocity for 30 degrees azimuth and 110108 LST. Range marks on the velocity display are in increments of 10 km. Scales are given at the bottom of each figure.
- Fig. 26. RHI scans of reflectivity and radial velocity. Radar is NCAR CP-4. (a) is reflectivity and (b) is radial velocity, both at 210 degrees azimuth at 125830 LST. Scales are given at the bottom of each figure. Range marks on the velocity display are in increments of 10 km.
- Fig. 27a. PPI scans of reflectivity (left) and velocity (right) from the NCAR CP-4 at 1052. Elevation angle is  $1.8^\circ$ . Scales are given at the bottom of each figure.
- Fig. 27b. VAD at 1052. Range is 5.0 km. Raw velocity values are given by the crosses, first harmonic by the heavy line, and the first and second harmonics together are given by the thin line.
- Fig. 27c. VAD at 1052. Range is 10.1 km. Raw velocity values are given by the crosses, first harmonic by the heavy line, and the first and second harmonics together are given by the thin line.
- Fig. 27d. VAD at 1052. Range is 19.8 km. Raw velocity values are given by the crosses, first harmonic by the heavy line, and the first and second harmonics together are given by the thin line.
- Fig. 28a. PPI scans of reflectivity (left) and velocity (right) from the NCAR CP-4 at 1152. Elevation angle is  $1.8^\circ$ . Scales are given at the bottom of each figure.
- Fig. 28b. VAD at 1152. Range is 5.0 km. Raw velocity values are given by the crosses, first harmonic by the heavy line, and the first and second harmonics together are given by the thin line.
- Fig. 29a. PPI scans of reflectivity (left) and velocity (right) from the NCAR CP-4 at 1230. Elevation angle is  $1.8^\circ$ . Scales are given at the bottom of each figure.
- Fig. 29b. VAD at 1230. Range is 5.0 km. Raw velocity values are given by the crosses, first harmonic by the heavy line, and the first and second harmonics together are given by the thin line.
- Fig. 29c. VAD at 1230. Range is 10.1 km. Raw velocity values are given by the crosses, first harmonic by the heavy line, and the first and second harmonics together are given by the thin line.

- Fig. 29d. VAD at 1230. Range is 19.8 km. Raw velocity values are given by the crosses, first harmonic by the heavy line, and the first and second harmonics together are given by the thin line.
- Fig. 30a. PPI scans of reflectivity (left) and velocity (right) from the NCAR CP-4 at 1249. Elevation angle is  $1.8^\circ$ . Scales are given at the bottom of each figure.
- Fig. 30b. VAD at 1249. Range is 5.0 km. Raw velocity values are given by the crosses, first harmonic by the heavy line, and the first and second harmonics together are given by the thin line.
- Fig. 30c. VAD at 1249. Range is 10.1 km. Raw velocity values are given by the crosses, first harmonic by the heavy line, and the first and second harmonics together are given by the thin line.
- Fig. 30d. VAD at 1249. Range is 19.8 km. Raw velocity values are given by the crosses, first harmonic by the heavy line, and the first and second harmonics together are given by the thin line.
- Fig. 31a. PPI scans of reflectivity (left) and velocity (right) from the NCAR CP-4 at 1329. Elevation angle is  $1.8^\circ$ . Scales are given at the bottom of each figure.
- Fig. 31b. VAD at 1329. Range is 5.0 km. Raw velocity values are given by the crosses, first harmonic by the heavy line, and the first and second harmonics together are given by the thin line.
- Fig. 31c. VAD at 1329. Range is 10.1 km. Raw velocity values are given by the crosses, first harmonic by the heavy line, and the first and second harmonics together are given by the thin line.
- Fig. 31d. VAD at 1329. Range is 19.8 km. Raw velocity values are given by the crosses, first harmonic by the heavy line, and the first and second harmonics together are given by the thin line.
- Fig. 31e. VAD at 1329. Range is 29.9 km. Raw velocity values are given by the crosses, first harmonic by the heavy line, and the first and second harmonics together are given by the thin line.
- Fig. A1. Terminal velocities from the adjusted Joss and Waldvogel (1970) equations. Plotted lines are done for: (A) 10 dBZ, (B) 20 dBZ, (C) 30 dBZ, (D) 40 dBZ, and (E) 50 dBZ. Negative velocities denote downward speed. All plots have a value of  $-2 \text{ ms}^{-1}$  above the 10 km height level.

## List of Symbols

|   |   |
|---|---|
| $\lambda$   | wavelength of radar   |
| $Z_e$   | effective radar reflectivity factor   |
| $Z_o$   | reference reflectivity ( $1 \text{ mm}^6 \text{ m}^{-3}$ )  |
| $W_i$   | the weight assigned to an observation at a grid point   |
| $d_i$   | distance from observation to grid point   |
| $R_i$   | influence radius  |
| $u, v, \text{ and } w$                            | three orthogonal components of motion   |
| $x, y, \text{ and } z$                            | position of grid points in Cartesian coordinates  |
| $x_1, y_1, z_1, \text{ and } x_2, y_2, z_2$       | coordinates for radar number 1 and 2, respectively  |
| $\kappa$  | logarithmic rate of change of density with height   |
| $R_1 \text{ and } R_2$                            | measures of range from radar 1 and 2, respectively  |
| $V_t$   | particle terminal velocity  |
| $\sigma_u^2, \sigma_v^2, \text{ and } \sigma_w^2$ | variances of the uncertainty in the<br>wind components due to sampling geometry                                 |
| $V_i$   | measured radial velocity  |
| $W$   | hydrometeor fall speed containing the vertical velocity<br>and the particle terminal fall speed ( $= w + V_t$ ) |
| $u^o \text{ and } v^o$                            | observed horizontal components of motion  |
| $\alpha^2 \text{ and } \beta^2$                   | weights which are inversely proportional to the<br>error variances in $u$ and $v$ , respectively                |
| $I$   | integrand of the functional   |
| $\theta$  | conventional definition of the azimuth angle  |
| $V_d$   | convention of negative Doppler velocity   |
| $\phi$  | beam elevation  |

## Radar Analysis of A TAMEX Frontal System

### Chapter 1

#### Introduction

##### 1.1 The TAMEX Experiment

The Taiwan Area Mesoscale Experiment (TAMEX) was conducted from 1 May through 29 June 1987. It was a joint United States-Republic of China research program. Its purpose was to gather data to enhance the understanding of the mesoscale dynamical and microphysical processes responsible for the rains that often lead to flash flooding in Taiwan. During the 13 intensive observational periods (IOP's), data was gathered on 1) the circulations associated with the *MEI-YU* front, which is a climatologically favored region of low-level convergence located over Taiwan and southern China; 2) the mesoscale convective systems that develop within the front; and 3) the effects of the topography of Taiwan on the mean flow, the *MEI-YU* front and mesoscale convective systems.

The *MEI-YU* front usually forms between the tropical and polar air masses in the late spring and early summer. It moves slowly southeastward to a quasi-stationary position extending from southern Japan to southern China. Although the *MEI-YU* front is characterized by a smaller horizontal temperature gradient

than is found in typical polar fronts, it is accompanied by a strong moisture gradient and horizontal wind shear. Synoptically, a southwesterly low level jet is often observed to the south of the *MEI-YU* front. Convection usually accompanies the front. Organized mesoscale convective elements are embedded within the frontal circulation and convection, predominately on the warm side of the front. The convective systems generally move east to west, sometimes interacting with island terrain to produce heavy rainfall (Chen and Yu, 1988).

#### 1.1.1 Geography

The dominant topographic feature is the Central Mountain Range, which is 300 km in length, 60–90 km wide, and has an average height of 3000 m. To the west of the mountains is a coastal plain that extends inland 25–50 km. On the east side of the island the coastal plane extends inland only about 10 km.

The three Doppler radars (C-band) were located on the northwest coast of Taiwan. The Chinese Civil Aeronautical Administration (CCAA) radar was located at Chaing Kai-Shek International Airport. The National Center for Atmospheric Research (NCAR) CP-4 radar was located approximately 68 km south of the CCAA radar, at a site known as Waipu Beach. The third Doppler radar, the National Oceanic Atmospheric Administration (NOAA) TOGA radar, was located at the CCK Air Force Base, just west of Taichung and approximately 45 km south of the NCAR radar. Placed in these areas, this radar network permitted good dual (sometimes triple) Doppler coverage of many of the IOP phenomena (Fig. 1).

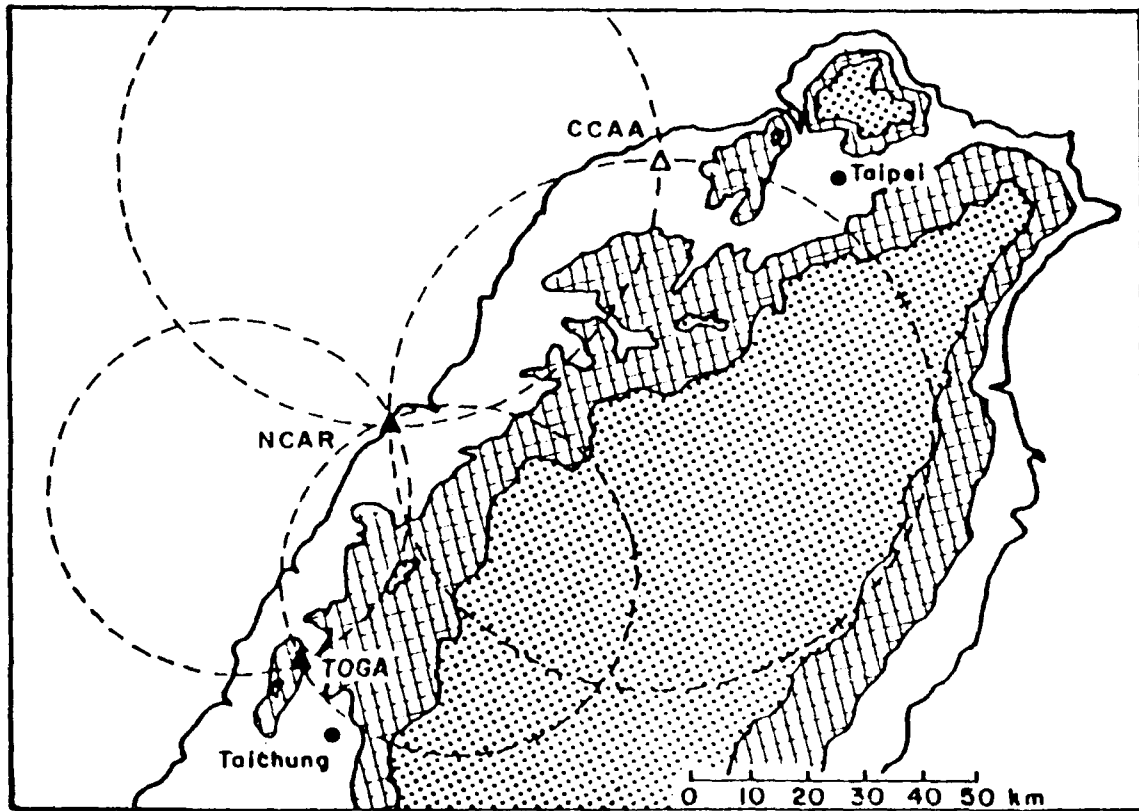


*Fig. 1. Doppler radar network for TAMEX. Cross hatched areas denote elevations greater than 250 m, and stippled areas denote elevations above 1000 m. From Cuning (1988).*

### 1.1.2 Synoptic Setting

The focus of this study is on IOP #8, which occurred from 1400 LST 7 June to 0800 LST, 9 June (0000 GMT corresponds to 0800 LST). The observations from this period were selected for study because of the apparent good quality of Doppler radar coverage and location of the storms with respect to the island. The radar data analyzed was recorded on 8 June from 0800 LST to 1630 LST. The objective of this IOP was to observe the structure of the convection developing over the Central Mountain Range (CMR) of Taiwan, and a frontal passage over the island. It was this frontal area that was studied. The ground-based Doppler radars first observed intense convection developing over the mountains on 7 June. That night, a prefrontal band of convection developed over the straits and moved over northern Taiwan. During the second day (8 June), the Doppler radars collected data on a second band of convection as it passed over the island. This data from the second band is the data that was analyzed to explore the similarities and/or differences with mid-latitude convection.

A surface cold front on 7 June was over mainland China moving eastward towards Taiwan, with a weak cloud band behind the front and scattered embedded convection within the band. The trough was expected to move through the TAMEX area within the next 36–48 hours. There was some weak convection, oriented in a north-south band, off the east coast of Taiwan. This convection band may have resulted from convergence forcing, created by the outflow from earlier convection

over the mountains to the west. The local soundings reflected a slight increase in stability, despite the fact that they were also becoming more moist. The forecast was for the front to move into the Taiwan area at about midnight, and for convection to form along the front (Figs. 2 and 3).

About 0100 LST, 8 June, showers developed in the straits. These became better organized, moving east-northeast, and by 0300 LST the line was in the dual-Doppler radar area. By 0500 LST, the line moved onshore over northern Taiwan, although most of the line missed the island. A 0600 LST mesoscale analysis by Trier *et al.* (1989) (See Fig. 4) revealed light winds over most of the island with weak offshore flow observed at many of the reporting stations. This was a typical nocturnal flow pattern observed during TAMEX, during undisturbed conditions. During the daylight hours, the flow tended to reverse to an onshore direction. For undisturbed conditions, a land-sea breeze circulation is typical. At this time (0600 LST) another area of convection moved off the Chinese mainland. This second complex of convection was located close to the surface front. Prior to the front reaching Taiwan, a surface pressure ridge was observed over the southwestern side of Taiwan, with a lower pressure observed on the eastern side. This pattern of a windward ridge and lee side trough is a typical pattern according to Wang (1986). This pressure pattern sets up a weak southwesterly flow from surface to 4 km over the island. As shown in Fig. 5, the 500 mb trough was still located west of Taiwan.

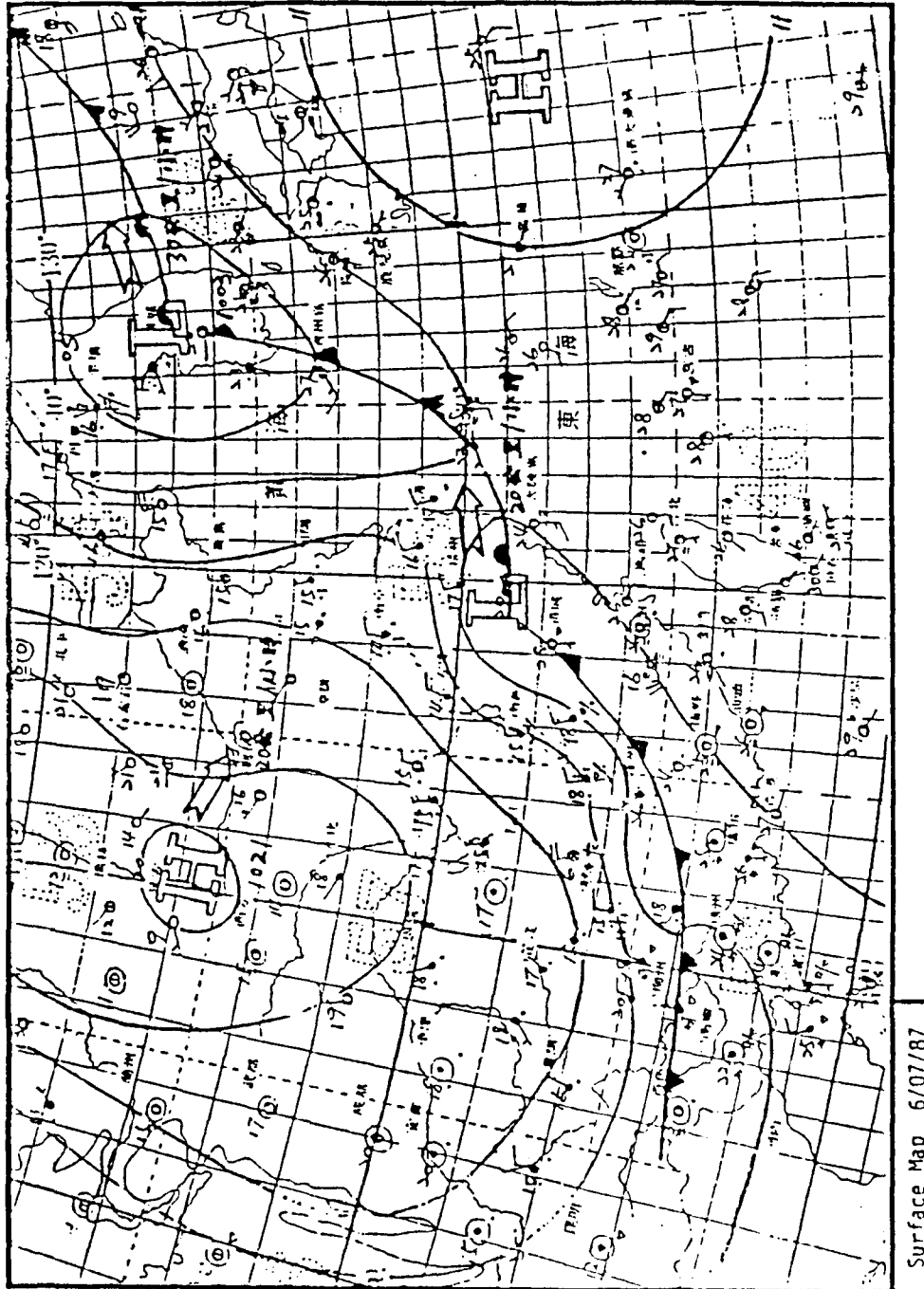


Fig. 2. Synoptic scale surface analysis for TAMEX on 7 June. From Cunning (1988).

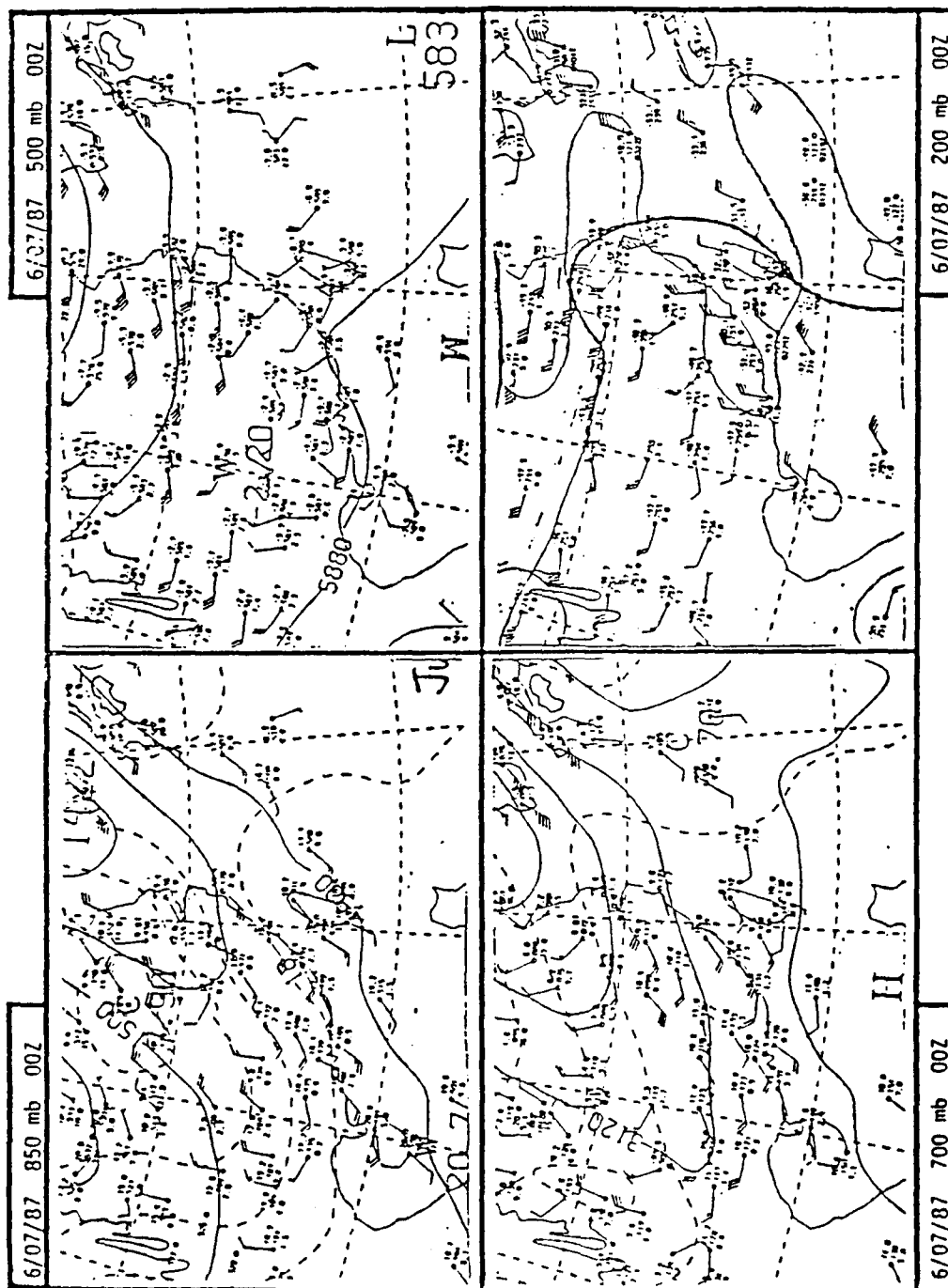
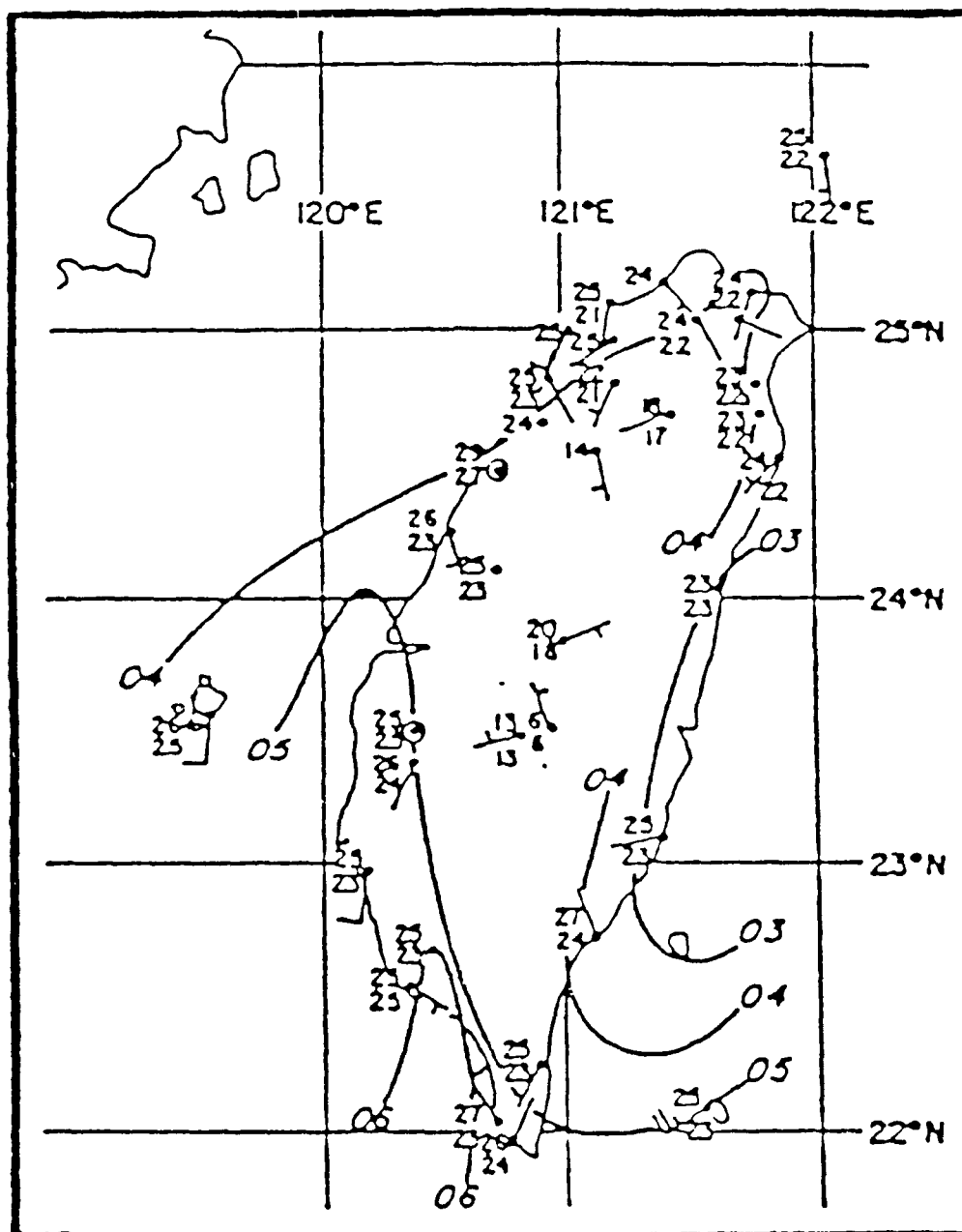


Fig. 3. Synoptic scale upper air analysis for TAMEX on 7 June. From Cunning (1988).



*Fig. 4. Sea-level pressure with 1-mb contour intervals. Station model symbols have conventional meanings at 0600 LST for 8 June. From Trier et al. (1989).*

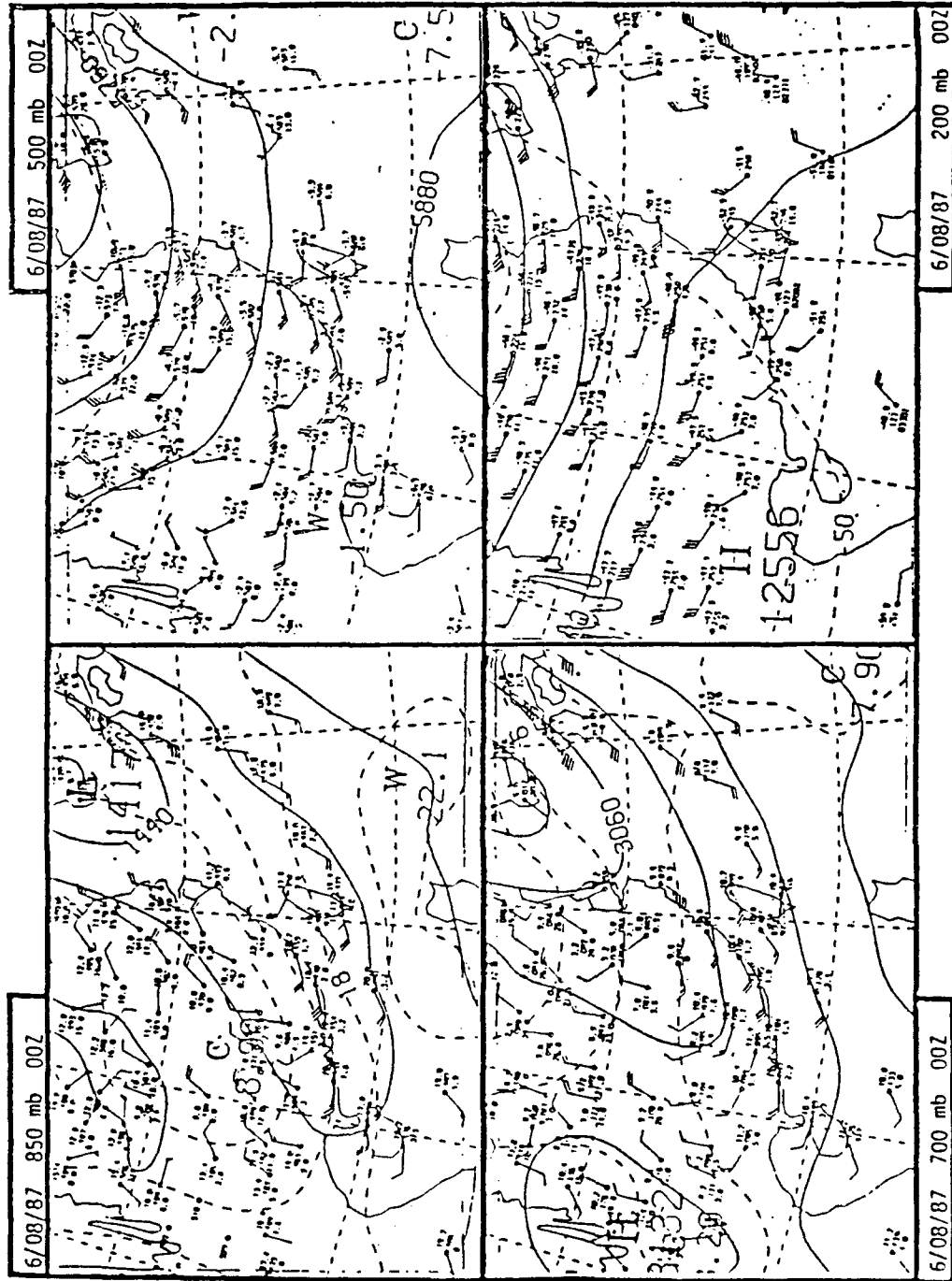


Fig. 5. Synoptic scale upper air analysis for TAMEX on 8 June. From Cuning (1988).

The forecast called for the front to continue to move eastward over the island. At 1200 LST, the surface ridge and trough pattern persisted over much of the island, except over the northern part, where analysis at this time showed the front in the Taiwan straits and over the northwest portion of the island (Fig. 6). A long line of frontal convection was observed with maximum reflectivity values of 40–45 dBZ. Trier *et al.* (1989) observed that this front was characterized by sharp temperature and moisture contrasts. Winds observed behind the front shifted from southerly to northeasterly, paralleling the coast. On the northeast side the flow turned onshore. The frontal convection continued to move onshore over the next few hours. The convection was quite extensive, as it covered the area from north of the island down to central and southern Taiwan. During this time the winds in the higher terrain of the Central Mountain Range remained predominately southwesterly, indicating that the front was a shallow phenomenon. Lower pressure replaced the pressure ridge on the windward side. The flow pattern suggests that the low-level northerly flow split, and was being channeled around the Central Mountain Range (Trier *et al.*, 1989). By 1800 LST, most of the convection ended in the dual-Doppler area, although some convection still moved onshore over southern Taiwan, as shown in Fig. 7.

Stations on the western side of the island reported that after the front had passed, dewpoints dropped 7°C, and pressure rose 1.7 mb, signaling the onset of



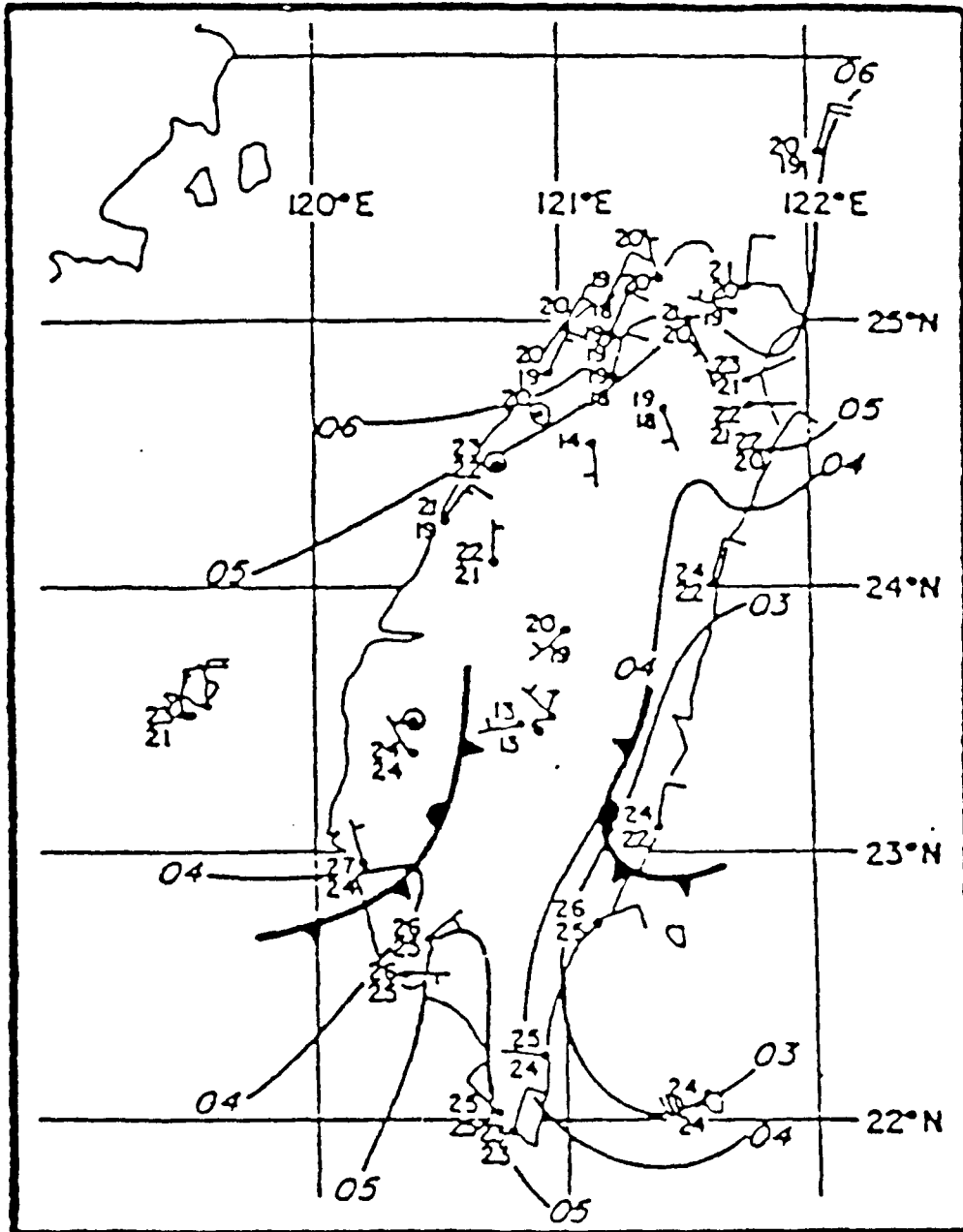


Fig. 7. Sea-level pressure with 1-mb contour intervals. Station model symbols have conventional meanings at 1800 LST for 8 June. From Trier et al. (1989).

the cold air mass. Pressure values remained stable through the afternoon and then rose significantly in the evening hours. This rise may have been the result of an increase in the depth of the cold air accompanying the northerly flow.

The eastern seaboard of the island experienced a different reaction to the frontal passage. In the east, surface heating created onshore flow by late morning, causing the flow to move back to the northeast by early afternoon. In the evening hours, the wind pattern returned to a weak offshore flow (even after frontal passage). This was in contrast to flow on the west coast where strong northeasterly flow was observed. The dewpoints on the east coast dropped only  $1^{\circ}\text{C}$ . The east coast surface pressure increase was the only real indication that the weather had changed. Thus, the strong diurnal forcing masked the east coast frontal passage. Trier *et al.* (1989) observed that the wind speed behind the front was about  $12 \text{ ms}^{-1}$ . At 0000 LST, 9 June, the Doppler radars ceased operations. By 0800 LST, 9 June, the surface cold front moved east of Taiwan and the island became dominated by a large high pressure system (Fig. 8) and IOP #8 ended.

## 1.2 Tropical Mesoscale Convective Life Cycle

Rotunno *et al.* (1988) used model simulations to deduce the structure and evolution of squall lines. In accord with observations, they found that squall lines are fed by air of high equivalent potential temperature,  $\theta_e$ , and that air at the rear

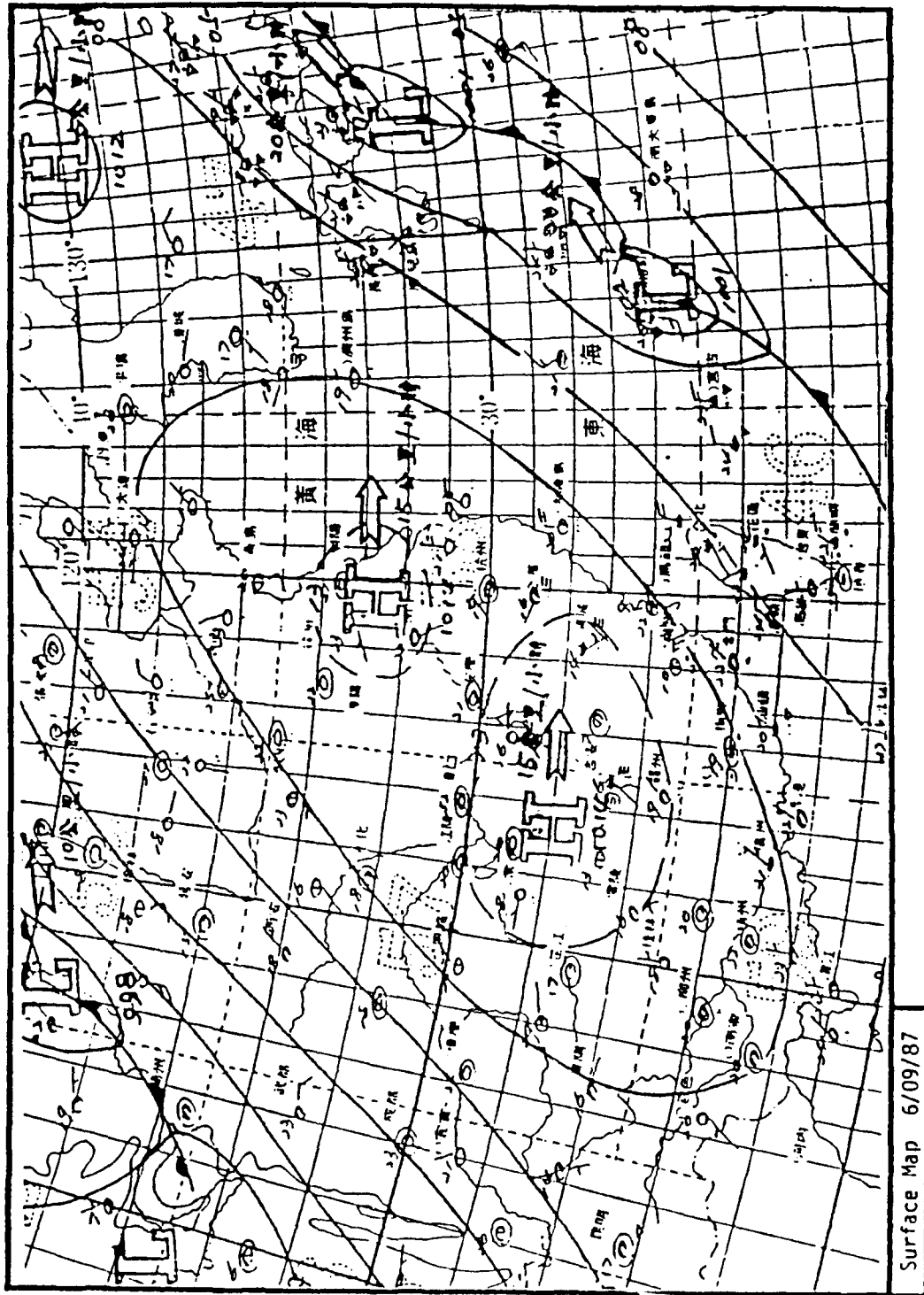


Fig. 8. Synoptic scale surface analysis for TAMEX on 9 June. From Cunning (1988).

of the line is cooler and has a lower  $\theta_e$  than the air in front of it. They used two- and three-dimensional models to examine whether a squall line is a system of long-lived cells, or a long-lived system composed of ordinary cells. Their experiments revealed that both types of squall lines can form. The type that forms depends on the magnitude and orientation of the environmental shear to the squall line. Shallow shear, oriented perpendicular to the squall line, develops a long-lived line with short-lived cells, suggesting an interaction between cells. Cold surface outflow and low-level shear creates much deeper lifting than is possible without the shear, allowing for new cell formation as the old cells decay. With deep shear, a line of long-lived cells form. The environment of the slow mover is characterized by little or no shear, and a significantly more moist layer above the boundary layer than that of the fast mover. Rotunno *et al.* (1988) showed that the value of the shear necessary to maintain a long-lived state depends on the properties of the cold pool. The cold pool, in turn, is dependent on the thermodynamic sounding and the type of the convection created. As the temperature in the cold pool decreases, it begins to overcome the low-level shear. It then starts to surge outward underneath the updraft in the downshear direction. This creates an upshear tilt; and it is this upshear tilt that signals the dominance of the cold pool circulation which leads to less intense convection.

Tropical convection is often classified as a Mesoscale Convective System (MCS) because tropical convection shares a similar structure and a common dynamical ba-

sis with mid-latitude convection. Leary and Houze (1979) studied tropical convection using GARP Atlantic Tropical Experiment (GATE) data. In this study they examined six mesoscale cloud clusters that occurred on 5 September 1974. The focus of the study was on the structure and evolution of the convection. The convective cycle is sub-divided into four stages: the formative stage, the intensifying stage, the mature stage, and the dissipating stage.

### 1.2.1 The Formative Stage

In the formative stage the tropical Mesoscale Convective System (MCS) consists of a line of isolated echoes. When a MCS organizes into a linear system it is called a squall line. There are special conditions that are believed to be required for the formation of squall lines. Most important is an unstable air mass, that is, an air mass that is warm and moist at low levels and relatively colder aloft. A dryline above the warm moist layer enhances the vigor of the squall line. Precipitation that evaporates in this dry region cools the air and increases the negative buoyancy, which in turn strengthens the downdraft and outflow. Once the squall line has formed, it will be able to maintain itself through convergence along the outflow boundary. This causes strong ascent into existing updraft areas, or initiates convection ahead of the storms that already exist (Hane, 1986).

Most convection forms in a conditionally unstable environment with a triggering mechanism. An unstable environment is insufficient to initiate squall line

convection; a triggering mechanism is required. An example of a triggering mechanism is a cold front. The triggering mechanism can be a cold front or a dryline. The intersection of a front and a dryline can produce frontogenesis, as examined by Kessinger and Bluestein (1979) and Bluestein and Berry (1982). Newton and Fankhauser (1964) examined a method in which a squall line grew by adding new cells to the southern edge of the line. This building occurs either as a result of an upper level disturbance moving south over a surface discontinuity, or because the outflow from a storm interacts with inflow at the southern end of the line. This forms a convergence zone, and thus an area conducive to new convective growth.

Leary and Houze (1979) stated that echoes viewed in a vertical cross-section have vertically-oriented contours of reflectivity. This initial formation is typical of situations that develop into areas of high intensity, as well as lines of echoes that dissipate without any further development. Thus, the factors that control the development are not structural, but dynamical. The lines that dissipate without an increase in development are found to be aligned nearly parallel to, and move in the same direction as, the surface wind. The lines of convection that are observed to intensify are found to be aligned more nearly perpendicular with, and move in the opposite direction of, the surface wind. The low-level outflow from the convective scale downdrafts in these echoes are aligned perpendicular to the surface wind. This causes a modification of the local low-level convergence pattern, making it conducive for new cell formation in the upwind direction. Further, if the convective downdraft

is assumed to propagate outward in a radial fashion, then low level convergence (and thus, new cell formation) is favored between the individual echoes in the line.

### 1.2.2 The Intensifying Stage

In the intensifying stage, development in the upwind direction contributes to the propagation speed of the mesoscale precipitation region. New cells form along the leading edge of precipitation before the older cells at the rear can dissipate. This broadens the mesoscale line. When new cells are generated between the older cells, they merge with each other. The resulting formation appears as a large echo, with many intense convective cores. These echoes grow in height, and the upper level winds carry the cloud and precipitation particles downwind, forming the cirrus shield, or anvil.

### 1.2.3 The Mature Stage

Leary and Houze (1979) state the mature stage resembles the intensifying stage in many respects. In the mature stage, the echoes exhibit extensive development both in surface precipitation pattern and in the vertical cross section. The deep convective cells at the leading edge overlie the most intense surface precipitation. Upper level winds continue to carry cloud and precipitation particles downwind. The major difference in the structure between the mature and the intensifying stage is that in the mature stage an extensive region of horizontally uniform precipitation

is to the rear of the most convective cells. This region to the rear is composed of cells from the leading edge of the line that have weakened as they blend together, and "moved" to the rear of the precipitation region. In this horizontally uniform region, often a bright band of radar reflectivity can often be seen. This bright band is located in the melting layer, just below the 0°C isotherm. This horizontally stratified reflectivity pattern is inconsistent with the patterns found in areas of convective scale up and downdrafts (Leary and Houze, 1979).

#### 1.2.4 The Dissipating Stage

The transition from the mature stage to the dissipating stage is a gradual one. Intense convective cells continue to form along the leading edge, but they become progressively shallower, and eventually cease to form at all. Then the large area of uniform precipitation begins to slowly dissipate until only a few fragments of the original mass remains (Leary and Houze, 1979).

### 1.3 Echo Scales and Sizes

Houze and Cheng (1977) analyzed the echoes observed during the GATE experiment. Although their study did not examine frontal systems specifically, it did describe the radar echoes in terms of area, heights, duration, intensity, motion, and the orientation of the echo lines. Their study was based on the analysis of radar data, but it did not involve radar intercomparisons, calibration studies or extensive

data processing. It was intended to serve as a predecessor for more quantitative analysis.

The horizontal area of precipitation was divided into a series of size scales. The scales were denoted: the B/C scale for  $10^3$ – $10^5$  km<sup>2</sup>, the C scale for  $10^2$ – $10^3$  km<sup>2</sup>, and the D scale for areas 1– $10^2$  km<sup>2</sup>, or less. The population of radar echoes recorded in GATE were predominately in the D scale range (67%) and the C scale accounted for 28%. These echoes, however, covered only 21% of the total area of echoes. Thus, only a relatively few large precipitating areas are found in tropical cloud populations, but these take on importance when their areal extent is considered. The average height for scale echoes D was 4.3 km; for C scale echoes, the average height was 5.8 km, and for B/C scale echoes, the average height was 9.9 km. The average height of the GATE echoes was 4.8 km. Echo duration was positively correlated with the echo area coverage. The overall mean echo duration was 88 minutes. Most of the echoes lasted less than 50 minutes. Echoes with high intensity cores were most often observed in the B/C regime. Echoes that exceeded  $10^4$  km<sup>2</sup> in area contained as many high intensity cores as moderate and low-level intensity cores. Higher intensity cores were more often found in the B/C scale, indicating that these large echoes form in an environment favorable for the development of intense cores, or that the more intense cores created surrounding areas of widespread precipitation. Houze and Cheng (1977) calculated that there was an average of one echo core for every 187 km<sup>2</sup> of echo area.

James and Browning (1979) used Doppler radar to study 15 examples of frontal convection. The Doppler radar data used in this study was collected by Meteorological Office Radar Research Laboratory during the years 1968-1977. The convection was often broken into cells with the average length of an element 22 km and the average gap between cells 9 km. Occasionally, the features ranged in size from a few kilometers to 100 km. The gaps between cells also varied in length. They were usually a few kilometers to tens of kilometers wide, but in one case they were observed to be 95 km wide. The lifetime of the elements was also found to vary, ranging from 10 minutes to 4 hours. However, James and Browning (1979) found that linear convection can be up to 200 km long, with no elemental structures present. In this situation, areas of higher echo intensity can be observed within the line. They found no distinguishing thermodynamic or dynamic characteristics that would account for the difference in the elemental and non-elemental structures. The convection in the cases with no elements was slower moving and exhibited a slightly greater vector wind and temperature change across the frontal zone.

#### 1.4 Echo Morphology

Continuity and geometric relationship of the echoes, and the persistence of precipitation are some of the characteristics of a squall line. Squall lines tend to favor formation in areas of quasi-linear forcing in the warm sector.

Kessler and Wexler (1959) used an incoherent radar to observe a passing cold front in New England in one of the first observations of a cold front with a radar. The front was characterized by strong gusty winds and heavy rain showers with a squall line ahead of the front. Convection in the squall line was limited to a height of 4 km, whereas the convection closer to the front reached heights up to 10 km. The most intense convection was below 4 km, where temperatures were greater than 0°C. The cold front had strong vertical velocities at low levels, and unusually heavy precipitation.

Browning and Harrold (1970) used a Doppler radar to study two cold fronts that passed through Great Britain. They studied the two-dimensionality of the frontal structure over a 25 km length. Intense echoes, extending to 3 km in the vertical, were observed at the leading edge. This is comparable to the heights found by Kessler and Wexler (1959). Behind the front, the tops of the echoes extended up to a height of 6 km. Behind the line of most active convection, a 500 m thick layer of warm air ascended at a small angle relative to the surface. The base of this warm-air layer was 1.5 km height immediately behind the front, ascending to a height of 4 km, 100 km behind the front. Radar data showed that the line was devoid of pronounced cellular structure. Cellular patterns are commonly associated with cumuloform convection. Thus, Browning and Harrold (1970) stated that, to a first approximation, the flow in the surface cold front could be treated as two-dimensional. This assumption was further justified when Browning and

Harrold examined 8 vertical sections that were taken over a 25 minute period along a 24 km section of the front. Each of these vertical sections had similar airflow patterns, supporting the two-dimensional approximation. An interesting feature of the observed echo pattern was the occasional appearance of a vault. A vault is a region of relatively (compared to its surroundings) weak echo within the updraft core. A vault, up to this point, had only been observed in severe local storms. In this case, the vault was 1-2 km wide and the echo was 15 dB less than the surrounding echo area.

Hobbs *et al.* (1980) examined a passing frontal system that was 125 km wide and composed of five mesoscale rainbands. The data was recorded by NCAR's CP-3 radar on 17 November 1976, during the University of Washington's Cyclonic Extratropical Storms (CYCLES) Project. Four of these rainbands were several tens of kilometers wide, and the other band, which was coincidental with the surface front, was only 4 km wide. These bands contained precipitation cores that varied in size from 25 to 300 km<sup>2</sup>. The wide cold-frontal rainbands had irregular shapes and were randomly positioned. The cores associated with the narrow cold-frontal bands were elliptical. The height of the core tops were determined by the Doppler radar observations. The tops of the wide rainbands extended to 5-6 km. The tops of the narrow band were between 1.5-4.5 km in height. Doppler measurements were used to deduce the wind directions throughout the frontal system. Near the leading edge of the frontal system, a one km thick overhanging cloud of precipitation extended

approximately 30 km in front of the system. Another overhanging area 5 km thick extended 90 km behind the main body of the frontal system. Precipitation from this rearward extending overhang evaporated prior to reaching the ground.

In general, the observations have shown that the echoes exhibit certain characteristics: a line of intense echoes, about 4 km high at the leading edge of the echo region, followed by an area of echoes that increase in height, corresponding to the front aloft. Finally, the examination of cross-sections revealed a two-dimensional character of the system.

### **1.5 Flow Patterns, Convergent and Divergent Patterns**

The understanding of dynamical forces and interactions has been greatly advanced by three-dimensional time-dependent numerical models. Coupled with this have been the advances in dual- and triple-Doppler radar analysis to illuminate the internal storm structure.

Bergeron (1954) and Pedgley (1962) studied the flow patterns within a squall line. They observed that the region of stratiform rain ascended at high levels and descended at low levels. An area of strong convection was found at the leading edge of the system. Smull and Houze (1985, 1987) used Doppler radar data to show that updraft flow exists ahead of the line's outflow, and that this updraft tilts backwards into the line. Another characteristic that they found was a region of back-to-front flow near the post-line rainband at 3-8 km height level. This rear

inflow is not commonly seen with tropical squall lines. This is most likely because the tropics lack the strong instability, strong cold pools, and strong shear needed for maintenance of this flow (Ray, 1988).

Kessler and Wexler (1959) observed that by increasing the gain, they were able to observe gaps of a few kilometers between the echoes from the heavy rain and the lighter precipitation on the upper side of the front. This suggested that the updraft currents were associated with adjacent compensating downdrafts.

Browning and Harrold (1970) analyzed a cold front by tracing the pattern of motion using the wet bulb potential temperature as a tracer of airflow. They observed a narrow tongue of warm air just ahead of the front. This warm air was advected (relative to system movement) by strong geostrophic flow, moving parallel to the front. It was this prefrontal warm tongue, ascending at the front, that was responsible for the growth of frontal precipitation. They treated the flow in this warm tongue in two parts. The first part was for the 1-3 km height flow, which was parallel to the front. Below the 1 km height, winds backed due to surface friction, and a component was observed toward the cold front. The overall flow pattern in the warm tongue showed mass flux toward the front in the lowest kilometer of the frontal zone. This was fed by subsiding air from the flow parallel to the front. The flux toward the cold front was seen to rise when it entered the line of convection accompanying the surface cold front.

The warm air flow parallel to the front had a component of velocity of  $24 \text{ ms}^{-1}$  parallel to the front, and a component of  $2 \text{ ms}^{-1}$  toward it. Below 1 km, flow into the front was in a region where convergence values were  $10^{-2} \text{ s}^{-1}$ . The updraft flow was seen tilted  $60^\circ$  from the horizontal, reaching a maximum speed of  $8 \text{ ms}^{-1}$  at 1.2 km in height. The updraft extended to 3 km height. Below this, the horizontal divergence values were as large as  $9 \times 10^{-3} \text{ s}^{-1}$ . Some of this divergent air flowed into the area ahead of the front, but most of it departed the surface frontal updraft area in the rear of the front between the heights of 1 and 3 km. This air then began to ascend on a gentle slope, as previously discussed. Downdraft flows were almost always less than  $1 \text{ ms}^{-1}$  in the cold air, which is consistent with the absence of pronounced surface gusts, or humidity drops, both of which are commonly observed in squall lines.

Radiosonde data taken prior to frontal passage revealed a neutral lapse rate at almost all levels. The Doppler observed streamlines showed that the cold air did not overrun the warm air mass. Instead, the warm air rose over the advancing cold air. Thus, the convection line was produced by forcing, rather than by free convection. This forced convection viewpoint is supported by the absence of cellular structure at the surface cold front. Almost the entire updraft at the surface was the result of frictional convergence. The large flux of air, and hence the precipitation, were associated with the large values of flow parallel the front at the leading edge (Browning and Harrold, 1970).

Behind the nearly vertical ascent at the surface, the warm air gradually ascended towards the rear of the system. This warm air was found in a shallow layer between the advancing cold air wedge and the stable layer at 3 km height. The circulation in this area was well marked, with updraft values in the warm air of  $20 \text{ cm s}^{-1}$ . The descent in the cold air was also evident, but it was weaker compared to the ascending warm air. This was not just a simple case of warm air riding up and over the advancing cold wedge, because the transition area from ascent to descent was within the warm air instead of the frontal zone. The cloud base, assumed to be at the level of this transition, was in the warm air. The cold air descended, with the strongest area of descent in the frontal zone itself. The downward velocities of the air in the frontal zone was comparable to the ascending warm air ( $20 \text{ cm s}^{-1}$ ). The maximum wind speed toward the surface front was  $8 \text{ ms}^{-1}$ . Browning and Harrold (1970) further noted that although the cold frontal zone was characterized by an area of descent, there was an apparent downward extension of the region of ascent into the frontal zone. This feature may have been associated with an undulation in the frontal zone boundaries such that air remained within this zone. It also may have been the result of a small flux of air upward through the frontal zone. Doppler radar resolution of this region showed that the airflow pattern was fluctuating rapidly on a scale of kilometers, indicating that this was an area of strong mixing. Mixing is consistent with earlier studies. In the lowest few hundred meters, the cold air was frictionally retarded to the point that a component

was seen in the direction away from the cold front. The depth of this rearward flow increased from near zero at the front to 1 km at 80 km behind the front.

Parsons *et al.* (1987) deduced the pressure fields in a squall line. A high pressure area was found below the maximum updraft, with pressure increasing at low levels when going from the warm sector to the cold sector, and a low pressure above the cold air with a pressure minimum above the front. It was this vertically-oriented pressure gradient that created the updrafts in the absence of potential instability. Examination of the buoyancy fields showed no evidence for buoyancy-created updrafts. Thus the theory of forced convergence and vertical pressure gradient forced updraft was further supported (Parsons *et al.*, 1987).

Moore and Heggli (1979) studied a winter squall line and cold front that passed through California on 5 February 1978. A low-level jet of  $25 \text{ ms}^{-1}$  was located just ahead of the front. Satellite cloud band tracking showed that the front moved at about  $30 \text{ ms}^{-1}$  over the Pacific ocean. Intense convection was observed by satellite 2–3 hours before landfall. A general area of subsidence was indicated around the squall line. Radar analysis of the front showed that the low-level jet was converging with the southwesterly winds from behind the front. The radar recorded reflectivities exceeding 50 dBZ. The size of the higher reflectivities areas extended up to 2 km wide. The reflectivities lacked the characteristics of cellular type formation. Other features were seen on the  $1.1^\circ$  elevation scan. An area of subsidence was seen proceeding the frontal band. This area extended 50 km ahead of the front. The

frontal position, as determined by the velocity discontinuity line on the Doppler radar, was placed just ahead of the line of the strongest reflectivities.

Soundings taken prior to frontal passage revealed that the environment was, in general, neutral to slightly stable. Doppler measurements showed that the low-level jet (1.2 km in height) and the area below it was the source of air drawn into the front as it passed. Updraft velocities reached  $17 \text{ ms}^{-1}$  at the 1.8 km height. One prefrontal unstable level was found between 0.5 and 2.0 km in height. By comparing the observed velocities with the velocities that could have been created by positive buoyancy ( $15 \text{ ms}^{-1}$ , in this case), Moore and Heggli (1979) concluded that the vertical motions were due to boundary layer forcing, and not hydrostatic instability. Post-frontal soundings revealed neutral stability below 1.7 km, an isothermal layer (associated with the upper level front) from 1.7-2.0 km, and stable layers above 2.0 km. Horizontal divergence was seen just above the frontal boundary. It was also observed that as the front moved over land it propagated at approximately  $20 \text{ ms}^{-1}$ , but it slowed to about  $10 \text{ ms}^{-1}$  as it encountered the mountains.

Newton (1950) and Newton and Newton (1959) showed that new convection formed in the convergence zone of the outflow boundary. They stated that this was maintained by the transfer of westerly momentum downward. Kessler and Wexler (1959) also observed very large horizontal convergences confined to a very narrow zone near the ground. This created a rapid increase in the vertical velocities with height at the lower levels. The radar also indicated the presence of strong horizontal

divergence above the frontal zone at the 2.5 km to 4.0 km levels. The radar detected heavy rain that maintained its position along the front, moving at the same speed as the front. Kessler and Wexler (1959) also observed that cell development appeared to occur on the forward edge of the heavy rain line, and that dissipation occurred on the back edge. The convective character of the front's precipitation was seen to strengthen as a result of daytime heating. Strong northwest winds were recorded that exceeded the winds aloft, as measured by radiosonde. Thus, it was determined that these gusts could not be due to transport of momentum through vertical motions alone. Kessler and Wexler theorized that the gusts were probably due to localized strong pressure gradients near the front.

Matejka and Houze (1978) analyzed the airflow in a vertical cross-section of the cold front. The data was recorded by NCAR's CP-3 radar on 17 November, 1976, during the University of Washington's Cyclonic Extratropical Storms (CYCLES) Project. To investigate the airflow within the cold front, they applied the equation of continuity to the horizontal component of the velocity in a single vertical plane, oriented perpendicular to the front. The vertical velocities were calculated assuming that no divergence occurred along the front, and the cross-front divergence was integrated upward in one-third km intervals from the surface. This was done using zero for vertical velocity at the surface. The analysis of the cross-front divergence showed that the strongest convergence ( $1.9 \times 10^{-3} \text{s}^{-1}$ ) occurred at the surface windshift in the lowest kilometer. Weaker convergence straddled the cold

front aloft and divergence was seen above and ahead of the front. The strongest area of divergence was at a height of 1.5 km, immediately in front of the surface wind shift. The pattern of vertical velocity revealed two distinct regions of ascent. One region, intense and small, was found in the area of convergence associated with the wind shift. The other region of ascent was larger and was located above the cold frontal surface aloft. The airflow in the warm sector moved toward the front (in a relative sense) at speeds of  $13 \text{ ms}^{-1}$ . When it reached the front, this air rose in a column 4 km wide at  $1 \text{ ms}^{-1}$ . When the air reached approximately 3 km in height, wind carried it forward. Thus, it is possible that precipitation from this area may have fallen into the convection at the leading edge of the system, ahead of the surface wind shift. A  $0.5 \text{ ms}^{-1}$  downdraft, 4–5 km wide, was observed just ahead of the updraft. The base of this downdraft was at the 1.5 km height, which coincided with the location of maximum divergence. The updraft-downdraft couplet observed by Matejka and Houze is typical of cumulonimbus storms. Thus, they were able to distinguish smaller scale flows within the broader band of frontal motions. The broader region of ascent associated with the cold front aloft had vertical motions of a fraction of a  $\text{ms}^{-1}$ . This was a result of the convergence that straddled the front aloft. Matejka and Houze (1978) also observed that this ascent was not uniform throughout the frontal band, and in areas where the velocities were stronger heavier precipitation was observed. Their results confirm the earlier results of Browning and Harrold (1970) showing two distinct regions of ascent.

Carbone and Serafin (1979) studied the same front as Moore and Heggli (1979). Their data set had two limitations—one was that a power loss prevented data acquisition above elevation angles of  $15^\circ$ . The other limitation was that surface horizon prevented two of the radars from data collection below 0.9 km. The data was interpolated to a Cartesian grid using an isotropic Gaussian weighting function, with a 300 m half-weight radius. The sphere of influence extended to 750 m in radius. The grid spacing was 300 m in all directions. This filter radius and grid spacing combination resolves motions greater than 1.2 km in wavelength. Mass continuity was used to indirectly obtain vertical motions. An upper boundary condition of  $w = 0$  at  $z = 6.3$  km was used. This value was in line with the hydrostatically stable environment, especially when one takes into account the stratiform reflectivity structure and the weak divergence at the storm top. Downward integration of the continuity equation was the final step. The general circulation of the front and the squall line remained steady, until tornadic formation began to occur.

When the eddy velocity field was examined, at the 3.6 km height, strong two-dimensional divergence was observed. Carbone and Serafin (1979) also examined the storm relative wind field. In doing this, flow parallel to the main band was seen. This denoted the area of reflectivity overhang. Most of the diverging updraft exits to the rear of the line. Two-dimensional cross sections of the line revealed an up/downdraft couplet that was similar to those found in multiple-Doppler syntheses. Carbone and Serafin (1979) observed that the vertical updraft was 4 km wide, and reached speeds

of  $17 \text{ ms}^{-1}$  at 1.8 km height, in agreement with Moore and Heggli (1979). Further, Carbone and Serafin (1979) found that the updraft became divergent at 2.1 km, decreasing in speed, and reached a maximum height of 6.0 km. The majority of this air exits the storm at the rear flank. The maximum downdraft speed was  $12 \text{ ms}^{-1}$ , and was found immediately behind the surface convergence line. This was also the area of the highest reflectivities and greatest rainfall. From the southwest, below 2 km, westerly momentum air was seen approaching the convergence line. Shallow post-frontal clouds were seen in this area. The average vertical velocity was  $3 \text{ ms}^{-1}$ .

Hobbs *et al.* (1980) conducted a more detailed study of the cold front examined by Matejka and Houze (1978). Not unexpectedly, many of the results in this study are in good agreement with those from the earlier work. The analysis by Hobbs *et al.* (1980) examined the frontal system over a longer time period, and, thus, it included a study of the front prior to landfall. The radar was used to obtain the cross-band component of the horizontal wind in vertical planes perpendicular to the rainbands. Vertical velocities were calculated using the continuity equation on the cross-band component. The values obtained were then plotted and a subjective isotach analysis was done. This smoothed the data by eliminating any cumulus scale irregularities in the wind field. Further smoothing was obtained when the cross-band speeds were obtained from the isotach analysis and applied to rectangular grid points, and then horizontal convergences were computed over grid spacings of 2.6, 5.2, and 10.4 km. These divergences were then integrated upward from

the surface in one third km steps. A vertical velocity of zero was assumed at the surface. The vertical velocities obtained were then combined with the cross-band components to obtain winds that represented the instantaneous airflow in a vertical plane oriented perpendicular to the rainbands. Examination of the results showed that the figures obtained with a 2.6 km grid spacing were too noisy, and the ones obtained with a 10.4 km spacing were too smooth. Thus, Hobbs *et al.* (1980) used the 5.2 km grid spacing for analysis. The original assumption of nondivergence in the direction parallel to the rainbands was checked by radar. Hobbs *et al.* (1980) compared Doppler measurements in the north-northeast and the south-southwest, that is, the directions parallel to the frontal system. The magnitude of divergences found were almost always less than  $1.0 \times 10^{-4} \text{ s}^{-1}$ . The cross-band values ranged from  $3 \times 10^{-4} \text{ s}^{-1}$  to  $19 \times 10^{-4} \text{ s}^{-1}$ . These results indicate that the rainbands are approximately two-dimensional, and that the general flow pattern in the rainbands can be found by using the cross-band velocity component.

The divergence field of one of the wide bands was examined after it passed the surface front. At the ground a very shallow layer of convergence was seen. Above this, up to 3 km, the lower layer was characterized by weak divergence. From 3–5 km in height there was an area of convergence with magnitude of  $5 \times 10^{-4} \text{ s}^{-1}$ . This created ascent aloft, with vertical velocities of approximately  $1 \text{ ms}^{-1}$ . The airflow through the rainband was generally from the front to the rear. The updraft area in the narrow band was about 5 km wide, and up to the height of 1.5 km with speeds

of  $1.2 \text{ ms}^{-1}$ . The updraft originated in an area of strong low-level convergence, with values of up to  $1.9 \times 10^{-3} \text{ s}^{-1}$ . The air that flowed parallel to the front in the lowest 500 m moved, in a relative sense, toward the surface pressure trough, where it ascended in the narrow updraft. When this updraft reached the 3 km height, strong upper-level westerly winds moved the precipitation eastward. A downdraft was coupled with this updraft. This downdraft was also about 5 km in width and had speeds of approximately  $0.5 \text{ ms}^{-1}$ . It was located between the heights of 1.5 and 3 km, and at its base the divergence reached a value of  $1.0 \times 10^{-3} \text{ s}^{-1}$ . The air within the cold airmass had little motion relative to the front, but the air above it flowed backwards and ascended relative to the front. This ascent was generally caused by convergence along the upper level front. The greatest values of vertical velocities ( $60 \text{ cm s}^{-1}$ ) were found over the wide rainbands to the rear of the surface front.

### 1.6 Storm Movement

When examining echo motion, the echoes associated with tropical squall lines were omitted by Houze and Cheng (1977), since the movement of these echoes is faster than, and unrepresentative of, the general population. It was determined that the remaining echoes moved at  $3\text{--}5 \text{ ms}^{-1}$ . The average direction of motion was compared to the streamlines of the 850 mb and 700 mb levels. From this it was determined that the echoes were mostly advected by the 850 mb wind flow.

Some of the echoes whose area was less than  $500 \text{ km}^2$  moved in an erratic fashion, but when the echoes of this size moved in a well-defined fashion, they followed the 850 mb streamline winds. Approximately 83% of the isolated echoes examined were elongated in the horizontal. Their orientations were compared to the GATE windfield. There was a tendency for the echo lines to be parallel with the lower level winds. The angles of the echo lines compared to the 850 mb streamlines was generally less than  $45^\circ$ . Houze and Cheng (1977) also observed that large groups of echoes tended to form into lines. These lines were strongly oriented more with the low level winds compared to the isolated echoes, having angles with the streamlines of  $\pm 25^\circ$ . The results of Houze and Cheng (1977) from GATE data (which is from the eastern tropical Atlantic Ocean) were analogous to those determined from western tropical Atlantic Ocean data.

James and Browning (1979) stated that despite the variation in sizes and lifetimes, the convective frontal elements displayed some common features. They were always oriented clockwise to the surface cold front and the cores all moved in the same direction with a component parallel to the direction of the low-level jet. The structure of the line showed no relation to topography. In many of the cases the fronts passed over the mountains in Wales without apparent modification. This lack of topographical effect seemed strange when it is considered that the linear formation is a low-level phenomenon. Another surprising find was that despite the low nature of the line convection, it produced that intense rain.

### 1.7 Mid-Latitude and Tropical Comparison

As a whole, studies seem to support the conclusion that there are very few features which distinguish tropical squall lines from those in the mid-latitudes. The most significant difference cited is that mid-latitude squall lines occasionally are composed of individually steady supercell-type storms, tropical squall lines are not. Several similar key features have been noted, they are:

- (1) The wind field appears to be stationary when compared to the squall line reference frame.
- (2) There is a nearly two-dimensional air circulation over part of the squall line.
- (3) Two horizontal flows are observed: one is a flow toward the squall line caused by the lines motion relative to the environmental motions, and the other is a rear-to-front flow below 4 km.
- (4) Intense updrafts are located at the leading edge.
- (5) The downdrafts are weak and do not appear to play a significant role in the system's dynamics.
- (6) Leading edge forcing is caused by a cold pool and low-level convergence which are maintained by the rear-to-front flow during the mature phase of the squall line system.
- (7) The leading edge, referred to as the "convective region", is the area of the maximum reflectivity values.

- (8) The area under the trailing anvil referred to as the "stratiform" region exhibits lower and more uniform reflectivity values, and may have a radar bright band (Ray, 1988).

## Chapter 2

### Methodology

#### 2.1 Doppler Radar Analyses

Two main types of synthesis were performed. They were: dual-Doppler analysis and Velocity Azimuth Display (VAD). Each of these is described in this chapter.

##### 2.1.1 Dual-Doppler Analysis

The TAMEX data used in the dual-Doppler analyses was collected by the NCAR CP-4 and the NOAA TOGA radars. The wavelengths ( $\lambda$ ) of these radars are 5.49 cm and 5.38 cm, respectively. The beamwidth for the CP-4 radar was  $1.02^\circ$  and the beamwidth for the TOGA radar was  $1.60^\circ$ . The Pulse Repetition Frequency (PRF) was 1250 Hz for both radars. The maximum unambiguous Doppler velocity, which defines the Nyquist co-interval, is given by

$$V_{max} = \pm \frac{(PRF)\lambda}{4} \quad (1)$$

Thus, the NCAR CP-4 has a maximum unambiguous Doppler velocity, or Nyquist co-interval, of  $\pm 17.16 \text{ ms}^{-1}$ , and the NOAA TOGA radar has a Nyquist co-interval of  $\pm 16.81 \text{ ms}^{-1}$ . All velocities exceeding this interval are aliased (folded), and are indistinguishable from the ones in the fundamental Nyquist co-interval, if conventional Doppler processing is used (Ray, 1988). For example, a

wind of  $20 \text{ ms}^{-1}$  toward the NCAR radar would appear as  $14.32 \text{ ms}^{-1}$ , because it exceeds the Nyquist co-interval. The raw data contained folded velocities and noise that would create errors in synthesis. Thus, these data were manually edited using a version of the RDSS editor ported to a Sun UNIX system.

Once all necessary deleting and unfolding was accomplished, the data was analyzed using a dual-Doppler synthesis method similar to that described in Ray *et al.* (1980). First, the analysis domain was chosen. The NCAR CP-4 radar was chosen to be the origin of the grid system. For this system, the NOAA TOGA radar was then located at the Cartesian coordinates of  $(-14.7, -41.3, 0.2)$  km, using a Lambert conformal map projection with  $23.50^\circ\text{N}$  and  $25.50^\circ\text{N}$  as reference latitudes. The grid spacing used was 1.0 km in all directions and the spherical influence radius used in the objective analysis was also 1.0 km. The grid domain was a square, 90 km on a side and 20 km in the vertical. Three versions of this grid size were used for the dual-Doppler synthesis. The location of these grids was dependent upon the location of the data. In each case, the NCAR CP-4 was located at the origin. The grids were: TAMEX West, a grid designed to encompass the western dual-Doppler analysis area over the Straits of Taiwan. The lower left-hand corner point of this grid is defined by the coordinates  $(-70.0, -60.0, 0.0)$ . TAMEX East, a grid designed to cover the eastern dual-Doppler analysis area over the central and eastern part of island. The lower left-hand corner point of this grid is defined by the coordinate point  $(-20.0, -70.0, 0.0)$ . TAMEX central, a grid designed to encompass

a central area that covers parts of both TAMEX West and TAMEX East. The lower left-hand corner point of this grid is defined by the coordinates (-45.0, -60.0, 0.0).

A radar collects data in a spherical coordinate system. Each sample volume is located at a given range, azimuth, and elevation from a radar. The radar's beam samples the atmosphere at regularly-spaced intervals along the beam. These sample volumes are called gates, and are defined by the beam width and a spacing (typically 150-250 meters) along the radial. For ease of analysis, the data which are collected in spherical coordinates are converted to Cartesian coordinates. During the time that it takes to scan through a storm the storm evolves. For the purpose of analysis, steady state is assumed. However, the data are adjusted to account for storm translation.

The reflectivity values are thresholded at 0 dBZ, where dBZ is a unitless quantity defined by

$$dBZ = 10 \times \log_{10} \left\{ \frac{Z_e}{Z_o} \right\} \quad . \quad (2)$$

The term  $Z_e$  represents the effective radar reflectivity factor ( $\text{mm}^6 \text{ m}^{-3}$ ), and  $Z_o$  is  $1 \text{ mm}^6 \text{ m}^{-3}$ . Power, not the logarithm of power, is averaged in the synthesis. This conversion is performed in order to avoid the low bias of the values that would result if averaging was in the logarithm of power. However, all displayed reflectivities are in dBZ.

The data are distance-weighted averaged using the weighting function given by the Cressman (1959). The Cressman weighting function is mathematically expressed as

$$W_i = \left\{ \frac{R_i^2 - d_i^2}{R_i^2 + d_i^2} \right\} \quad (3)$$

Here  $W_i$  represents the weight assigned to an observation at a grid point. The variable  $d_i$  is the observation to grid point distance and  $R_i$  is the influence radius, that is, the maximum distance allowed between a grid point and an observation point to which a weight is assigned. For this analysis, the value of  $R_i$  is 1.0 km.

By using data from two radars and the continuity equation it is possible to uniquely determine the three orthogonal components  $u$ ,  $v$ , and  $w$  of motion (See Appendix A). These correspond to the  $x$ ,  $y$ , and  $z$  directions, respectively. The equations for these components of motion are

$$u = \frac{R_1 V_1 (y - y_2) - R_2 V_2 (y - y_1) - W[(z - z_1)(y - y_2) - (z - z_2)(y - y_1)]}{(x - x_1)(y - y_2) - (x - x_2)(y - y_1)}, \quad (4)$$

$$v = \frac{R_2 V_2 (x - x_1) - R_1 V_1 (x - x_2) - W[(z - z_2)(x - x_1) - (z - z_1)(x - x_2)]}{(x - x_2)(y - y_1) - (x - x_1)(y - y_2)}, \quad (5)$$

$$0 = \frac{\partial u}{\partial x} + \frac{\partial v}{\partial y} + \frac{\partial w}{\partial z} - \kappa w \quad (6)$$

In these equations, the subscripts denote the radar number, the point  $(x_1, y_1, z_1)$  denotes the location of the radar one (NCAR), and  $(x_2, y_2, z_2)$  denotes radar

two (TOGA). The coordinate triple  $(x, y, z)$  is the grid point location,  $\kappa$  is the logarithmic rate of change of density with height,  $V_1$  and  $V_2$  are measured radial velocities,  $R_1$  and  $R_2$  are measures of range from each radar respectively, and  $W$  is described by the equation

$$W = w + V_t \quad . \quad (7)$$

Here,  $V_t$  is the particle terminal velocity. We assign a value to  $V_t$  by using the adjusted Joss and Waldvogel (1970) equations (See Appendix A). Then, using a value of zero for  $w$  for the boundary condition, values of  $W$  are computed. After calculating  $u$  and  $v$ , a new value of  $w$  is found using the inelastic continuity equation (Eq. 6). This equation is integrated down from the storm top, where the initial boundary condition was applied. This gives a new value of  $w$ , which, through Eq. 7, gives a new value of  $W$ . Through Eqs. 4 and 5, the computation is iterated. The iteration continues until the values of  $u$ ,  $v$ , and  $w$  converge, typically just a few times. The process is repeated at each level, using the value of  $w$  from the previous level as the first guess. The calculated components of motion are then variationally adjusted to an imposed constraint that sets the value of the vertically-integrated horizontal divergence (See Appendix B).

## 2.2 Errors

Errors are introduced in the collection and analysis of the Doppler velocities from several sources. One source is the rotation of the antenna. The rotating

antenna means that gates are displaced. This creates overlapping areas that are averaged and one value is assigned to a given gate. This averaged value may not be representative of the Doppler velocity in the space the gate occupies. Interpolation to a grid point is another source of errors. The velocity at the grid point is an average of nearby measured values. This interpolated value will vary from the true velocity at the grid point. Temporal errors can be caused by the advection and evolution of the storm. Some advection errors can be corrected by inducing storm motion into the analysis.

Both radar locations and the baseline (the line joining the radar location) are visible in all wind field plots. There are no wind vectors close to the baseline due to large errors that arise from the sampling geometry. The variances of the uncertainty in the wind components due to sampling geometry is given by  $\sigma_u^2$ ,  $\sigma_v^2$ , and  $\sigma_w^2$ , respectively (See Appendix C).

$$\sigma_u^2 = \frac{[R_1(y - y_2)]^2(\sigma_{V_1}^2) + [R_2(y - y_1)]^2(\sigma_{V_2}^2)}{[(x - x_1)(y - y_2) - (x - x_2)(y - y_1)]^2} + \frac{\{[(z - z_2)(y - y_1) - (z - z_1)(y - y_2)]^2\}(\sigma_W^2)}{[(x - x_1)(y - y_2) - (x - x_2)(y - y_1)]^2} \quad (8)$$

$$\sigma_v^2 = \frac{[R_2(x - x_2)]^2(\sigma_{V_2}^2) + [R_1(x - x_1)]^2(\sigma_{V_1}^2)}{[(x - x_2)(y - y_1) - (x - x_1)(y - y_2)]^2}$$

$$+ \frac{\{[(z - z_2)(x - x_1) - (z - z_1)(x - x_2)]^2\}(\sigma_W^2)}{[(x - x_2)(y - y_1) - (x - x_1)(y - y_2)]^2} \quad (9)$$

$$\sigma_{wk}^2 = \frac{1}{4} \left[ 1 + \left( \frac{\frac{1}{\Delta z} - \frac{\kappa}{2}}{\frac{1}{\Delta z} + \frac{\kappa}{2}} \right)^2 \right] (\sigma_{wk+\frac{1}{2}})^2 + \frac{1}{2} \left[ \frac{\sigma_u^2}{(\frac{2\Delta x}{\Delta z} + \kappa\Delta x)^2} + \frac{\sigma_v^2}{[\frac{2\Delta y}{\Delta z} + \kappa\Delta y]^2} \right] \quad (10)$$

To examine more closely the spatial distribution of uncertainty, location of radar 1 is placed at the origin, then all geometric variables ( $x_1$ ,  $y_1$ , and  $z_1$ ) are zero for a given level of analysis. Further, if radar 2 is located on the x axis, then  $y_2$  and  $z_2$  are also zero. Note that in this configuration, the x axis is the baseline. This reduces Eqs. 8 and 9 to

$$\sigma_u^2 = \frac{[R_1(y)]^2(\sigma_{V_1}^2) + [R_2(y)]^2(\sigma_{V_2}^2)}{[(x)(y) - (x - x_2)(y)]^2} \quad (11)$$

$$\sigma_v^2 = \frac{[R_2(x - x_2)]^2(\sigma_{V_2}^2) + [R_1(x)]^2(\sigma_{V_1}^2)}{[(x - x_2)(y) - (x)(y)]^2} \quad (12)$$

It is obvious that for a point on the baseline (x axis) the value of  $y$  is zero and the variances  $\sigma_u^2$  and  $\sigma_v^2$  in Eqs. 11 and 12 are unbounded. Thus, the uncertainty variances due to geometry are unbounded. Generally, if the point measured is close to the baseline (small  $y$  values), the error variances are very large. This large variance at points close to the baseline is what makes the near baseline plotted vectors suspect.

Equation 10 is dependent upon the values of the error variances of  $u$  and  $v$ . The error variance of  $w$  is either unbounded or suspect at or near the baseline, respectively.

### 2.3 Velocity Azimuth Display

One method of using the measurements of horizontal winds from a radar scan is the Velocity Azimuth Display (VAD) (Lhermitte and Atlas, 1961). When the wind and precipitation fields are horizontally homogeneous, a Doppler radar may be used to measure both wind particle and fall velocity. Given a tilted radar beam, the radial velocity is caused by both the particle fall velocity and the motion of the particle with the horizontal wind. Browning and Wexler (1968) used VAD technique to analyze the harmonics of the VAD. The mean of the Doppler velocity, or the magnitude of the "zeroth" harmonic, permits an estimate of the divergence. The first moment will be displayed as a sine curve. The amplitude of this curve will give a measure of the maximum velocity at the range at which the winds are examined. The phase of the first harmonic gives the direction of the wind at the sampled altitude. Lhermitte and Atlas (1961) concurred with this by stating that the direction of the horizontal wind was given by the azimuth of the maximum velocity. The displacement of the entire curve from the zero of velocity is a measurement of the precipitation fall speed or divergence. The second spectral moment yields resultant deformation and orientation axis of dilatation. Browning and Wexler's VAD analysis was done for the cases where neither the wind velocity field nor the

precipitation fall speed field were horizontally uniform, as was done by Lhermitte and Atlas (1961). It was proposed that, provided certain precautions were maintained, the effects of the inhomogeneities in fall speeds and vertical wind shear will be minimized. The method of VAD analysis used follows Browning and Wexler (1968) and is found in Appendix D.

Lhermitte and Atlas (1961), Browning and Wexler (1968), and Rabin and Zrnic (1980) all discuss the problems involved with using the radial velocity values when the elevation angles are greater than  $10^\circ$ . At elevation angles above this, the radial velocity component, given by the fall velocity, produces significant error in the interpretation that the radial velocities represent the horizontal wind flow. At low elevation angles this fall velocity component is not a significant factor in the measurements of radial velocity; that is, the radar return represents the horizontal wind component.

The best way to avoid these errors caused by inhomogeneities is to employ an optimum scanning procedure. This procedure was outlined by Browning and Wexler (1968). They proposed that for a rain-only (no frozen precipitation present) situation, the elevation angle should not exceed  $9^\circ$ , and that the horizontal distance over the earth's surface should not exceed 20 km. When examining cases that involve nonuniform rain or appreciable amounts of convection, these restrictions do not apply. The elevation angle maximum is set as a result of the errors introduced by fall speed inhomogeneities, and the range maximum is set as a result of the

errors introduced by vertical wind shear. Browning and Wexler (1968) do state, however, that if there is reason to believe that the fields examined are relatively homogeneous that the limits can be relaxed. The choice of operating criteria, given the limitations, is a compromise among three considerations:

1. Higher altitudes can be observed only at longer slant ranges.
2. The accuracy of estimates of divergence is enhanced by making the zeroth harmonic coefficient as large as possible, and this is done by using longer ranges.
3. A large percentage of the scan's range ring examined must be filled with useable velocity values. This tends to occur at shorter ranges.

Browning and Wexler (1968) further suggested a method of determining the accuracy of the technique by comparing the results from different elevation angles where the different ranges are at the same altitude.

## Chapter 3

### Analysis

#### 3.1 Dual-Doppler Analysis

Dual-Doppler analysis at 082029 LST (Figs. 9a-g) depicts the leading areas of the echo as it enters the dual-Doppler radar analysis network. At the surface (Fig. 9a), a small echo is observed in the southwestern corner of the plot. The main body of the echo is to the west of the area depicted. The echo core intensity is greater than 30 dBZ, and the wind flow is from the southwest. All plots show the outline of Taiwan, the NCAR and TOGA radar locations. Only intensities greater than 20 dBZ are indicated. In some figures there are echoes that do not have velocity vectors associated with them. This is caused by a lack of velocity data from one or both of the radars. Velocity data from both radars is required for the dual-Doppler velocity synthesis. The echo at 0820 LST (Fig. 9b) is not associated with the front, since at this time the front is still to the northwest of this analysis domain. This echo is caused by the confluence between the mesoscale ridging over the island (Trier *et al.* 1989) (Fig. 4) and the synoptic scale flow from the approaching frontal trough (Fig. 5). Flow remains from the southwest up through the 3.0 km height (Figs. 9a-d), then it begins to veer to a more zonal flow (Figs. 9e-g). This veering of the winds with height is an indication of warm air advection. The flow pattern

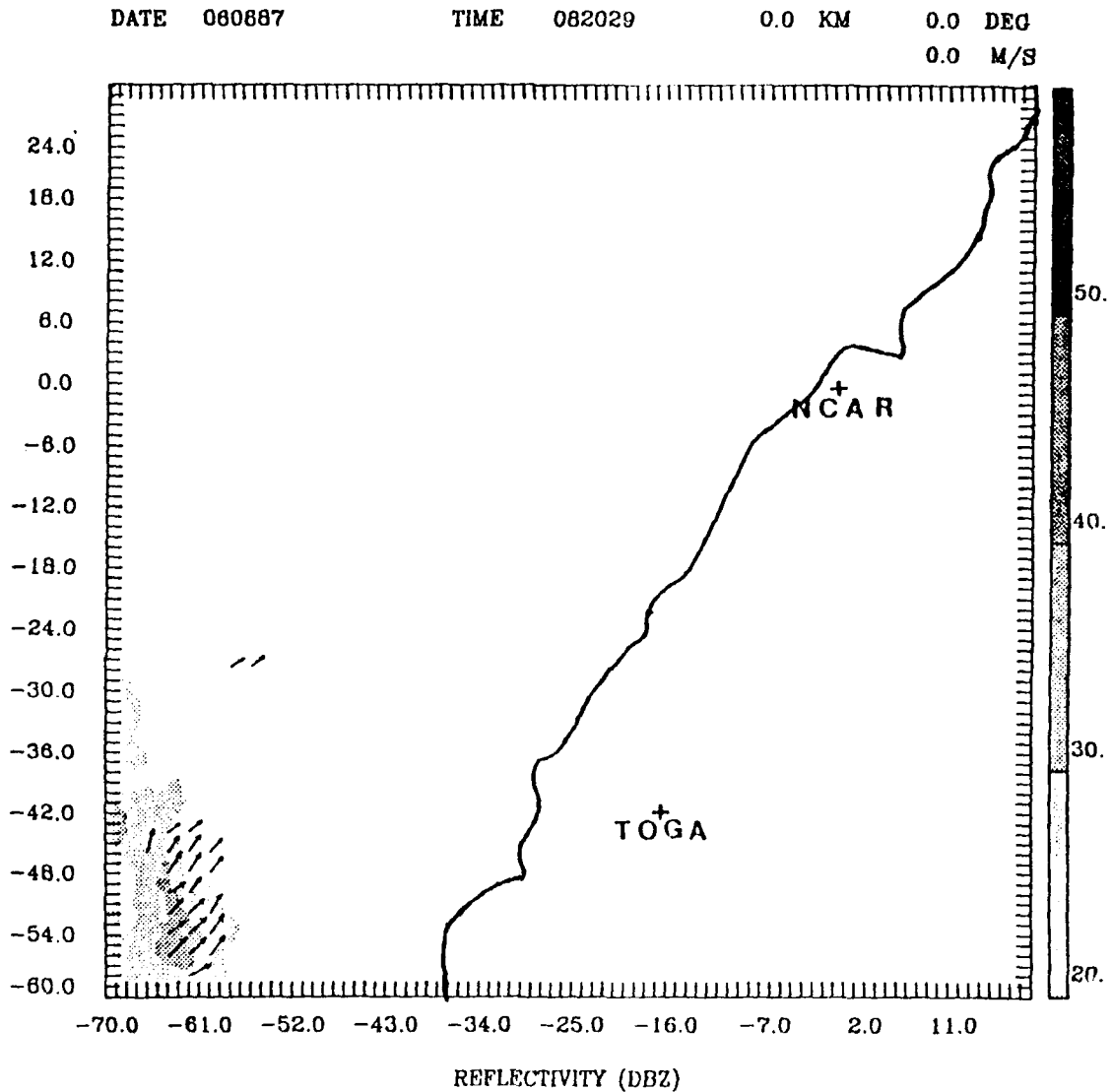


*Fig. 9a. Dual-Doppler analysis of reflectivities and horizontal velocities for 082029, at the surface. The length scale for the vectors is given in the lower right-hand corner. The reflectivity gray scale is given on the right side of the figure. Radar positions and the coastline of Taiwan are also given.*

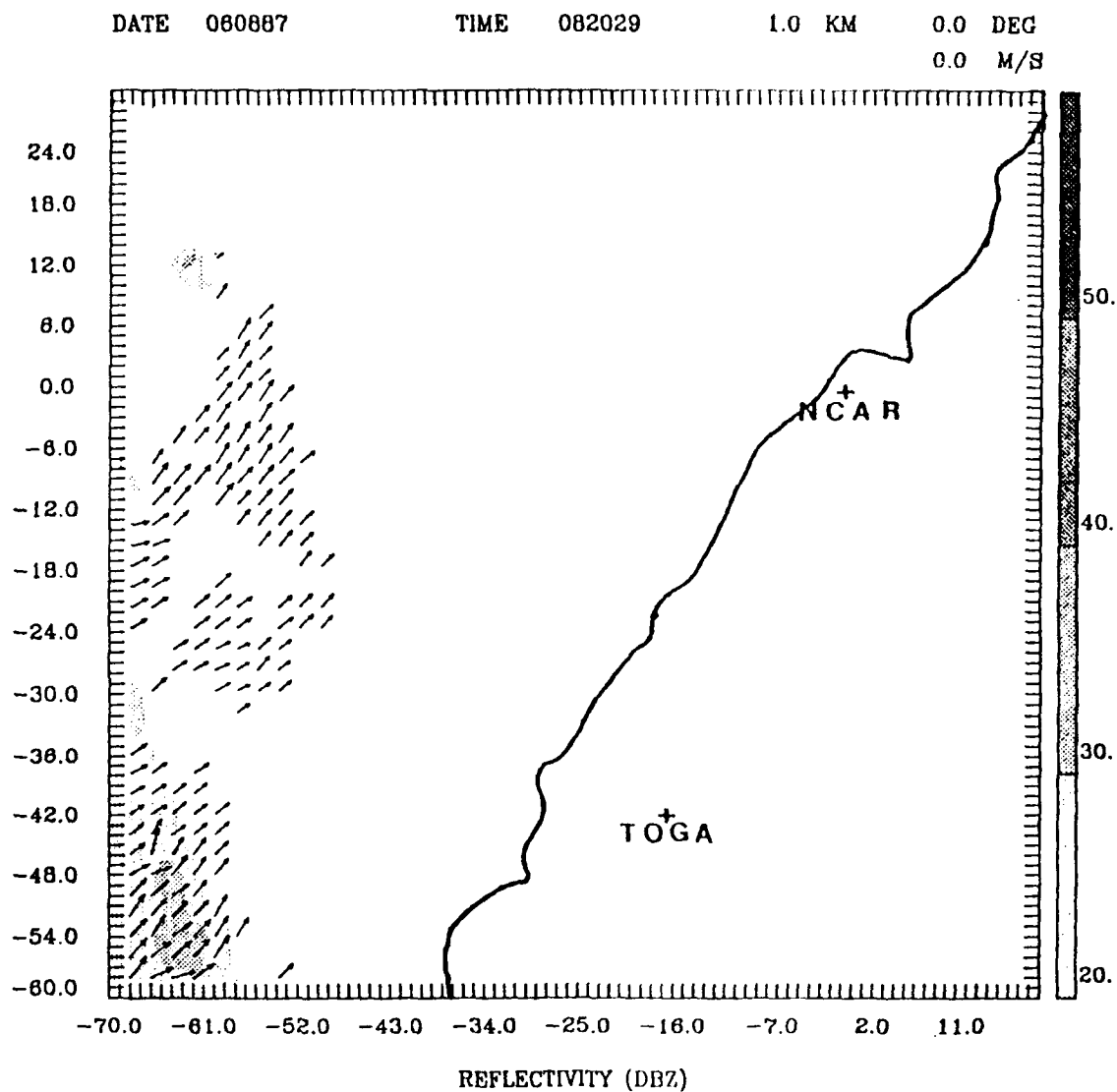


Fig. 9b. Dual-Doppler analysis of reflectivities and horizontal velocities for 082029, at 1.0 km above the ground. The length scale for the vectors is given in the lower right-hand corner. The reflectivity gray scale is given on the right side of the figure. Radar positions and the coastline of Taiwan are also given.

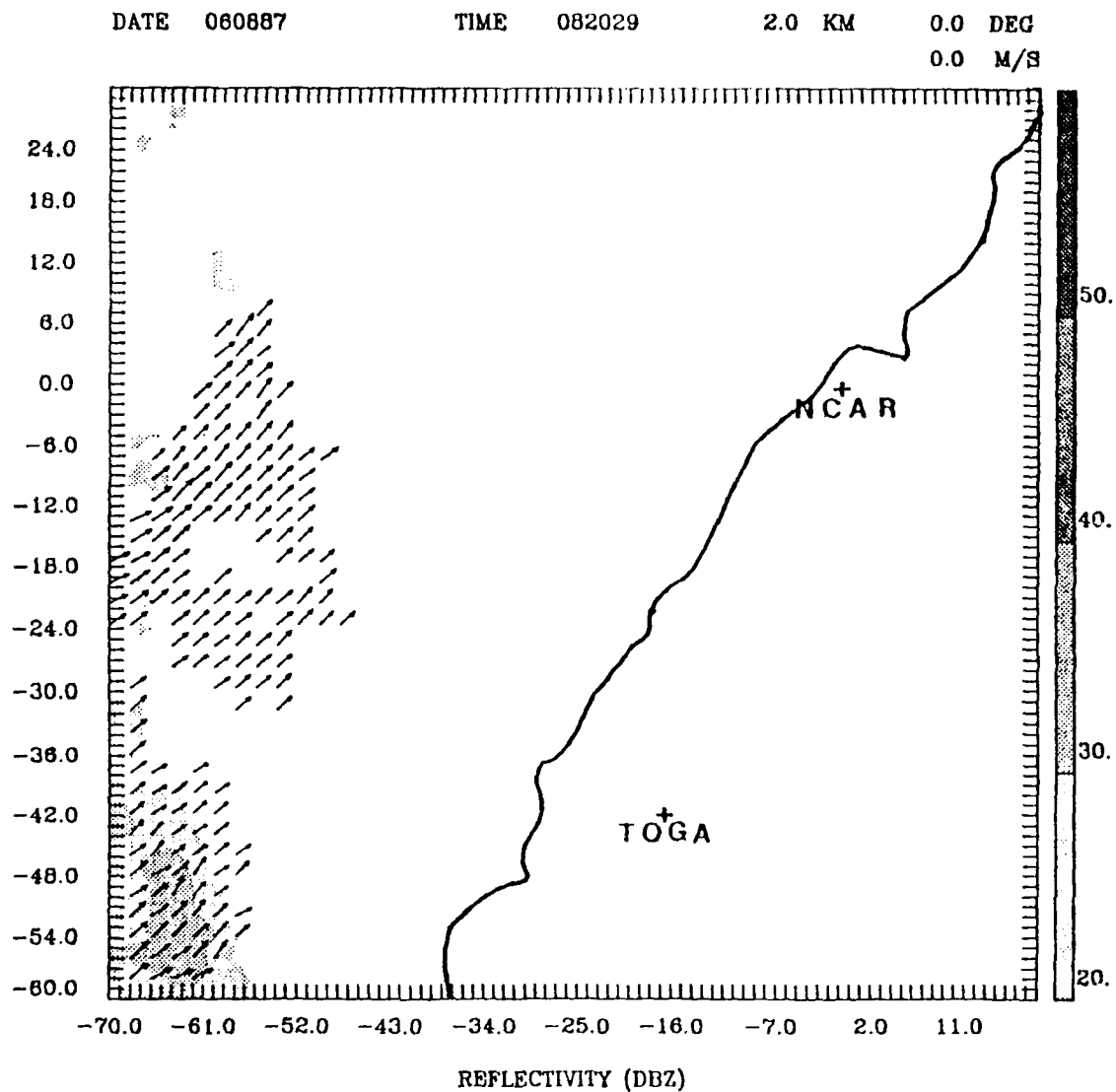


Fig. 9c. Dual-Doppler analysis of reflectivities and horizontal velocities for 082029, at 2.0 km above the ground. The length scale for the vectors is given in the lower right-hand corner. The reflectivity gray scale is given on the right side of the figure. Radar positions and the coastline of Taiwan are also given.

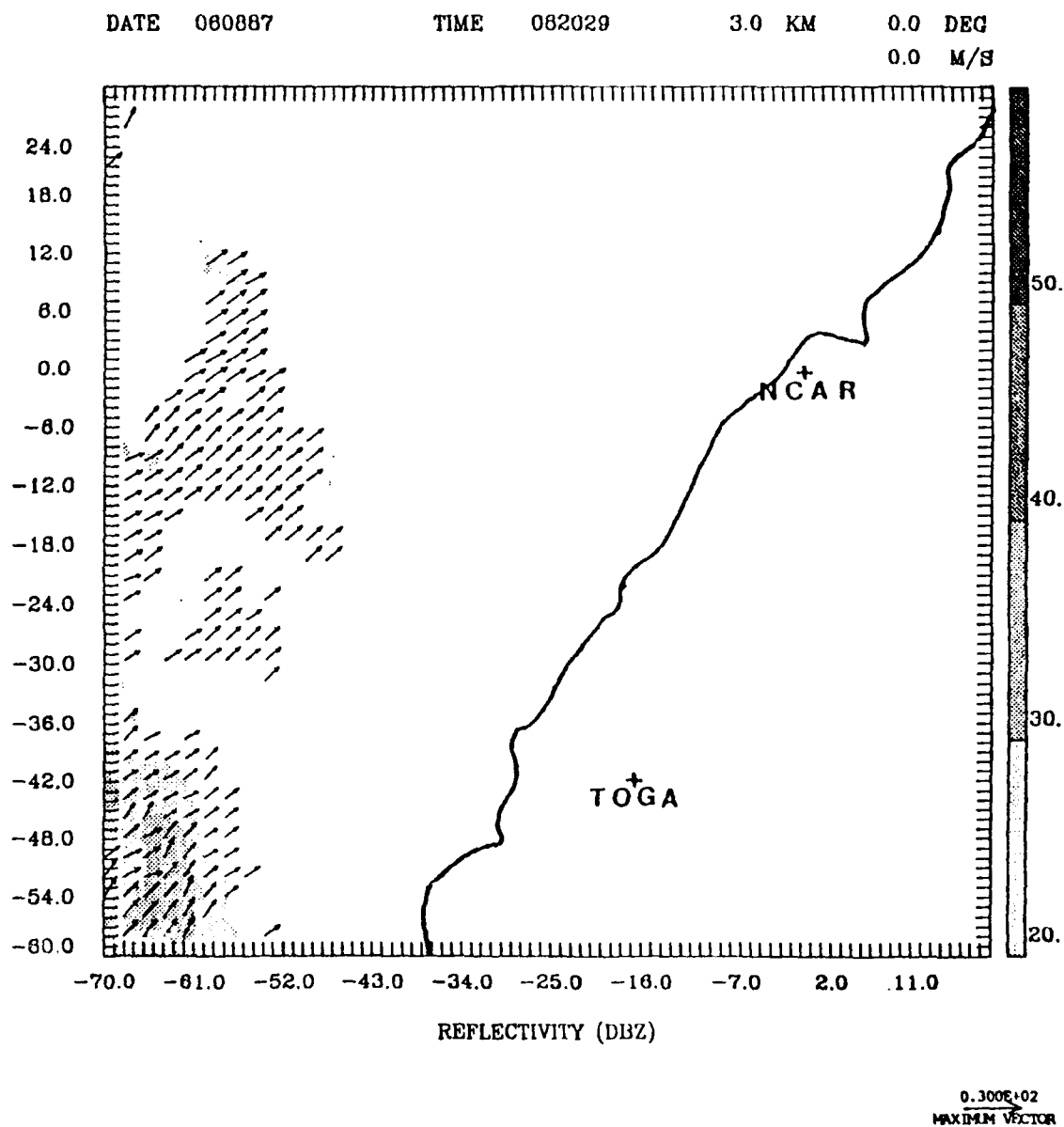


Fig. 9d. Dual-Doppler analysis of reflectivities and horizontal velocities for 082029, at 3.0 km above the ground. The length scale for the vectors is given in the lower right-hand corner. The reflectivity gray scale is given on the right side of the figure. Radar positions and the coastline of Taiwan are also given.

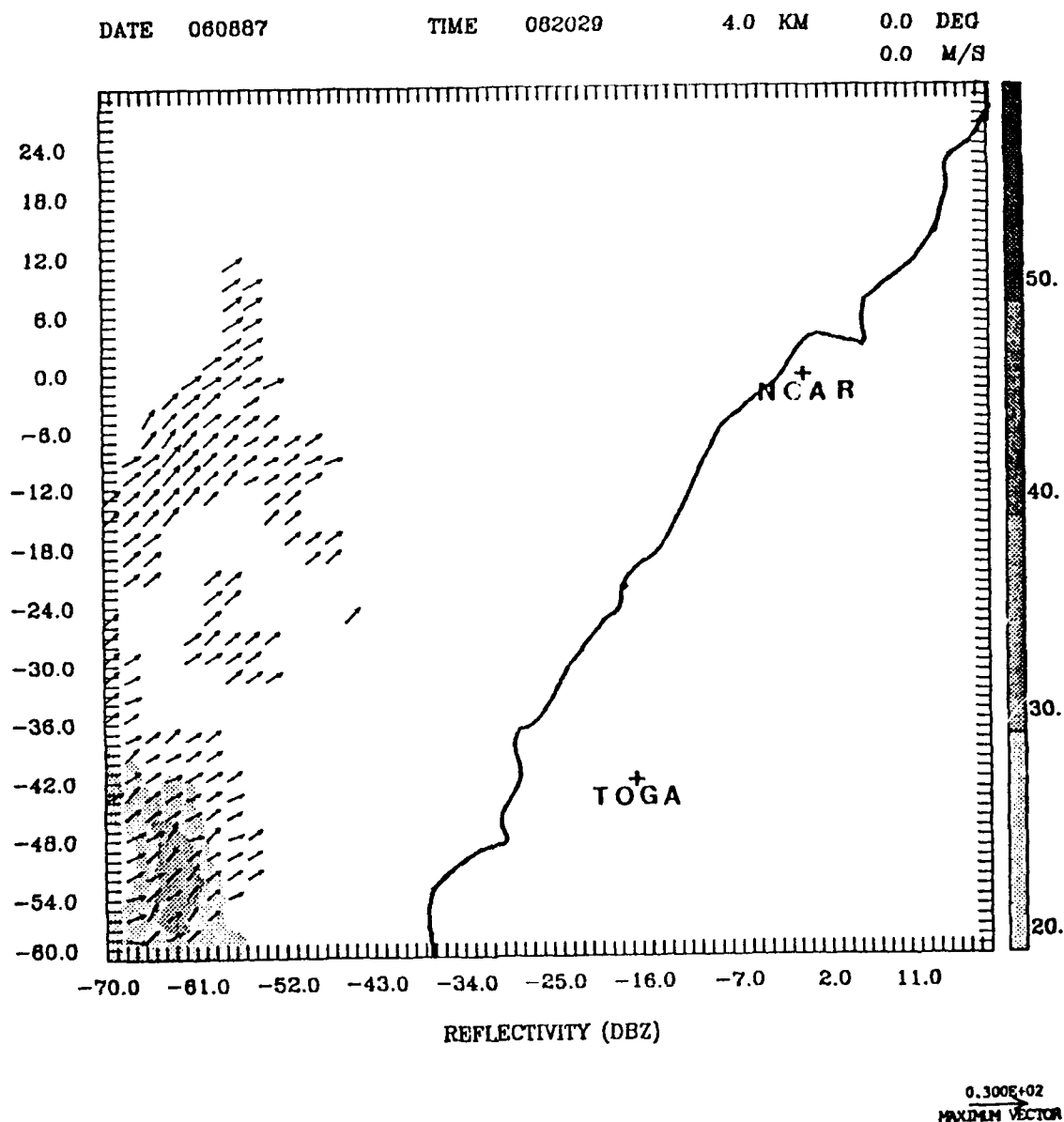


Fig. 9e. Dual-Doppler analysis of reflectivities and horizontal velocities for 082029, at 4.0 km above the ground. The length scale for the vectors is given in the lower right-hand corner. The reflectivity gray scale is given on the right side of the figure. Radar positions and the coastline of Taiwan are also given.

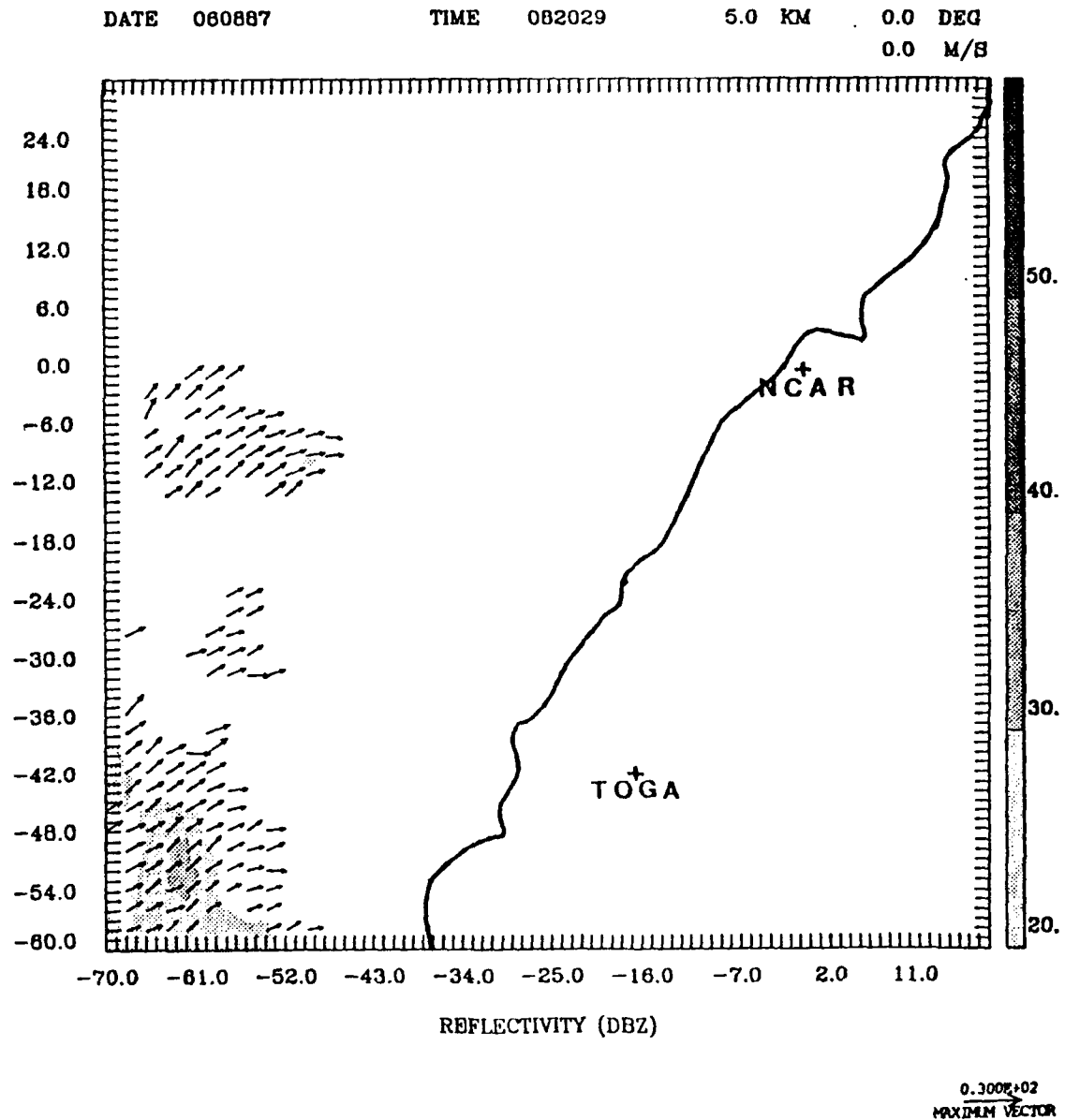


Fig. 9f. Dual-Doppler analysis of reflectivities and horizontal velocities for 082029, at 5.0 km above the ground. The length scale for the vectors is given in the lower right-hand corner. The reflectivity gray scale is given on the right side of the figure. Radar positions and the coastline of Taiwan are also given.

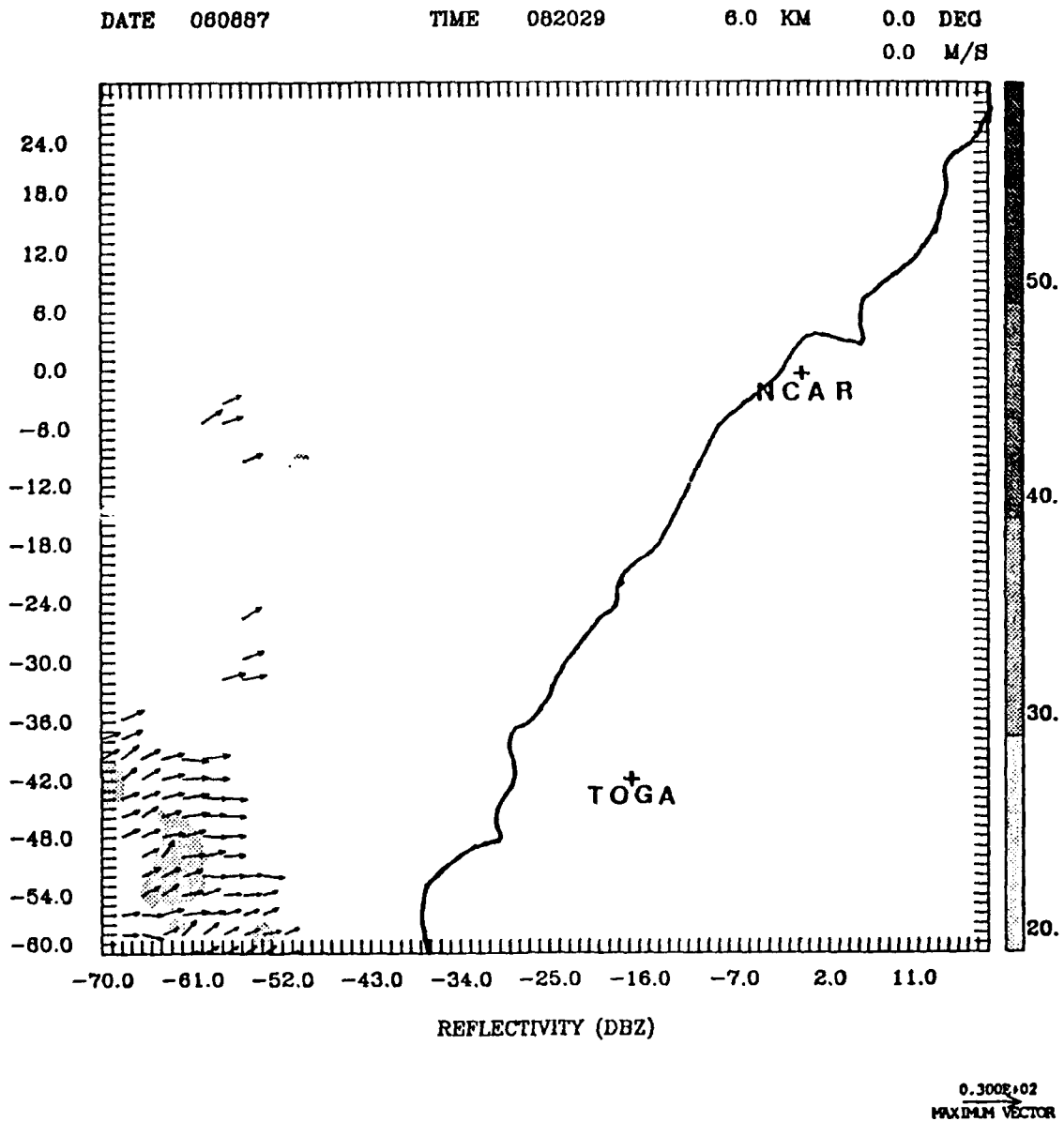


Fig. 9g. Dual-Doppler analysis of reflectivities and horizontal velocities for 082029, at 6.0 km above the ground. The length scale for the vectors is given in the lower right-hand corner. The reflectivity gray scale is given on the right side of the figure. Radar positions and the coastline of Taiwan are also given.

also corresponds to the synoptic scale flows seen in the upper levels of Fig. 5. The wind speed is approximately  $13 \text{ ms}^{-1}$ . The echo core increases in size from the surface to the 2.0 km height (Fig. 9a-c), then decreases in area until it vanishes between the 5.0 km and 6.0 km height (Fig. 9e-f). The top of the echo is just over the 6.0 km height.

The dual-Doppler analysis at 083559 LST (Figs. 10a-h) also shows southwesterly flow at low heights (Figs. 10a-d), that turns westerly aloft (Fig. 10e-g). The storm echo in the southwest increased in area from 0820 LST, and the tops extend up to 7.0 km in height. At the surface (Fig. 10a) several small echo cores greater than 30 dBZ are observed. These increase in size until they merge into one large core at the 2.0 km height (Fig. 10a-c). It is at this height that the largest core area is observed. The largest core area at 082029 LST was also observed at the 2.0 km height (Fig. 9c). The large core at 2.0 km breaks up into smaller cores at the 4.0 km height (Fig. 1e) and tops at just over the 5.0 km height (Fig. 10f). Weak convergence at the surface and 1.0 km height is found below this core. Divergent flow is found above this core at the upper levels (Figs. 10f-g). There is also more echo area observed to the north of the southwestern echo area (north of  $y = -33$ ). During this time the mesoscale ridge is undergoing a sharpening in its configuration as the synoptic scale front approaches. This ridge sharpening continues until the front arrives (Figs. 4, 6, and 7). The echo propagation speed was calculated to be  $13.4 \text{ ms}^{-1}$ .

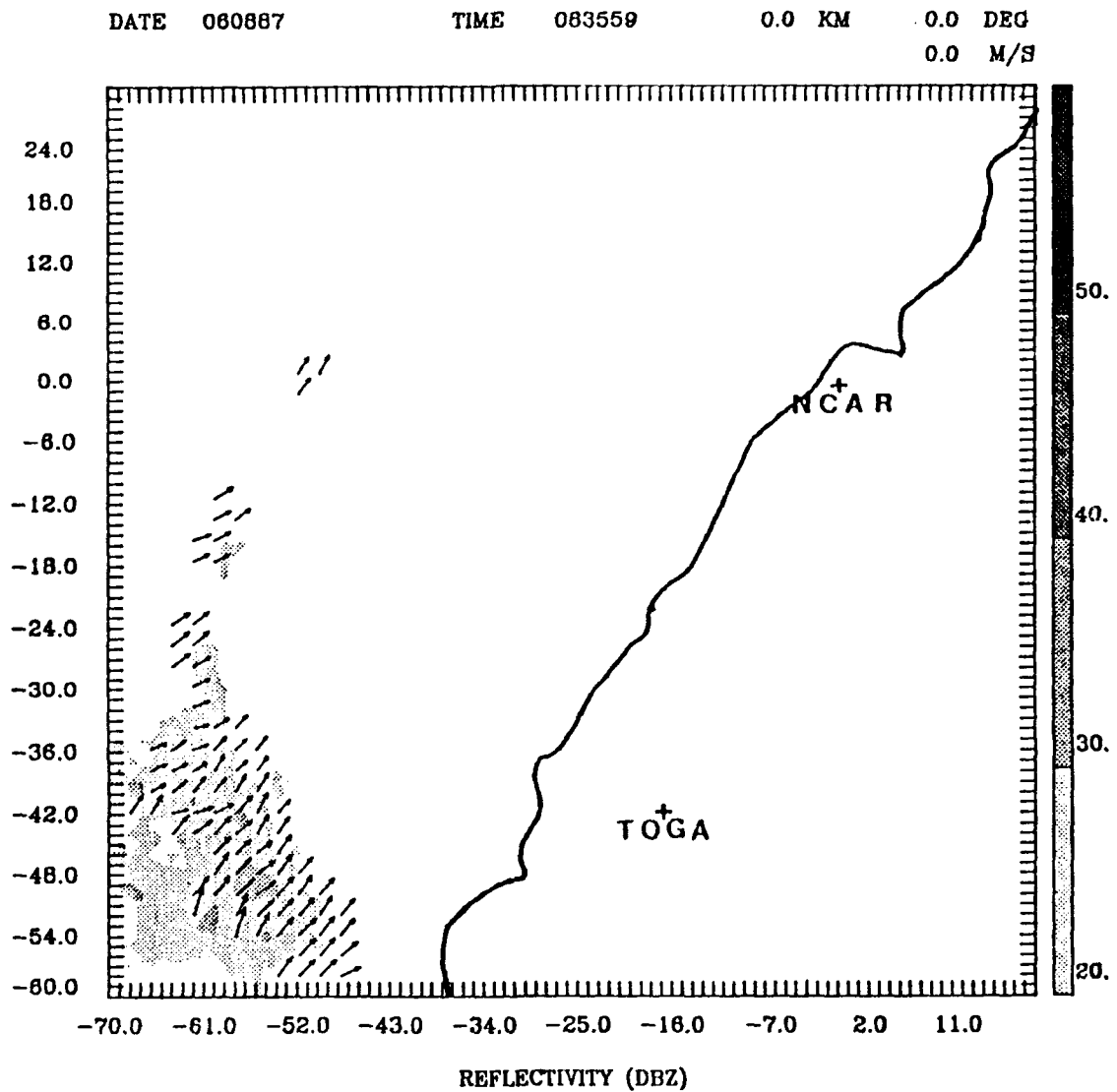


Fig. 10a. Dual-Doppler analysis of reflectivities and horizontal velocities for 083559 at the surface. The length scale for the vectors is given in the lower right-hand corner. The reflectivity gray scale is given on the right side of the figure. Radar positions and the coastline of Taiwan are also given.

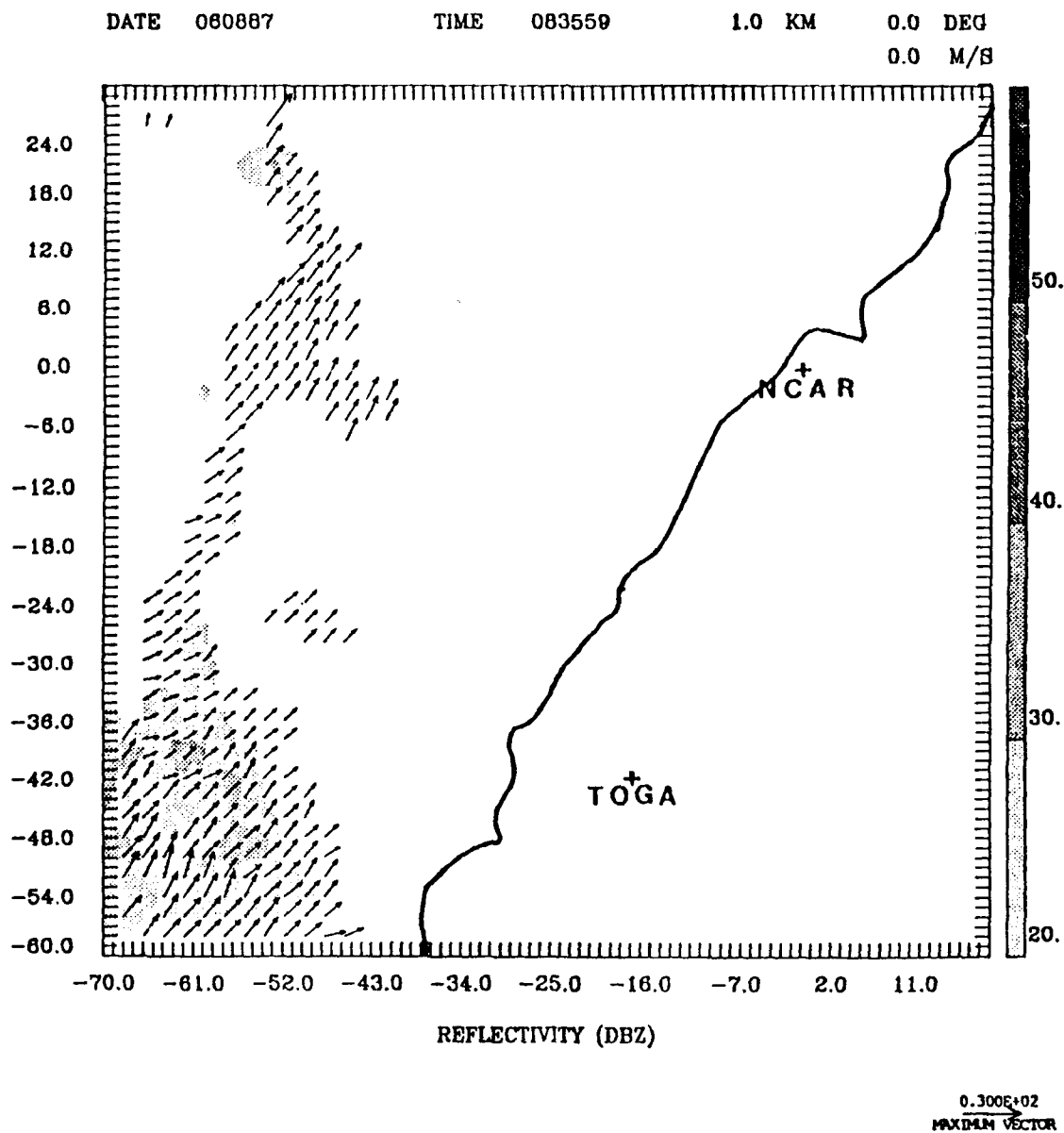


Fig. 10b. Dual-Doppler analysis of reflectivities and horizontal velocities for 083559, at 1.0 km above the ground. The length scale for the vectors is given in the lower right-hand corner. The reflectivity gray scale is given on the right side of the figure. Radar positions and the coastline of Taiwan are also given.

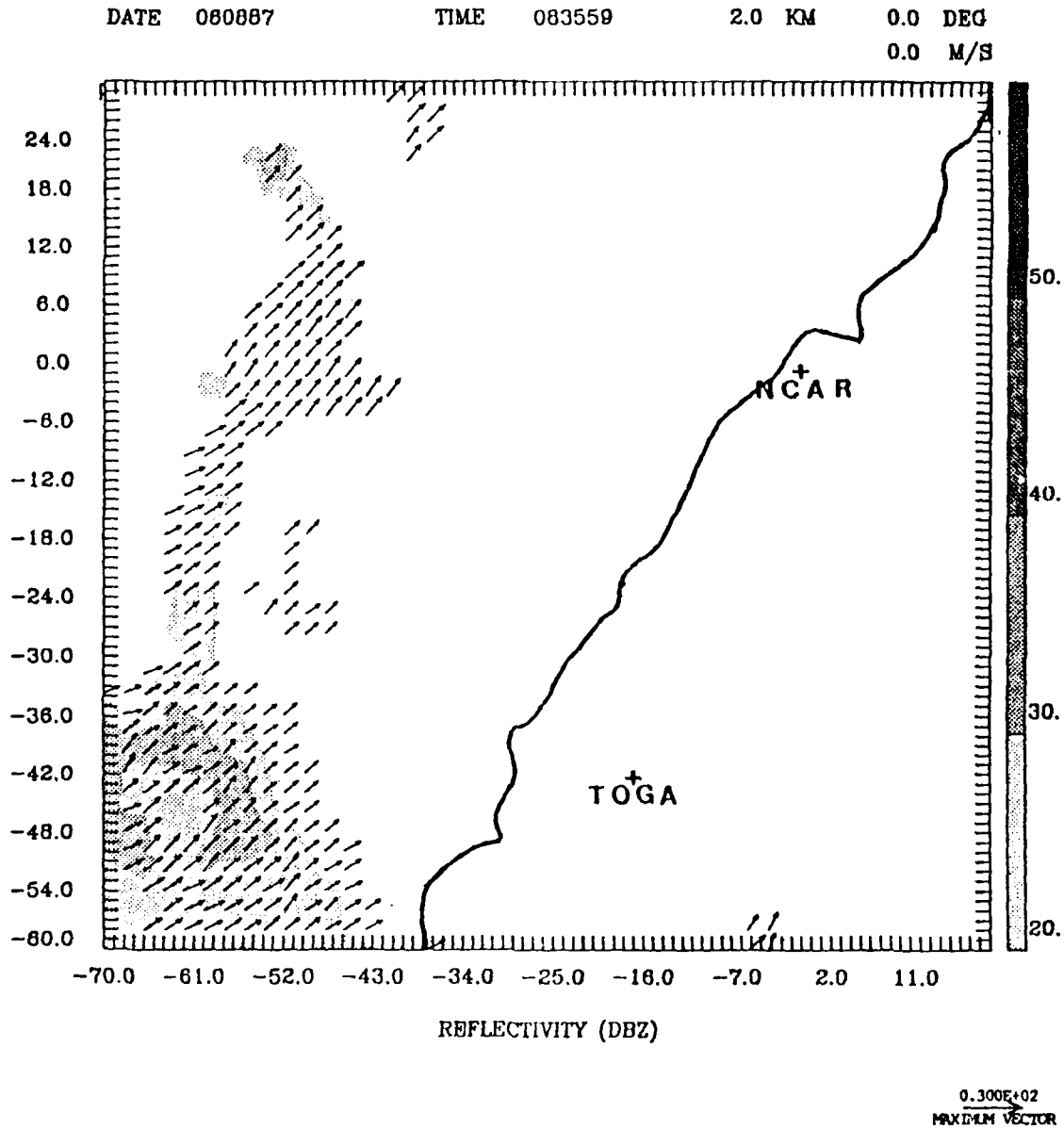


Fig. 10c. Dual-Doppler analysis of reflectivities and horizontal velocities for 083559, at 2.0 km above the ground. The length scale for the vectors is given in the lower right-hand corner. The reflectivity gray scale is given on the right side of the figure. Radar positions and the coastline of Taiwan are also given.

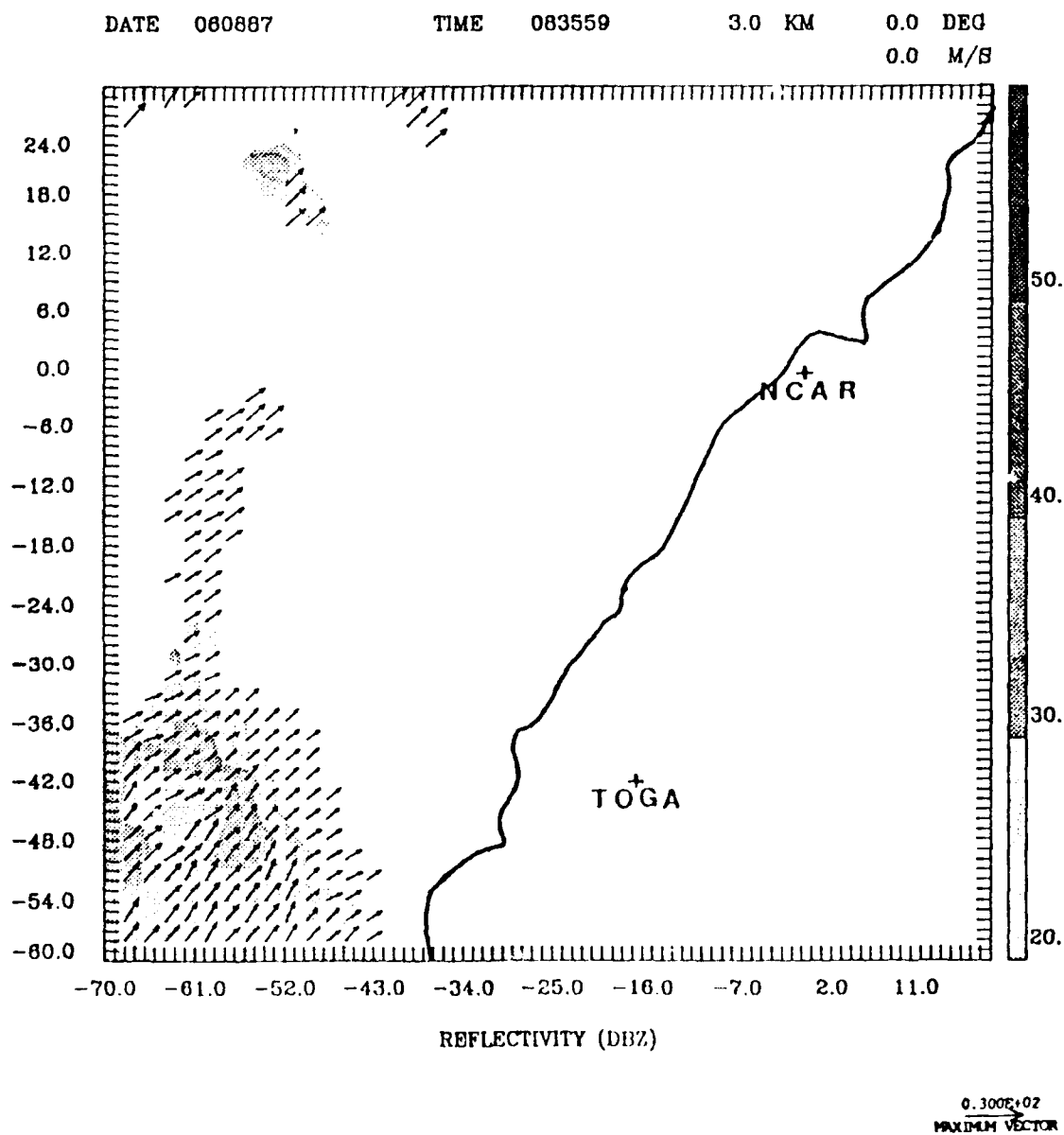
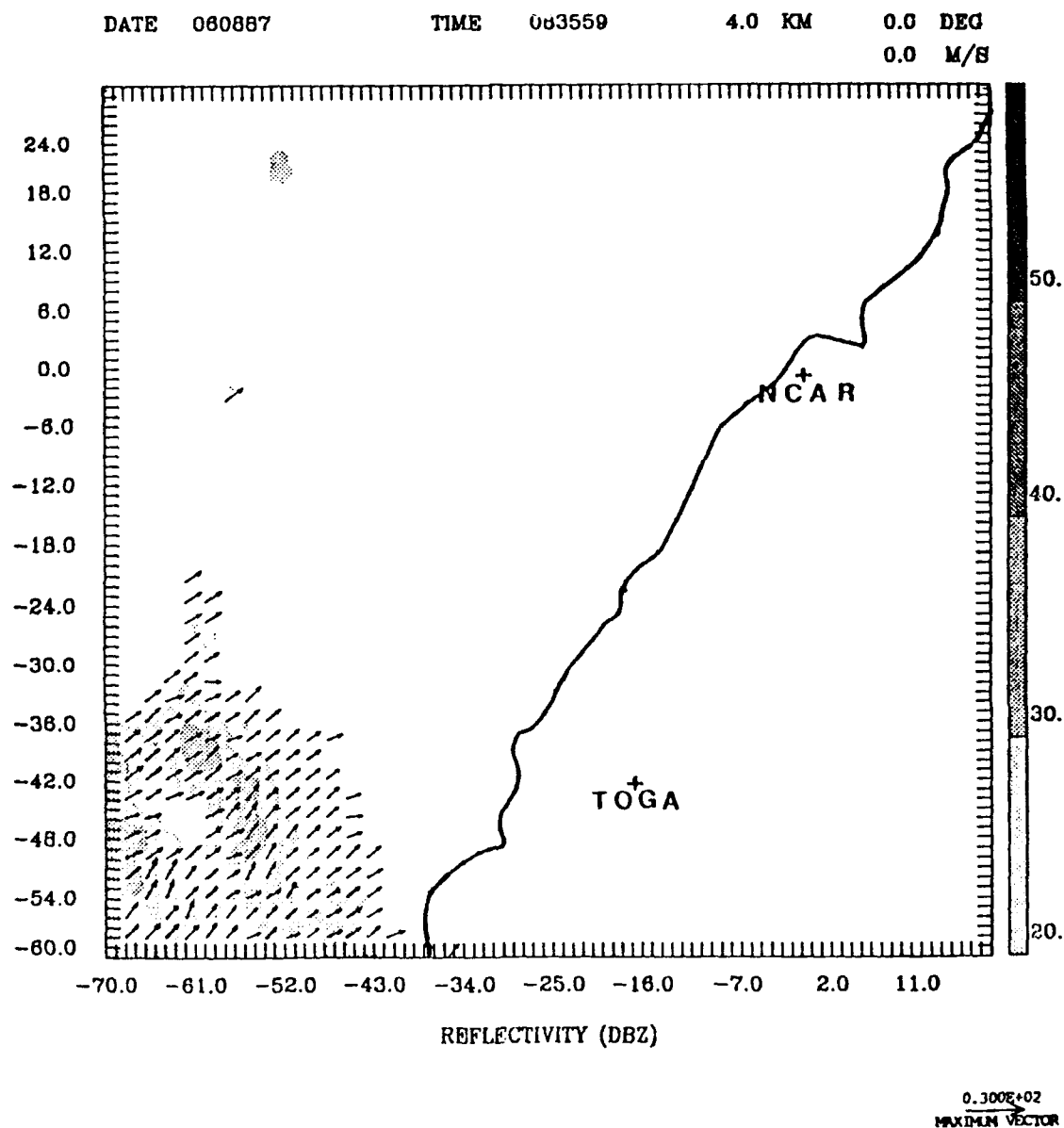


Fig. 10d. Dual-Doppler analysis of reflectivities and horizontal velocities for 083559, at 3.0 km above the ground. The length scale for the vectors is given in the lower right-hand corner. The reflectivity gray scale is given on the right side of the figure. Radar positions and the coastline of Taiwan are also given.



*Fig. 10e. Dual-Doppler analysis of reflectivities and horizontal velocities for 063559, at 4.0 km above the ground. The length scale for the vectors is given in the lower right-hand corner. The reflectivity gray scale is given on the right side of the figure. Radar positions and the coastline of Taiwan are also given.*

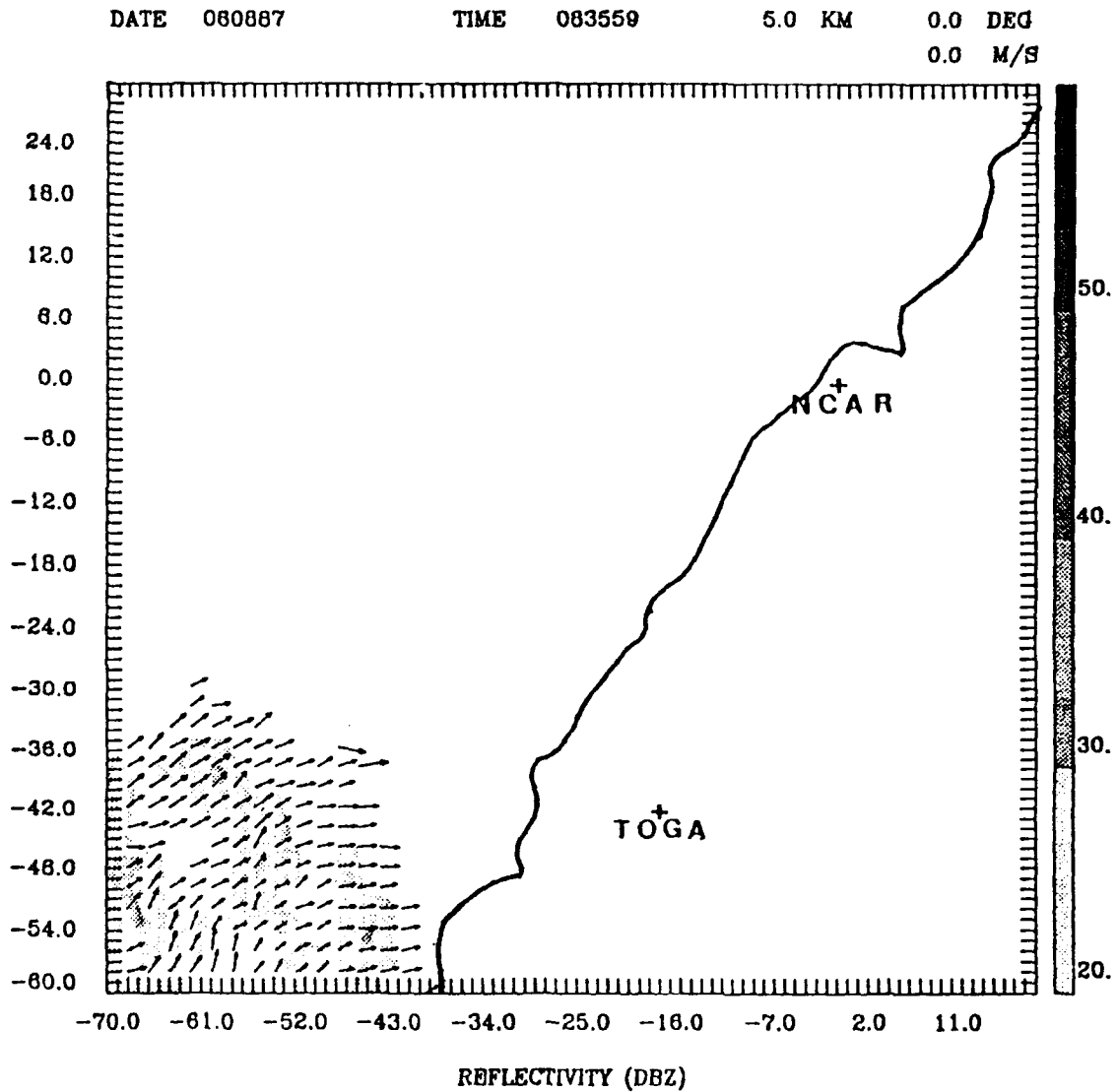


Fig. 10f. Dual-Doppler analysis of reflectivities and horizontal velocities for 083559, at 5.0 km above the ground. The length scale for the vectors is given in the lower right-hand corner. The reflectivity gray scale is given on the right side of the figure. Radar positions and the coastline of Taiwan are also given.

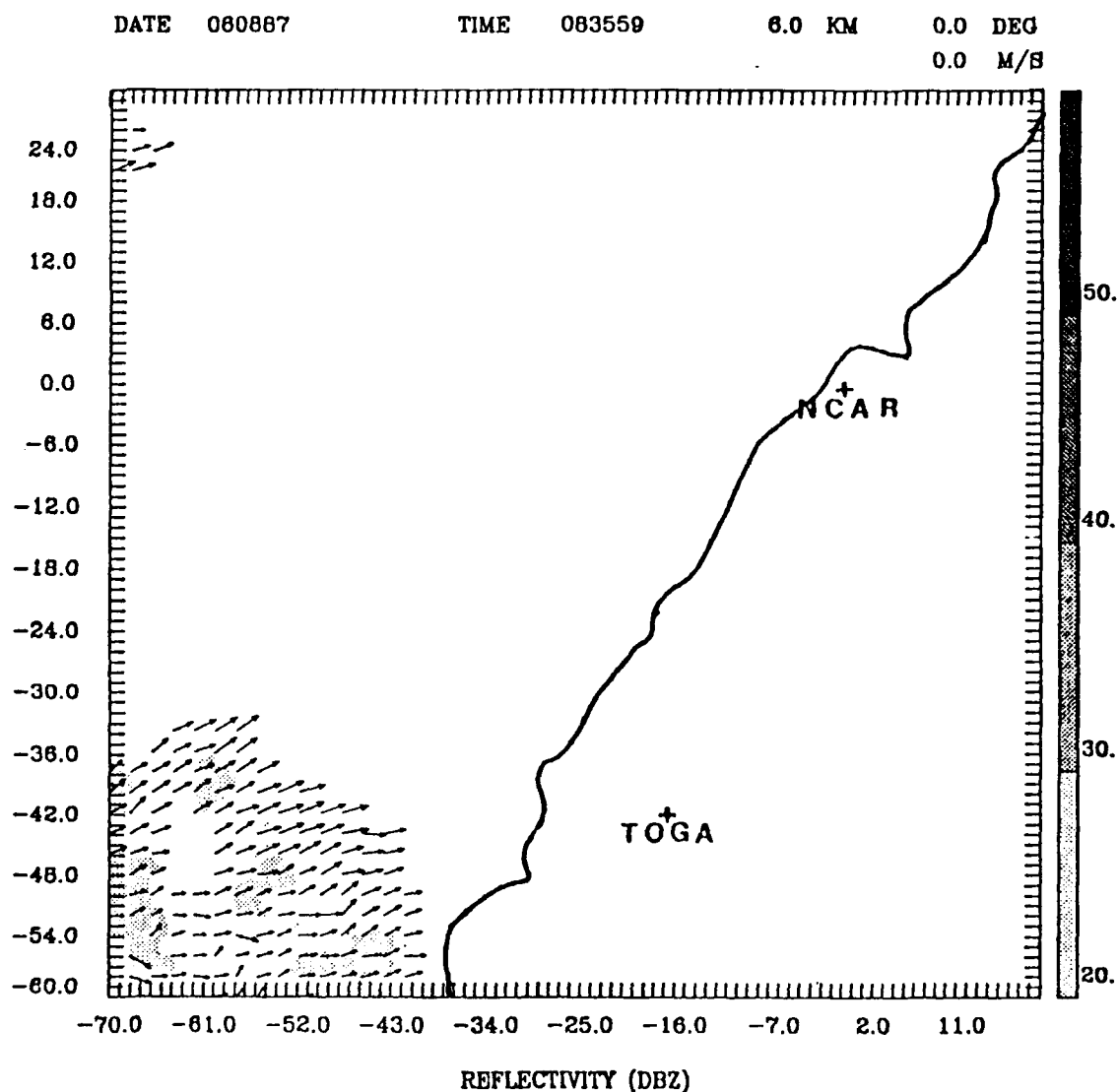


Fig. 10g. Dual-Doppler analysis of reflectivities and horizontal velocities for 083559, at 6.0 km above the ground. The length scale for the vectors is given in the lower right-hand corner. The reflectivity gray scale is given on the right side of the figure. Radar positions and the coastline of Taiwan are also given.

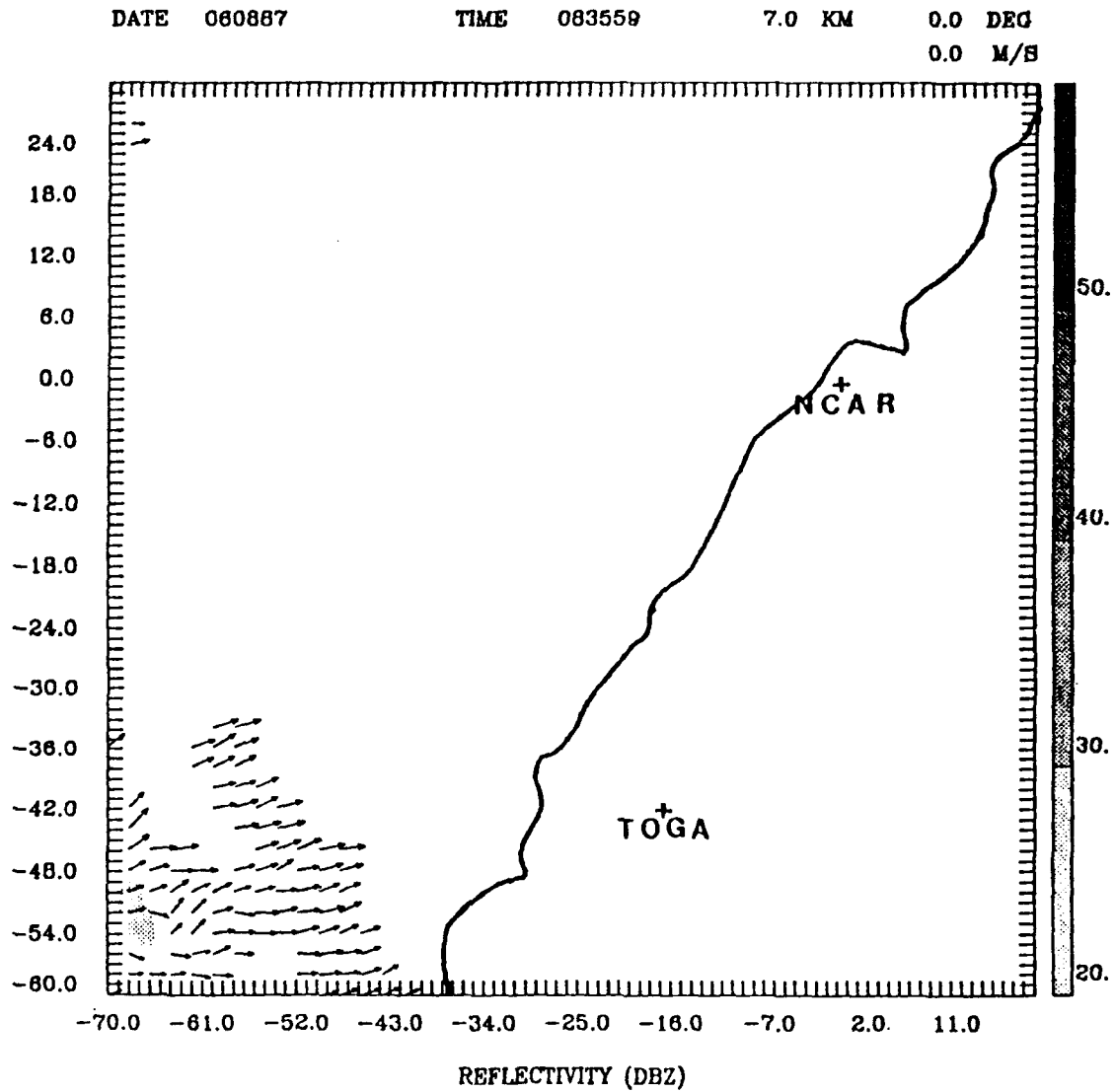
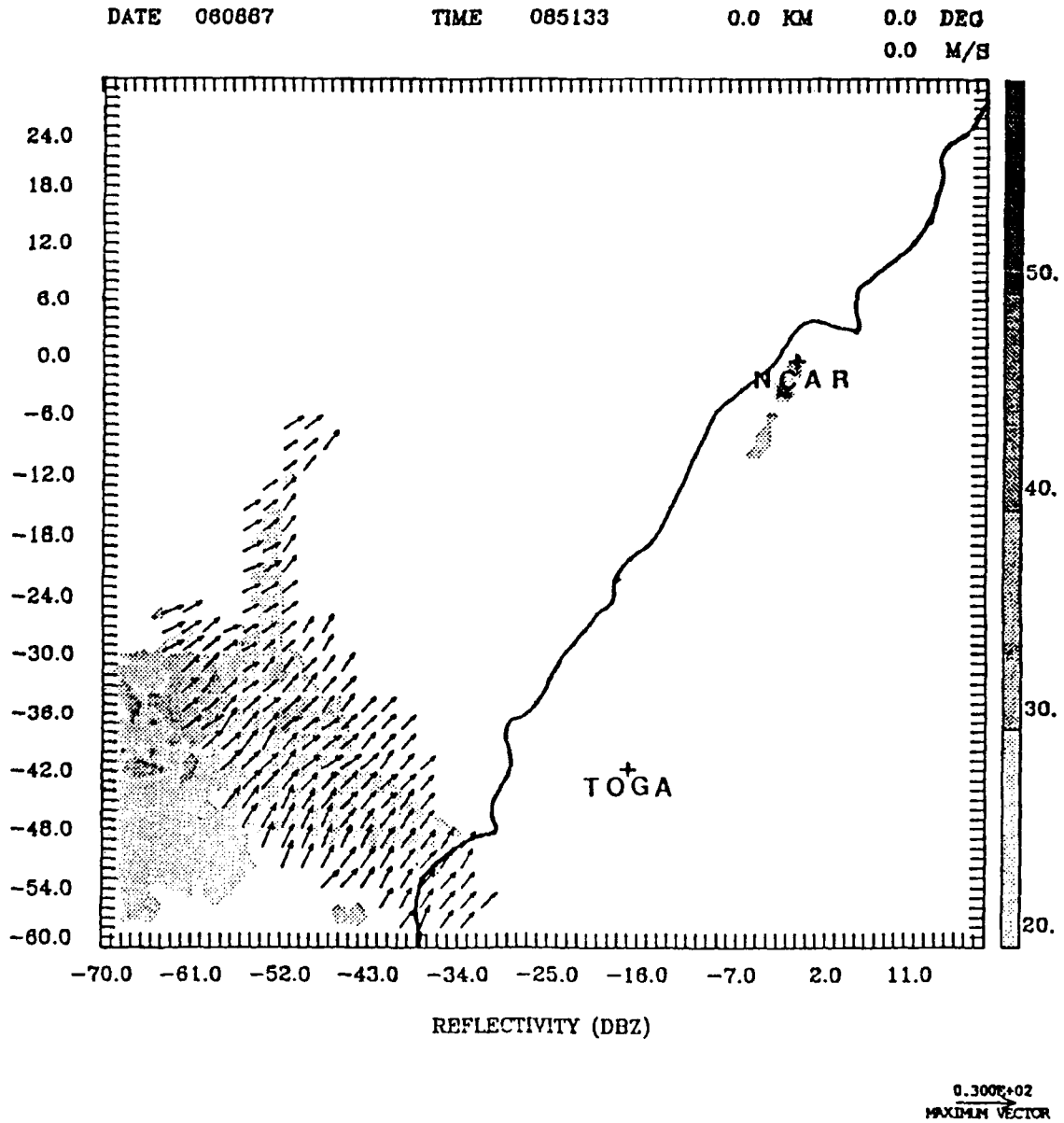


Fig. 10h. Dual-Doppler analysis of reflectivities and horizontal velocities for 083559, at 7.0 km above the ground. The length scale for the vectors is given in the lower right-hand corner. The reflectivity gray scale is given on the right side of the figure. Radar positions and the coastline of Taiwan are also given.

Figures 11a-g depict the analysis at 085133 LST. The front still has not entered the analysis domain. Since 083559 LST, the echo propagated toward the NCAR radar another 13.5 km, giving a speed of  $14.3 \text{ ms}^{-1}$ . The average horizontal wind speed in the echo area is approximately  $15 \text{ ms}^{-1}$ . Several echo cores greater than 30 dBZ are now found at the surface (Fig. 11a) in the southwestern echo area. As before, these cores merge into a larger core aloft, which has its greatest extent at the 2.0 km level (Fig. 11c). Above this height the core, for the first time, stays relatively unified as a single area (Figs. 11d-f). The top of the echo core now reaches 6.0 km in height (the echo tops are still just over 7.0 km in height). This increase in core height, along with a larger core area, indicates that the echo core has grown. Again, associated with this echo core is convergence near the surface, (Figs. 11a-c) and divergence aloft (Figs. 11f-h). The average winds continue to veer (from southwest to west) with increasing height. In the upper levels (Figs. 11f-h) at the northwestern portion of the wind vectors associated with the southwestern echo (near  $y = -30$ ), the winds do not turn westerly. This is most likely due to the increasing influence of the synoptic scale frontal trough.

The 090524 LST analysis is depicted by Figs. 12a-h. This analysis displays the same general flow pattern as the two previous analyses. The echo propagated 11 km closer to the NCAR radar since 085133 LST, giving it a speed of  $11.1 \text{ ms}^{-1}$ . The average analyzed speeds are still near  $15 \text{ ms}^{-1}$ , but a few winds exceed  $18 \text{ ms}^{-1}$ . The northerly extending line has intensified. At the surface (Fig. 12a), a large



*Fig. 11a. Dual-Doppler analysis of reflectivities and horizontal velocities for 085133, at the ground. The length scale for the vectors is given in the lower right-hand corner. The reflectivity gray scale is given on the right side of the figure. Radar positions and the coastline of Taiwan are also given.*

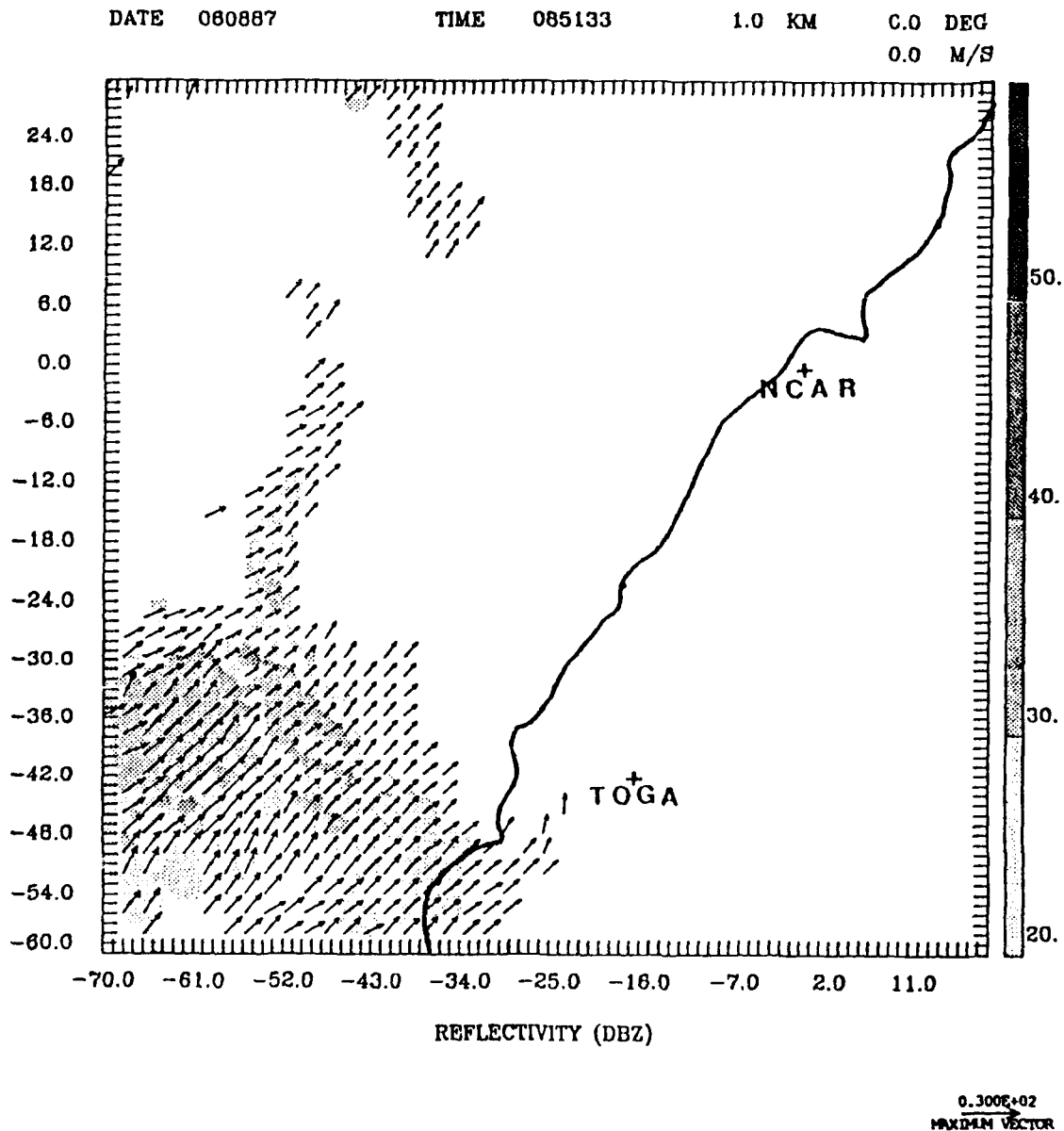


*Fig. 11b. Dual-Doppler analysis of reflectivities and horizontal velocities for 085133, at 1.0 km above the ground. The length scale for the vectors is given in the lower right-hand corner. The reflectivity gray scale is given on the right side of the figure. Radar positions and the coastline of Taiwan are also given.*

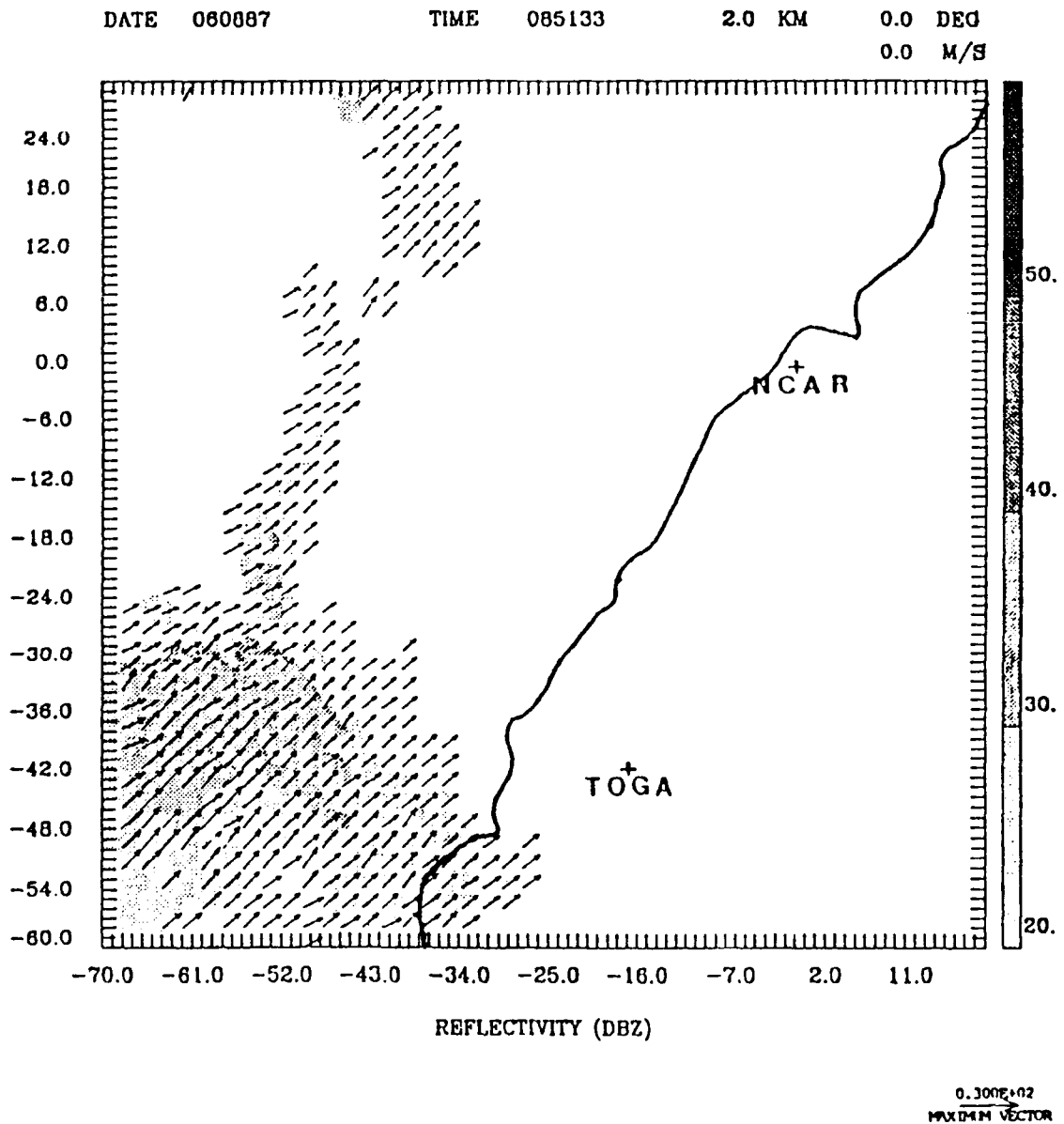
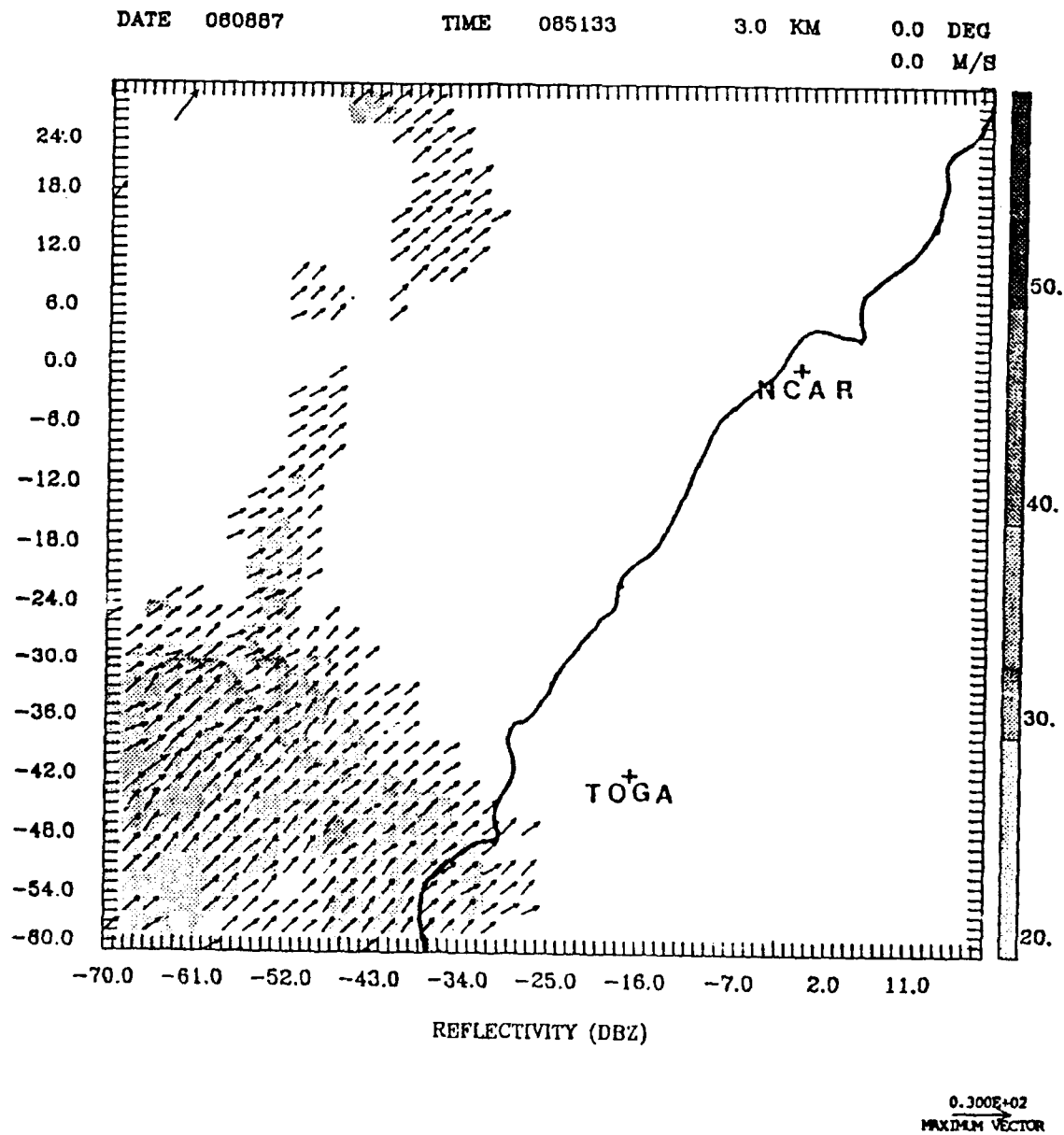


Fig. 11c. Dual-Doppler analysis of reflectivities and horizontal velocities for 085133, at 2.0 km above the ground. The length scale for the vectors is given in the lower right-hand corner. The reflectivity gray scale is given on the right side of the figure. Radar positions and the coastline of Taiwan are also given.



*Fig. 11d. Dual-Doppler analysis of reflectivities and horizontal velocities for 085133, at 3.0 km above the ground. The length scale for the vectors is given in the lower right-hand corner. The reflectivity gray scale is given on the right side of the figure. Radar positions and the coastline of Taiwan are also given.*

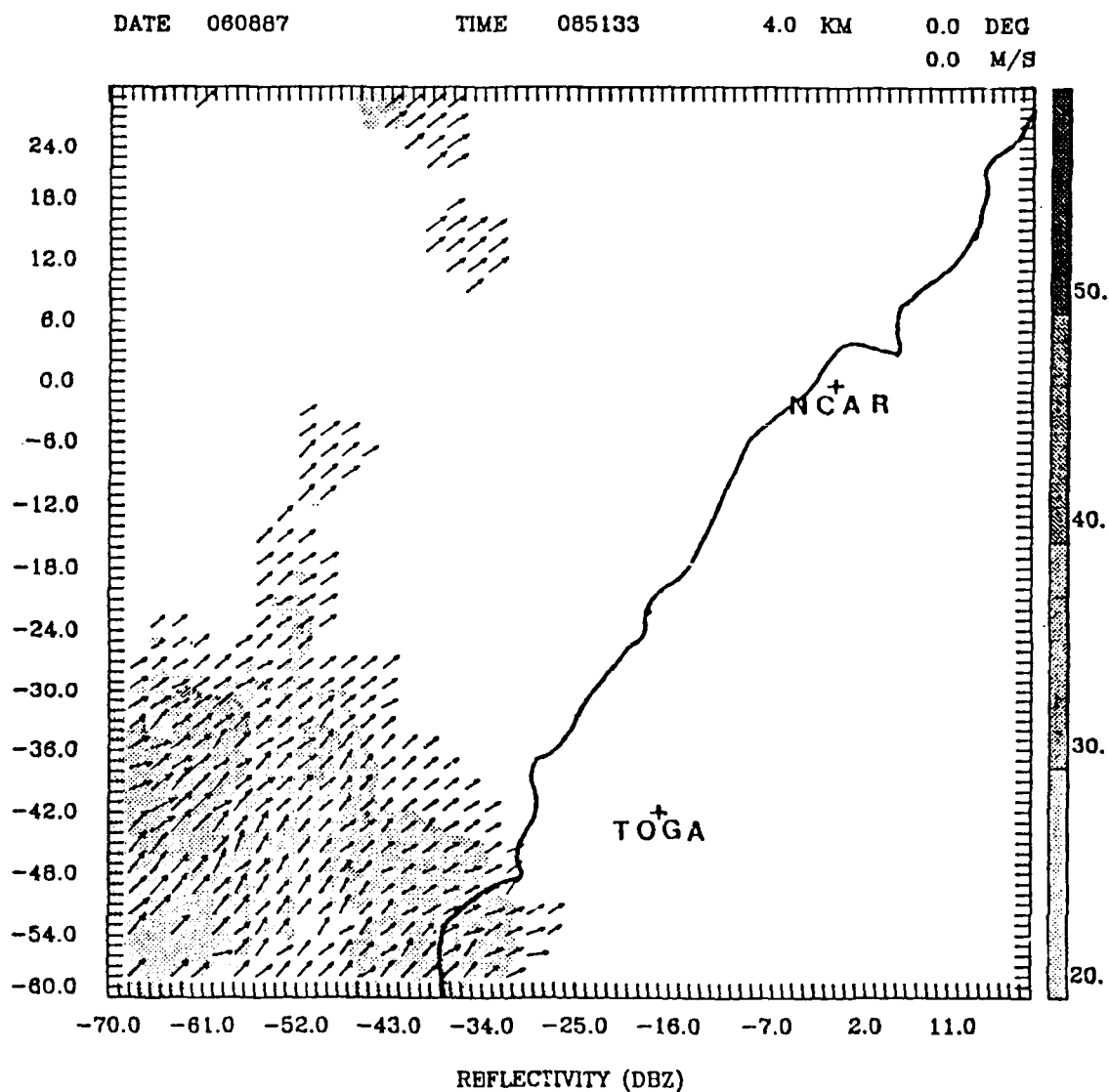
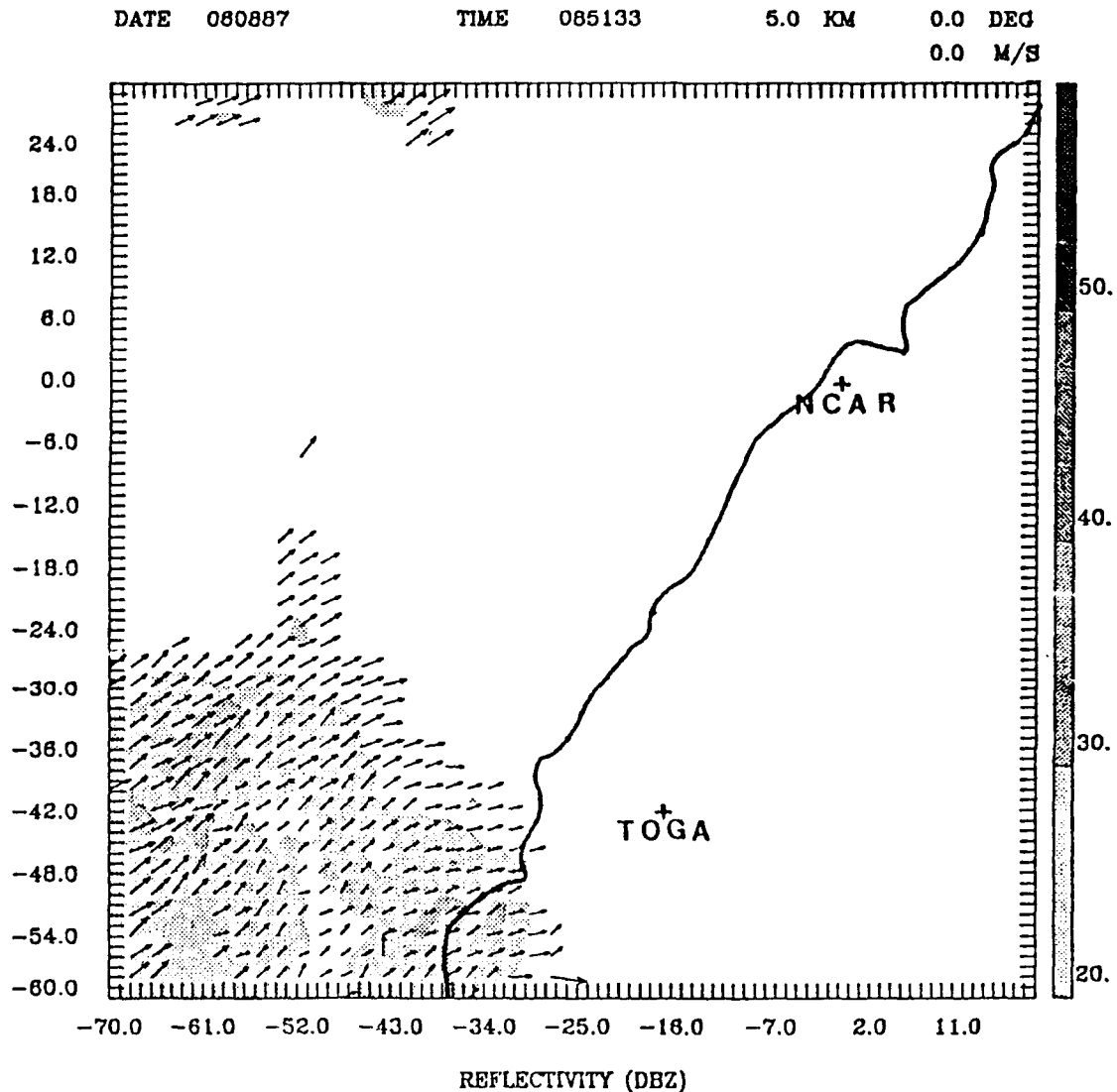
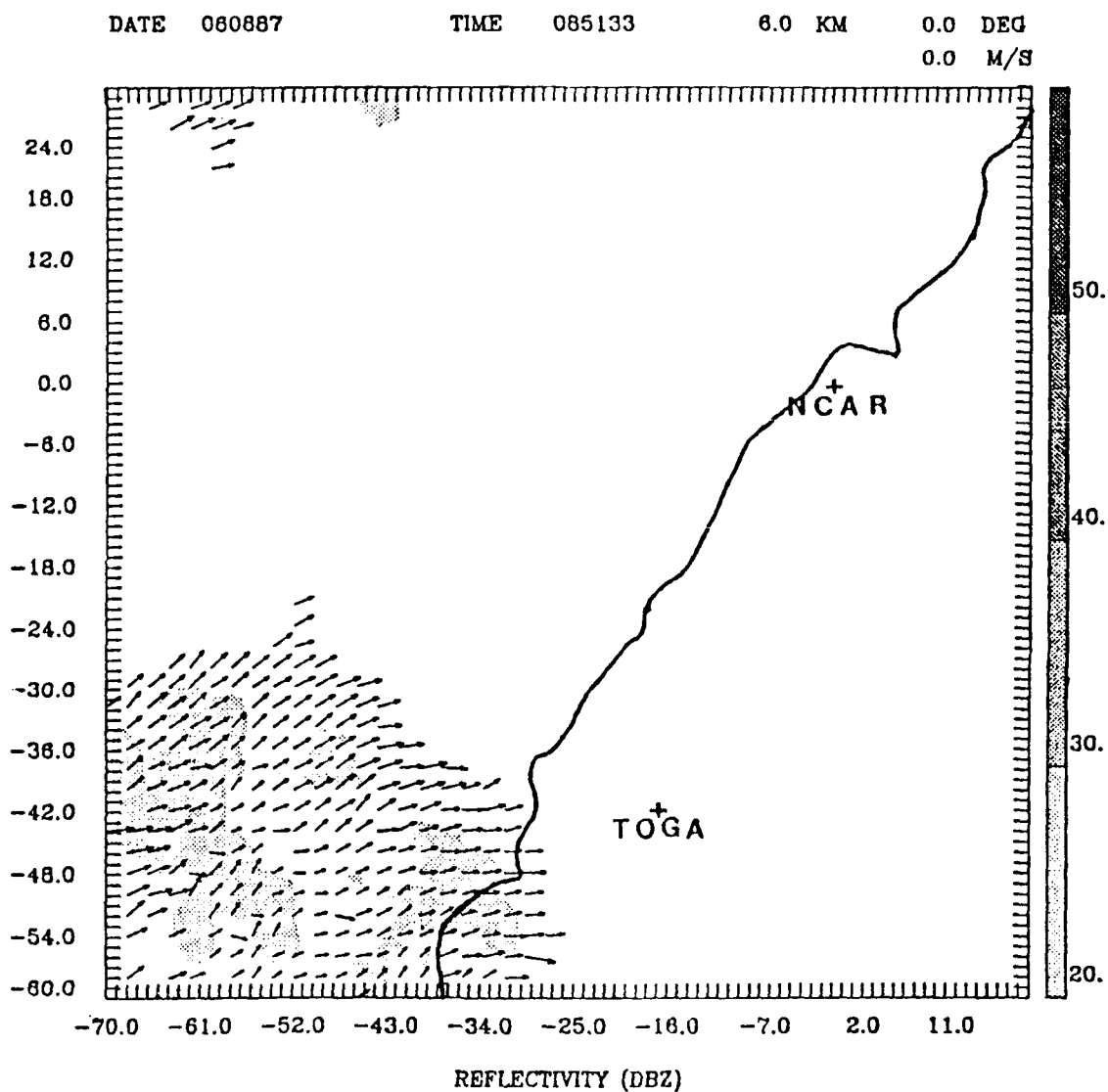


Fig. 11c. Dual-Doppler analysis of reflectivities and horizontal velocities for 085133, at 4.0 km above the ground. The length scale for the vectors is given in the lower right-hand corner. The reflectivity gray scale is given on the right side of the figure. Radar positions and the coastline of Taiwan are also given.



0.300E+02  
MAXIMUM VECTOR

Fig. 11f. Dual-Doppler analysis of reflectivities and horizontal velocities for 085133, at 5.0 km above the ground. The length scale for the vectors is given in the lower right-hand corner. The reflectivity gray scale is given on the right side of the figure. Radar positions and the coastline of Taiwan are also given.



*Fig. 11g. Dual-Doppler analysis of reflectivities and horizontal velocities for 085133, at 6.0 km above the ground. The length scale for the vectors is given in the lower right-hand corner. The reflectivity gray scale is given on the right side of the figure. Radar positions and the coastline of Taiwan are also given.*

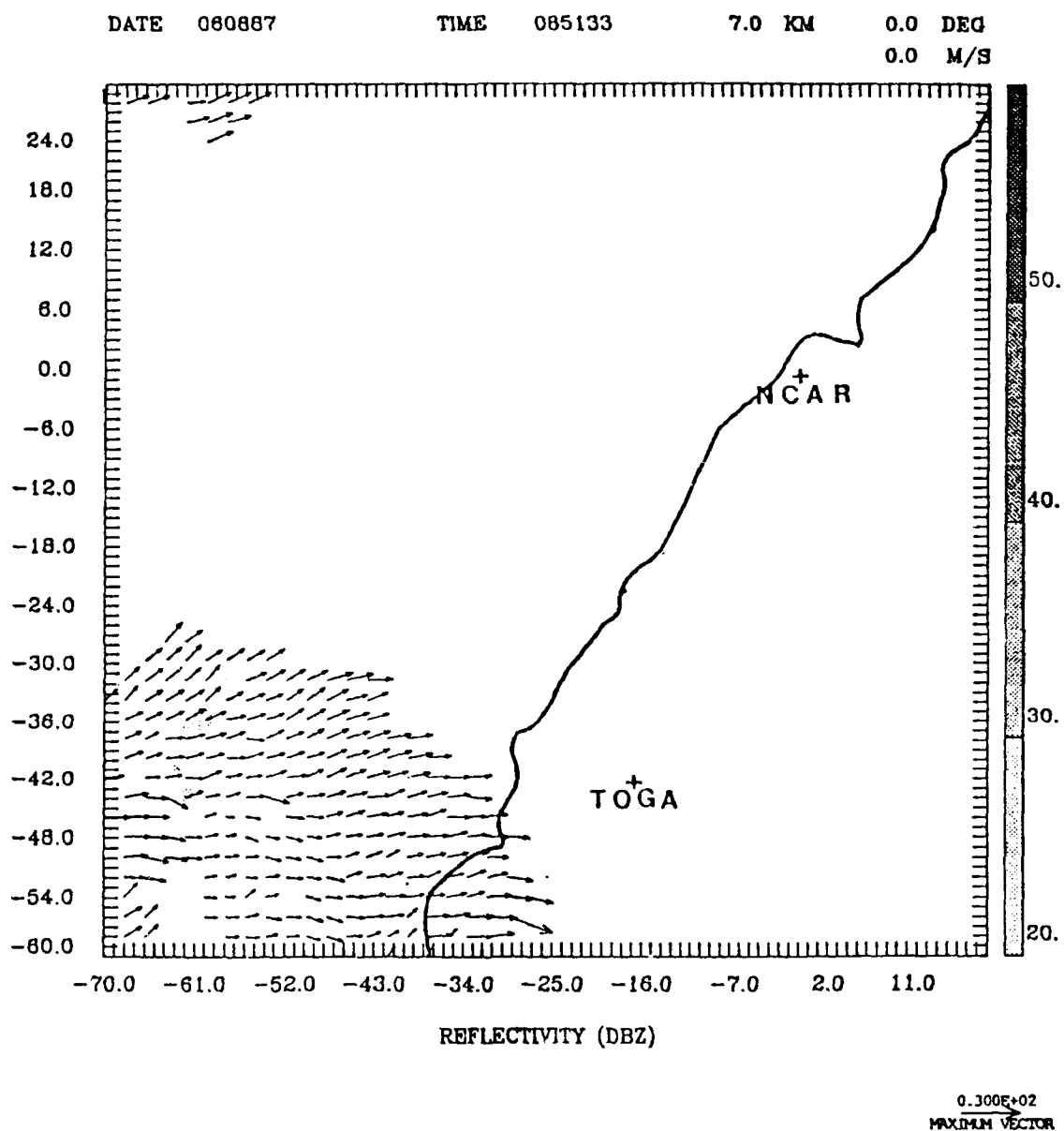


Fig. 11h. Dual-Doppler analysis of reflectivities and horizontal velocities for 085133, at 7.0 km above the ground. The length scale for the vectors is given in the lower right-hand corner. The reflectivity gray scale is given on the right side of the figure. Radar positions and the coastline of Taiwan are also given.

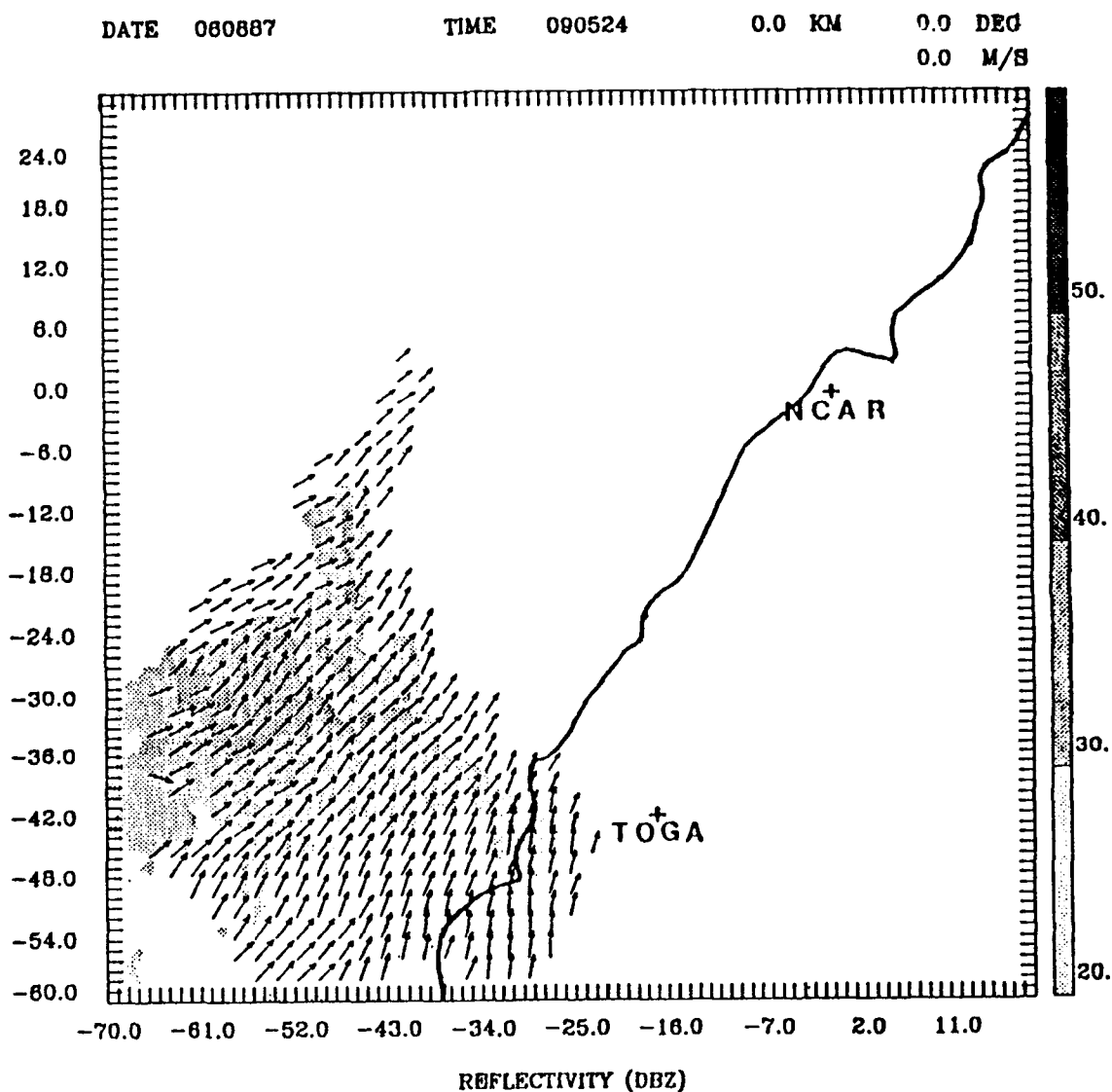


Fig. 12a. Dual-Doppler analysis of reflectivities and horizontal velocities for 090524, at the ground. The length scale for the vectors is given in the lower right-hand corner. The reflectivity gray scale is given on the right side of the figure. Radar positions and the coastline of Taiwan are also given.

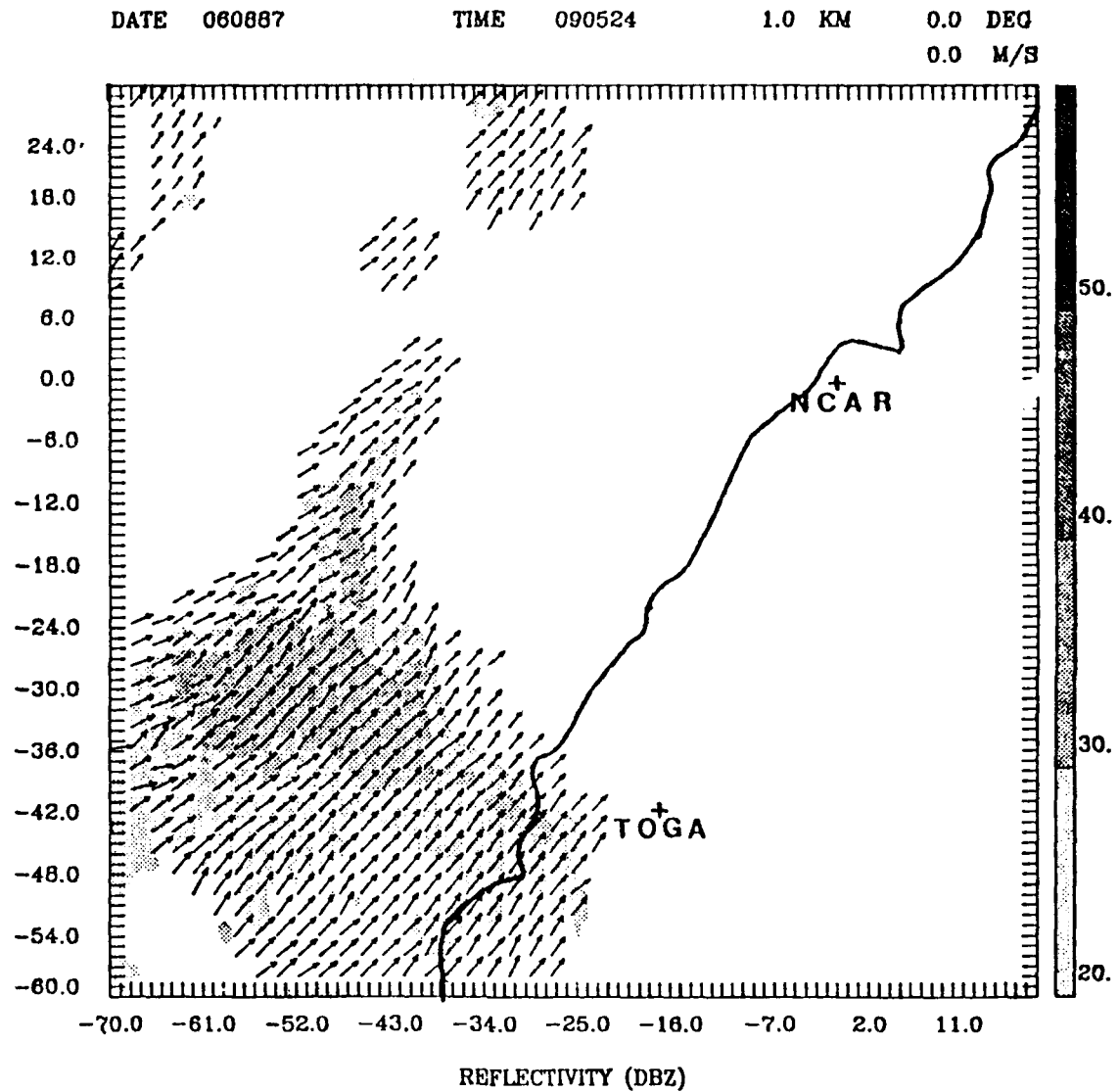
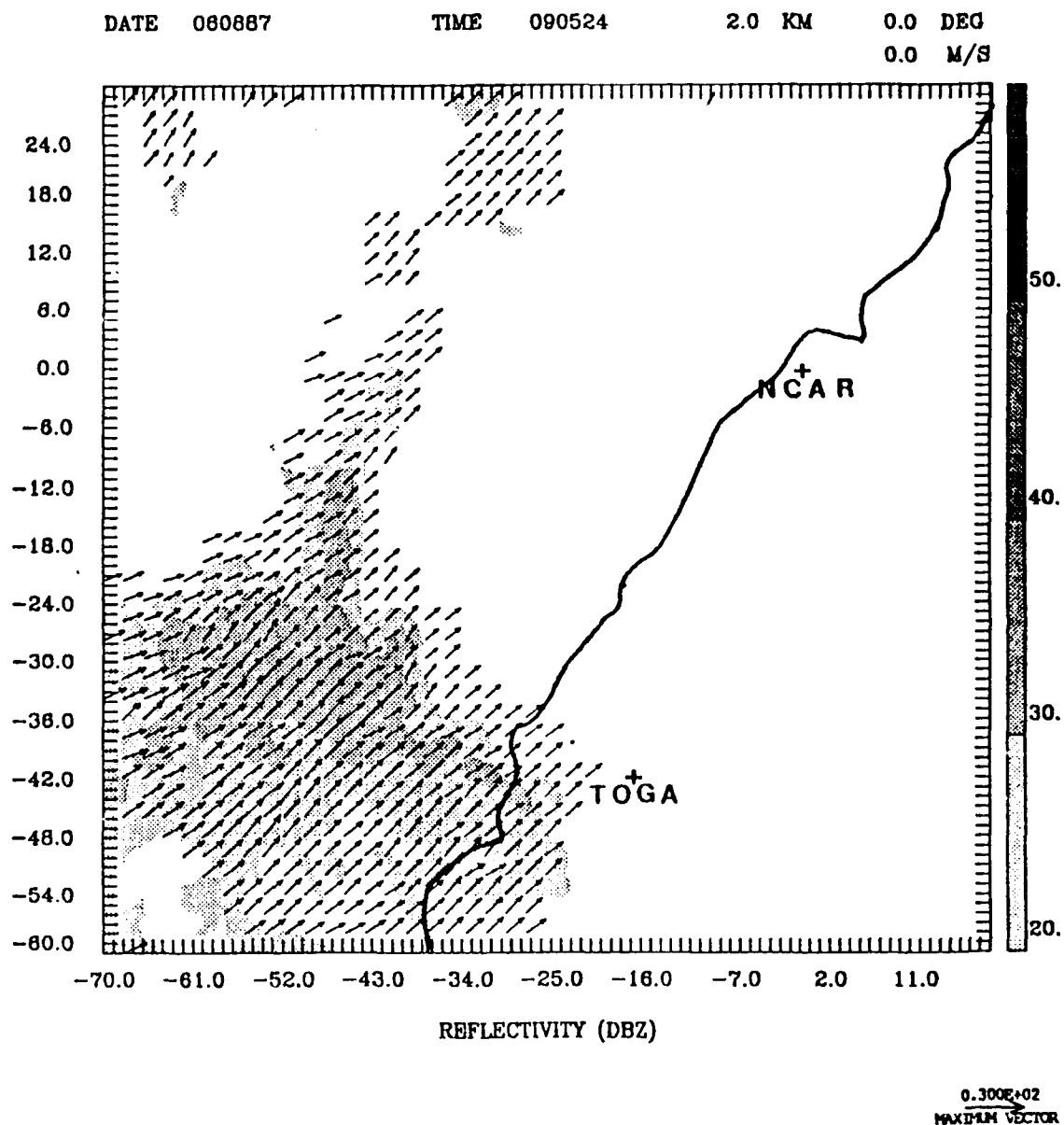


Fig. 12b. Dual-Doppler analysis of reflectivities and horizontal velocities for 090524, at 1.0 km above the ground. The length scale for the vectors is given in the lower right-hand corner. The reflectivity gray scale is given on the right side of the figure. Radar positions and the coastline of Taiwan are also given.



*Fig. 12c. Dual-Doppler analysis of reflectivities and horizontal velocities for 090524, at 2.0 km above the ground. The length scale for the vectors is given in the lower right-hand corner. The reflectivity gray scale is given on the right side of the figure. Radar positions and the coastline of Taiwan are also given.*

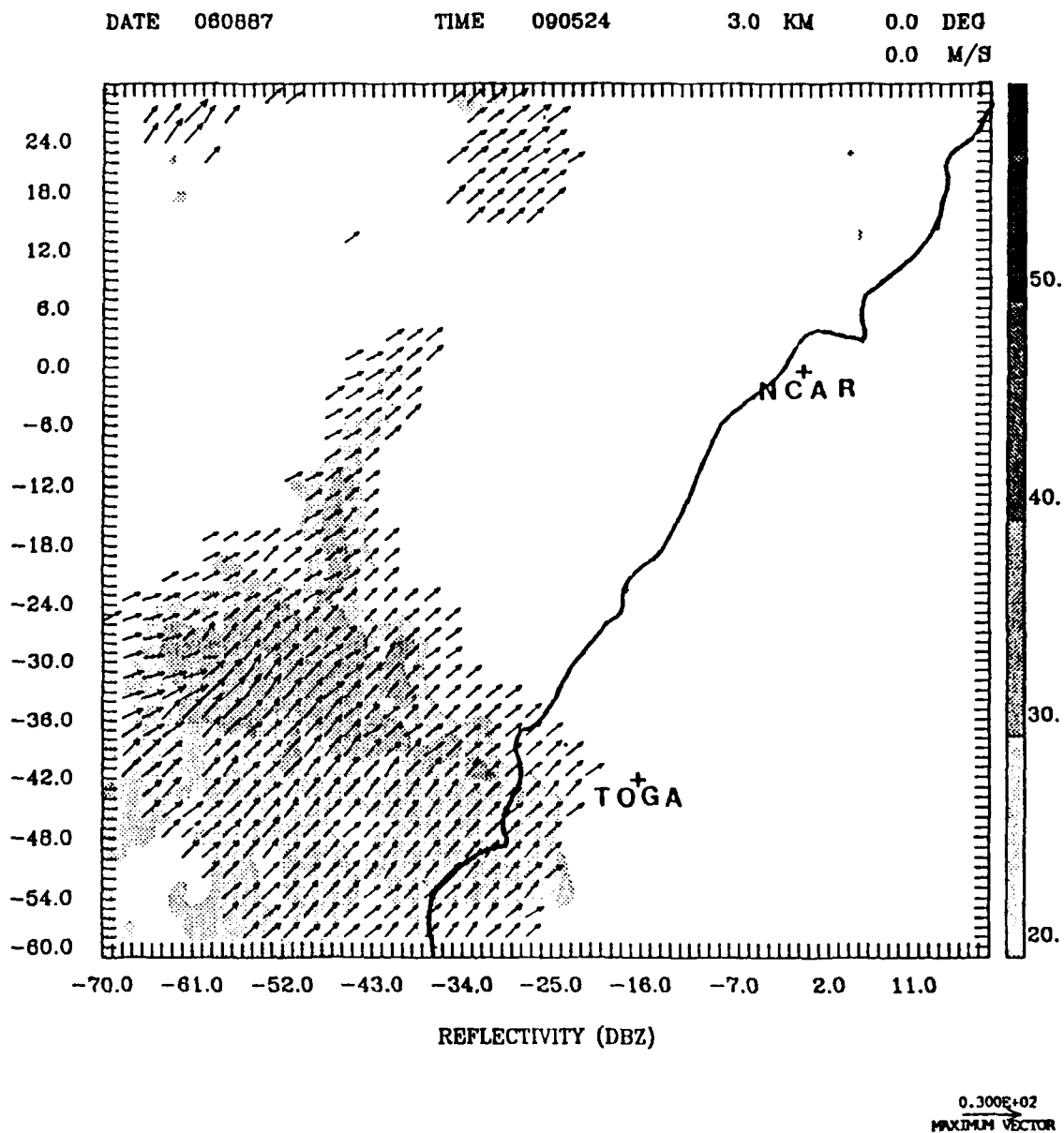


Fig. 12d. Dual-Doppler analysis of reflectivities and horizontal velocities for 090524, at 3.0 km above the ground. The length scale for the vectors is given in the lower right-hand corner. The reflectivity gray scale is given on the right side of the figure. Radar positions and the coastline of Taiwan are also given.

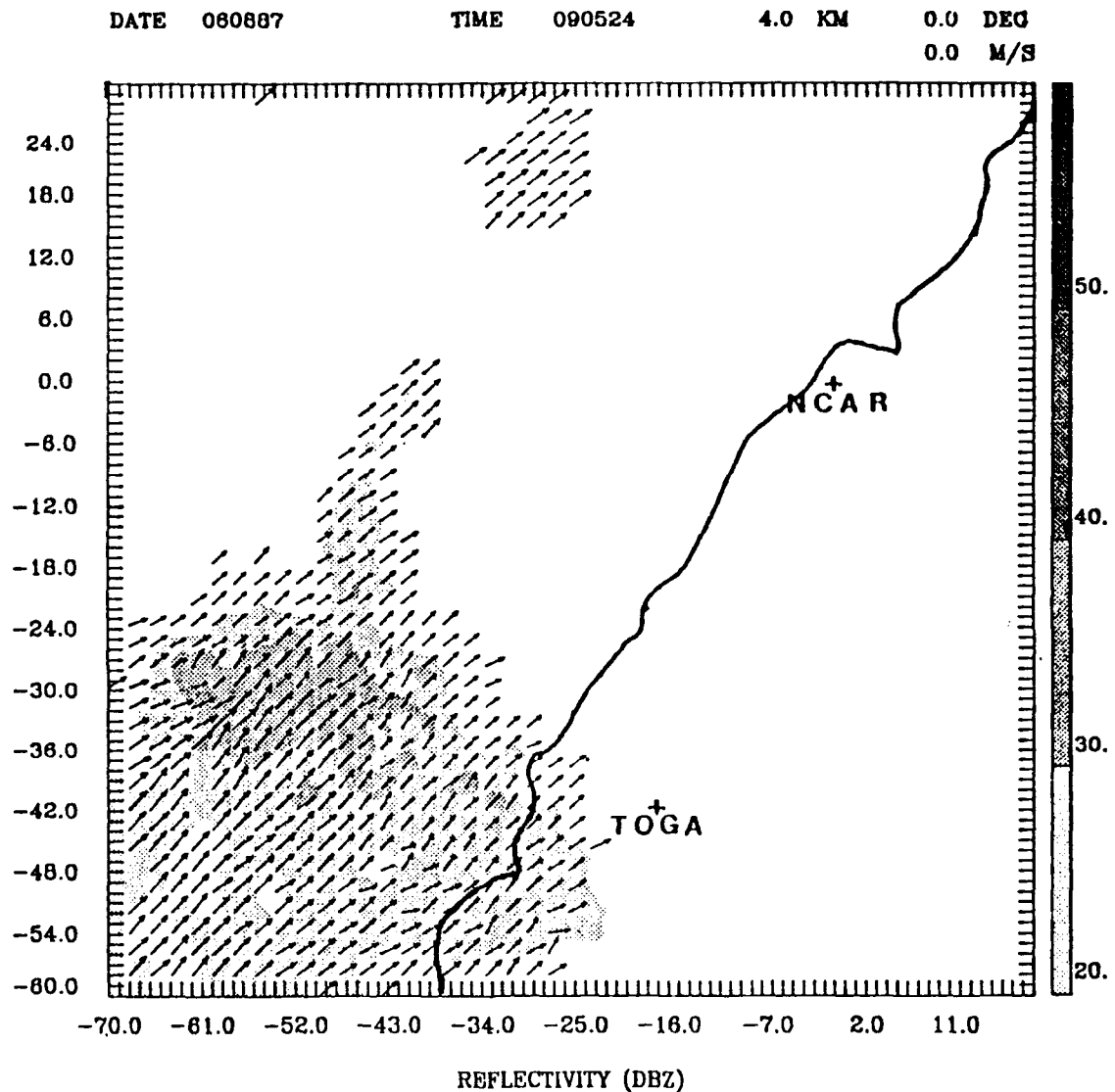


Fig. 12e. Dual-Doppler analysis of reflectivities and horizontal velocities for 090524, at 4.0 km above the ground. The length scale for the vectors is given in the lower right-hand corner. The reflectivity gray scale is given on the right side of the figure. Radar positions and the coastline of Taiwan are also given.

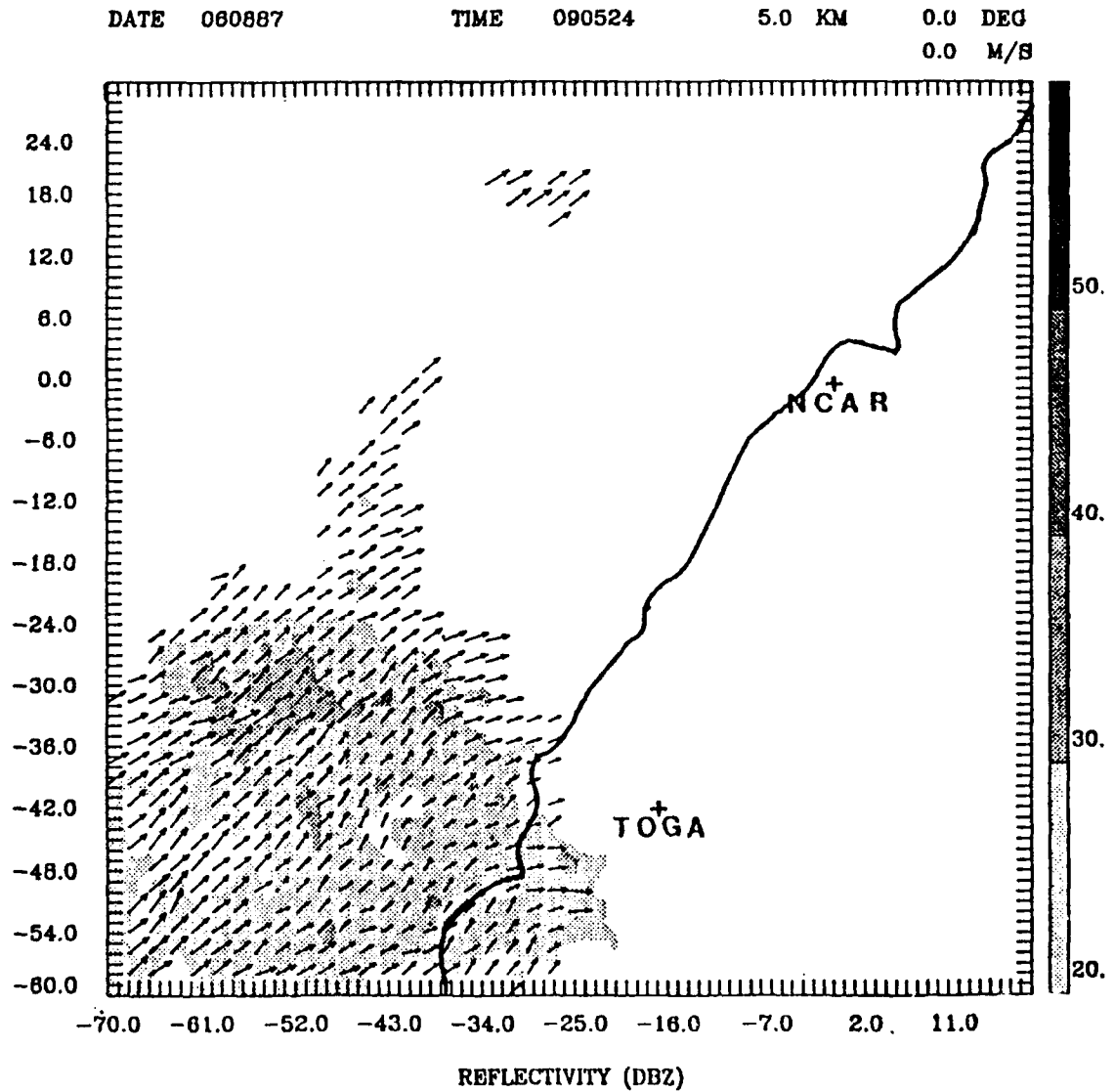
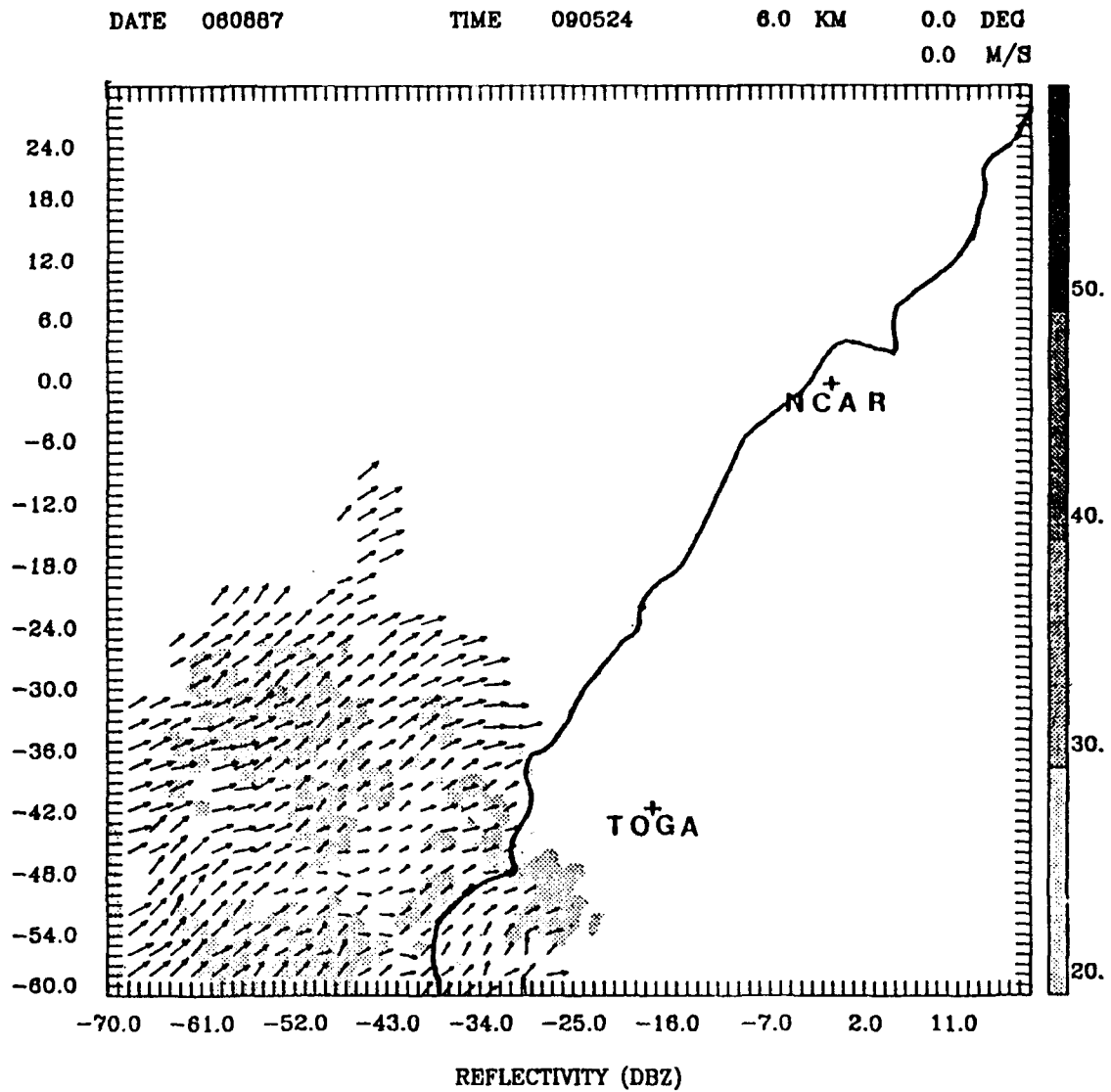
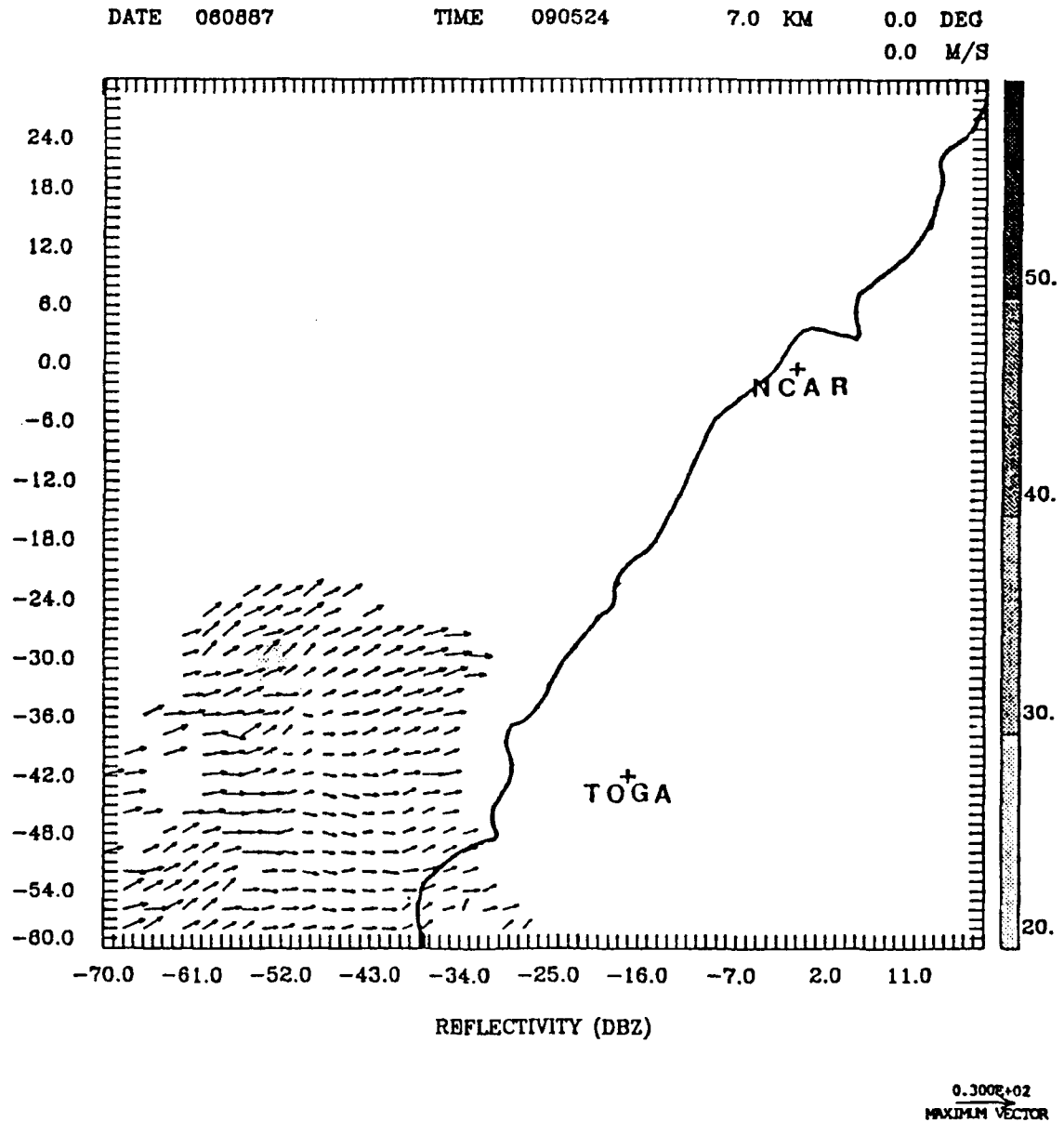


Fig. 12f. Dual-Doppler analysis of reflectivities and horizontal velocities for 090524, at 5.0 km above the ground. The length scale for the vectors is given in the lower right-hand corner. The reflectivity gray scale is given on the right side of the figure. Radar positions and the coastline of Taiwan are also given.



*Fig. 12g. Dual-Doppler analysis of reflectivities and horizontal velocities for 090524, at 6.0 km above the ground. The length scale for the vectors is given in the lower right-hand corner. The reflectivity gray scale is given on the right side of the figure. Radar positions and the coastline of Taiwan are also given.*



*Fig. 12h. Dual-Doppler analysis of reflectivities and horizontal velocities for 090524, at 7.0 km above the ground. The length scale for the vectors is given in the lower right-hand corner. The reflectivity gray scale is given on the right side of the figure. Radar positions and the coastline of Taiwan are also given.*

echo core and several smaller echo cores. For the first time, a large area of echo greater than 30 dBZ is found. Prior to this, the surface maximum intensities have been relatively small in area and have merged together at the 2.0 km height. Wind vectors near the coastline are almost from the south. The other winds are principally from the southwest. Thus, there is confluent flow between the mesoscale ridging (as indicated by the southerly flow) and the synoptic scale troughing (as indicated by the southwesterly flow). It is expected that this area would be conducive for further development. This southerly flow, however, is very shallow, for even at the 1.0 km height (Fig. 12b) all flow is from the southwest. At the 2.0 km (Fig. 12c) height, the echo cores have once again merged. The core associated with the northerly extension appears to merge with the core in the main echo. From this height upwards (Figs. 12d-f) the larger core area once again breaks into smaller areas. The echo depicting the line shows the most rapid decrease with height. The core is almost nonexistent at the 4.0 km height, and the line echo itself is almost gone by the 5.0 km height. Thus, at this time the line is relatively intense, but shallow. Almost all of the echo is gone by the 7.0 km height (Figs. 12f-h). The highest echo top just reaches the 6.0 km height. In Figs. 12f-h, the southwest flow and westerly flow that was present at 085133 LST (Figs. 11f-h) is dominant.

The propagation speed of the echo (towards the NCAR radar) at 095308 LST (Figs. 13a-h) is estimated at  $12.6 \text{ ms}^{-1}$ . At 095308 LST, several horizontal velocity values exceed  $17 \text{ ms}^{-1}$ . Examination of the lowest heights (surface to 2.0 km,

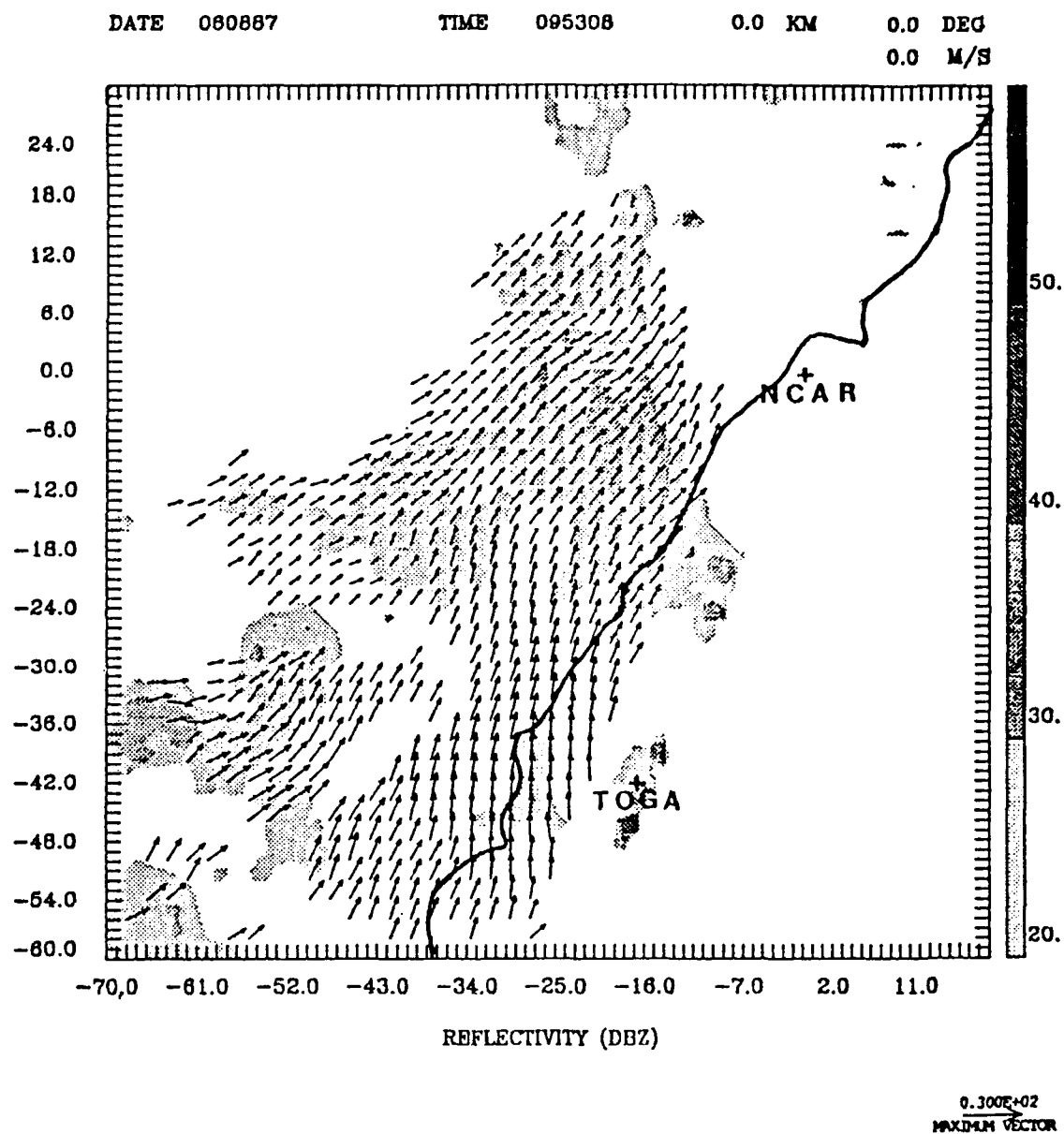


Fig. 13a. Dual-Doppler analysis of reflectivities and horizontal velocities for 095308, at the ground. The length scale for the vectors is given in the lower right-hand corner. The reflectivity gray scale is given on the right side of the figure. Radar positions and the coastline of Taiwan are also given.

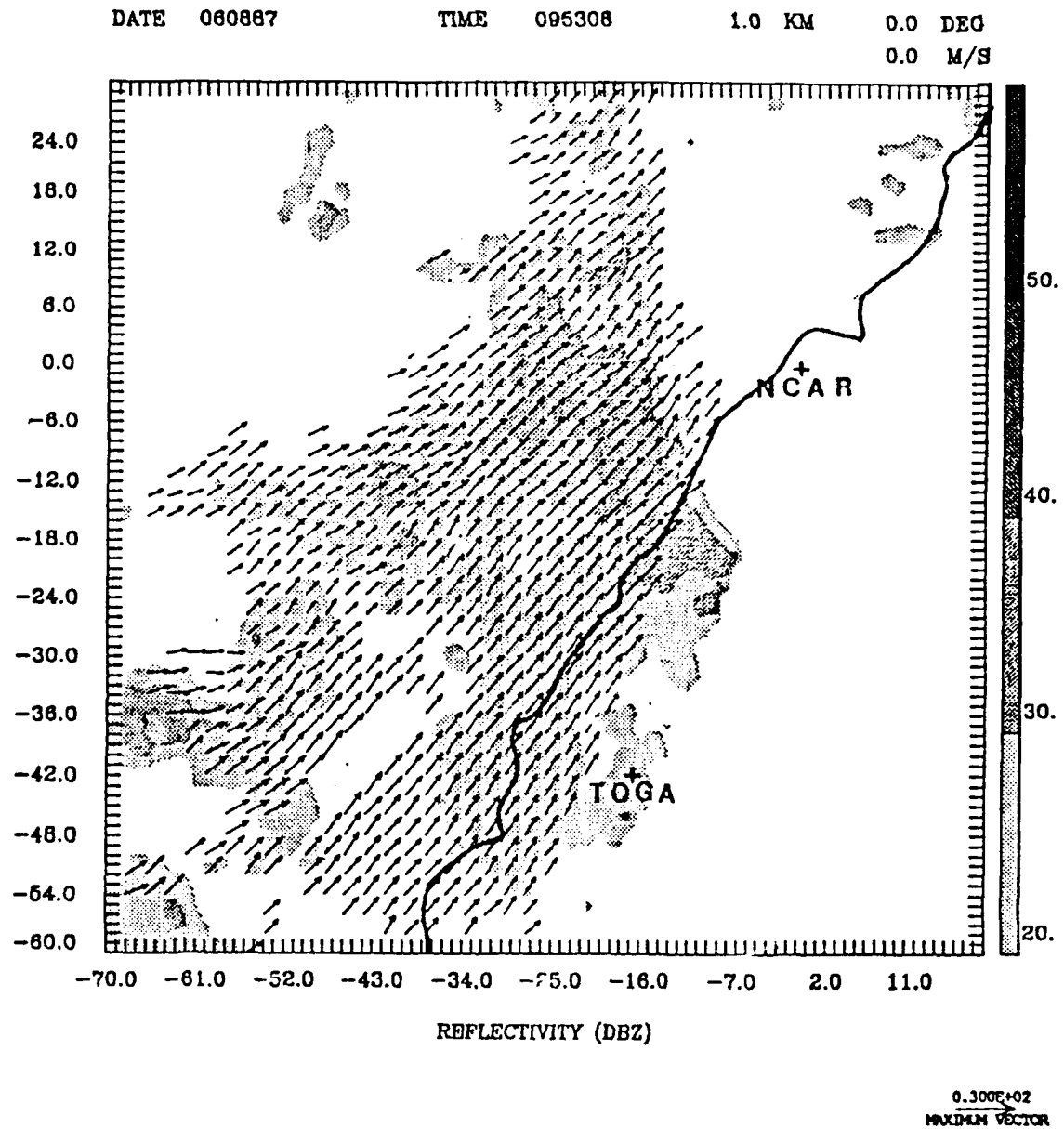


Fig. 19b. Dual-Doppler analysis of reflectivities and horizontal velocities for 095308, at 1.0 km above the ground. The length scale for the vectors is given in the lower right-hand corner. The reflectivity gray scale is given on the right side of the figure. Radar positions and the coastline of Taiwan are also given.

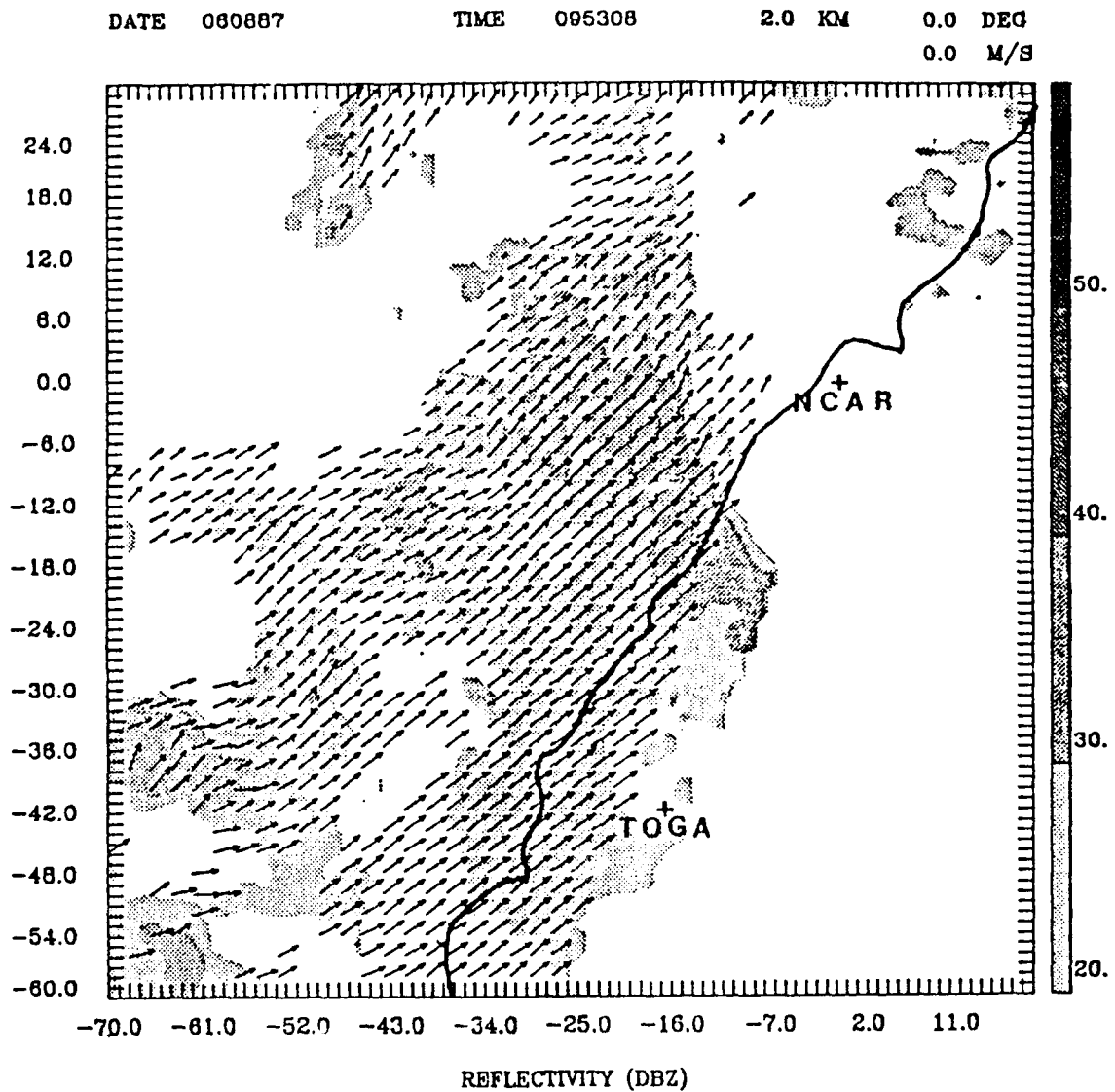


Fig. 19c. Dual-Doppler analysis of reflectivities and horizontal velocities for 095308, at 2.0 km above the ground. The length scale for the vectors is given in the lower right-hand corner. The reflectivity gray scale is given on the right side of the figure. Radar positions and the coastline of Taiwan are also given.

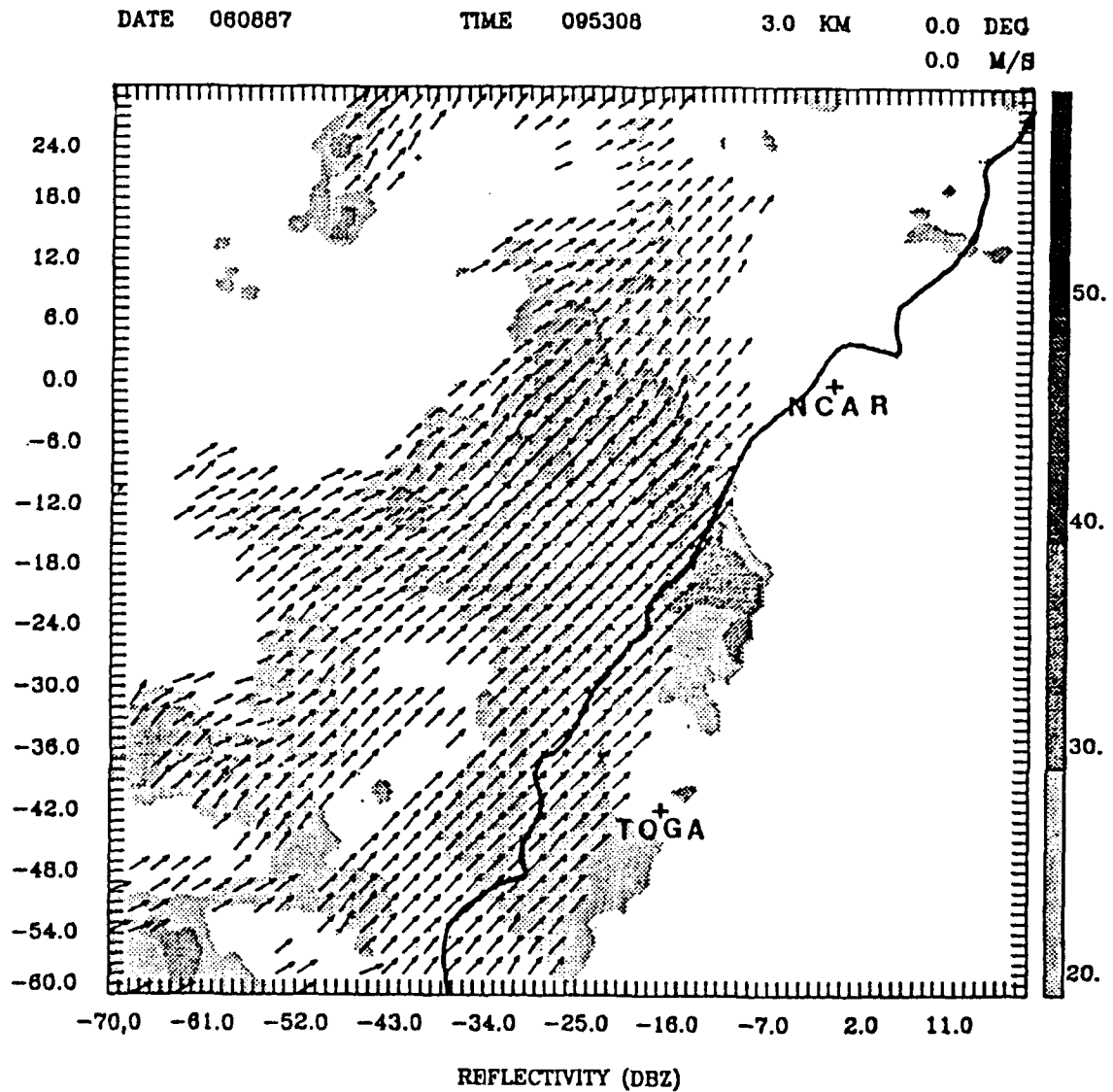
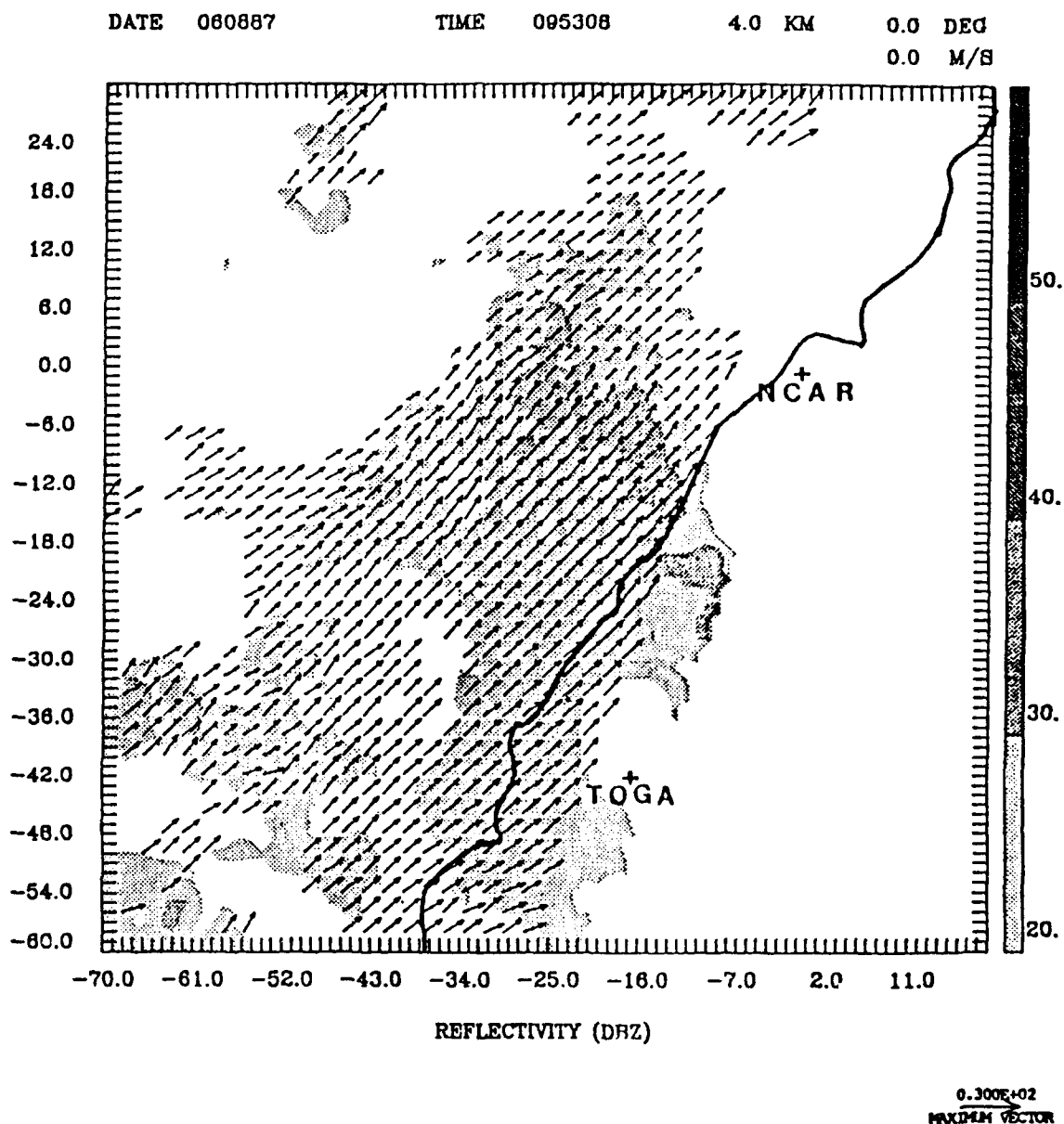


Fig. 13d. Dual-Doppler analysis of reflectivities and horizontal velocities for 095308, at 3.0 km above the ground. The length scale for the vectors is given in the lower right-hand corner. The reflectivity gray scale is given on the right side of the figure. Radar positions and the coastline of Taiwan are also given.



*Fig. 19e. Dual-Doppler analysis of reflectivities and horizontal velocities for 095308, at 4.0 km above the ground. The length scale for the vectors is given in the lower right-hand corner. The reflectivity gray scale is given on the right side of the figure. Radar positions and the coastline of Taiwan are also given.*

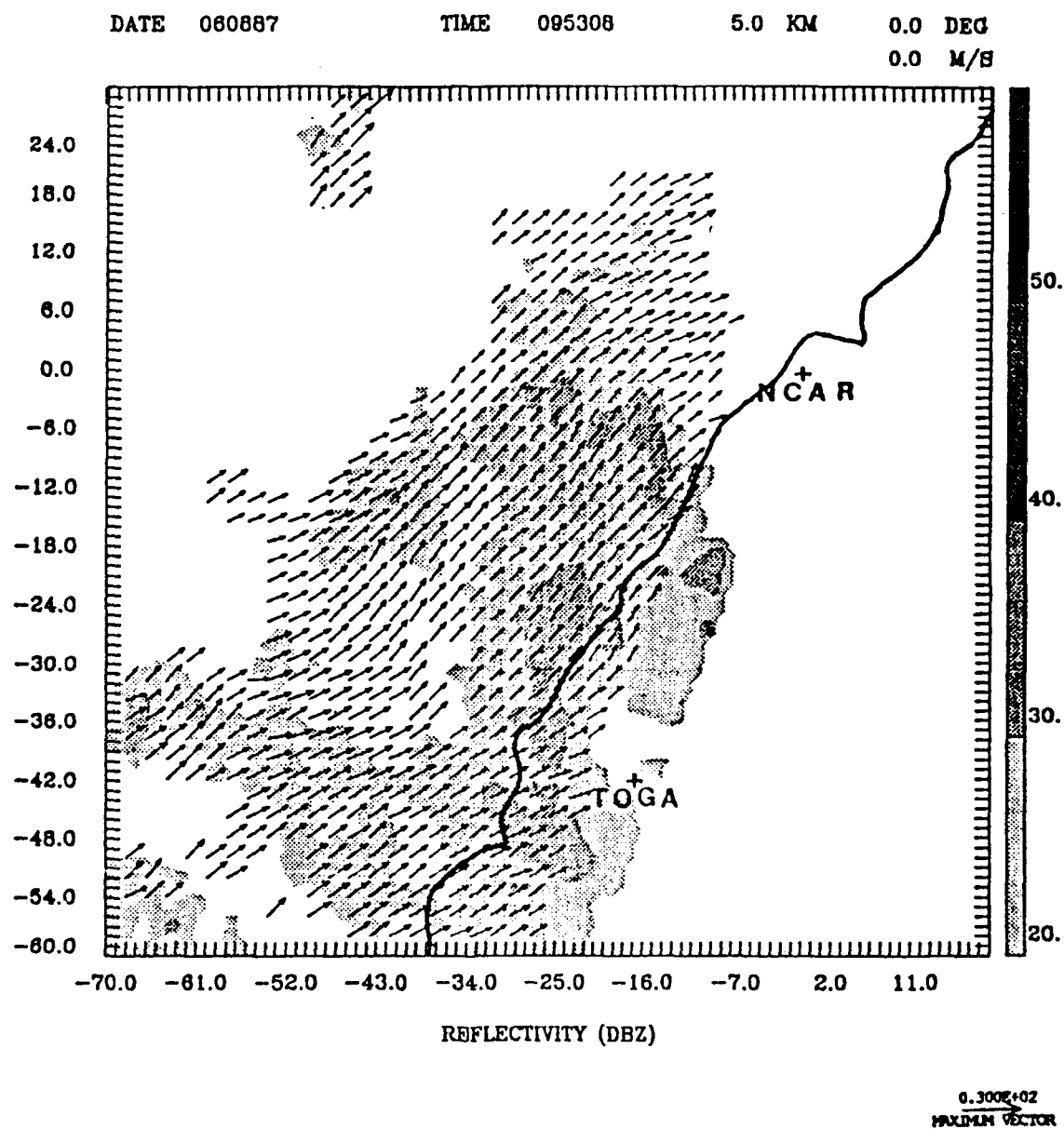


Fig. 13f. Dual-Doppler analysis of reflectivities and horizontal velocities for 095308, at 5.0 km above the ground. The length scale for the vectors is given in the lower right-hand corner. The reflectivity gray scale is given on the right side of the figure. Radar positions and the coastline of Taiwan are also given.

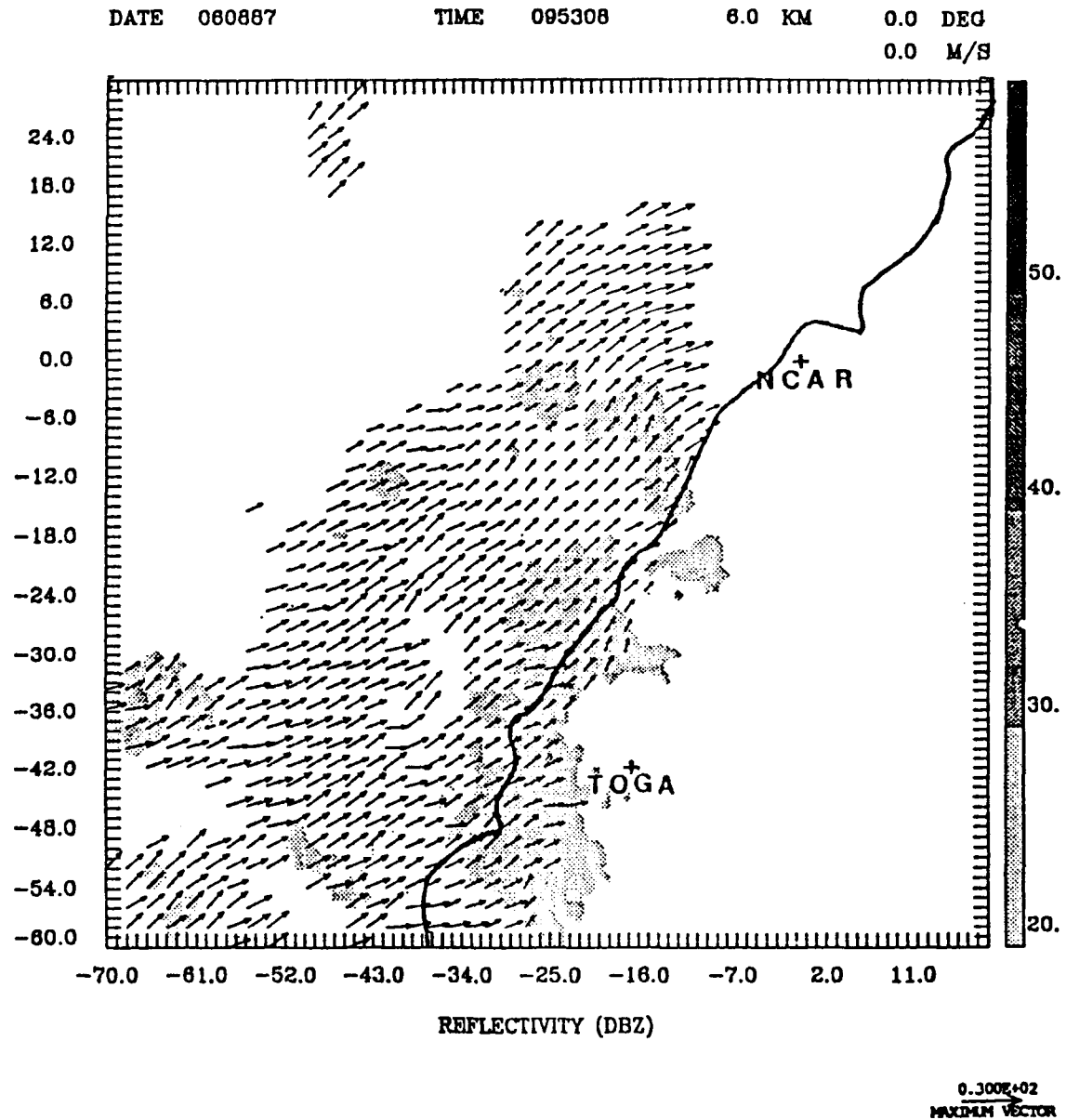


Fig. 19g. Dual-Doppler analysis of reflectivities and horizontal velocities for 095308, at 6.0 km above the ground. The length scale for the vectors is given in the lower right-hand corner. The reflectivity gray scale is given on the right side of the figure. Radar positions and the coastline of Taiwan are also given.

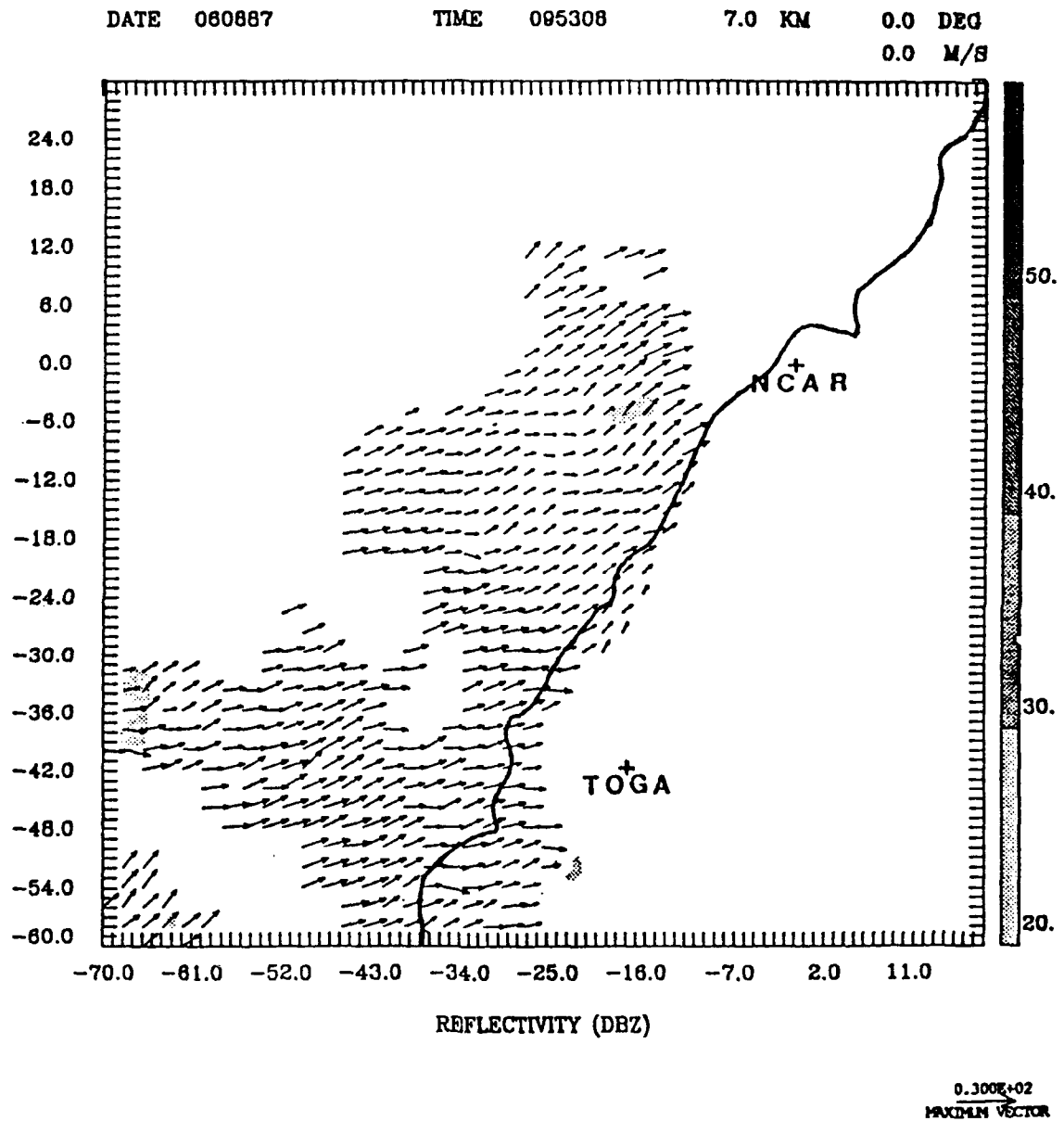


Fig. 13h. Dual-Doppler analysis of reflectivities and horizontal velocities for 095308, at 7.0 km above the ground. The length scale for the vectors is given in the lower right-hand corner. The reflectivity gray scale is given on the right side of the figure. Radar positions and the coastline of Taiwan are also given.

Figs. 13a-c) fails to clearly show the linear formation that was seen at 090524 LST (Figs. 12a-f). Instead, several reflectivity maxima are seen at the surface (Fig. 13a). Up to this time, only one large echo area has been present. Two large cores (greater than 30 dBZ) and several smaller cores now exist. The area of low-level convergence between the southerly and southwesterly flow is still present. By the 1.0 km height, (Fig. 13b), the flow is southwesterly and the echo area has increased compared to the area at the surface. Fig. 13c shows the 2.0 km height. Consistent with the past analysis times, the cores have expanded and/or merged to give the largest core area yet observed. The cores and reflectivities maxima begin to decrease in size and area between the 3.0 km and 5.0 km heights (Figs. 13d-f). However, at the 5.0 km height (Fig. 13f), a large area of greater than 30 dBZ is seen over the location of the low level convergence. The cause for this, since it is only at this height, is that it corresponds to the local height of the melting level ( $0^{\circ}\text{C}$ ), creating the radar "brightband". At this height, melting will cause an increase in the reflectivity as large frozen particles begin to melt and develop a liquid water coat that makes them more reflective. This height will be verified by the examination of Range Height Scans (RHI) later in this chapter. At 6.0 km height (Fig. 13g), the flow is predominately southwesterly. At 7.0 km height (Fig. 13h), the flow becomes westerly. Flow prior to this was westerly at lower heights.

Figures 14a-g depict the analysis at 105232 LST. At this time the front is just to the north of the analysis domain. There are several areas of high reflectivity to

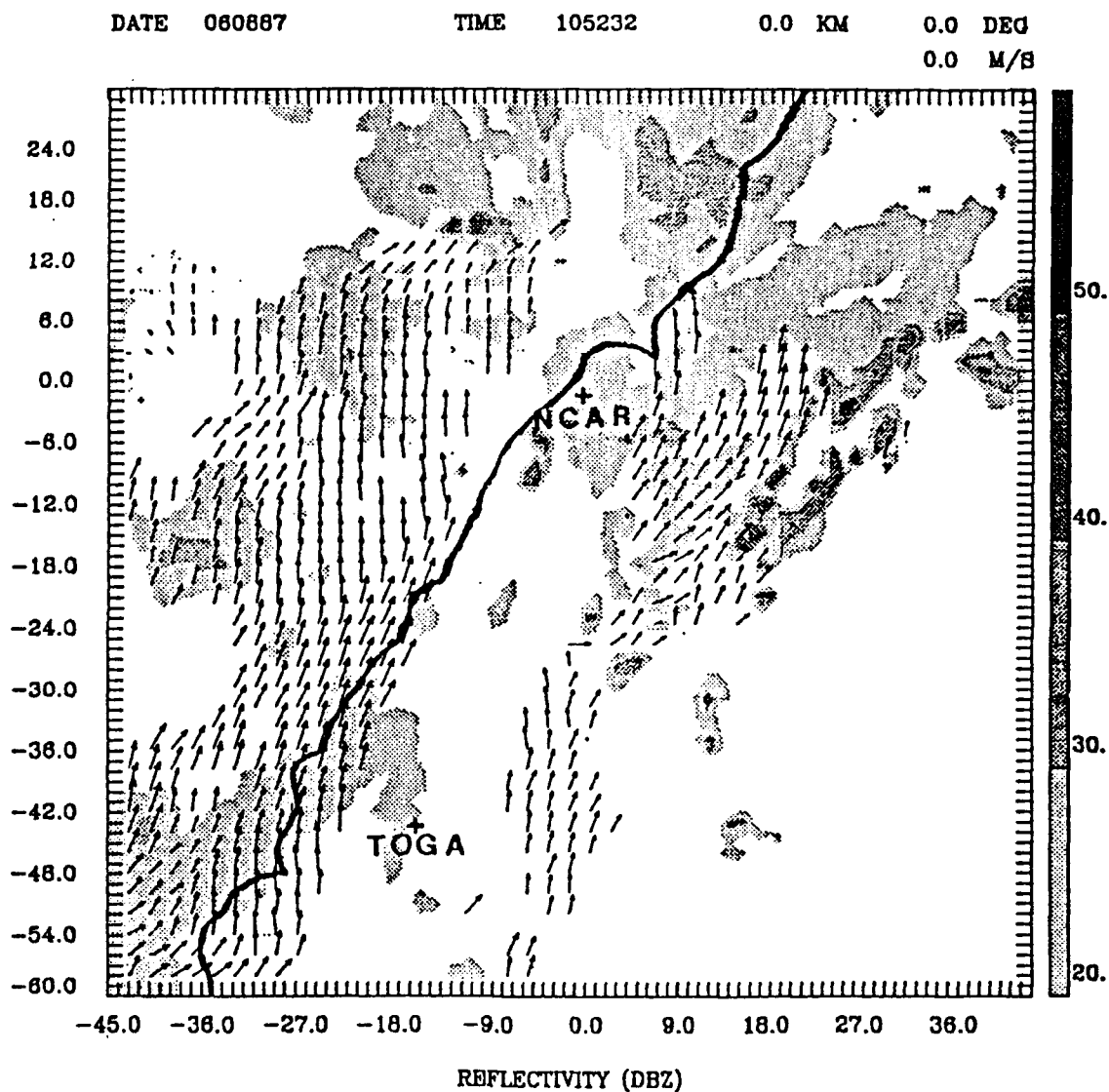


Fig. 14a. Dual-Doppler analysis of reflectivities and horizontal velocities for 105232, at the ground. The length scale for the vectors is given in the lower right-hand corner. The reflectivity gray scale is given on the right side of the figure. Radar positions and the coastline of Taiwan are also given.

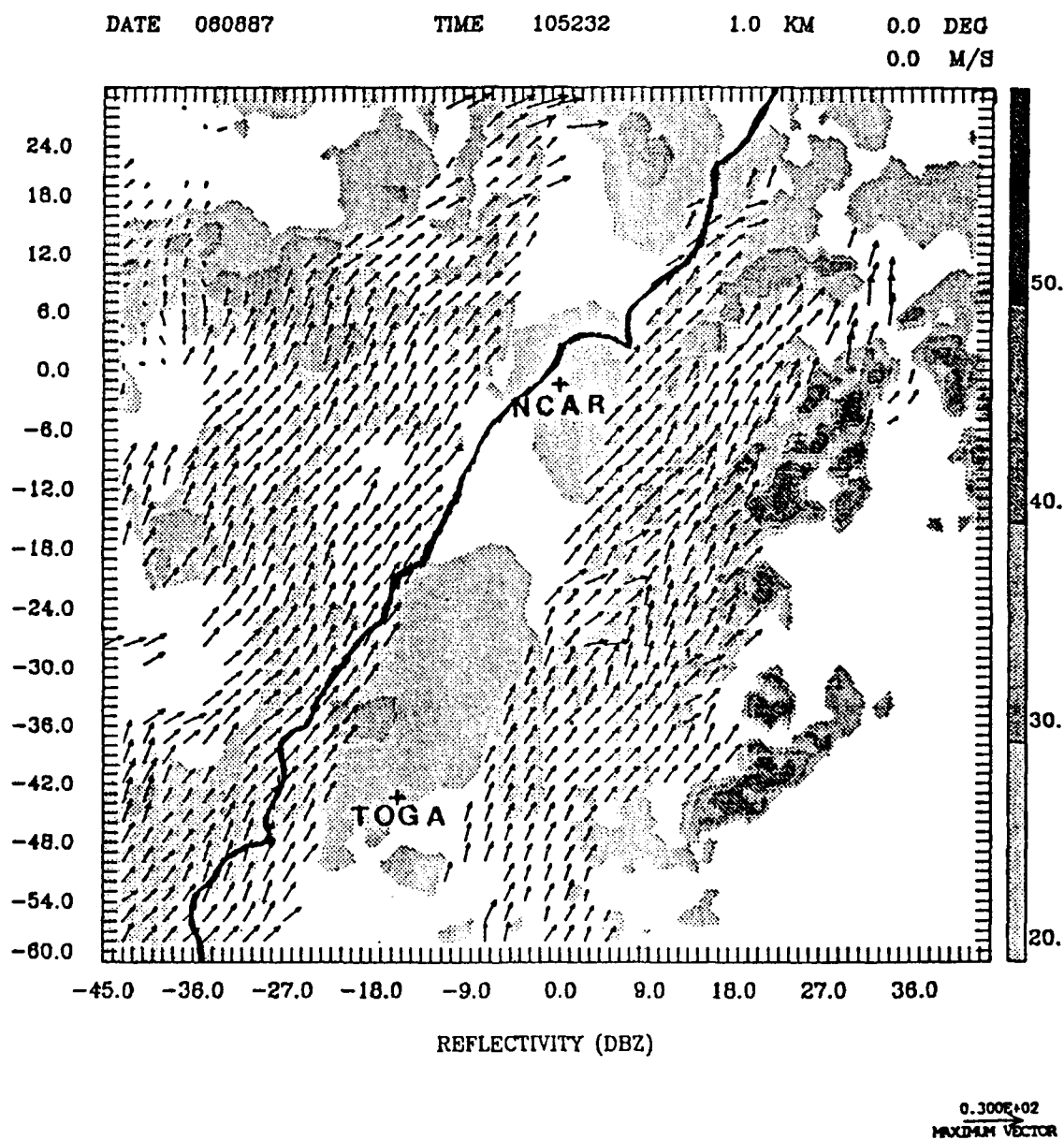


Fig. 14b. Dual-Doppler analysis of reflectivities and horizontal velocities for 105232, at 1.0 km above the ground. The length scale for the vectors is given in the lower right-hand corner. The reflectivity gray scale is given on the right side of the figure. Radar positions and the coastline of Taiwan are also given.

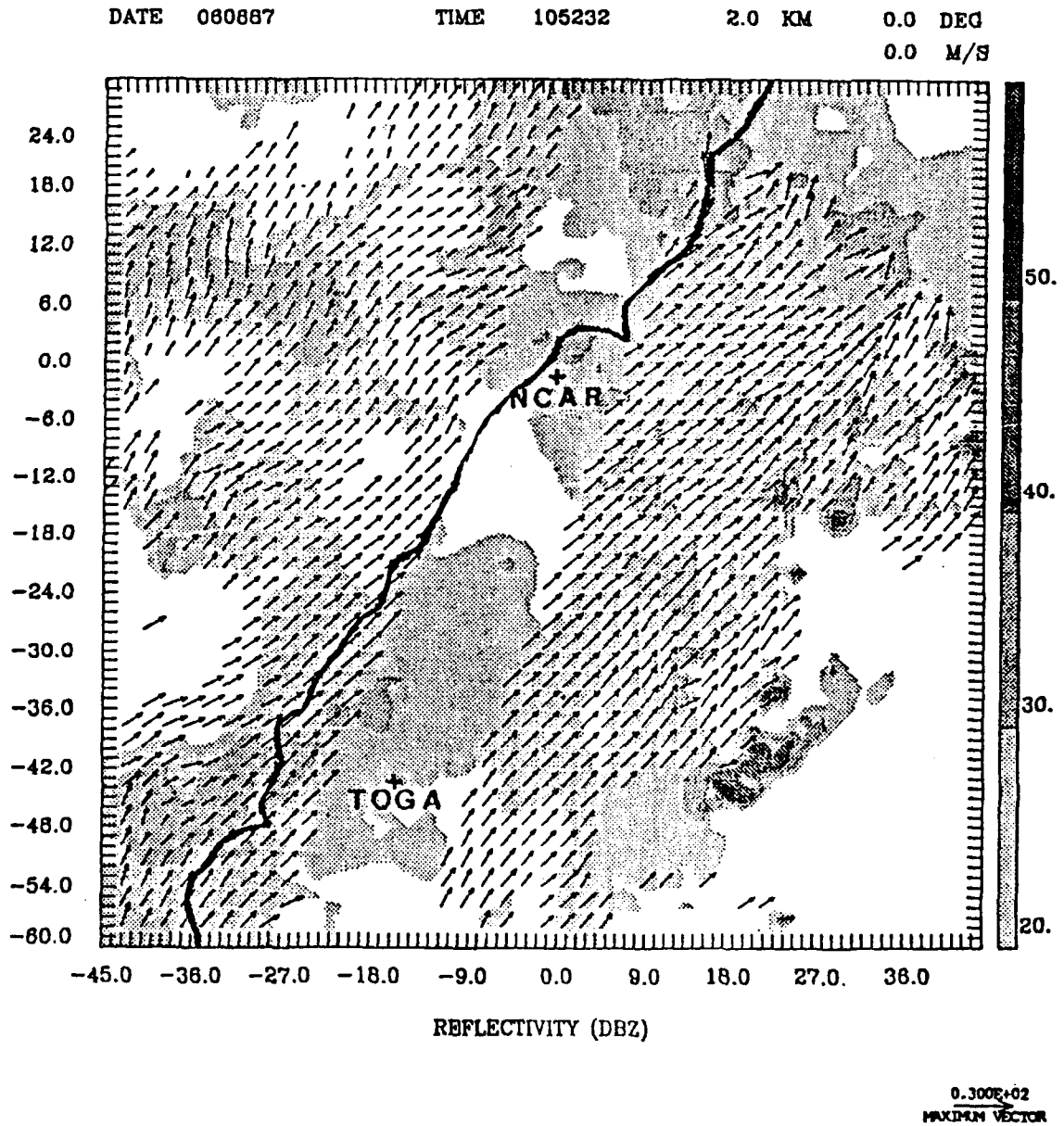


Fig. 14c. Dual-Doppler analysis of reflectivities and horizontal velocities for 105232, at 2.0 km above the ground. The length scale for the vectors is given in the lower right-hand corner. The reflectivity gray scale is given on the right side of the figure. Radar positions and the coastline of Taiwan are also given.

DATE 080887

TIME 105232

3.0 KM

0.0 DEG

0.0 M/S

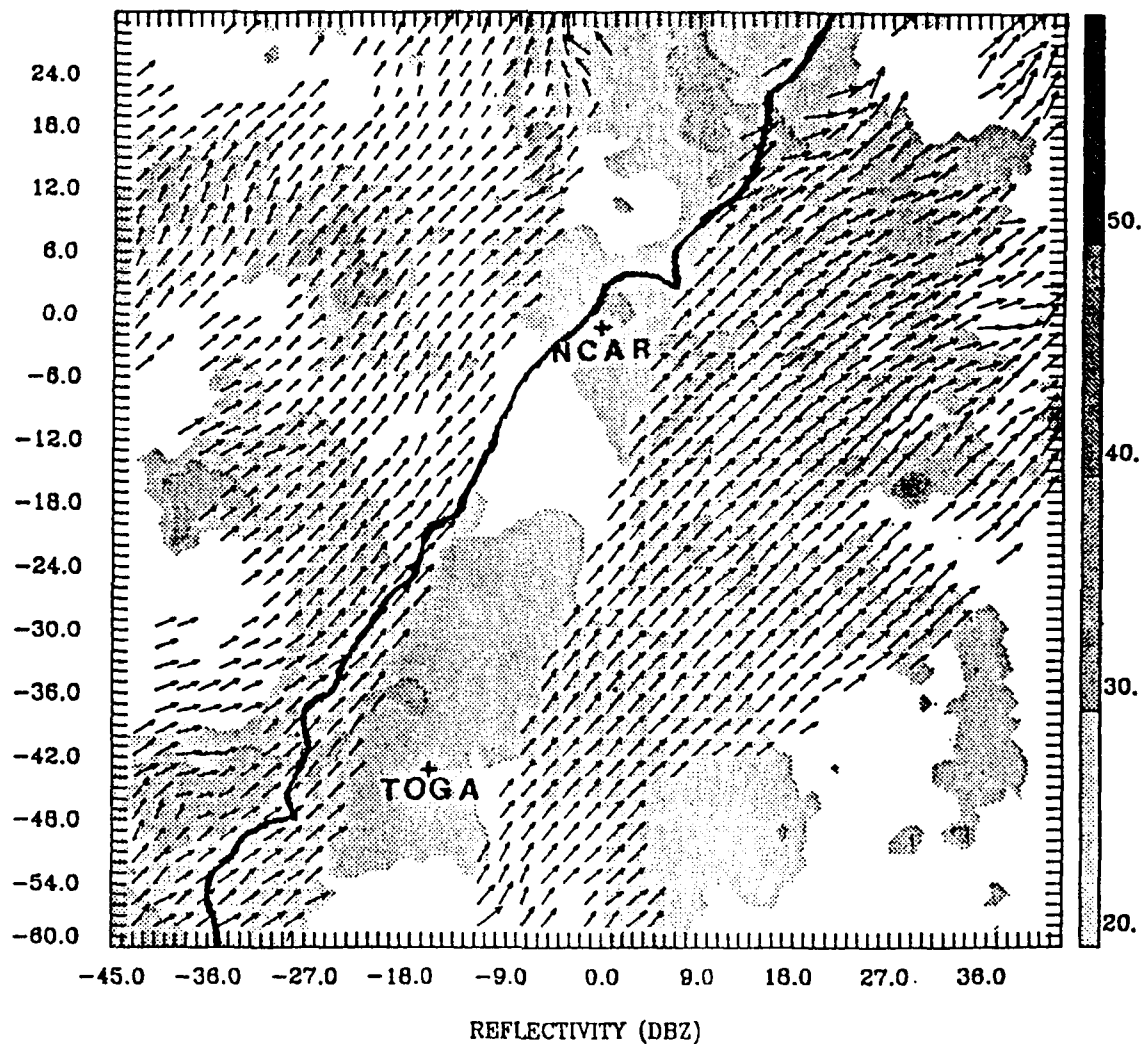


Fig. 14d. Dual-Doppler analysis of reflectivities and horizontal velocities for 105232, at 3.0 km above the ground. The length scale for the vectors is given in the lower right-hand corner. The reflectivity gray scale is given on the right side of the figure. Radar positions and the coastline of Taiwan are also given.

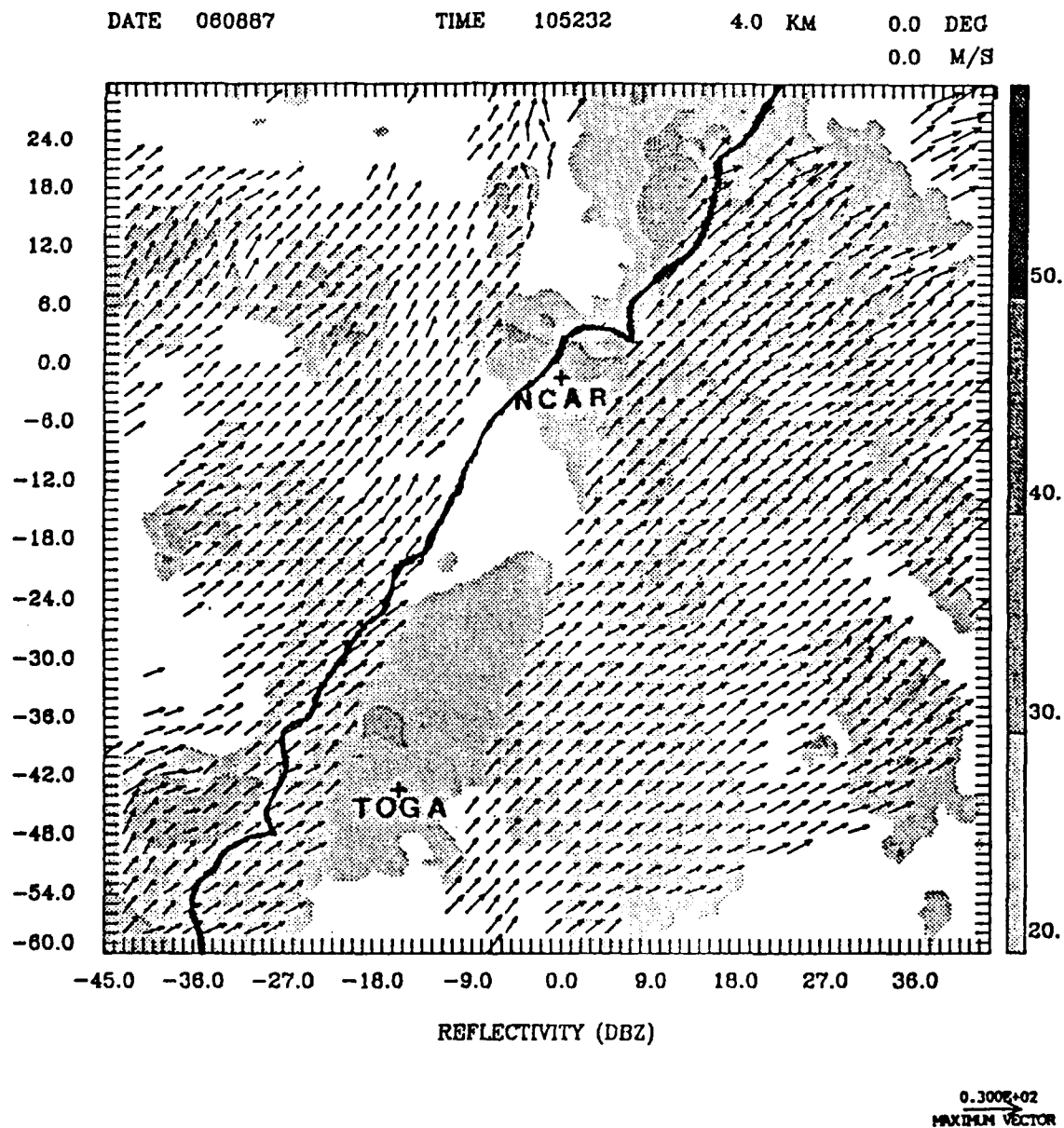


Fig. 14e. Dual-Doppler analysis of reflectivities and horizontal velocities for 105232, at 4.0 km above the ground. The length scale for the vectors is given in the lower right-hand corner. The reflectivity gray scale is given on the right side of the figure. Radar positions and the coastline of Taiwan are also given.

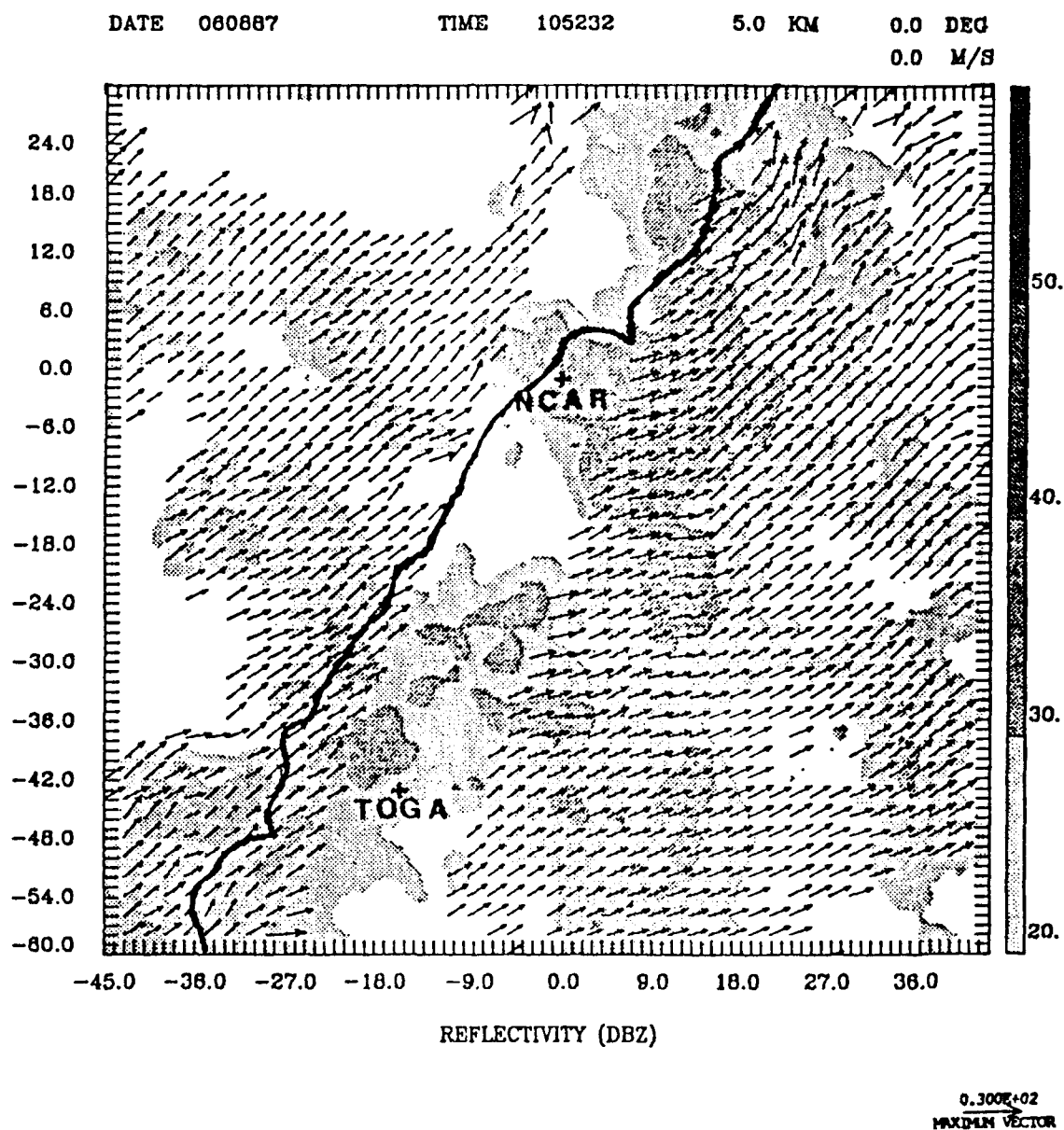


Fig. 14f. Dual-Doppler analysis of reflectivities and horizontal velocities for 105232, at 5.0 km above the ground. The length scale for the vectors is given in the lower right-hand corner. The reflectivity gray scale is given on the right side of the figure. Radar positions and the coastline of Taiwan are also given.

DATE 060887

TIME 105232

6.0 KM

0.0 DEG

0.0 M/S

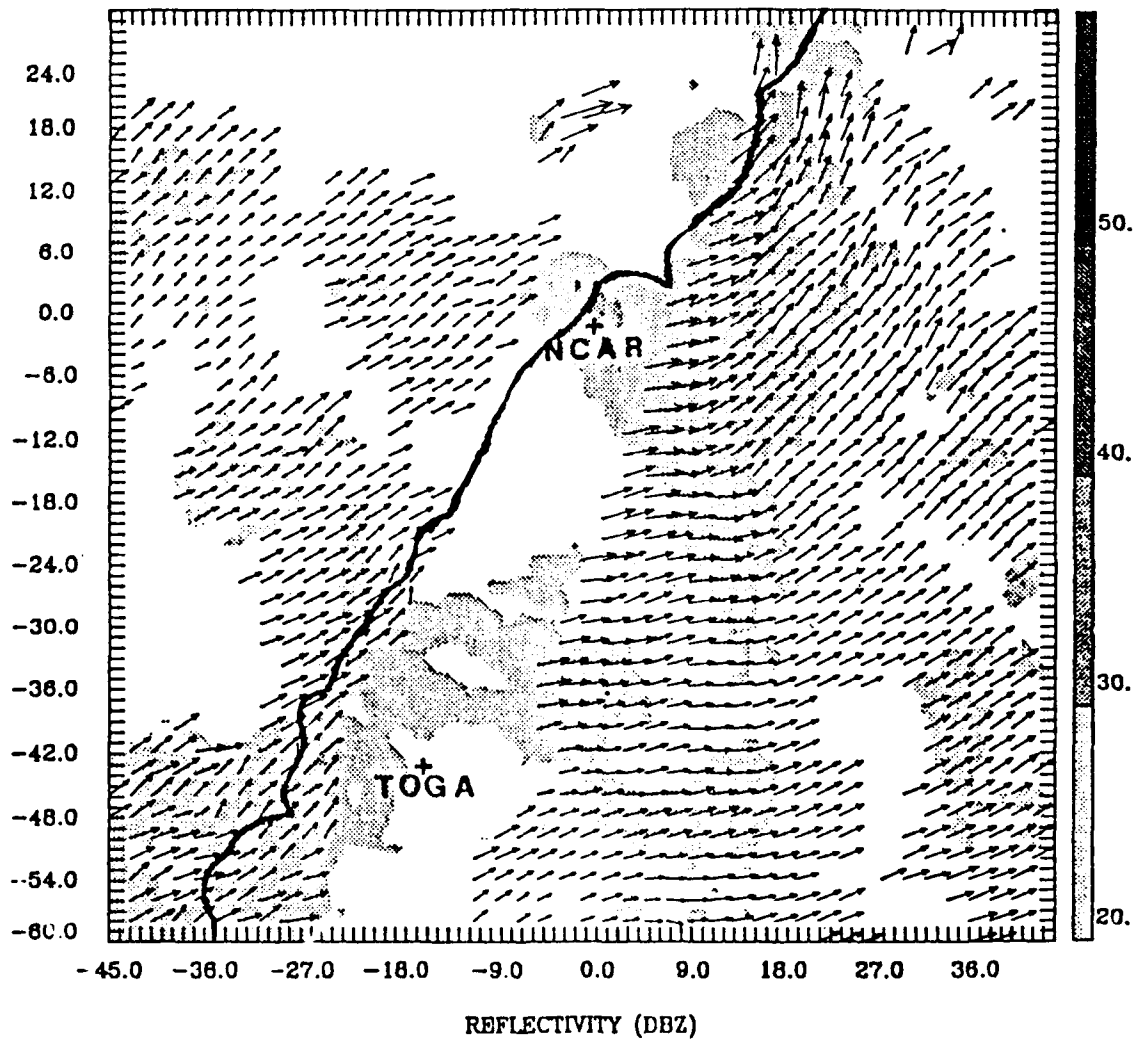


Fig. 14g. Dual-Doppler analysis of reflectivities and horizontal velocities for 105232, at 6.0 km above the ground. The length scale for the vectors is given in the lower right-hand corner. The reflectivity gray scale is given on the right side of the figure. Radar positions and the coastline of Taiwan are also given.

the west and southwest of the NCAR radar. These echoes are ground clutter from the mountains to the west of the radar. Echo cores greater than 30 dBZ increase in size to a maximum area at 2.0 km (Figs. 14a-c), then decrease in size between the 2.0 km and 6.0 km height (Figs. 14d-g), where the core tops are. The echo tops appear to have decreased in height, as none are seen at 7.0 km (not shown), but there is still a large echo area at 6.0 km. At the 5.0 km height, an increase in reflectivity is due to the brightband effect. The flow at the 0.0 km (Fig. 14a) is from the south. By the 2.0 km height (Fig. 14b), the flow pattern has once again become southwesterly. Fig. 14c depicts the 2.0 km level; the wind vectors along the northern border of the domain depict southwesterly flow. If the vectors indicating west wind at the 1.0 km height are indeed caused by the approaching front, then the first evidence that the front is a shallow phenomenon is observed. Southwesterly flow is predominantly observed throughout the remain in heights (Figs. 14d-g).

The front is in the analysis domain at 113232 LST (Figs. 15a-i). At the surface (Fig. 15a) the front is depicted by a heavy dashed line. This method of depicting the frontal boundary will be used throughout. The lack of wind vectors makes frontal placement difficult, and it is done using the echo pattern depicted and the PPI scans from the radars (not shown). The front is approximately 5.0 km to the north of the NCAR radar. Winds from the south (blowing toward the front) are approximately  $13 \text{ ms}^{-1}$ , and some winds behind the front (estimated from the NCAR Doppler PPI scan) are as high as  $18 \text{ ms}^{-1}$ . A large echo core (greater than 30 dBZ) is observed

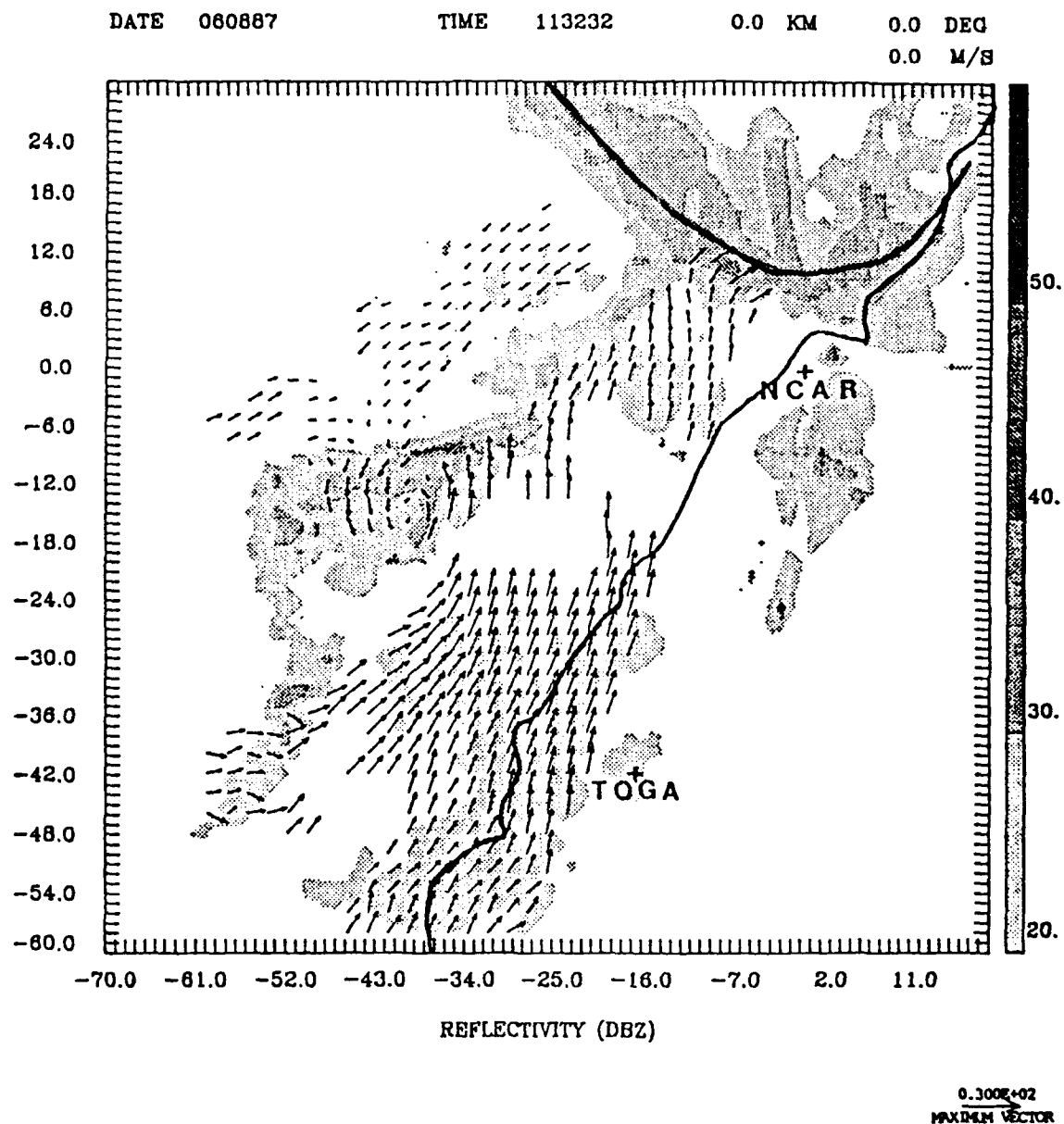


Fig. 15a. Dual-Doppler analysis of reflectivities and horizontal velocities for 113232, at the ground. The length scale for the vectors is given in the lower right-hand corner. The reflectivity gray scale is given on the right side of the figure. Radar positions and the coastline of Taiwan are also given. Frontal position is indicated by the heavy dashed line.

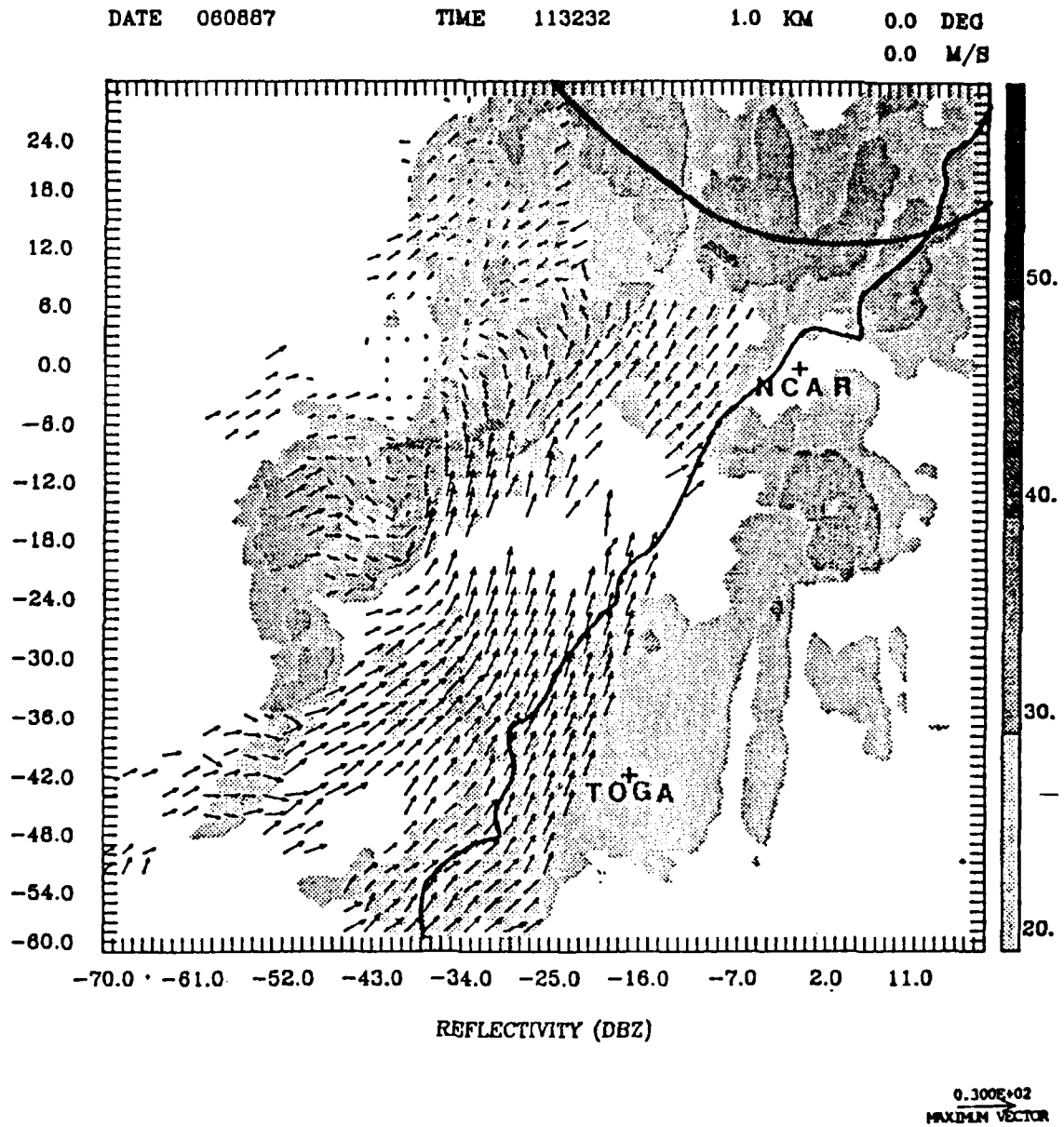


Fig. 15b. Dual-Doppler analysis of reflectivities and horizontal velocities for 113232, at 1.0 km above the ground. The length scale for the vectors is given in the lower right-hand corner. The reflectivity gray scale is given on the right side of the figure. Radar positions and the coastline of Taiwan are also given. Frontal position is indicated by the heavy dashed line.

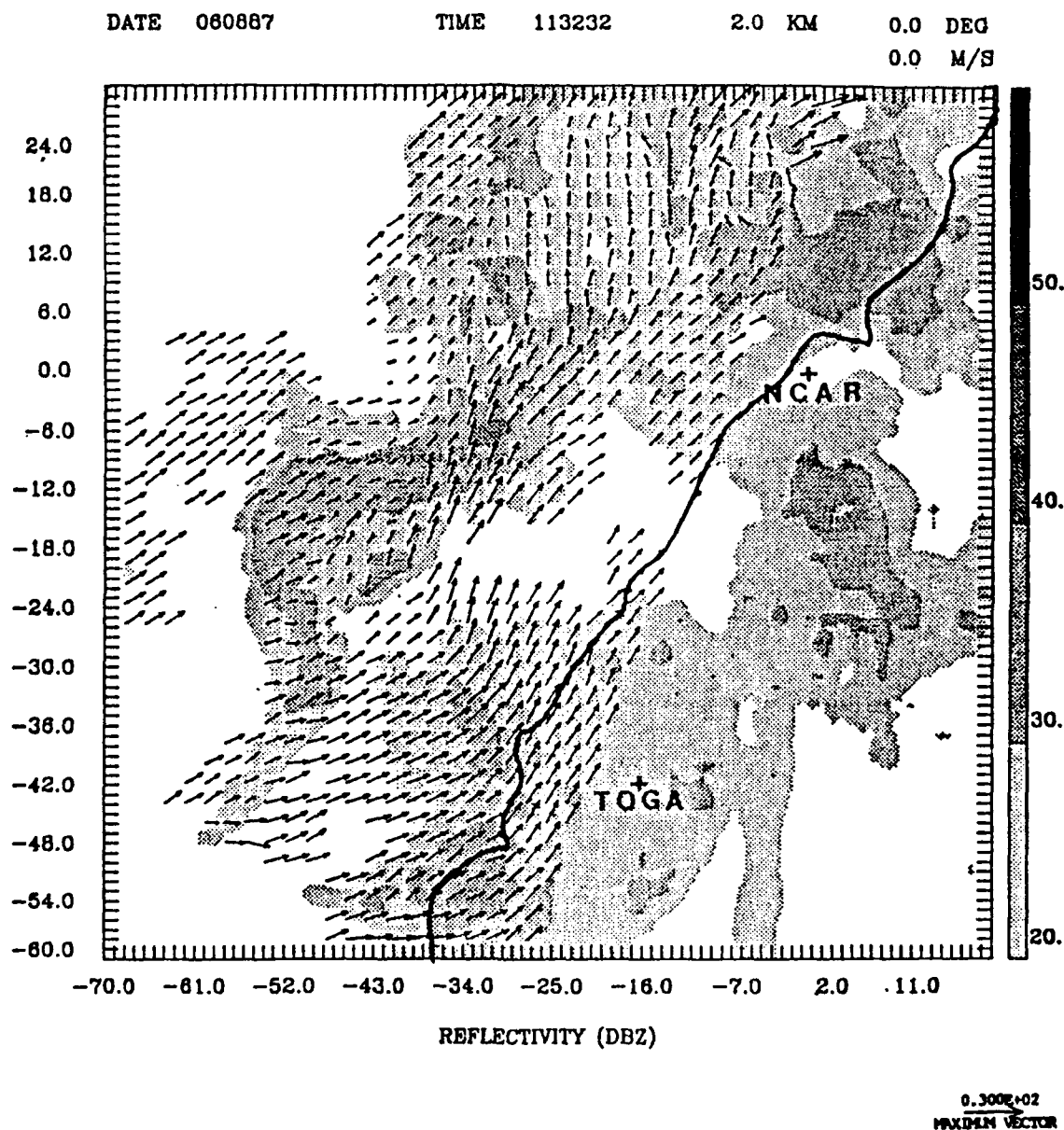


Fig. 15c. Dual-Doppler analysis of reflectivities and horizontal velocities for 113232, at 2.0 km above the ground. The length scale for the vectors is given in the lower right-hand corner. The reflectivity gray scale is given on the right side of the figure. Radar positions and the coastline of Taiwan are also given.

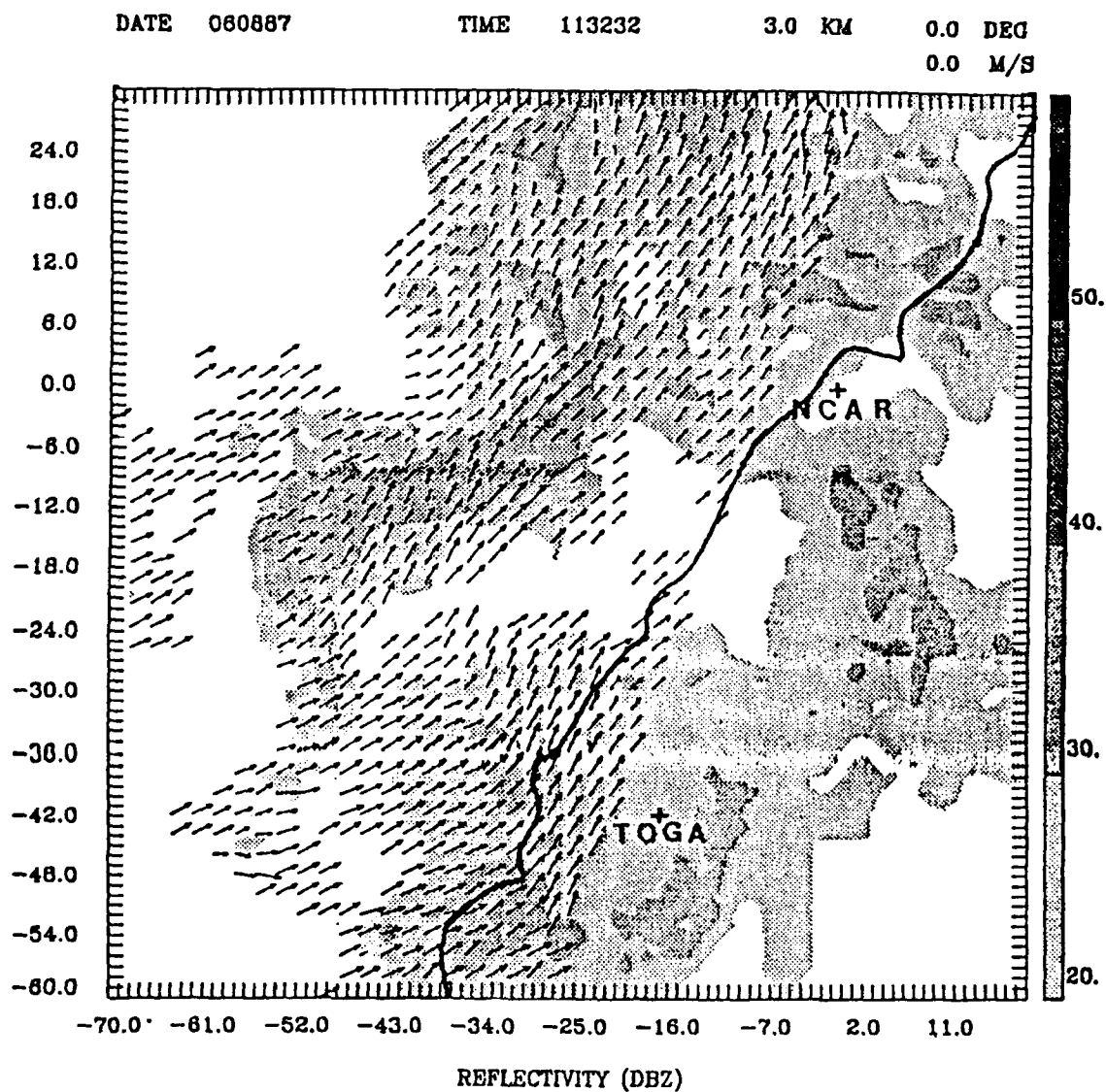
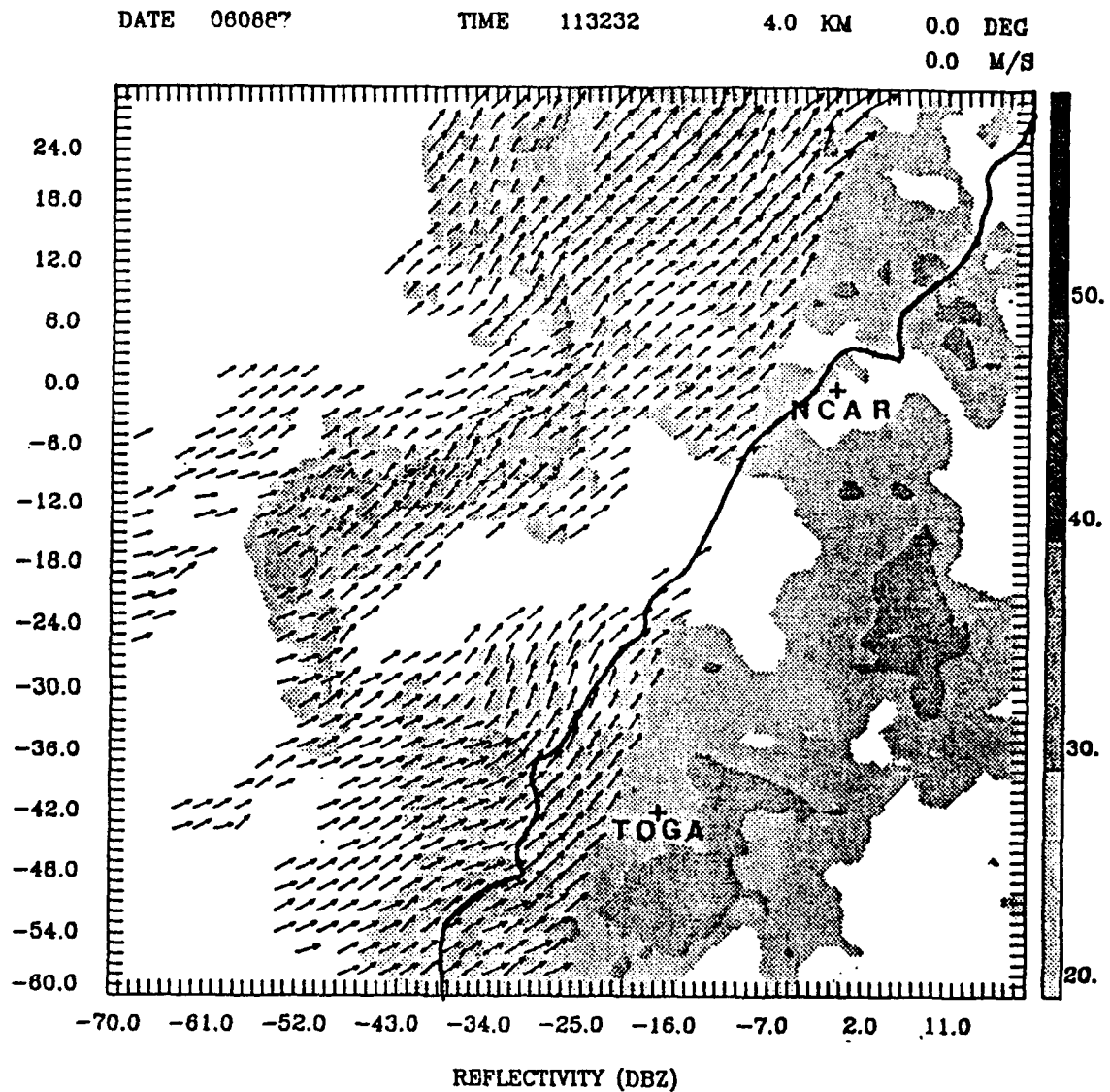


Fig. 15d. Dual-Doppler analysis of reflectivities and horizontal velocities for 113232, at 3.0 km above the ground. The length scale for the vectors is given in the lower right-hand corner. The reflectivity gray scale is given on the right side of the figure. Radar positions and the coastline of Taiwan are also given.



*Fig. 15e. Dual-Doppler analysis of reflectivities and horizontal velocities for 113232, at 4.0 km above the ground. The length scale for the vectors is given in the lower right-hand corner. The reflectivity gray scale is given on the right side of the figure. Radar positions and the coastline of Taiwan are also given.*

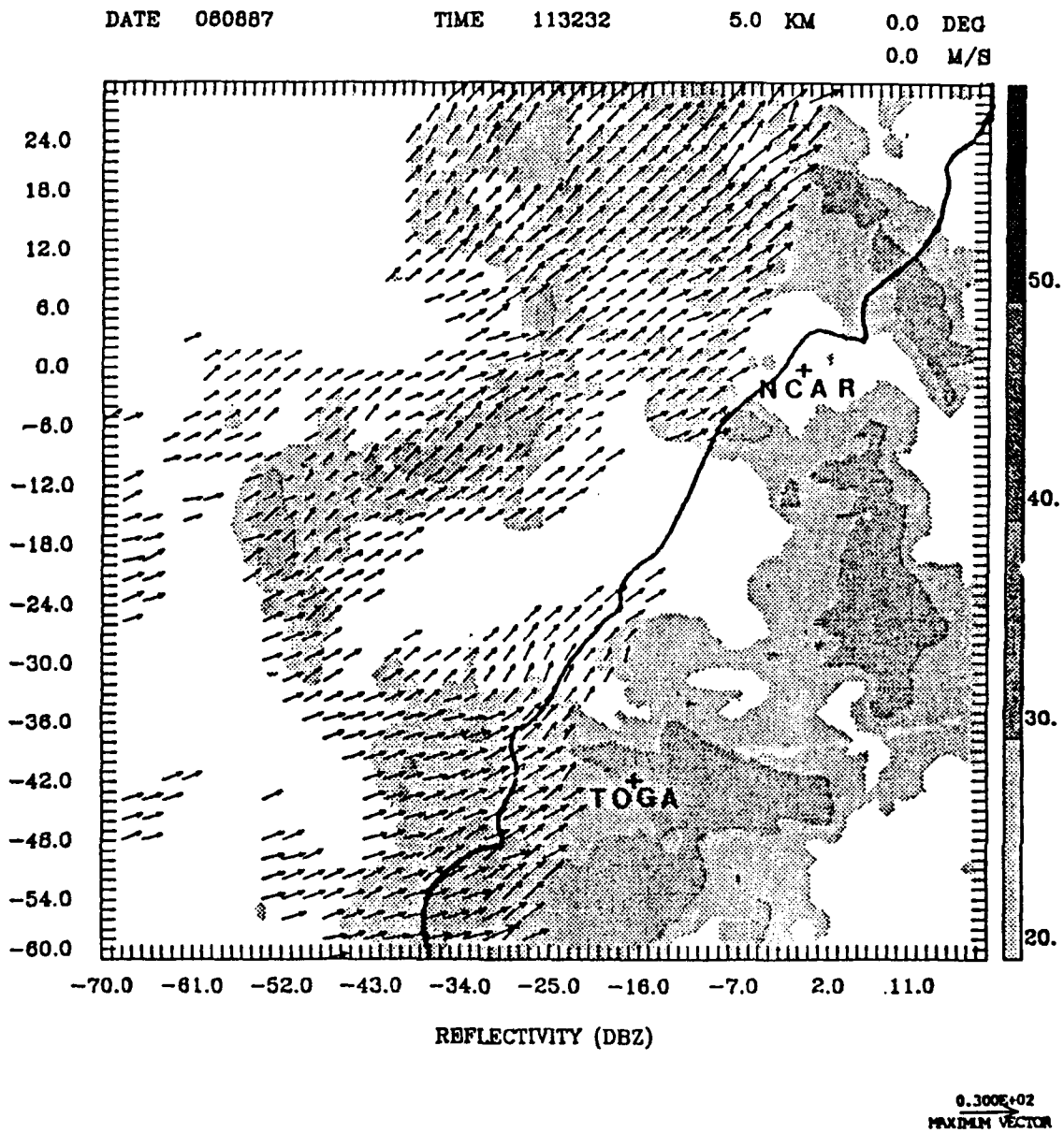


Fig. 15f. Dual-Doppler analysis of reflectivities and horizontal velocities for 113232, at 5.0 km above the ground. The length scale for the vectors is given in the lower right-hand corner. The reflectivity gray scale is given on the right side of the figure. Radar positions and the coastline of Taiwan are also given.

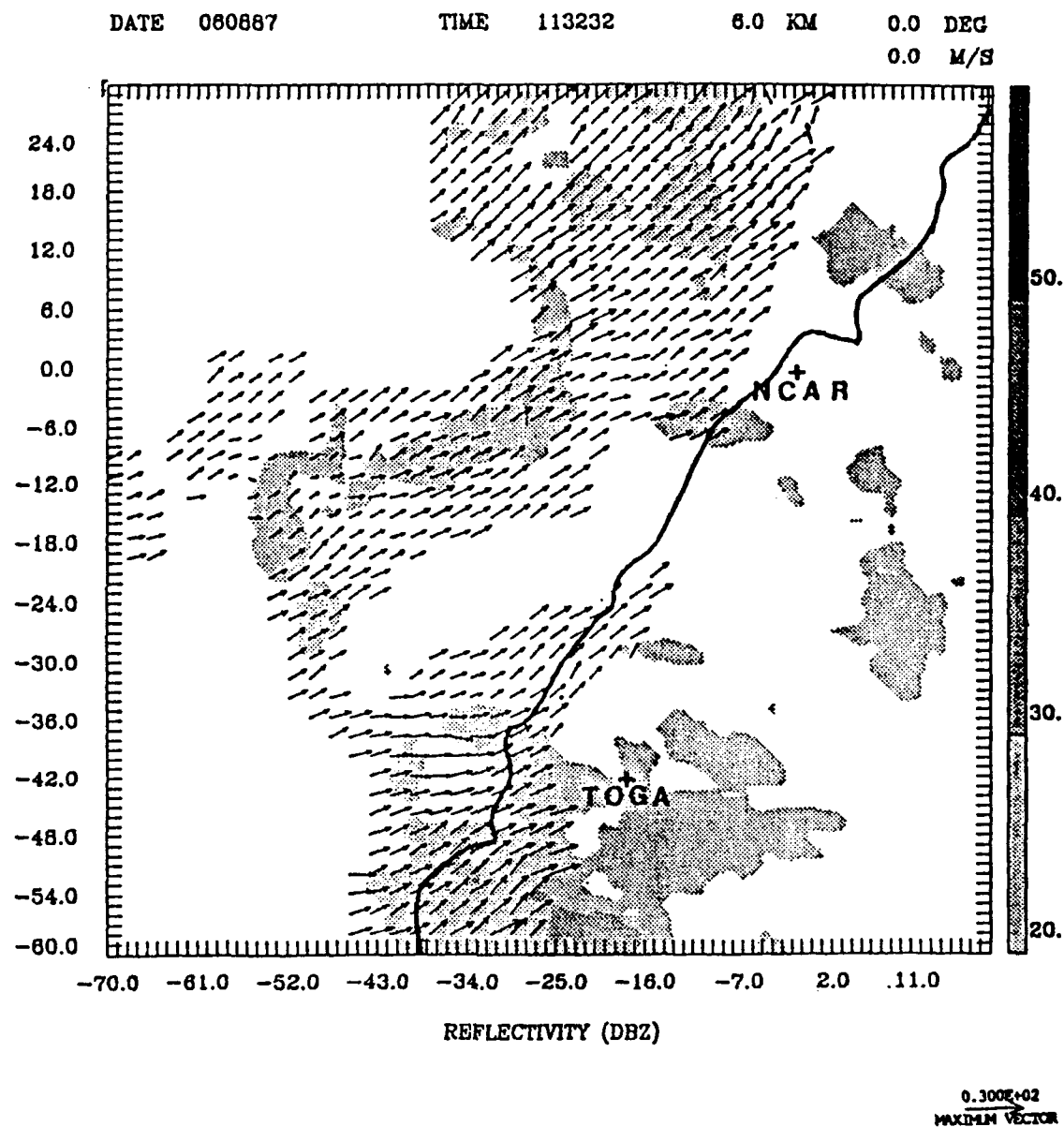


Fig. 15g. Dual-Doppler analysis of reflectivities and horizontal velocities for 113232, at 6.0 km above the ground. The length scale for the vectors is given in the lower right-hand corner. The reflectivity gray scale is given on the right side of the figure. Radar positions and the coastline of Taiwan are also given.

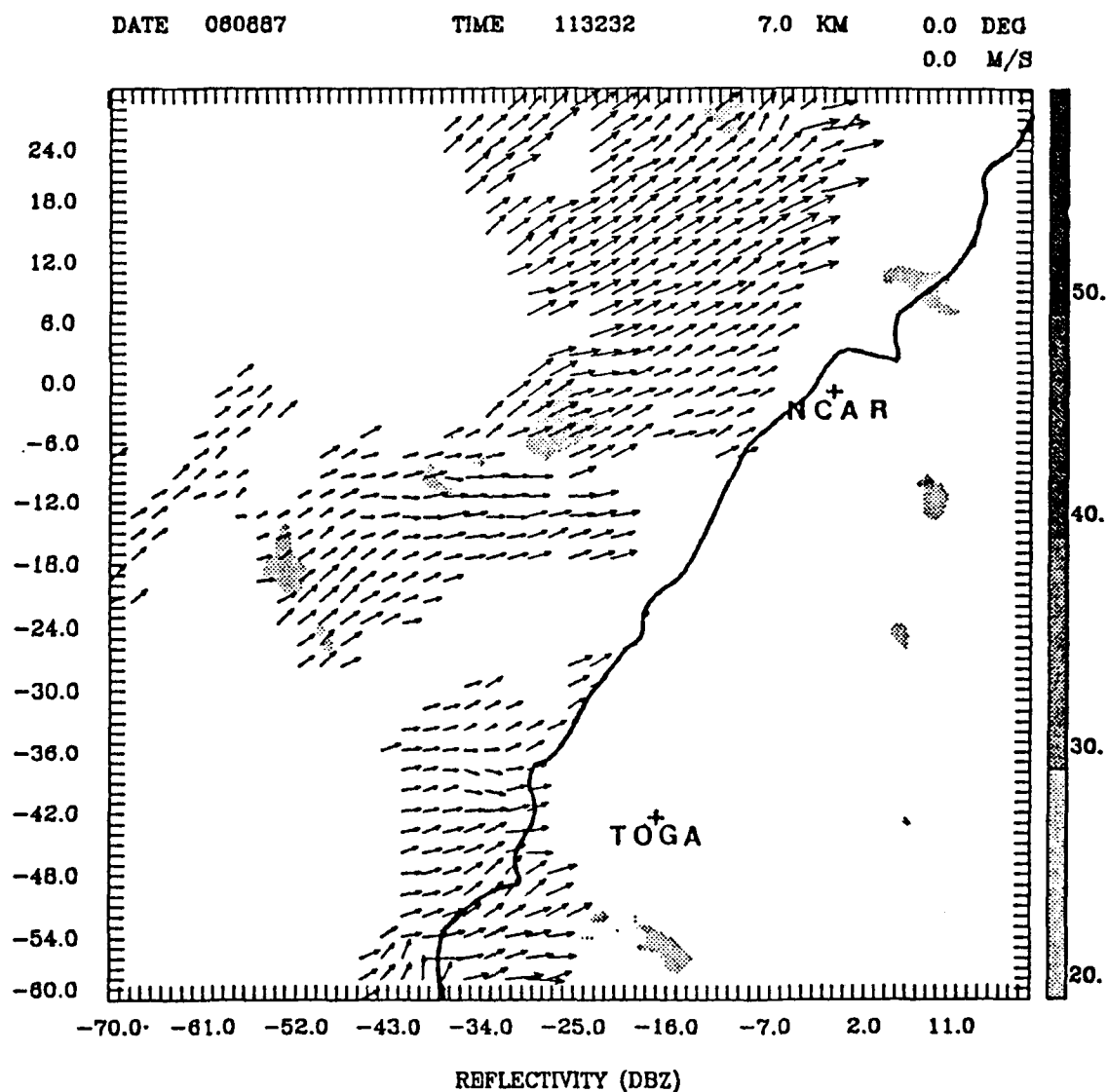


Fig. 15h. Dual-Doppler analysis of reflectivities and horizontal velocities for 113232, at 7.0 km above the ground. The length scale for the vectors is given in the lower right-hand corner. The reflectivity gray scale is given on the right side of the figure. Radar positions and the coastline of Taiwan are also given.

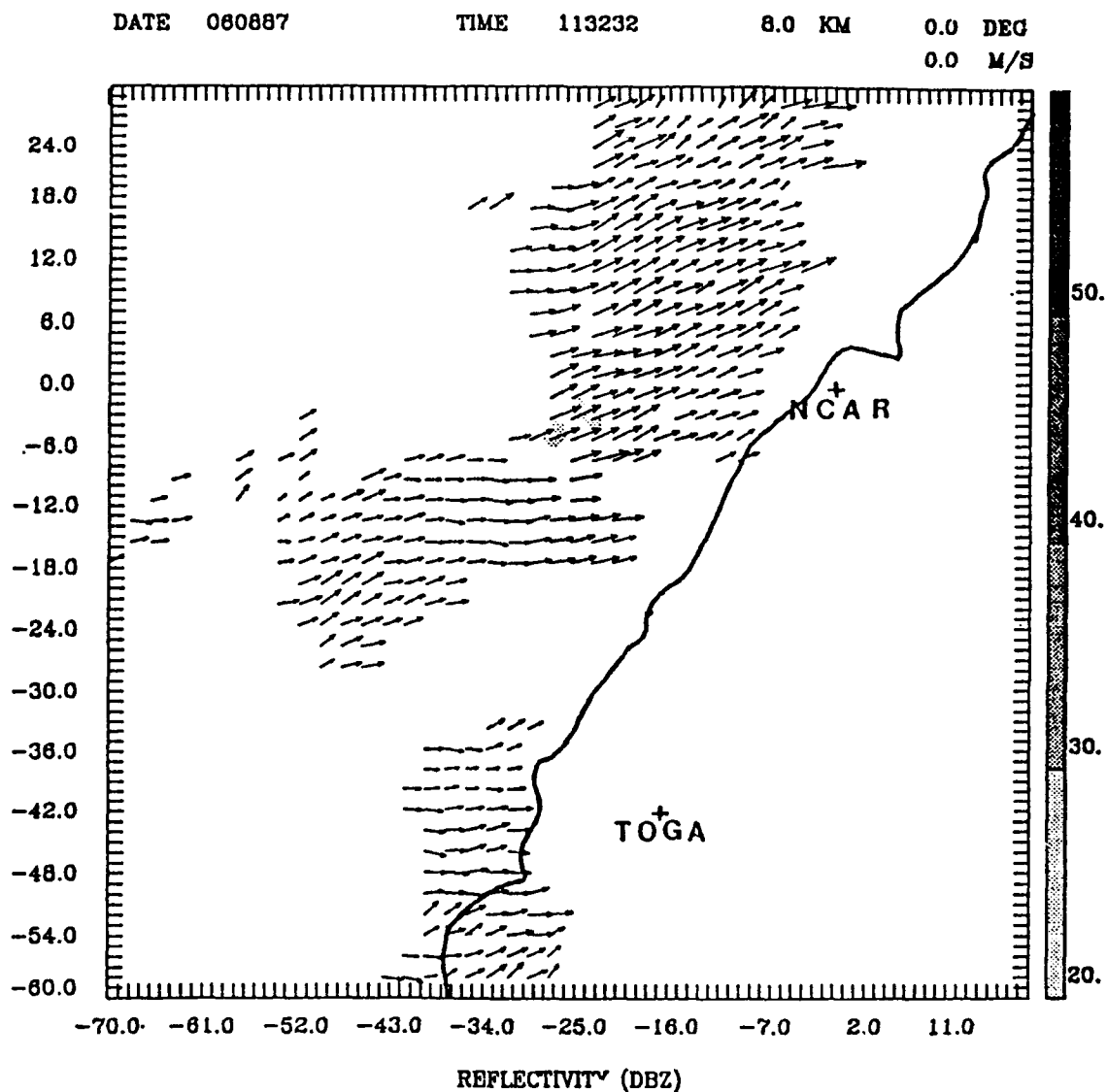


Fig. 15i. Dual-Doppler analysis of reflectivities and horizontal velocities for 113232, at 8.0 km above the ground. The length scale for the vectors is given in the lower right-hand corner. The reflectivity gray scale is given on the right side of the figure. Radar positions and the coastline of Taiwan are also given.

along the frontal boundary. At the point  $(-10, 12)$  there is a small echo greater than 40 dBZ. This is the first time reflectivities this large were observed. The 30 dBZ cores have almost disappeared by the 4.0 km height (Figs. 15a-e), but again, at 5.0 km (Fig. 15f) brightband data distort this perception. All of the cores along the front have vanished by the 6.0 km height (Fig. 15g). An elongated echo extends from the front northward along the line  $x = -5.0$ . This is a range-folded echo. This is an echo that is at a distance greater than the maximum unambiguous range that appears as an echo at a distance less than the maximum unambiguous range, caused by the radar's inability to distinguish between a return from the most recent pulse and more distant returns from a prior pulse. These echoes will appear elongated in the plots (and on the radar screen) as their angular width is unchanged when displayed at the apparent range (Ray, 1988). An echo that parallels the coastline is also seen. This line of echoes is associated with the mesoscale ridge and synoptic trough confluent line as analyzed by Trier *et al.* (1989). Echo cores of greater than 40 dBZ are observed along this line from the 1.0 km height to the 3.0 km height. Echo cores greater than 30 dBZ extend up above 6.0 km, but are not present at the 7.0 km height (Fig. 15g and 15h). Not only do the echo intensities increase at this time, but the tops are now up to a maximum of 8.0 km height (Fig. 15i). To the northeast of this line of echoes there is weak northeasterly wind flow. This flow becomes stronger and southwesterly by the 2.0 km height. It is noted that the echoes along the front greater than 40 dBZ are located at the intersection of the

front and the ridge/trough confluent line, referred to as the "triple point". At the 2.0 km height (Fig. 15c), wind vectors are observed north of the frontal boundary. Since these vectors are unaffected by the front (as they are still depicting southerly or southwesterly flow) the fact that the front is shallow is supported. At the upper levels, southwesterly flow dominates, except in the area just to the west of the TOGA radar, where the ridging is strongest.

Figures 16a-h depict the dual-Doppler analysis at 115142 LST. At the surface, the front is now just south of the NCAR radar. Frontal speed between the 113232 LST position and the current position is estimated at  $18 \text{ ms}^{-1}$ . Winds behind the front (from the NCAR PPI scan) have a maximum value of  $20 \text{ ms}^{-1}$ . Further, just south of the radar is the area of highest reflectivities (greater than 40 dBZ). This core is located in the approximate area of the triple point. It is also in the area where orographic lifting may begin to influence convection. This echo core (greater than 40 dBZ) is observed up to the 2.0 km height (Figs. 16a-c). The only area of greater than 40 dBZ seen at the 2.0 km height (Fig. 16c) is at the triple point. At the surface, to the southeast of the front, a small shallow area of cyclonic turning is observed. This area is associated with several cores of greater than 30 dBZ. By the 1.0 km height (Fig. 16b), the cyclonic circulation appears to break down, and southwesterly flow begins to dominate. At this time precipitation is developing over the island in the vicinity of the TOGA radar. This results from the southwesterly flow and upslope effects. In Fig. 16c, south and southwesterly

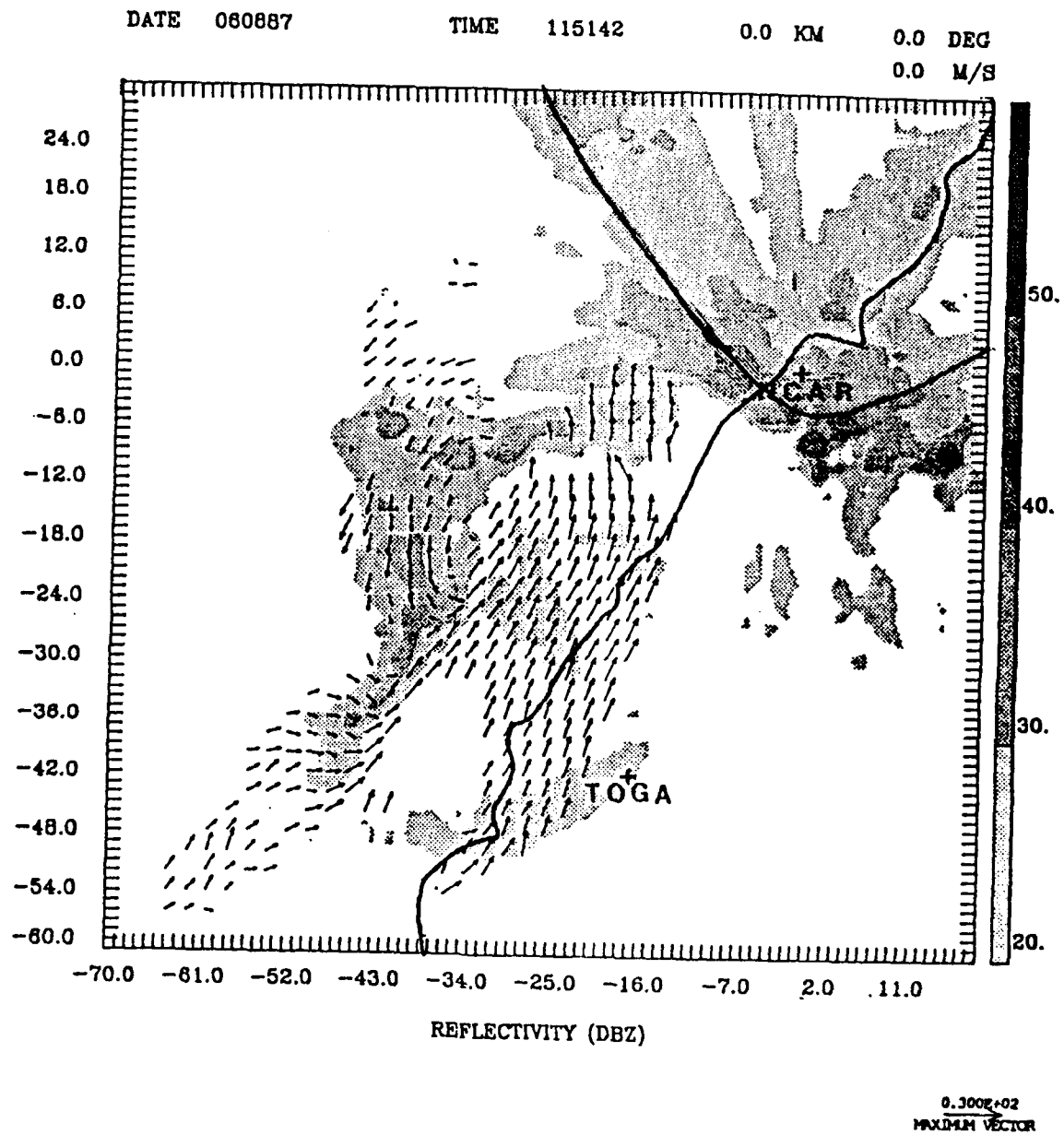


Fig. 16a. Dual-Doppler analysis of reflectivities and horizontal velocities for 115142, at the ground. The length scale for the vectors is given in the lower right-hand corner. The reflectivity gray scale is given on the right side of the figure. Radar positions and the coastline of Taiwan are also given. Frontal position is indicated by the heavy dashed line.

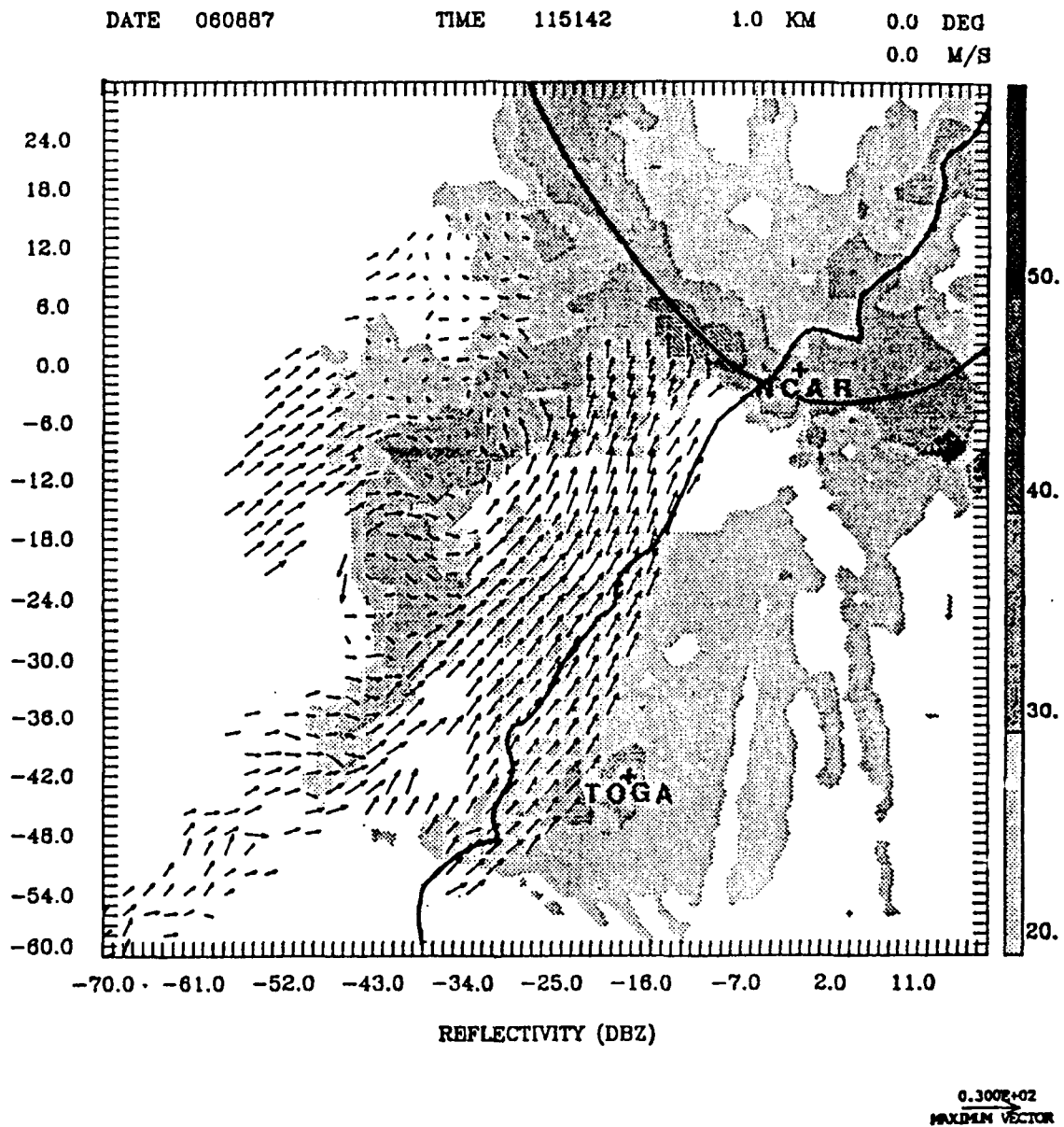


Fig. 16b. Dual-Doppler analysis of reflectivities and horizontal velocities for 115142, at 1.0 km above the ground. The length scale for the vectors is given in the lower right-hand corner. The reflectivity gray scale is given on the right side of the figure. Radar positions and the coastline of Taiwan are also given. Frontal position is indicated by the heavy dashed line.

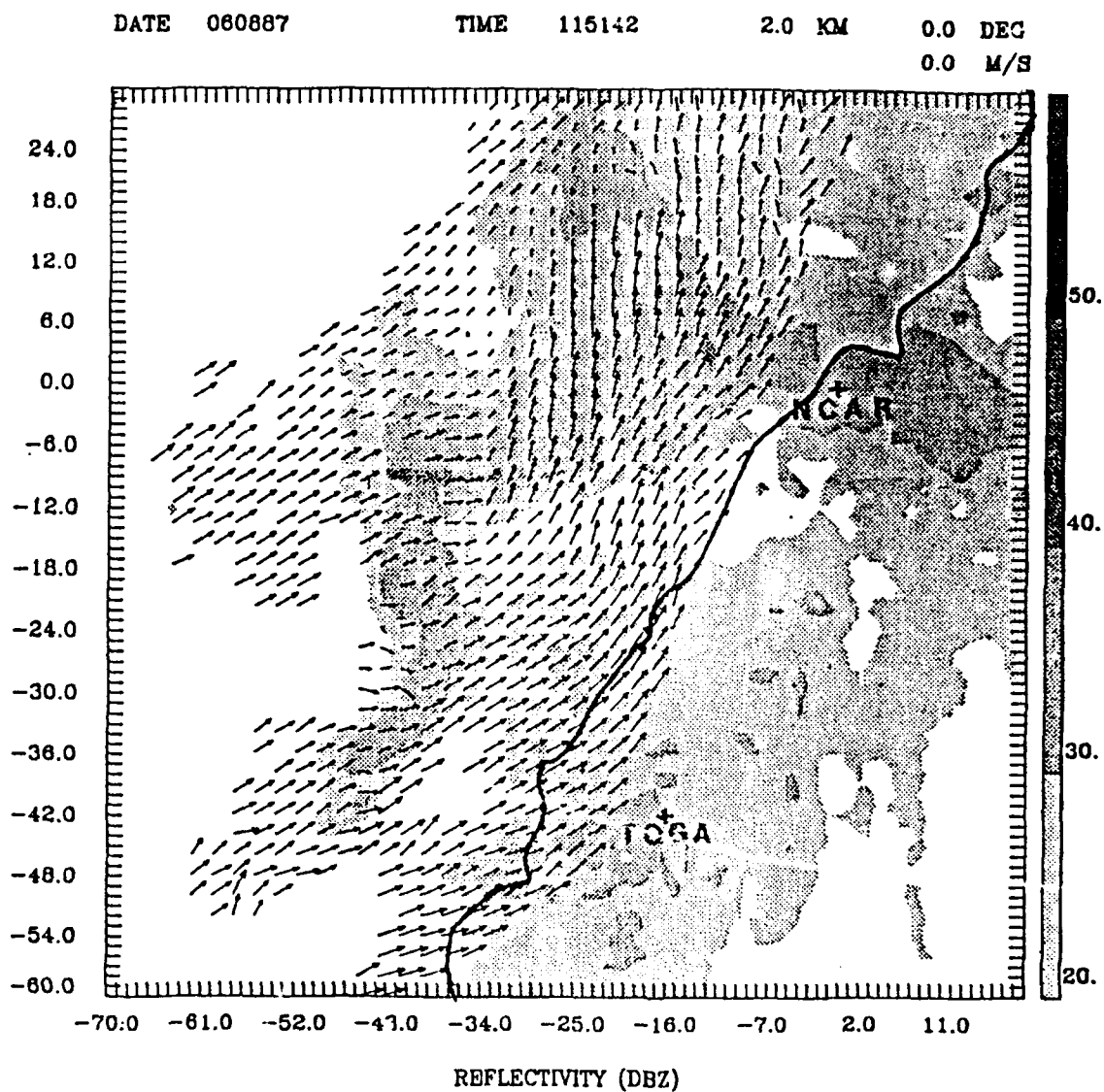


Fig. 16c. Dual-Doppler analysis of reflectivities and horizontal velocities for 115142, at 2.0 km above the ground. The length scale for the vectors is given in the lower right-hand corner. The reflectivity gray scale is given on the right side of the figure. Radar positions and the coastline of Taiwan are also given.

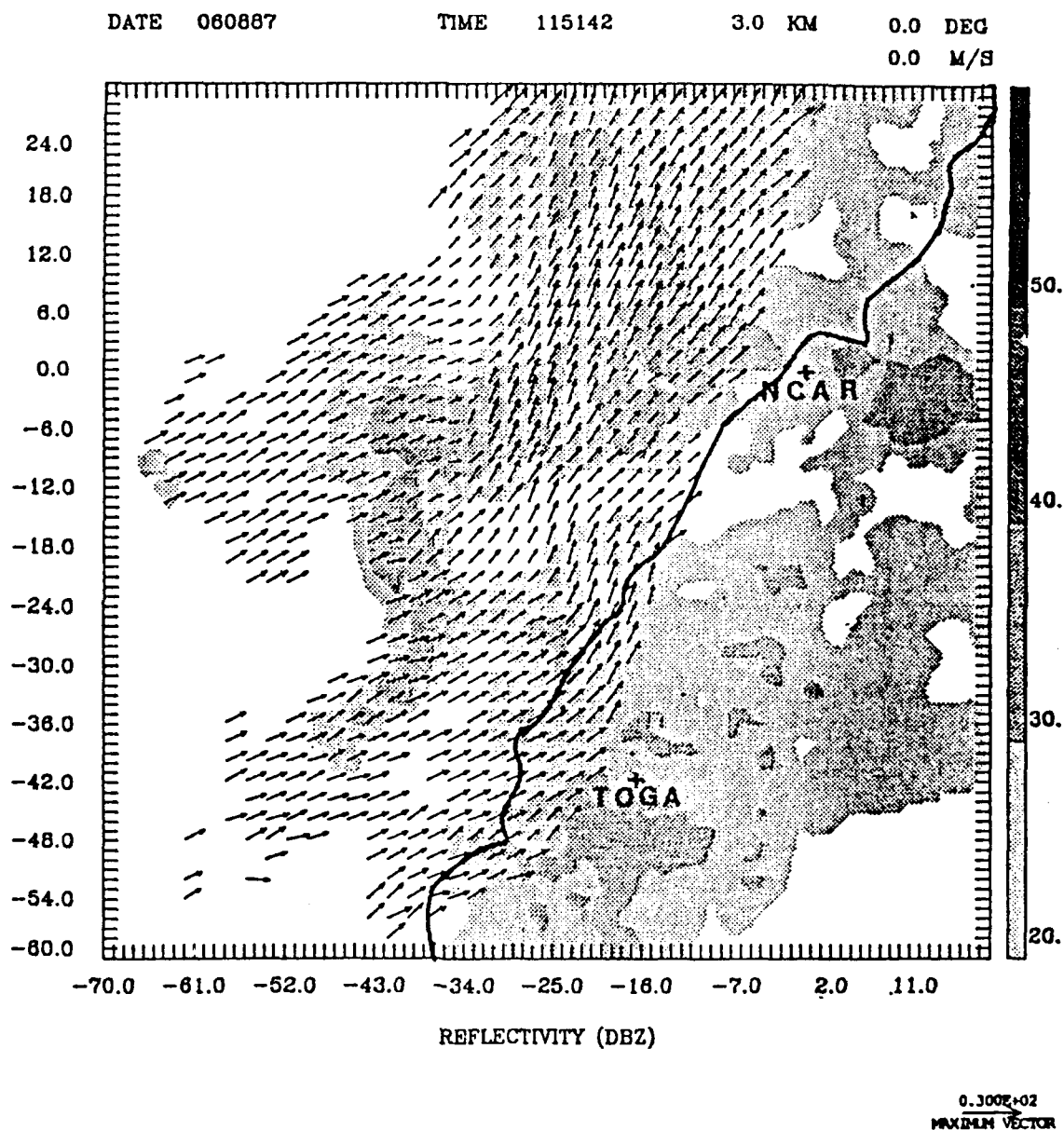


Fig. 16d. Dual-Doppler analysis of reflectivities and horizontal velocities for 115142, at 3.0 km above the ground. The length scale for the vectors is given in the lower right-hand corner. The reflectivity gray scale is given on the right side of the figure. Radar positions and the coastline of Taiwan are also given.

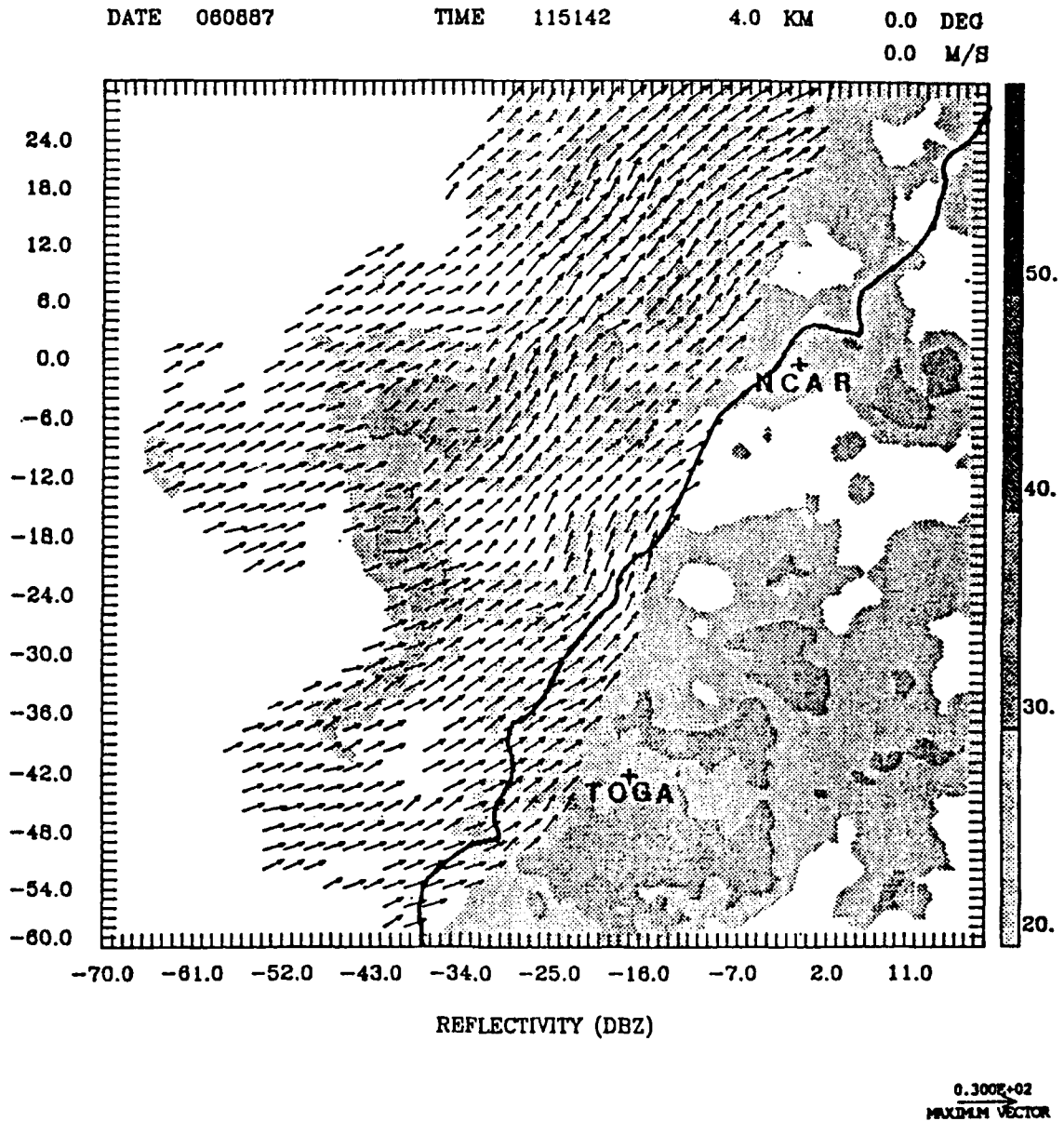


Fig. 16e. Dual-Doppler analysis of reflectivities and horizontal velocities for 115142, at 4.0 km above the ground. The length scale for the vectors is given in the lower right-hand corner. The reflectivity gray scale is given on the right side of the figure. Radar positions and the coastline of Taiwan are also given.

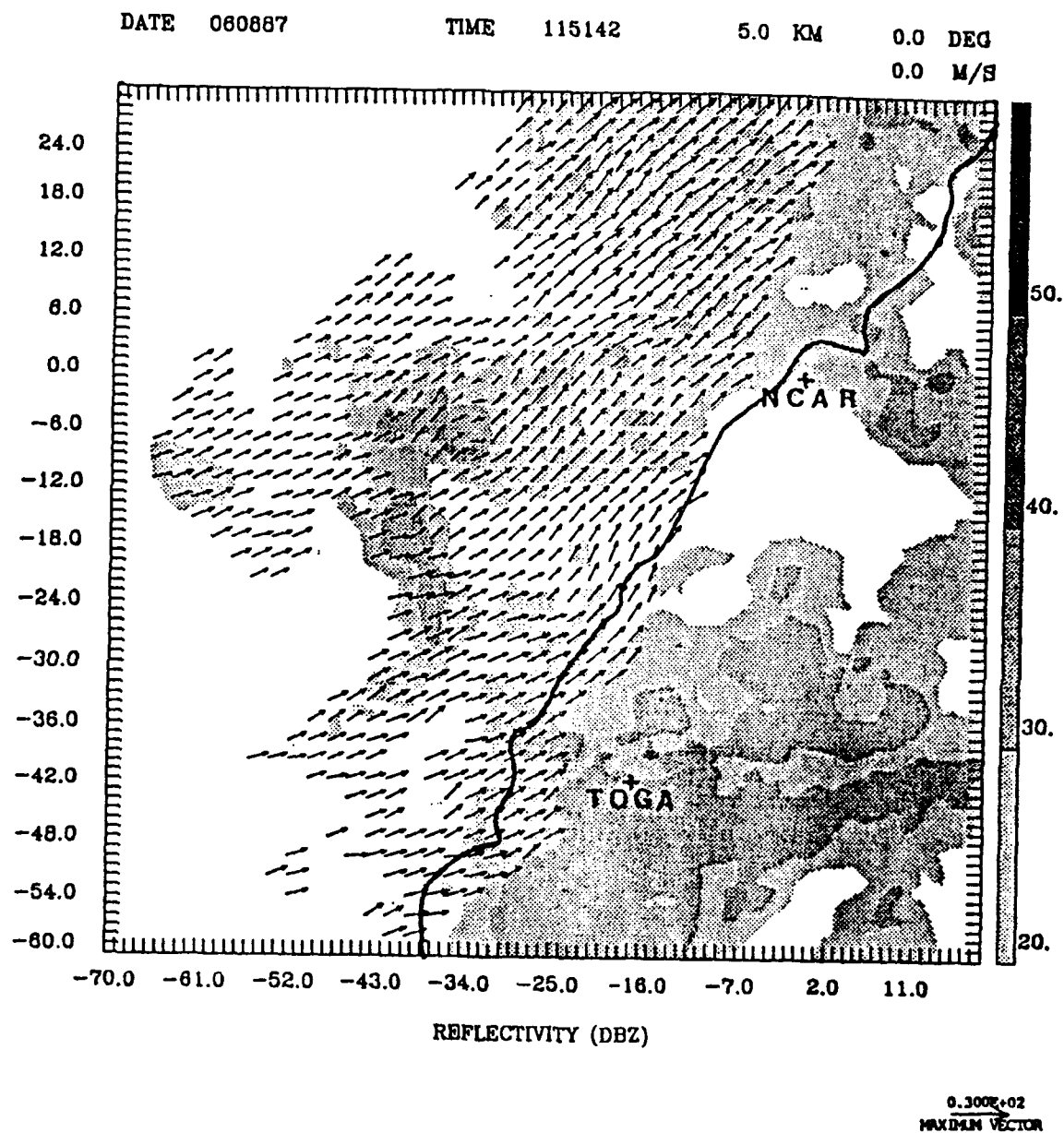
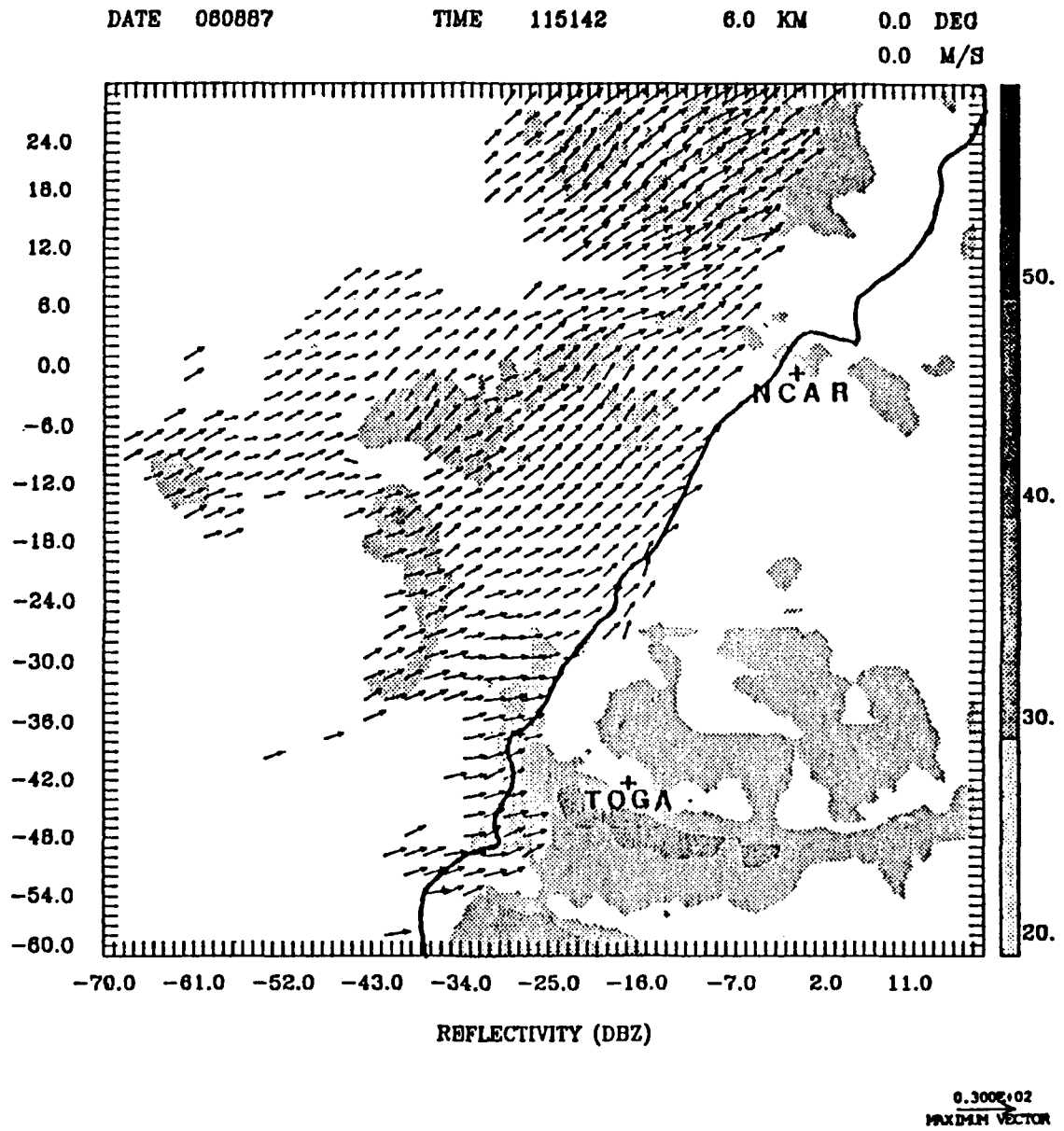


Fig. 16f. Dual-Doppler analysis of reflectivities and horizontal velocities for 115142, at 5.0 km above the ground. The length scale for the vectors is given in the lower right-hand corner. The reflectivity gray scale is given on the right side of the figure. Radar positions and the coastline of Taiwan are also given.



*Fig. 16g. Dual-Doppler analysis of reflectivities and horizontal velocities for 115142, at 6.0 km above the ground. The length scale for the vectors is given in the lower right-hand corner. The reflectivity gray scale is given on the right side of the figure. Radar positions and the coastline of Taiwan are also given.*

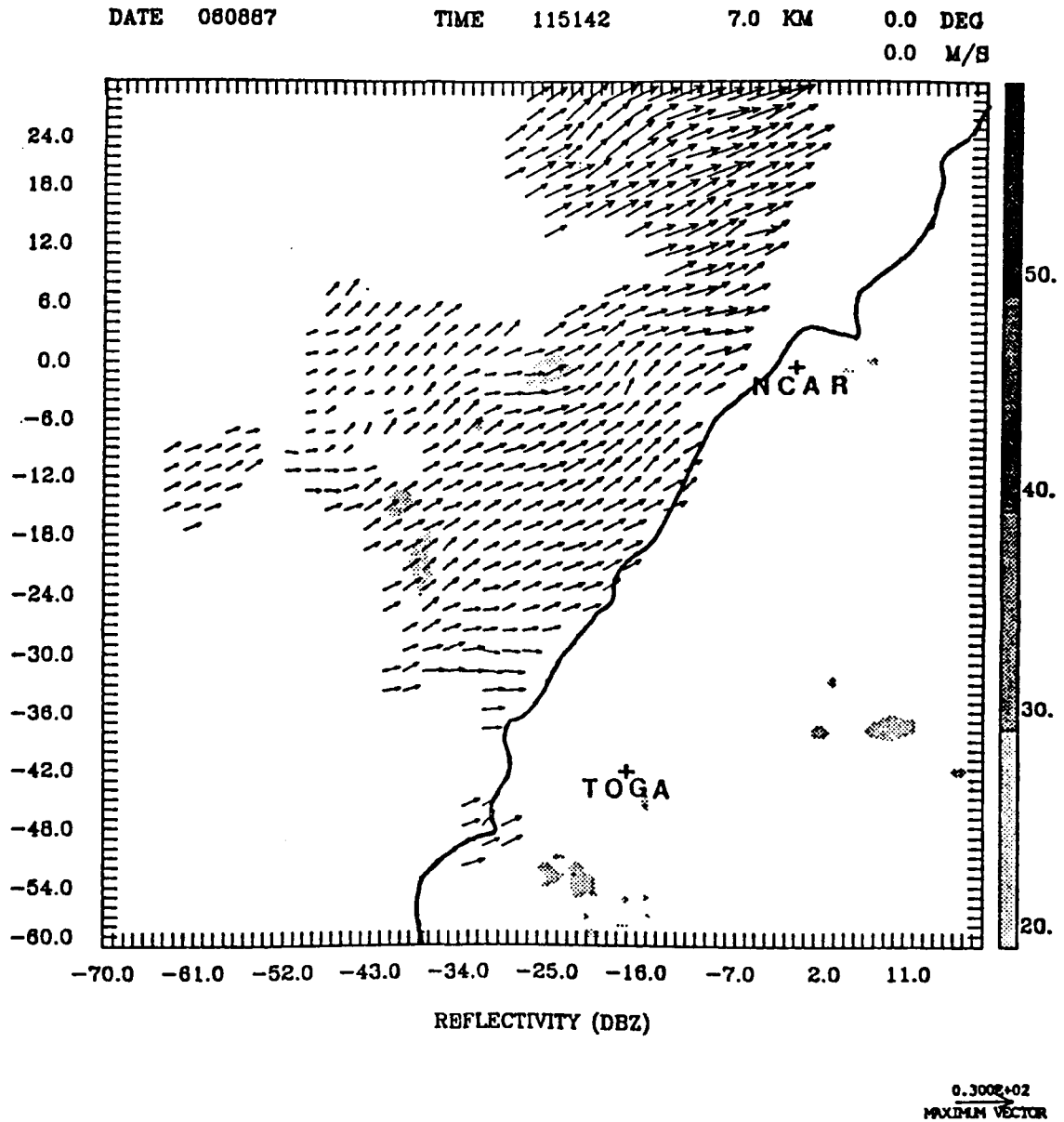


Fig. 16h. Dual-Doppler analysis of reflectivities and horizontal velocities for 115142, at 7.0 km above the ground. The length scale for the vectors is given in the lower right-hand corner. The reflectivity gray scale is given on the right side of the figure. Radar positions and the coastline of Taiwan are also given.

flow predominates. In the vicinity of the TOGA radar, the area of reflectivities exceeding 30 dBZ is growing. As before, the echoes of this intensity their maximum areal extent at 2.0 km in height. The echoes associated with the upslope effects do not, however, exhibit this characteristic. These echoes continue to increase in size up to the 5.0 km height (Figs. 16d-f). It is possible that the echoes only increase up to the 4.0 km height, and the illusion of continued size growth is enhanced by brightband effects. The core size rapidly decreases by the 6.0 km height (Fig. 16g). At the 7.0 km height, almost all the echo has vanished, and only a few small areas greater than 20 dBZ remain. Southwesterly wind flow in the upper levels is clearly dominate.

Analysis at 123013 LST is shown in Figs. 17a-i. At the surface (Fig. 17a) the front is clearly observed in the wind field. Winds behind the front (having speeds of approximately  $19.0 \text{ ms}^{-1}$ ) are northerly, while winds ahead of the front remain southerly. The western portion of the front is observed to have moved southward (compared to the position at 115142 LST) (Figs. 17a and 17b) at approximately  $18 \text{ ms}^{-1}$ . Conversely, the portion of the front directly south of the NCAR radar has moved at less than  $1.0 \text{ ms}^{-1}$ , and the fronts to the east and northeast of the NCAR radar are virtually stationary. The lack of movement in these areas is caused by the shallow front being blocked by island terrain. Near the front, just off the island coast, echoes exceed 40 dBZ. These cores reach their maximum area at 1.0 km

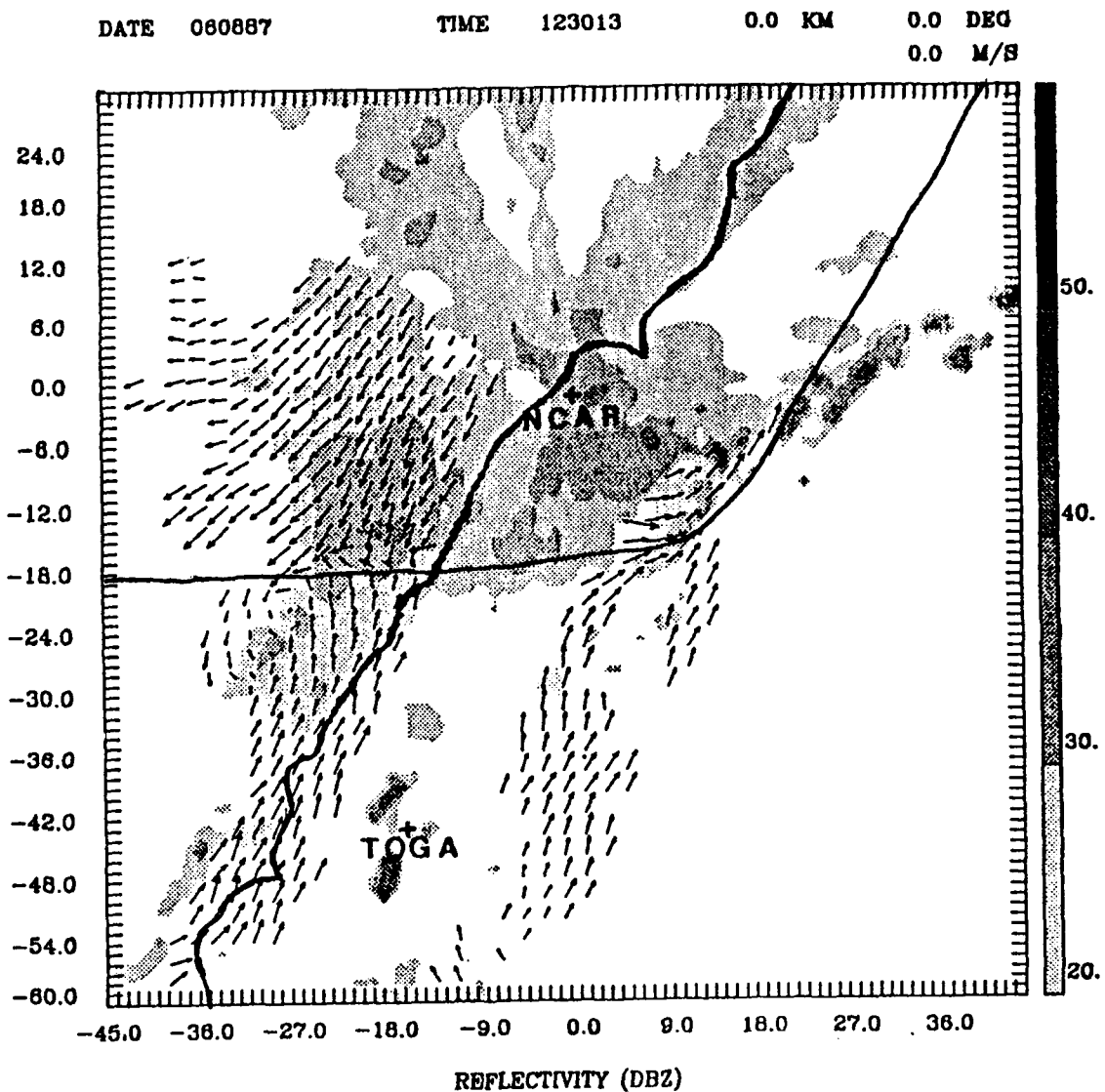


Fig. 17a. Dual-Doppler analysis of reflectivities and horizontal velocities for 1129013, at the ground. The length scale for the vectors is given in the lower right-hand corner. The reflectivity gray scale is given on the right side of the figure. Radar positions and the coastline of Taiwan are also given. Frontal position is indicated by the heavy dashed line.

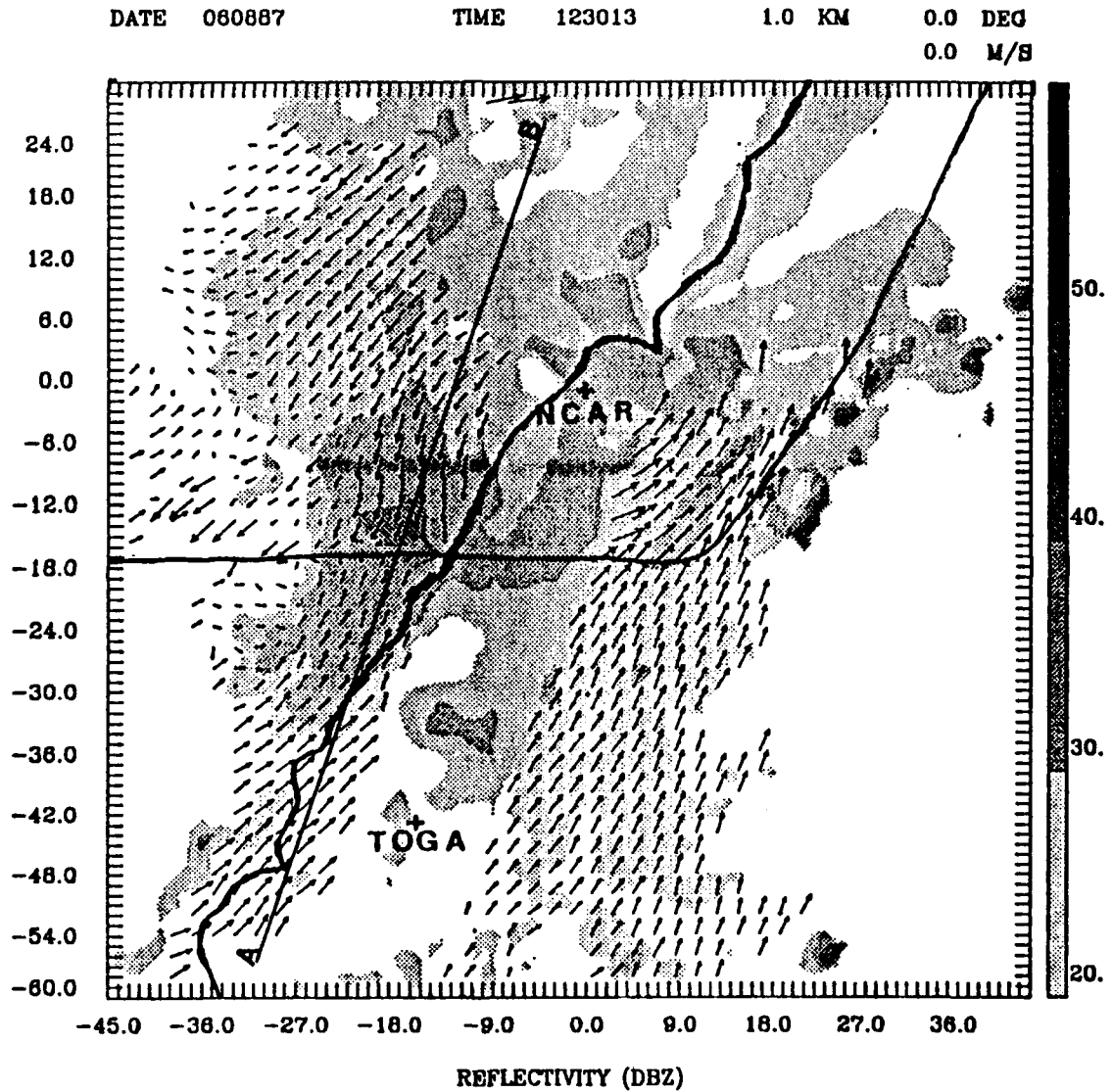


Fig. 17b. Dual-Doppler analysis of reflectivities and horizontal velocities for 123013, at 1.0 km above the ground. The length scale for the vectors is given in the lower right-hand corner. The reflectivity gray scale is given on the right side of the figure. Radar positions and the coastline of Taiwan are also given. Frontal position is indicated by the heavy dashed line. Cross-sectional plot given in Figure 19 is denoted by line A-B.

DATE 060687

TIME 123013

2.0 KM

0.0 DEG

0.0 M/S

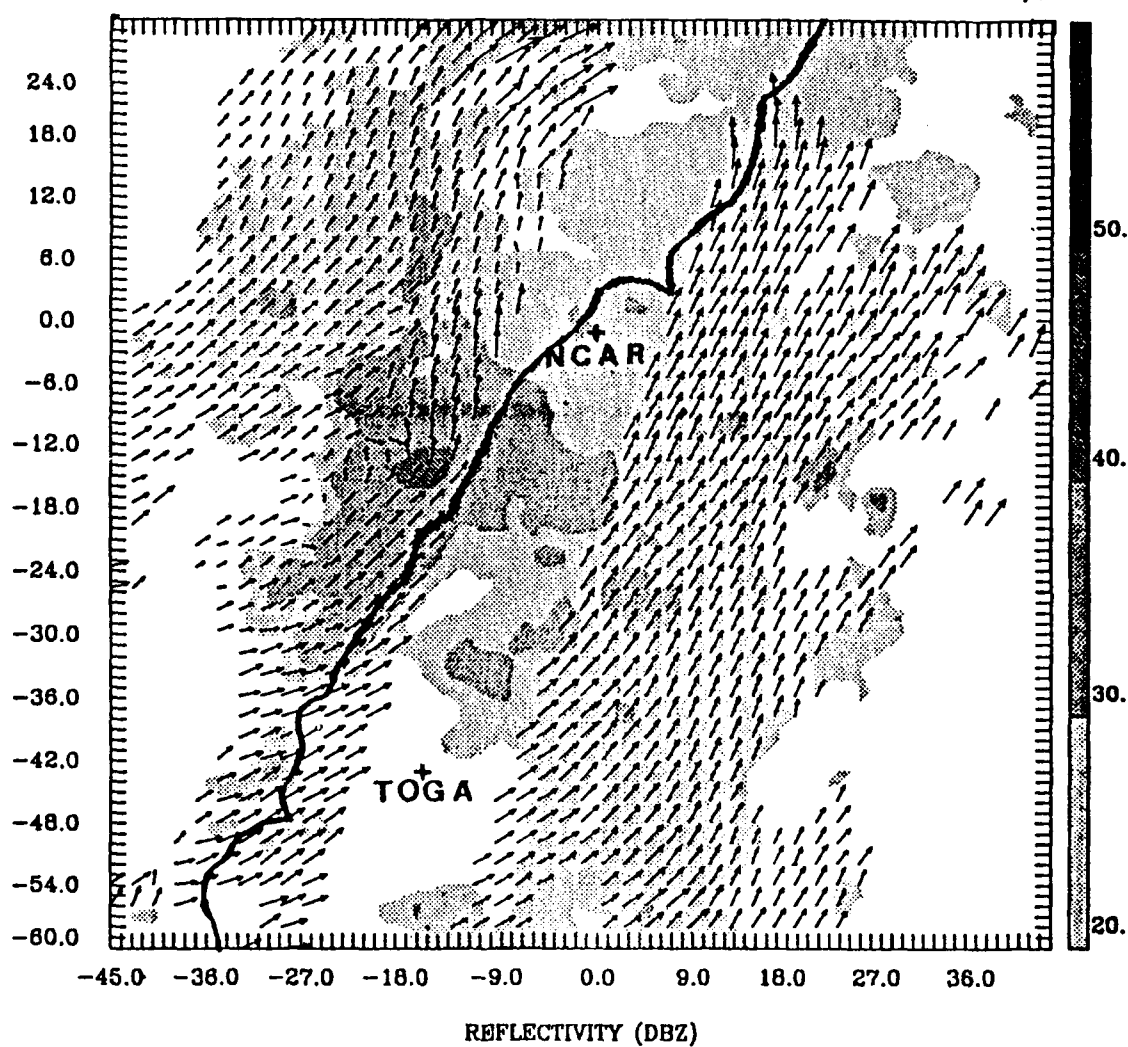


Fig. 17c. Dual-Doppler analysis of reflectivities and horizontal velocities for 123013, at 2.0 km above the ground. The length scale for the vectors is given in the lower right-hand corner. The reflectivity gray scale is given on the right side of the figure. Radar positions and the coastline of Taiwan are also given.

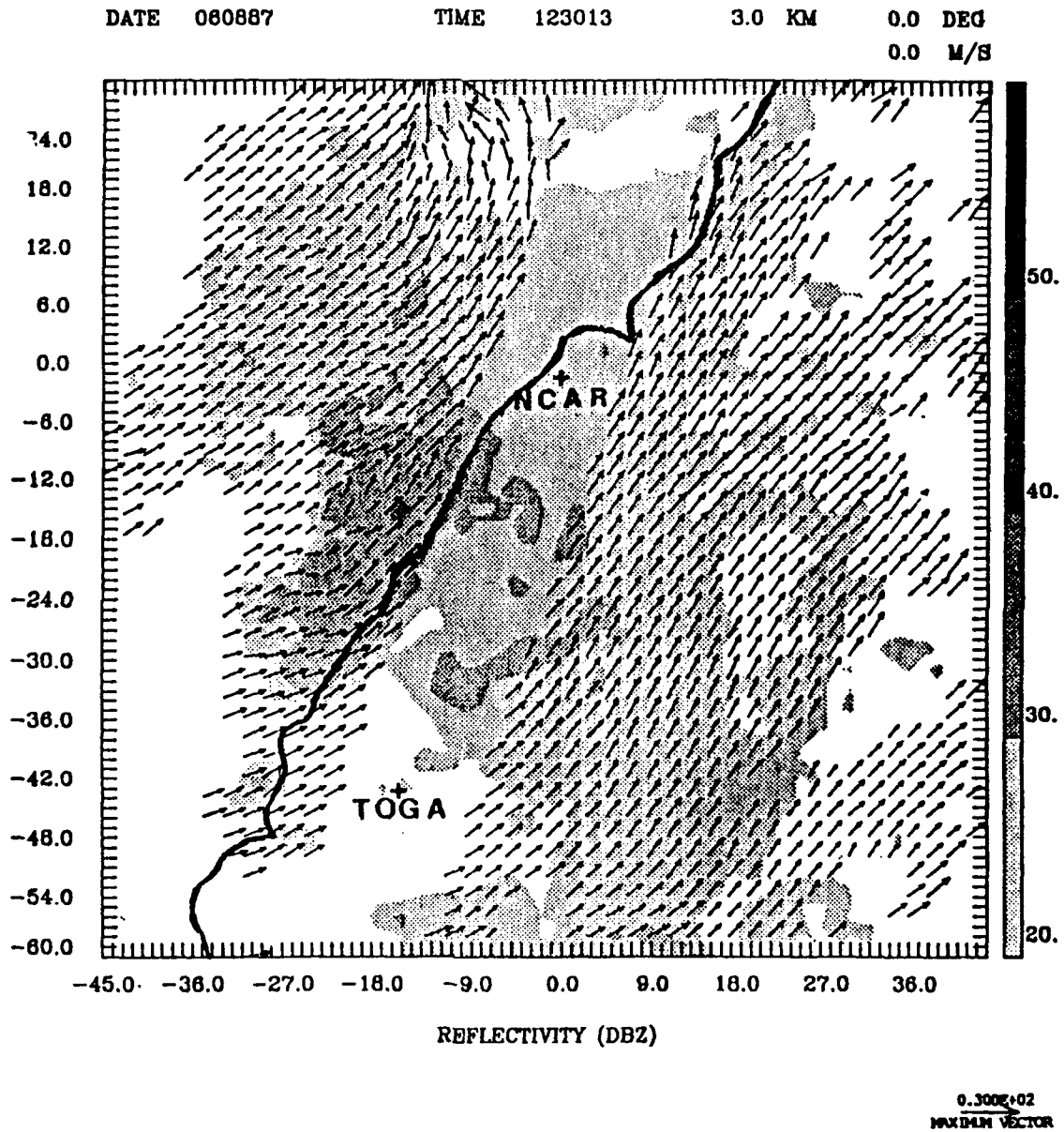


Fig. 17d. Dual-Doppler analysis of reflectivities and horizontal velocities for 123013, at 3.0 km above the ground. The length scale for the vectors is given in the lower right-hand corner. The reflectivity gray scale is given on the right side of the figure. Radar positions and the coastline of Taiwan are also given.

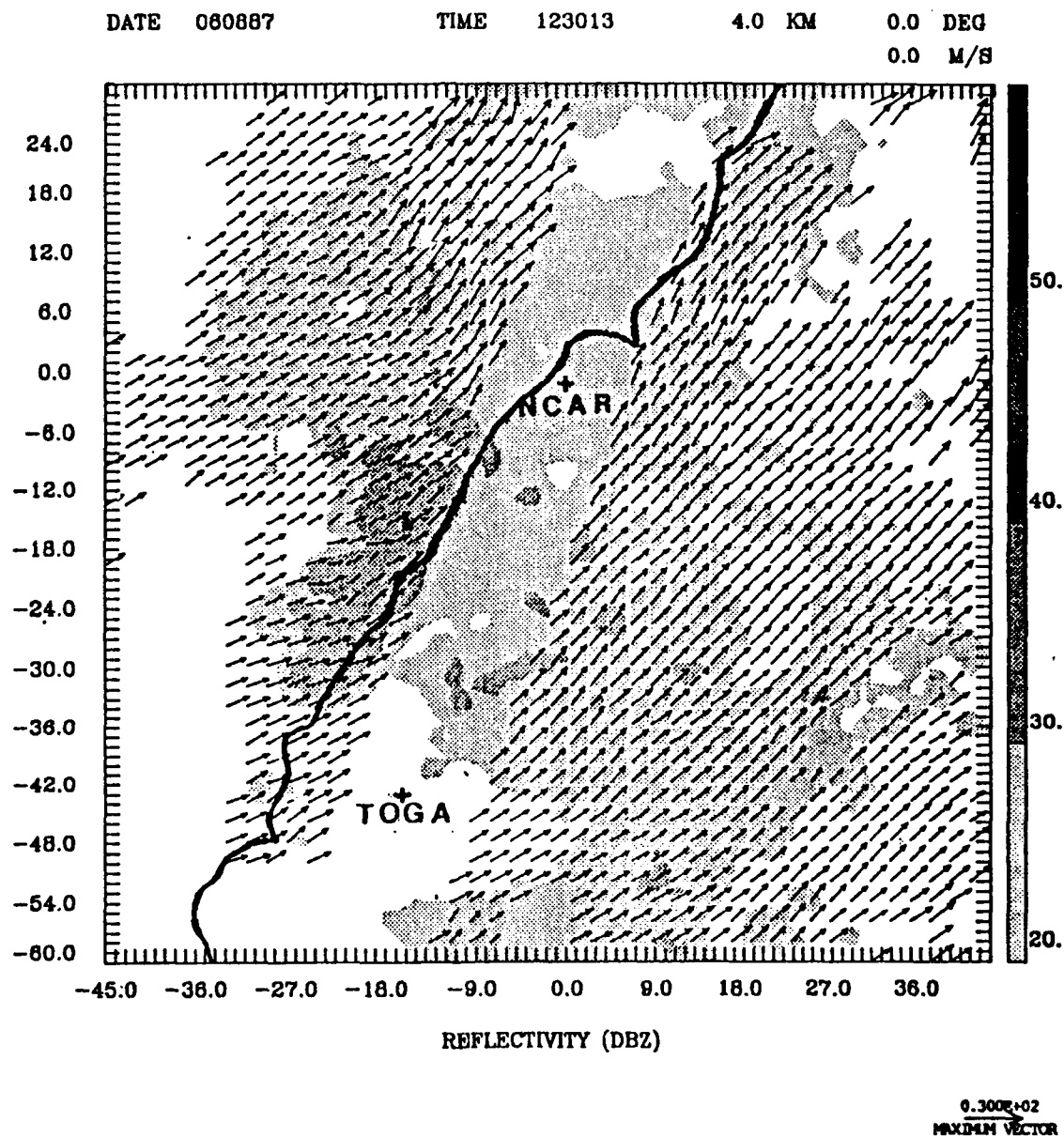


Fig. 17e. Dual-Doppler analysis of reflectivities and horizontal velocities for 123013, at 4.0 km above the ground. The length scale for the vectors is given in the lower right-hand corner. The reflectivity gray scale is given on the right side of the figure. Radar positions and the coastline of Taiwan are also given.

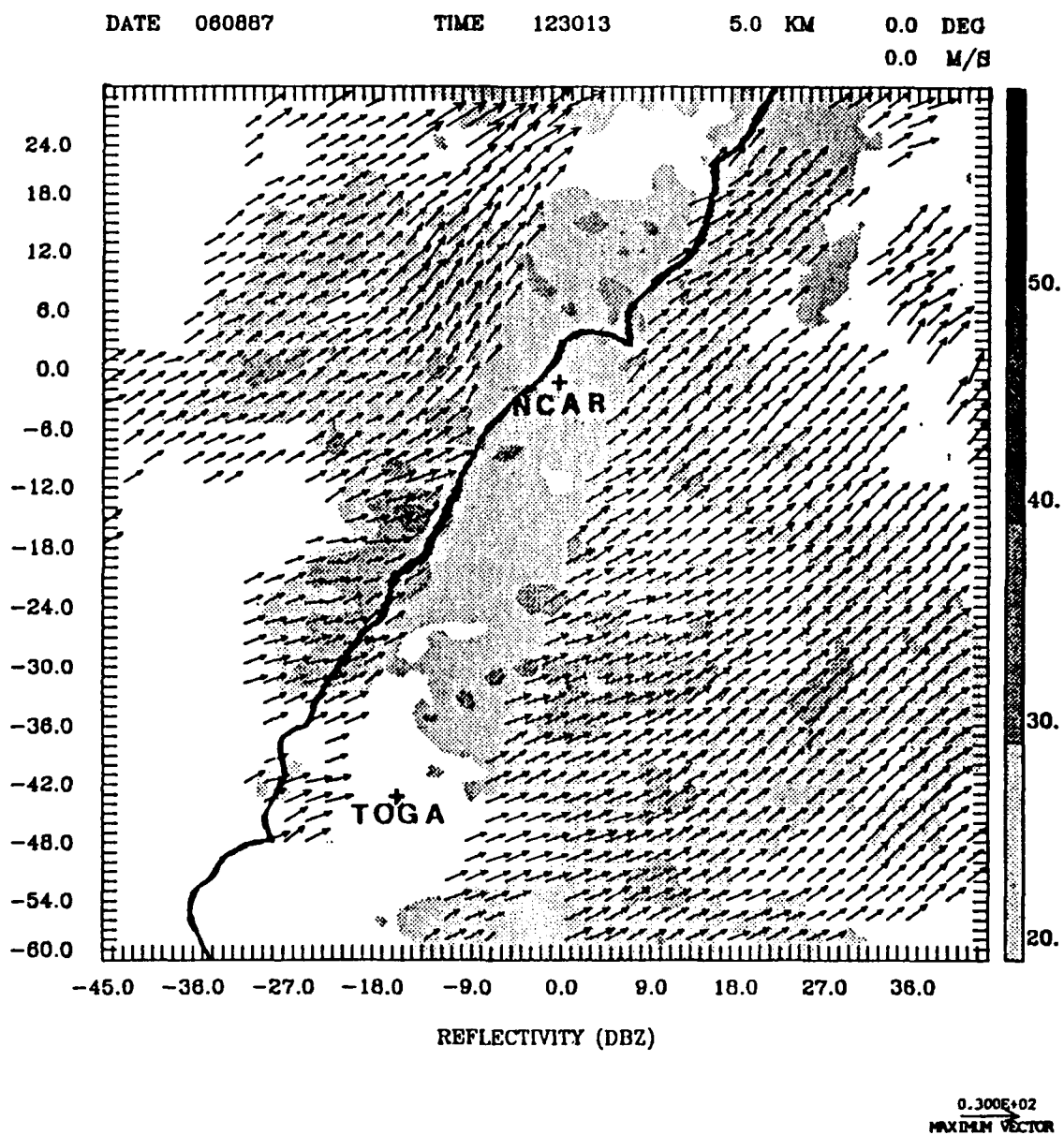


Fig. 17f. Dual-Doppler analysis of reflectivities and horizontal velocities for 123013, at 5.0 km above the ground. The length scale for the vectors is given in the lower right-hand corner. The reflectivity gray scale is given on the right side of the figure. Radar positions and the coastline of Taiwan are also given.

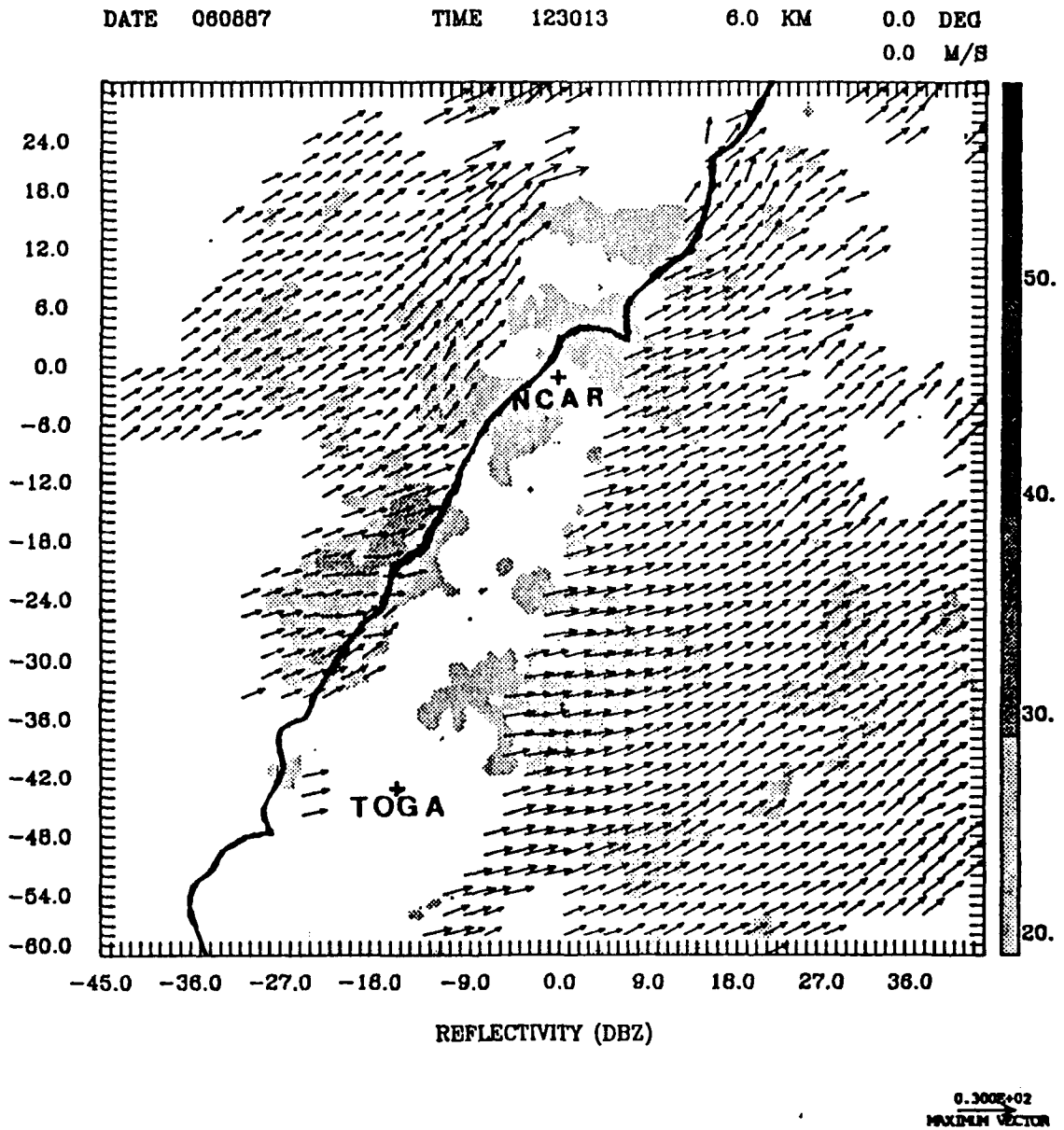


Fig. 17g. Dual-Doppler analysis of reflectivities and horizontal velocities for 123013, at 6.0 km above the ground. The length scale for the vectors is given in the lower right-hand corner. The reflectivity gray scale is given on the right side of the figure. Radar positions and the coastline of Taiwan are also given.

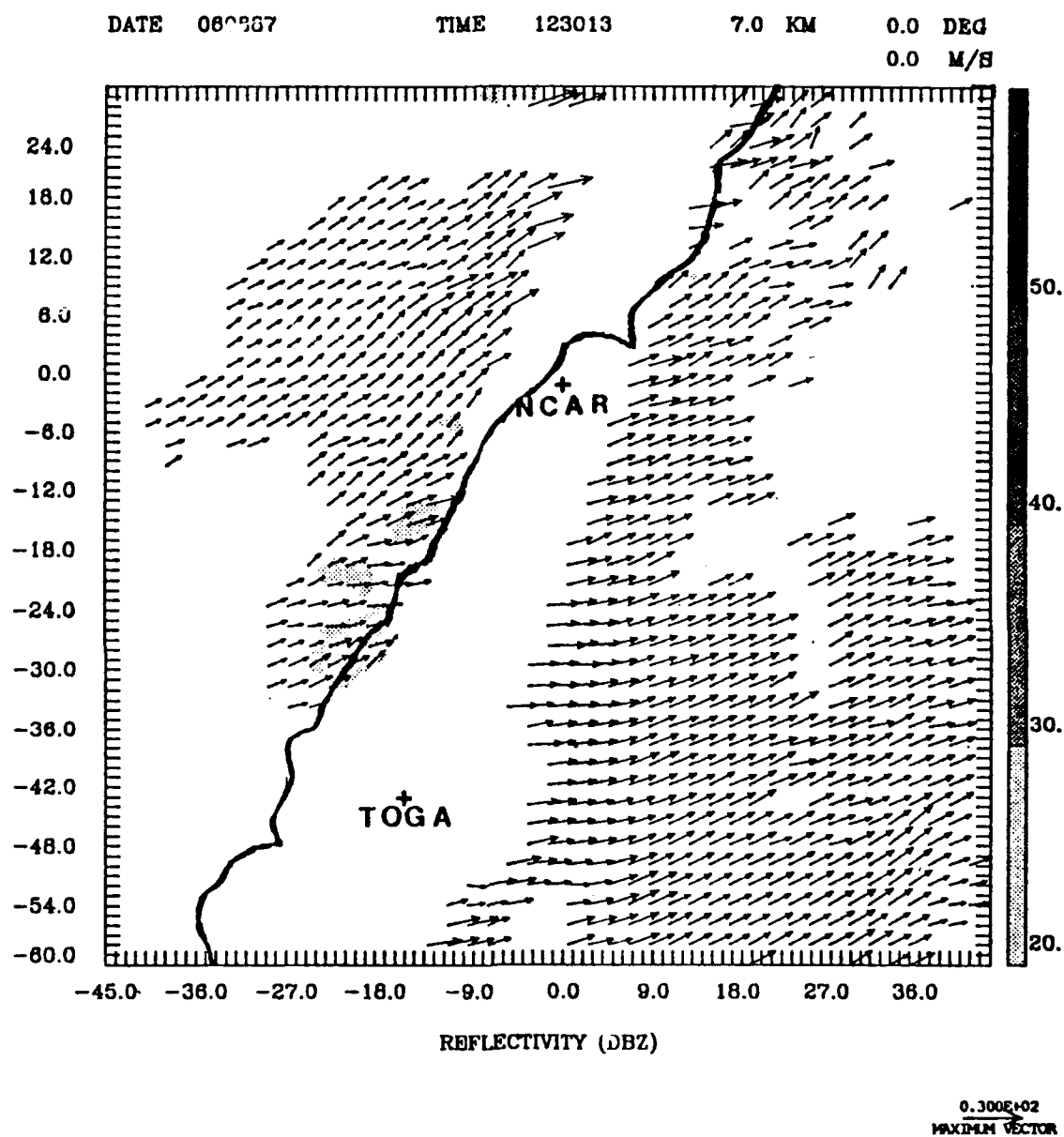


Fig. 17h. Dual-Doppler analysis of reflectivities and horizontal velocities for 123013, at 7.0 km above the ground. The length scale for the vectors is given in the lower right-hand corner. The reflectivity gray scale is given on the right side of the figure. Radar positions and the coastline of Taiwan are also given.

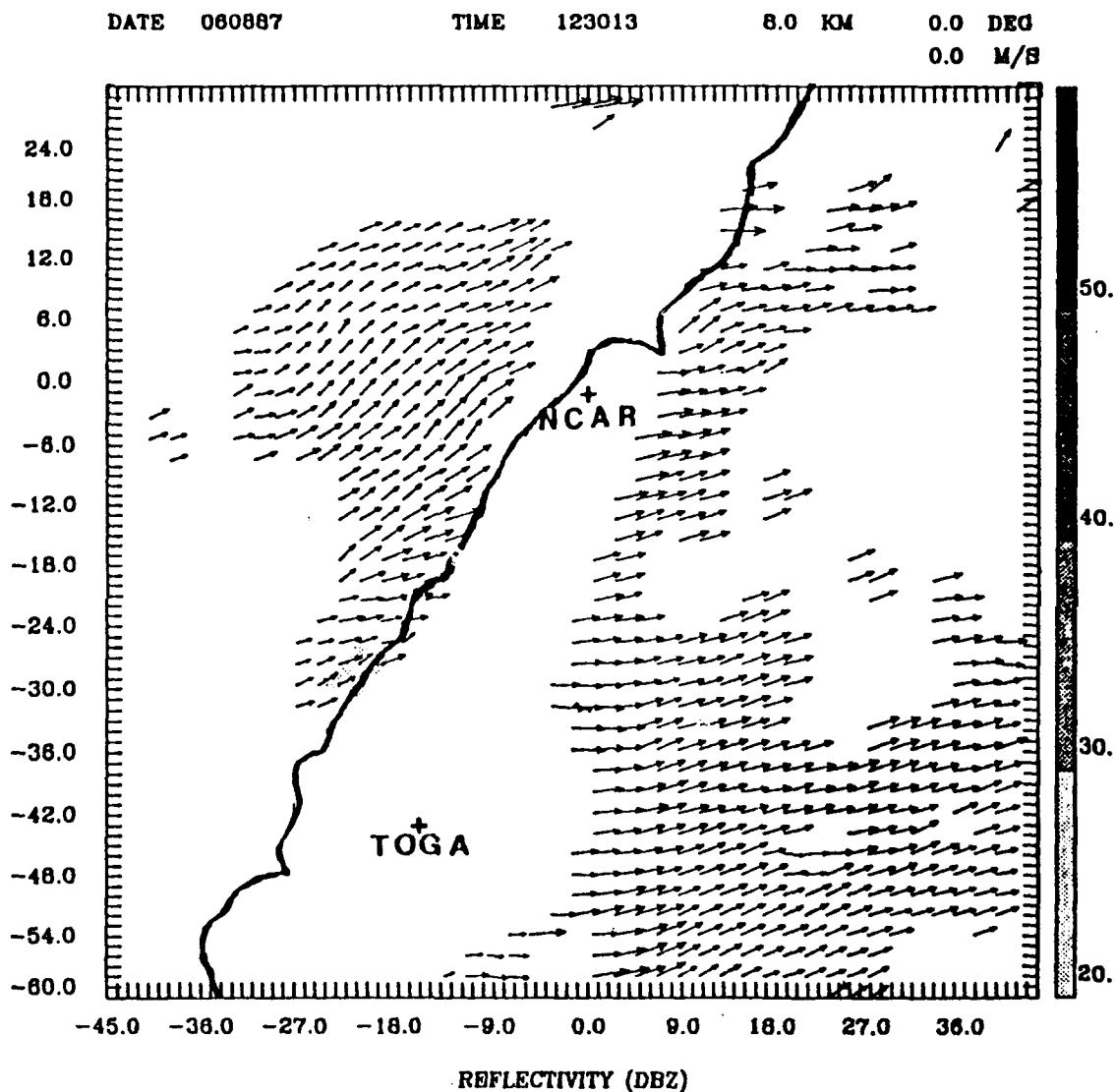


Fig. 17i. Dual-Doppler analysis of reflectivities and horizontal velocities for 123013, at 8.0 km above the ground. The length scale for the vectors is given in the lower right-hand corner. The reflectivity gray scale is given on the right side of the figure. Radar positions and the coastline of Taiwan are also given.

height, but are observed up to 6.0 km height (Figs. 17a-g). The areal extent of cores greater than 30 dBZ also maximizes at 1.0 km height (Fig. 17b). These cores extend to a height of 6.0 km (Fig. 17g). The echoes (greater than 20 dBZ) have increased in height, with some tops reaching the 8.0 km (Fig. 17i). The upsloping echo area (to the northwest of the TOGA radar) is seen at the 1.0 km height. Cores (associated with this area only) greater than 30 dBZ are observed to reach a maximum areal extent at the 3.0 km (Fig. 17d) height. Again, brightband effects are observed at the 5.0 km height (Fig. 17f). The echoes in this upslope area do not reach heights greater than 6.0 km. It is also possible that the convection in this area is not only caused by upsloping winds, but also may be aided by a confluence between the southerly and southwesterly flow. However, lack of data along the baseline makes this difficult to determine. Northerly frontal winds have vanished by 2.0 km, again supporting the shallow front concept. This is verified by a cross-section plot (Fig. 18) corresponding to line A-B in Fig. 17b. In Fig. 18, the frontal flow does not reach the 2.0 km height level. Figure 18 also shows that the most intense echo core, greater than 40 dBZ, is located near the leading edge of the front. Further, we can see from this cross-section that the flow is an anafont. As discussed by Barry and Chorely (1982), the frontal area is characterized by rising motion in the warm sector ahead of, and over, the front itself. It is also a very active front, as indicated by the relatively intense echoes associated with it. The cold anafronts studied by Browning and Harrold (1970) had a narrow band of convection associated with a

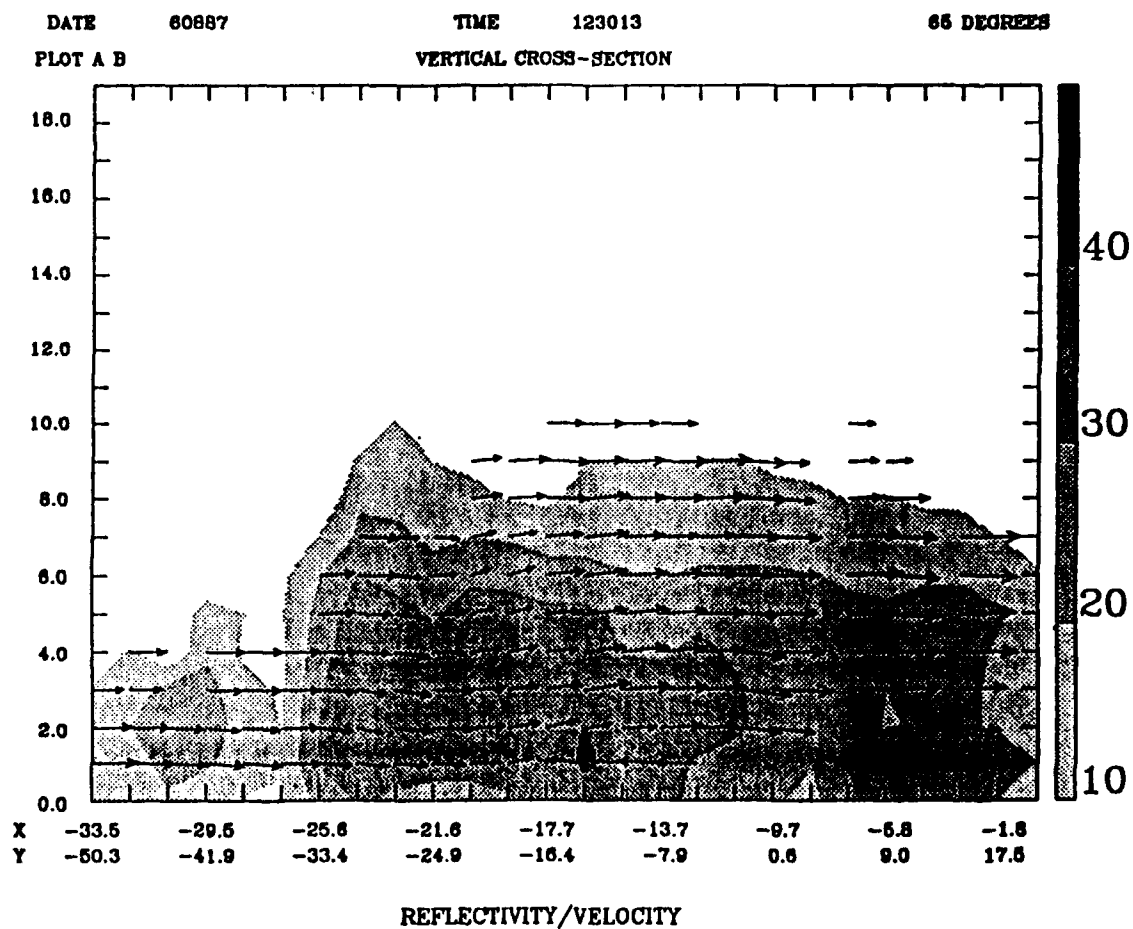
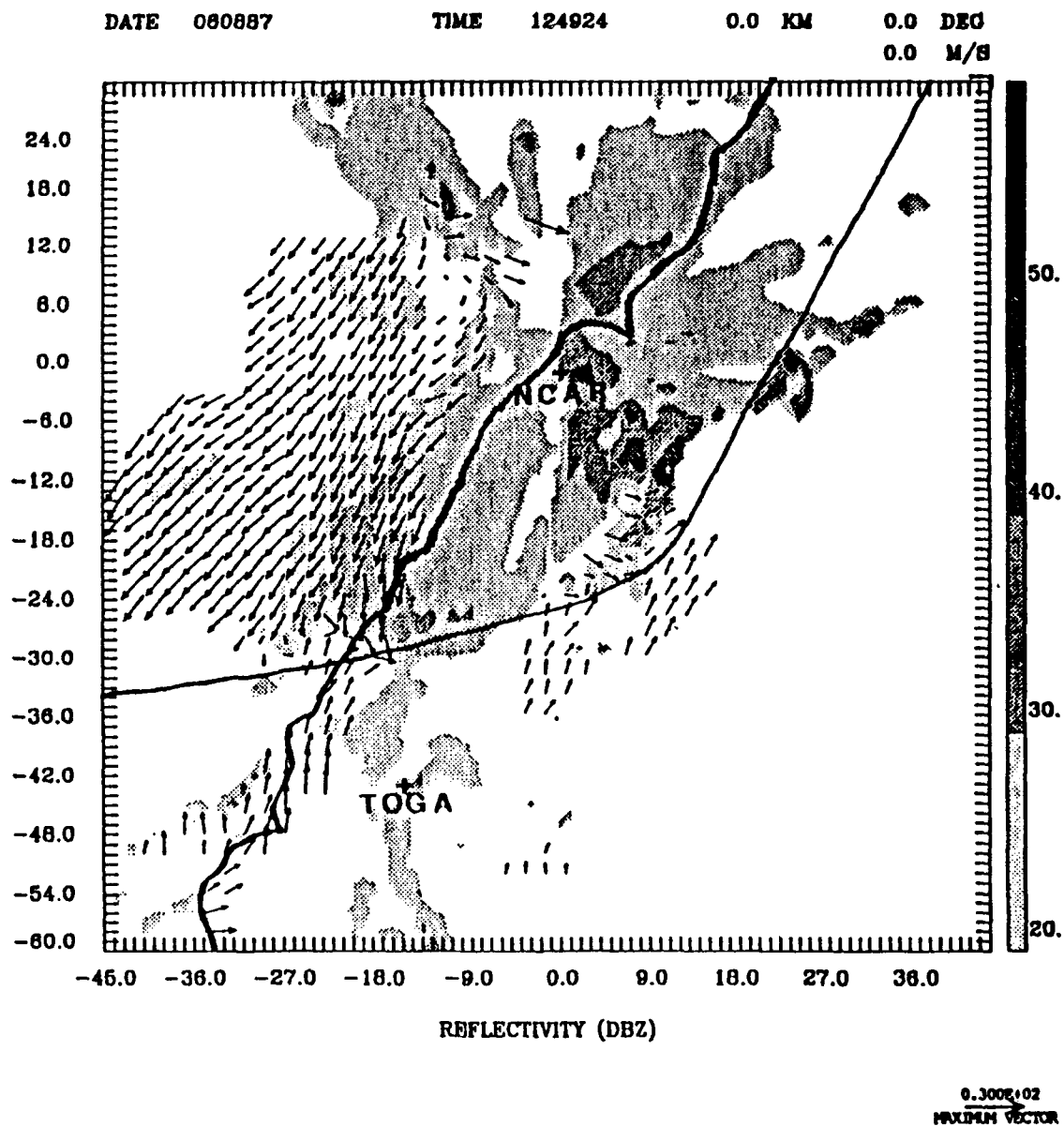


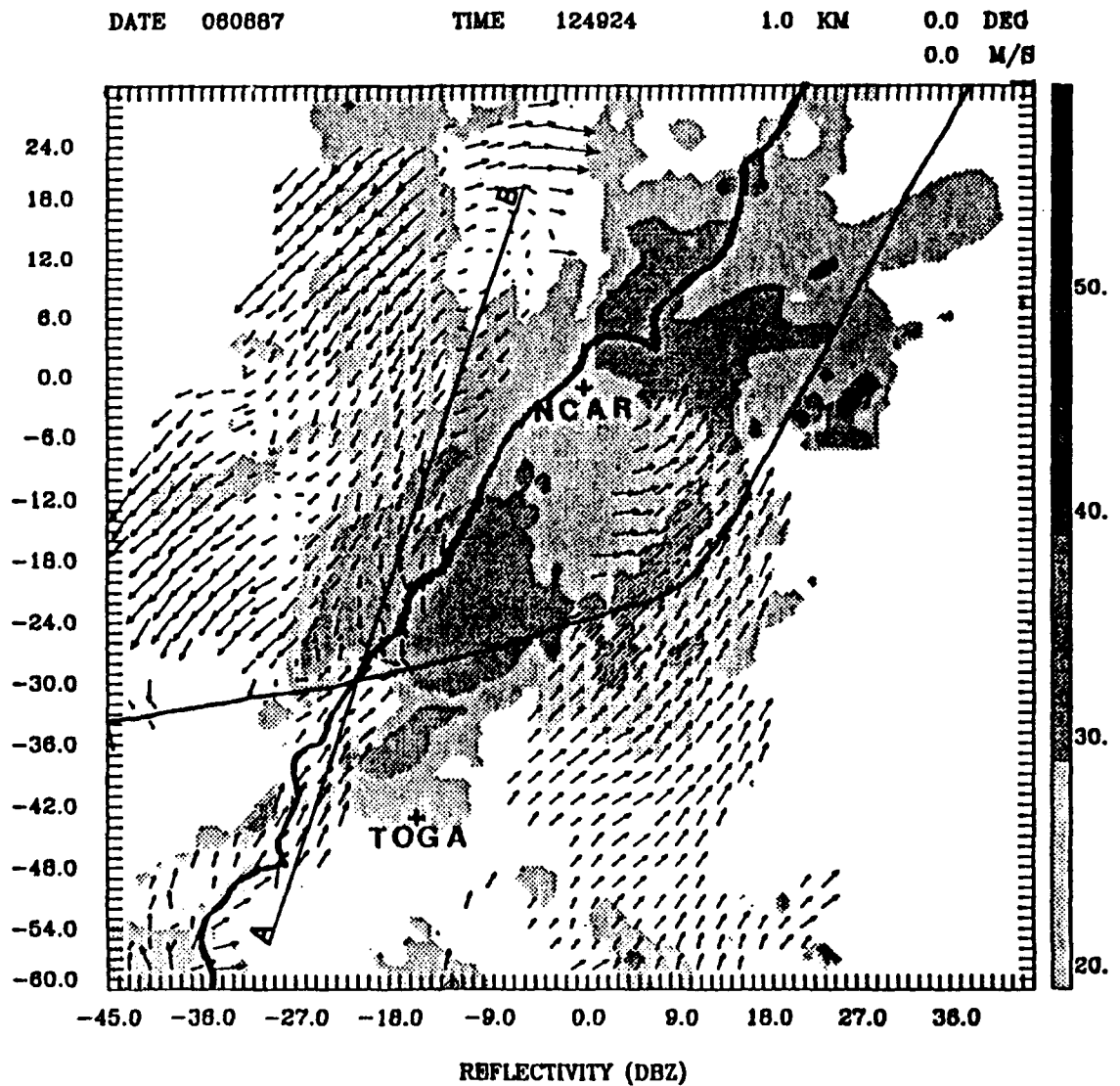
Fig. 18. Vertical cross-section of reflectivity and wind. View is toward the WNW along the cross-section (A-B) indicated in Fig. 17b.

broad area of precipitation. The echo pattern in Fig. 18 indicates that this also occurred with this front.

By 124924 LST (Figs. 19a-h), the western portion of the front (relative to the analysis grid) has moved south of the NCAR radar to a point  $y = -36$  (Fig. 19a). This gives frontal speed of approximately  $16 \text{ ms}^{-1}$  for the western part of the front. The front lies in an east to west direction. Trier *et al.* (1989) in their 12 LST analysis (Fig. 6) analyzed a wave on the front; however, it is not seen in the present analysis. This could be due to a lack of data. The eastern portion of the front is oriented from the southwest to the northeast. This part of the front is approximately co-located with the western edge of the island elevations greater than 1.0 km (Fig. 1). This gives credibility to the assumption that the island terrain served to block the front as it moved southward. Further, in the mesoscale analysis by Trier *et al.* (1989), the frontal areas depicted in Figs. 6 and 7 also conform to the location of the island elevations greater than 1.0 km. The upper level flow patterns at 124924 LST (Figs. 19d-h) are analogous to the ones at 123013 LST (Figs. 17d-i). The maximum echo tops are at 7.0 km (Fig. 19h). Only a few cores greater than 40 dBZ are seen at this time, but none appear to be associated with the moving portion of the front. Cores greater than 30 dBZ have tops at 5.0 km (Fig. 19f). In the lower levels (Figs. 19a and 19b), the flow is predominately northeasterly behind the front. Figure 20 is a cross-section through the front. The location of this plot



*Fig. 19a. Dual-Doppler analysis of reflectivities and horizontal velocities for 124924, at the ground. The length scale for the vectors is given in the lower right-hand corner. The reflectivity gray scale is given on the right side of the figure. Radar positions and the coastline of Taiwan are also given. Frontal position is indicated by the heavy dashed line.*



0.300E+02  
HORIZONTAL VECTOR

**Fig. 19b.** Dual-Doppler analysis of reflectivities and horizontal velocities for 124924, at 1.0 km above the ground. The length scale for the vectors is given in the lower right-hand corner. The reflectivity gray scale is given on the right side of the figure. Radar positions and the coastline of Taiwan are also given. Frontal position is indicated by the heavy dashed line. Line A-B depicts the position of the cross-sectional plot depicted in Fig. 21.

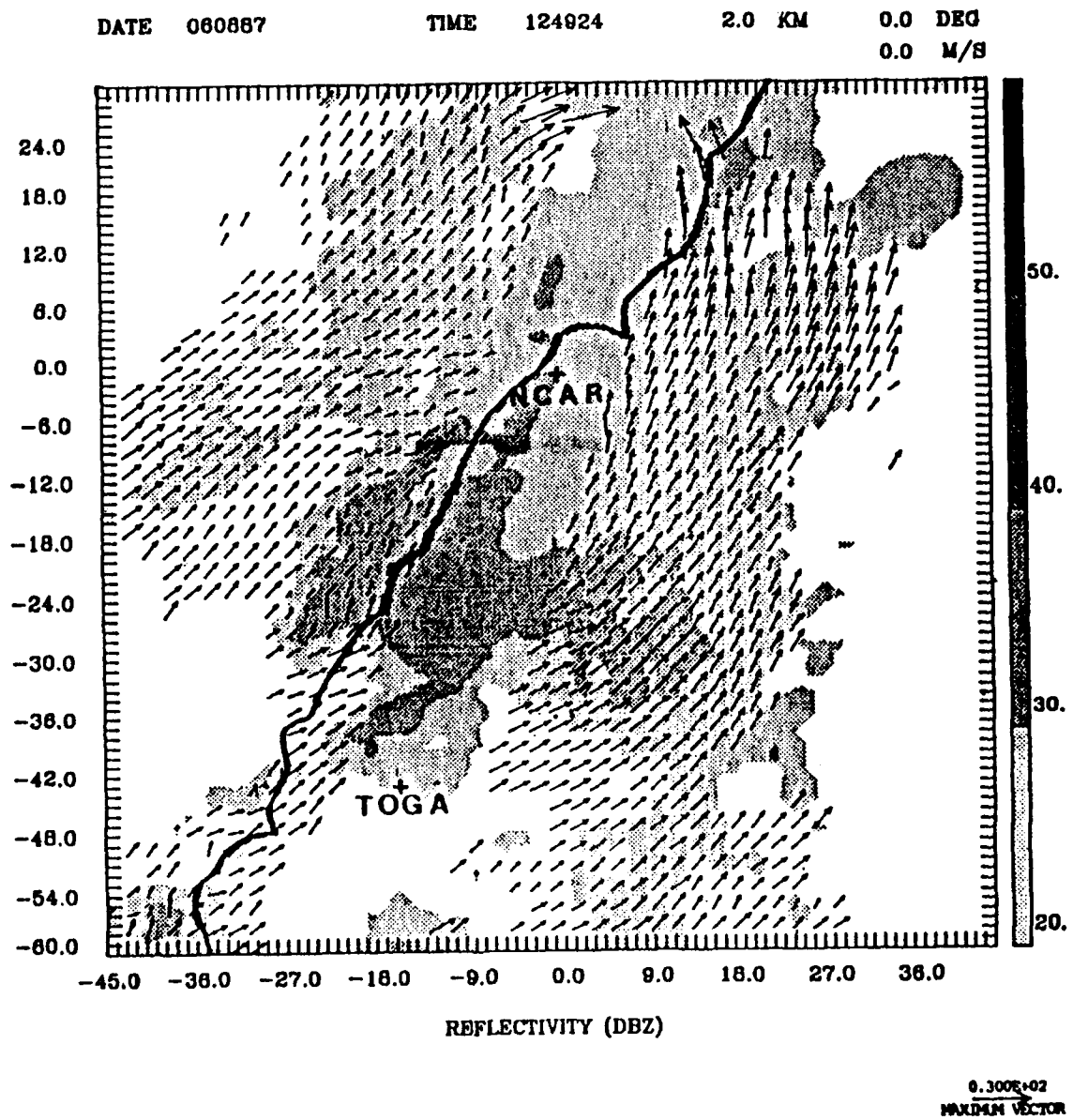


*Fig. 19c. Dual-Doppler analysis of reflectivities and horizontal velocities for 124924, at 2.0 km above the ground. The length scale for the vectors is given in the lower right-hand corner. The reflectivity gray scale is given on the right side of the figure. Radar positions and the coastline of Taiwan are also given.*

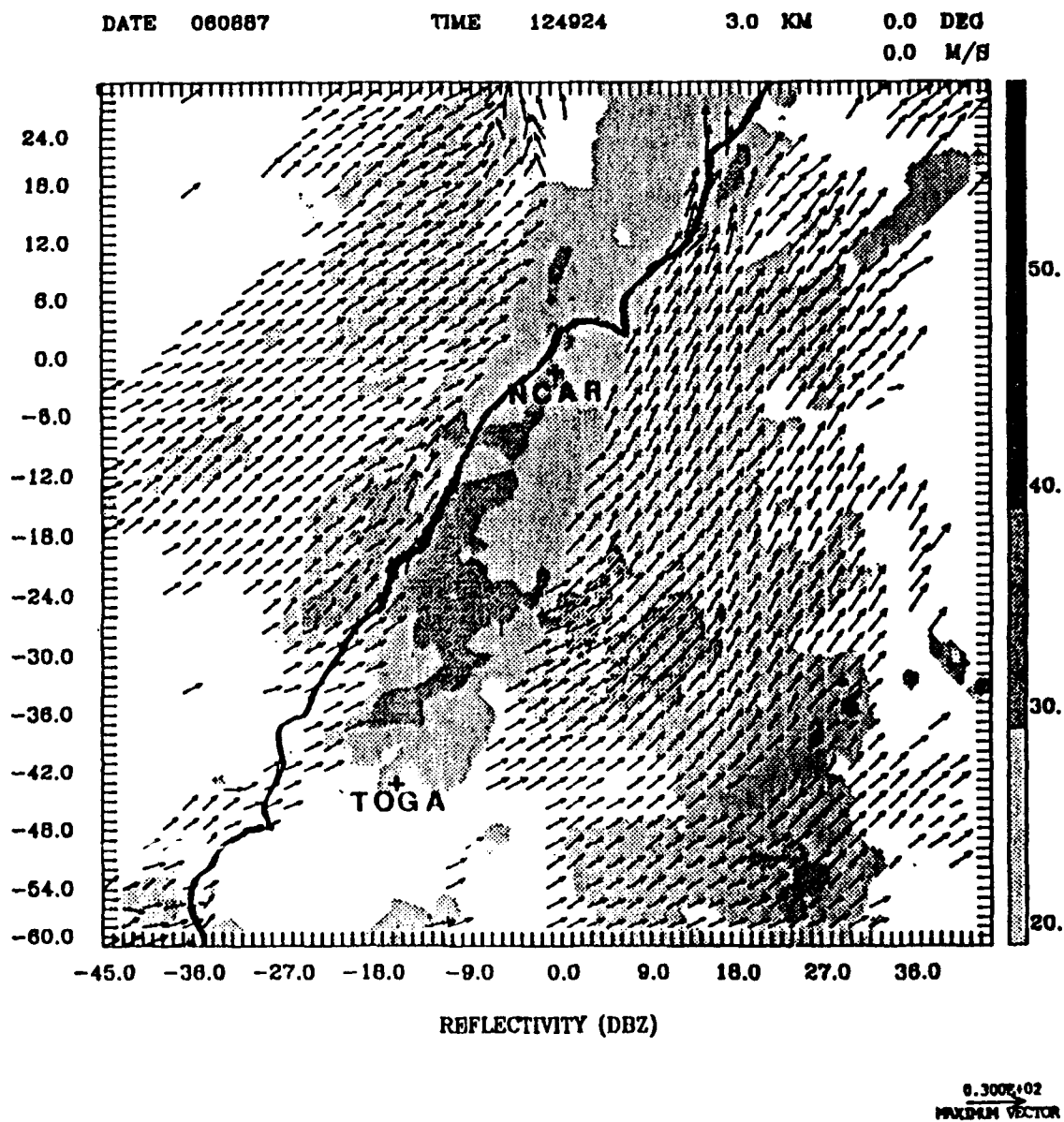


*Fig. 19d. Dual-Doppler analysis of reflectivities and horizontal velocities for 12/924, at 3.0 km above the ground. The length scale for the vectors is given in the lower right-hand corner. The reflectivity gray scale is given on the right side of the figure. Radar positions and the coastline of Taiwan are also given.*

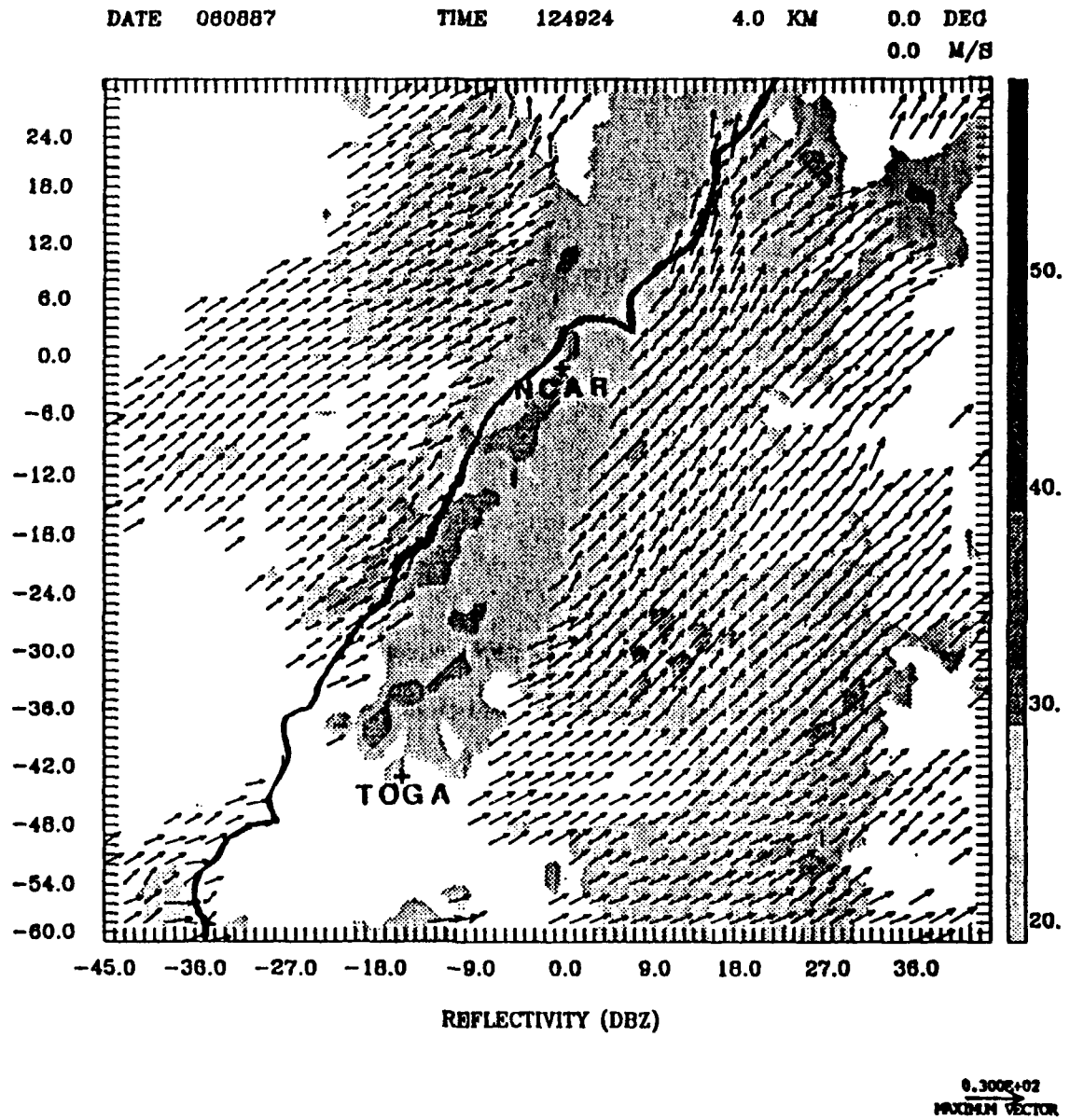


*Fig. 19e. Dual-Doppler analysis of reflectivities and horizontal velocities for 124924, at 4.0 km above the ground. The length scale for the vectors is given in the lower right-hand corner. The reflectivity gray scale is given on the right side of the figure. Radar positions and the coastline of Taiwan are also given.*

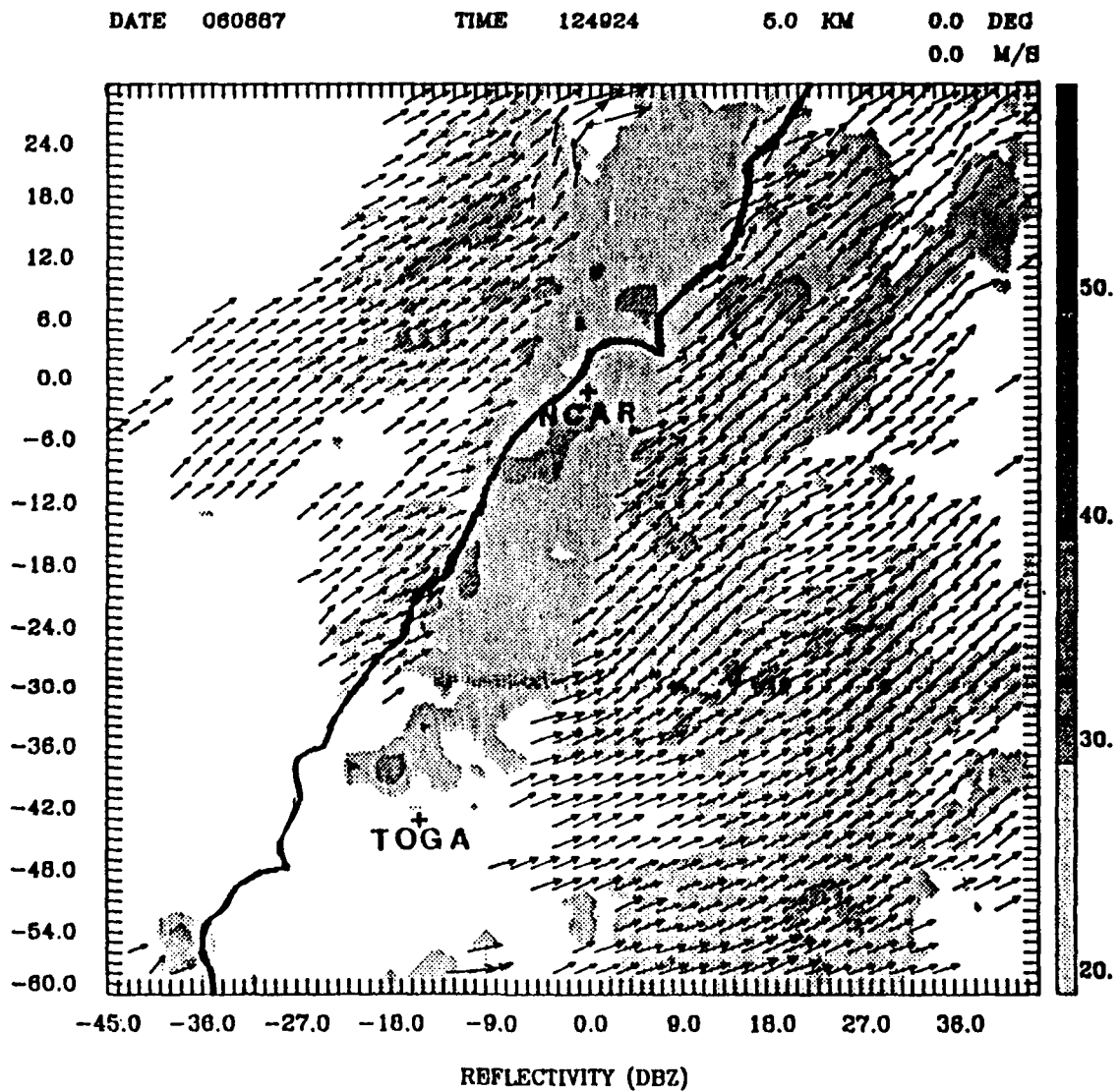


*Fig. 19f. Dual-Doppler analysis of reflectivities and horizontal velocities for 124924, at 5.0 km above the ground. The length scale for the vectors is given in the lower right-hand corner. The reflectivity gray scale is given on the right side of the figure. Radar positions and the coastline of Taiwan are also given.*

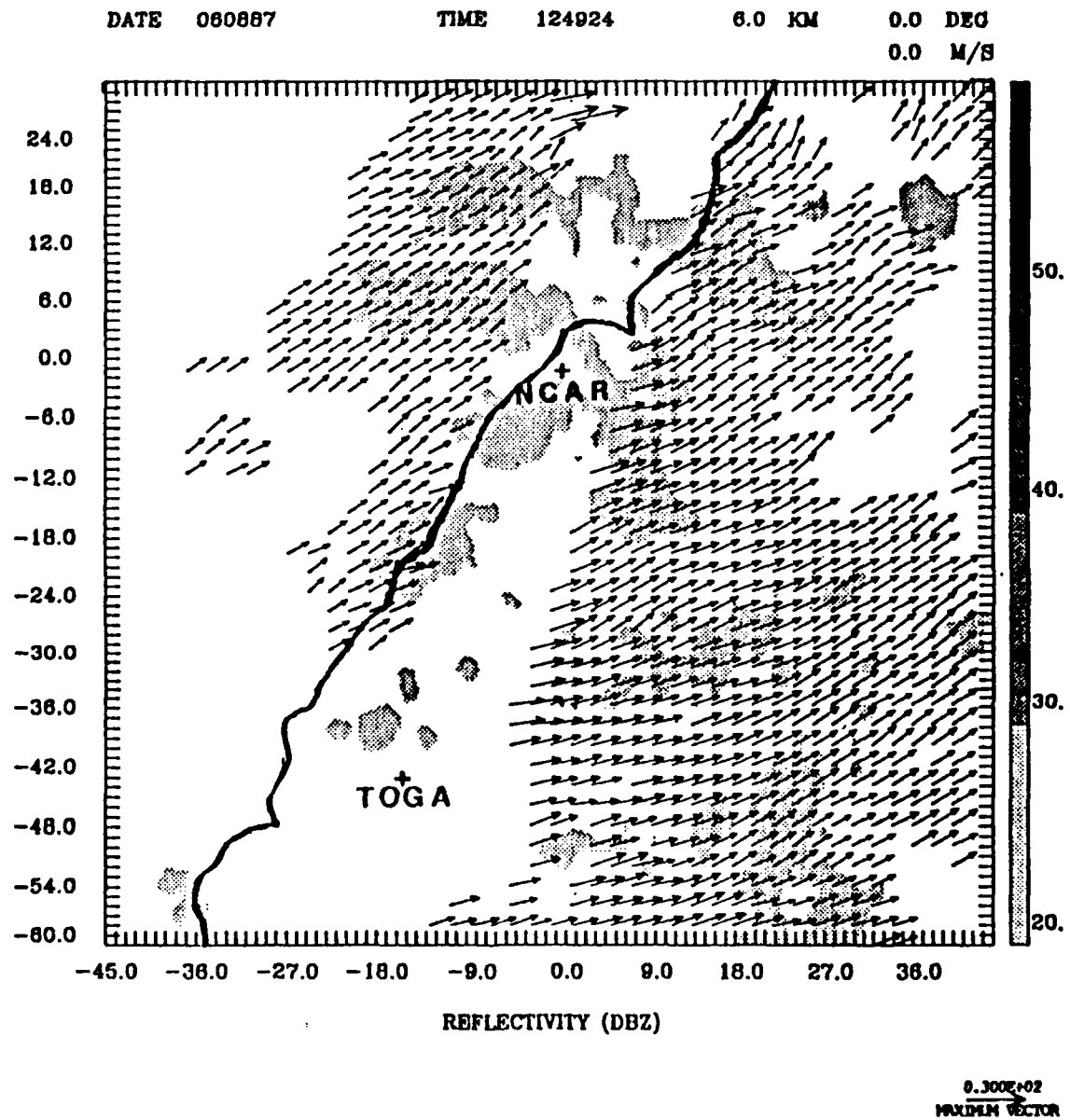
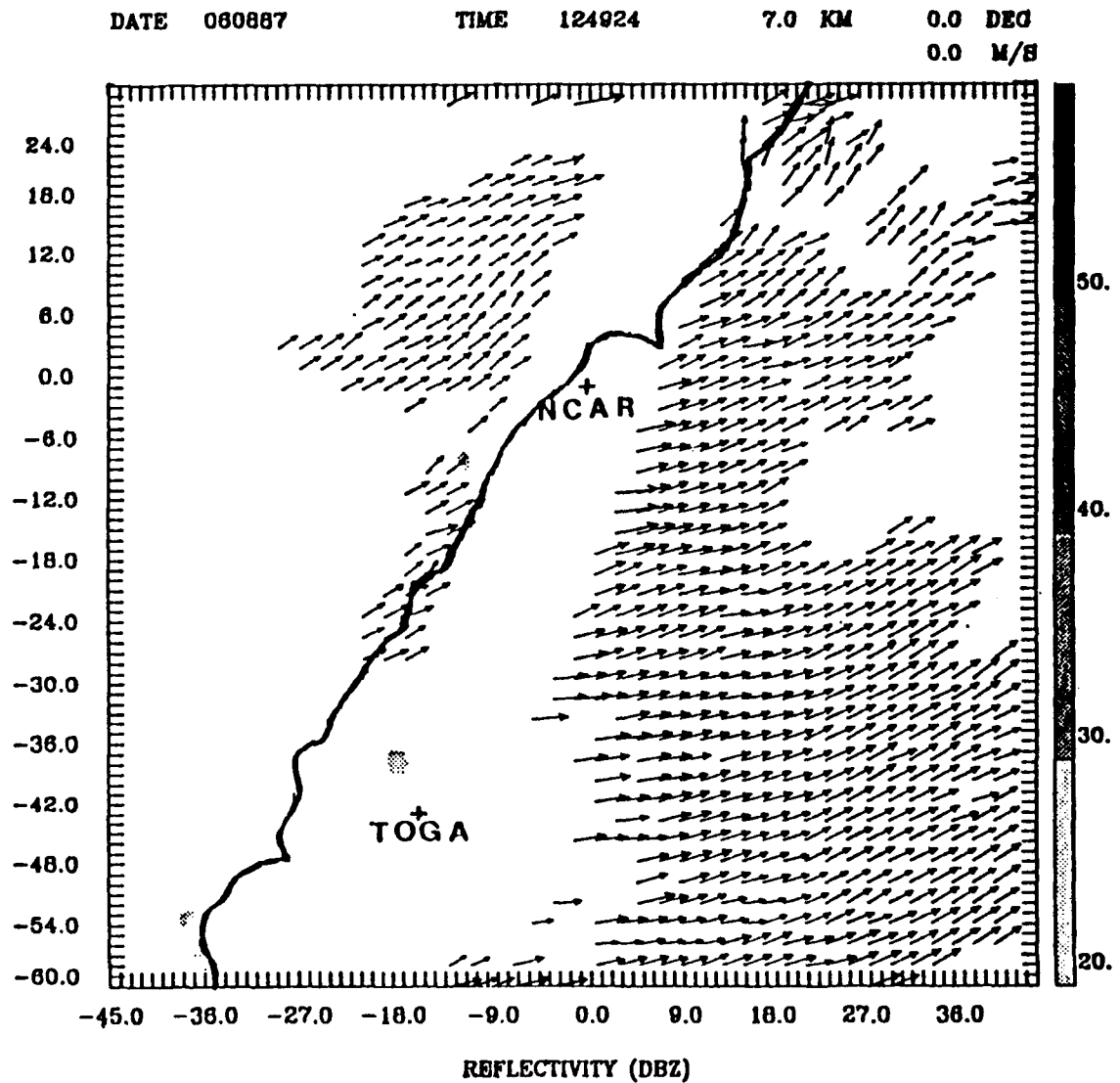


Fig. 19g. Dual-Doppler analysis of reflectivities and horizontal velocities for 124924, at 6.0 km above the ground. The length scale for the vectors is given in the lower right-hand corner. The reflectivity gray scale is given on the right side of the figure. Radar positions and the coastline of Taiwan are also given.



*Fig. 19h. Dual-Doppler analysis of reflectivities and horizontal velocities for 124913, at 7.0 km above the ground. The length scale for the vectors is given in the lower right-hand corner. The reflectivity gray scale is given on the right side of the figure. Radar positions and the coastline of Taiwan are also given.*

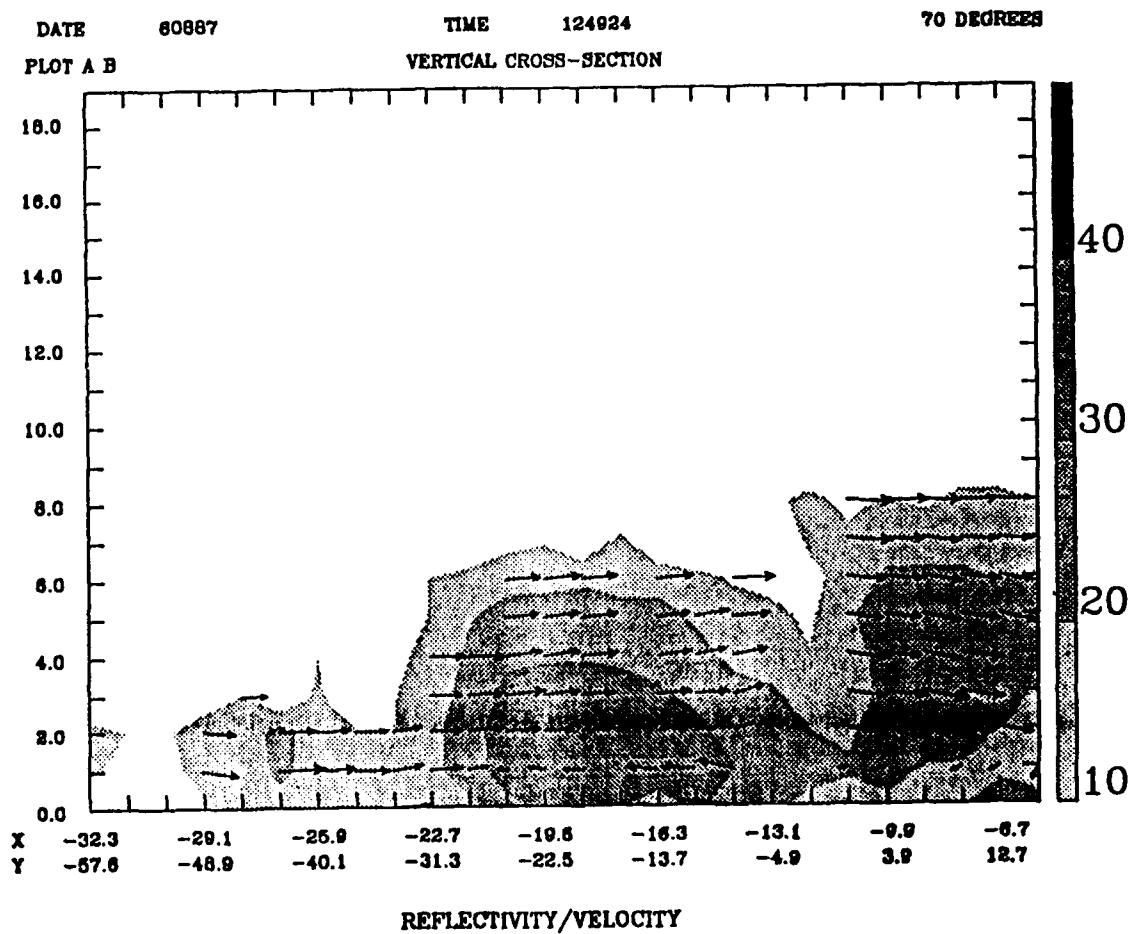


Fig. 20. Vertical cross-section of reflectivity and wind. View is toward the WNW along the cross-section (A-B) indicated in Fig. 19b.

is defined by line A-B in Fig. 19b. The leading edge of reflectivities greater than 30 dBZ is approximately at the same location as the leading edge of the front.

At 132902 LST (Figs. 21a-c), the front is just north of the TOGA radar. The portion of the front over the coast is moving at approximately  $7 \text{ ms}^{-1}$ . The portion of the front over the island has not moved. Near the frontal boundary, large cores greater than 30 dBZ are seen. Smaller cores with reflectivities greater than 40 dBZ are seen at the surface (Fig. 21a). These 40 dBZ cores have tops less than 2.0 km in height. Some of the 30 dBZ cores extend to 6.0 km in height, and some extend to 7.0 km. The 1.0 km height (Fig. 21b) shows the orientation of the cross-section plot (lines A-B) depicted by Fig. 22. The most interesting feature in Fig. 22 is found at the frontal boundary (near the lower left-hand corner of the plot). At the edge of the front, winds are observed to point toward the surface. This flow is co-located with an echo core of greater than 30 dBZ. Thus, this flow most likely represents the outflow from the convective core. Figure 23 shows the 1.0 km height frontal position at 140905. Lack of data make the other levels unusable. It is observed in this figure that the front still has not changed position. Since this position is approximately the same as the island elevations greater than 1.0 km, terrain blocking is further supported. When the front was over land, prior to reaching the island elevations greater than 1.0 km (where blocking occurred), frontal speed is estimated at  $6 \text{ ms}^{-1}$ . This speed corresponds to the speeds of  $3\text{--}5 \text{ ms}^{-1}$  found in the GATE study by Houze and Cheng (1977). The over water speeds of the

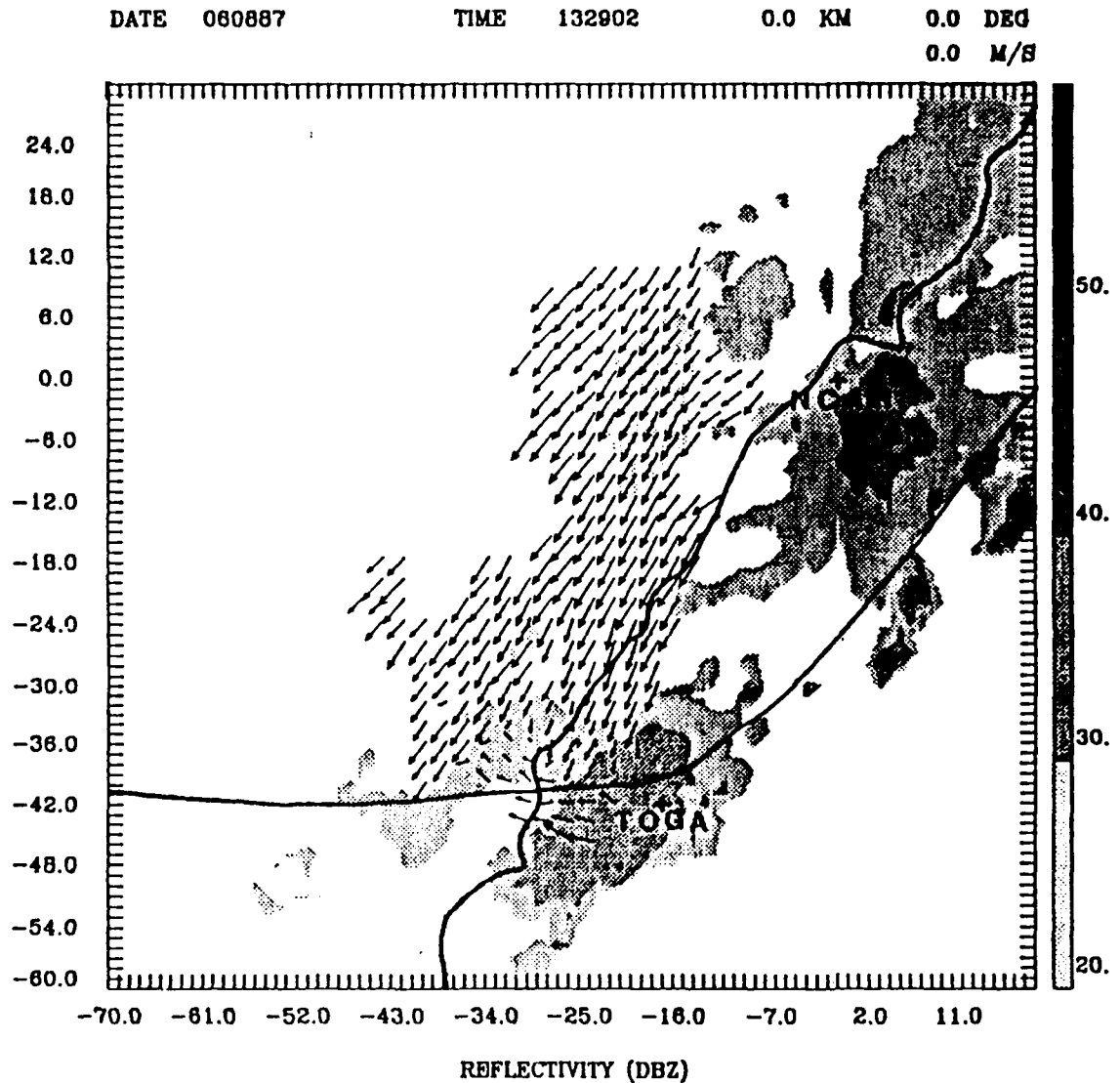
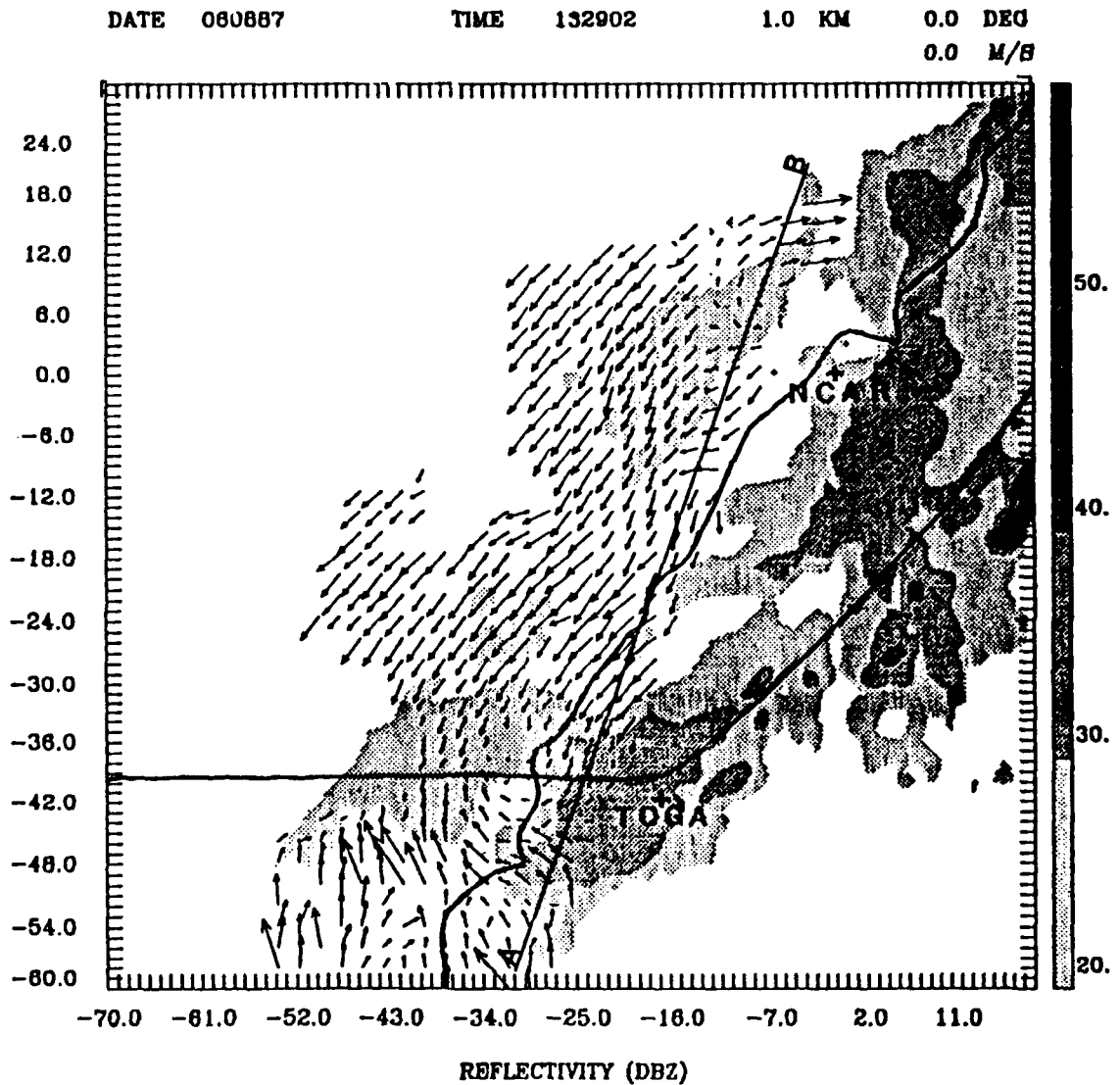
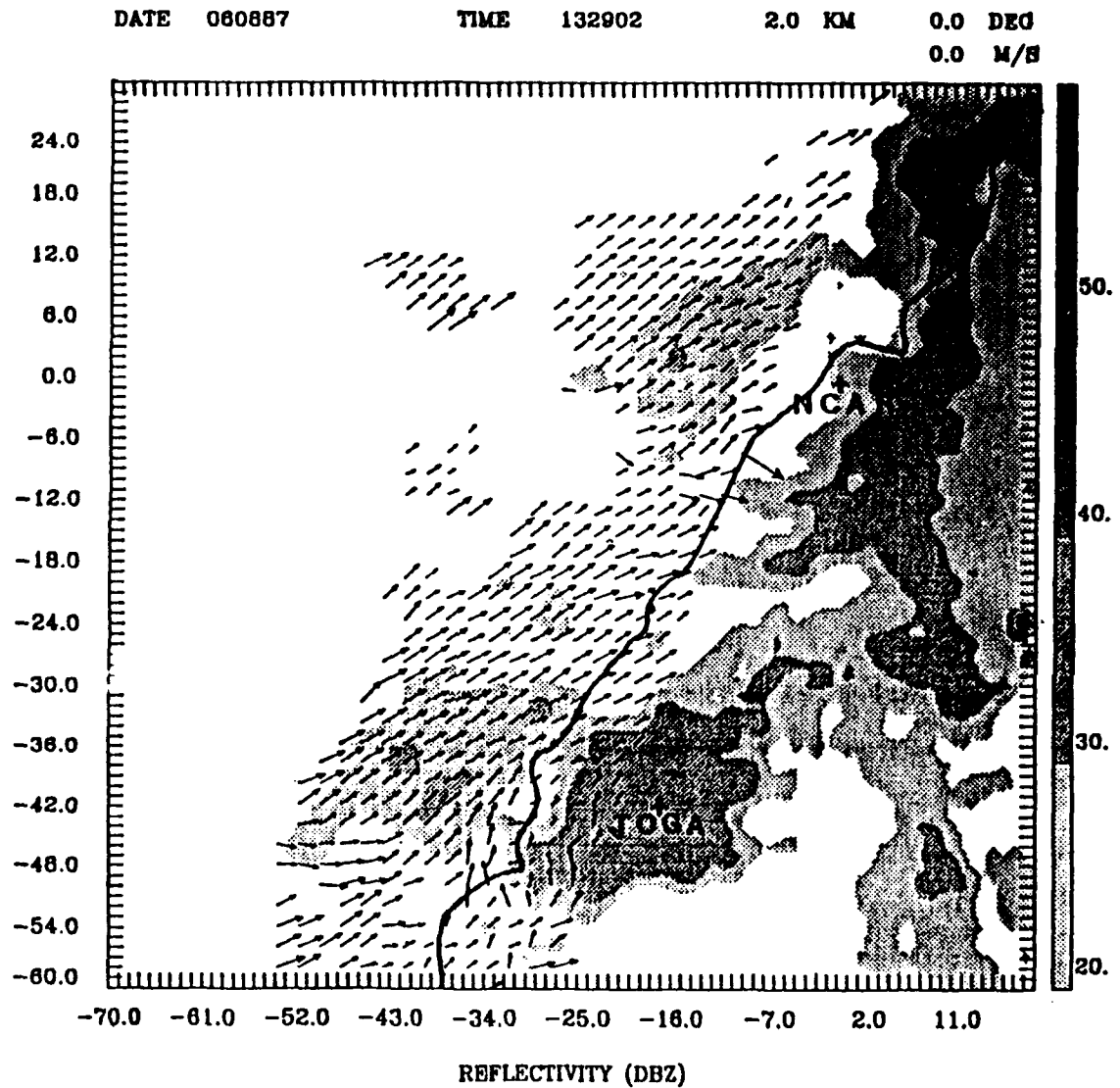


Fig. 21a. Dual-Doppler analysis of reflectivities and horizontal velocities for 132902, at the ground. The length scale for the vectors is given in the lower right-hand corner. The reflectivity gray scale is given on the right side of the figure. Radar positions and the coastline of Taiwan are also given. Frontal position is indicated by the heavy dashed line.



**Fig. 21b.** Dual-Doppler analysis of reflectivities and horizontal velocities for 132902, at 1.0 km above the ground. The length scale for the vectors is given in the lower right-hand corner. The reflectivity gray scale is given on the right side of the figure. Radar positions and the coastline of Taiwan are also given. Frontal position is indicated by the heavy dashed line. Line A-B denotes the position of the cross-sectional plot in Fig. 22.



*Fig. 21c. Dual-Doppler analysis of reflectivities and horizontal velocities for 132902, at 2.0 km above the ground. The length scale for the vectors is given in the lower right-hand corner. The reflectivity gray scale is given on the right side of the figure. Radar positions and the coastline of Taiwan are also given.*

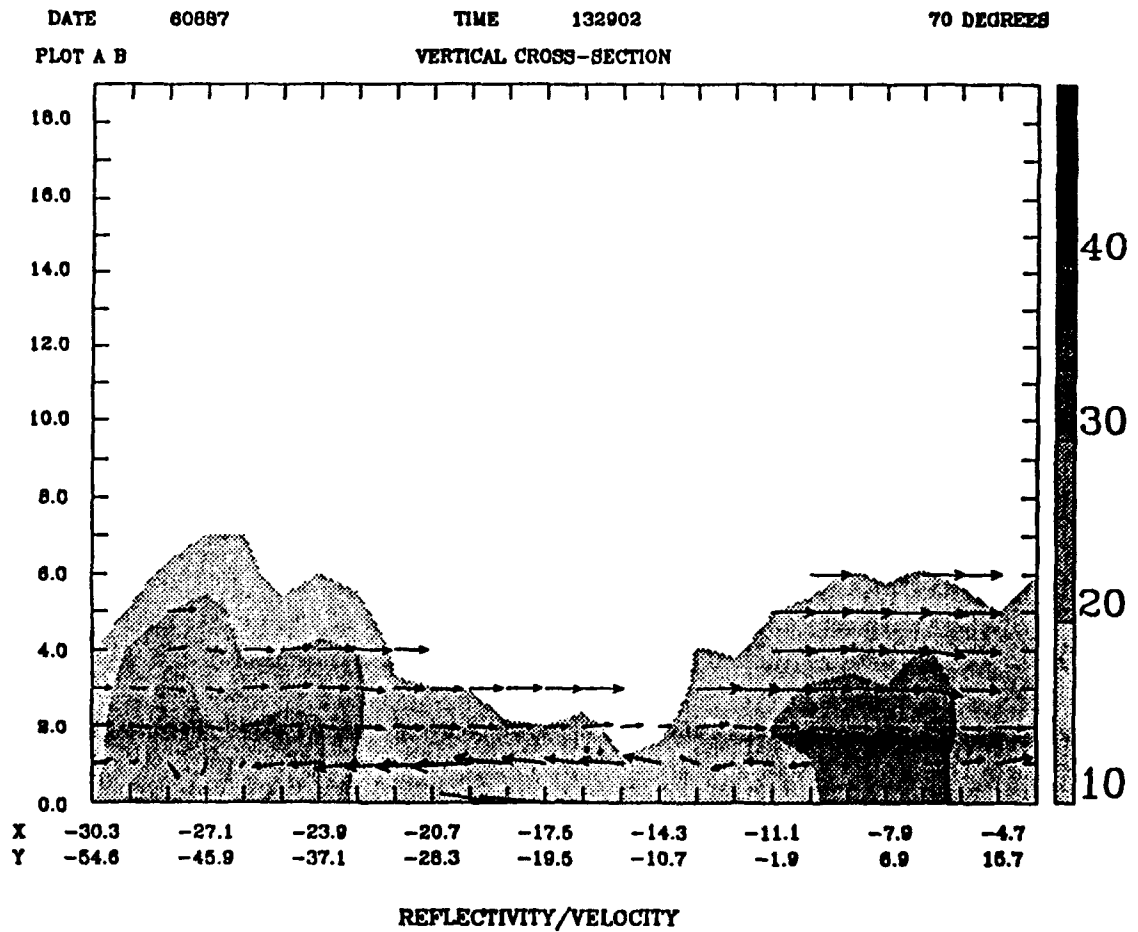


*Fig. 22. Vertical cross-section of reflectivity and wind. View is toward the WNW along the cross-section (A-B) indicated in Fig. 21b.*

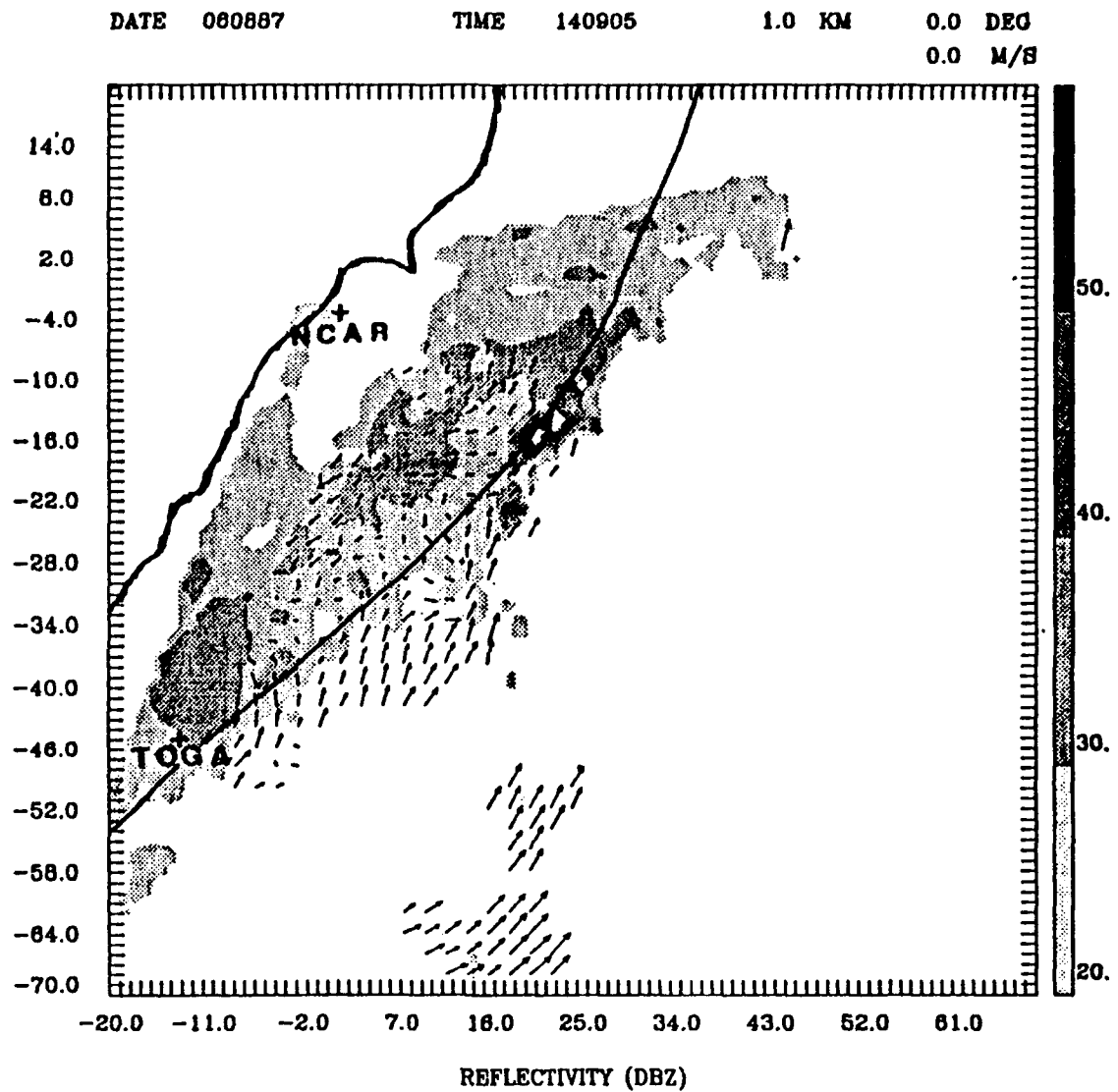


Fig. 29. Dual-Doppler analysis of reflectivities and horizontal velocities for 140905, at 1.0 km above the ground. The length scale for the vectors is given in the lower right-hand corner. The reflectivity gray scale is given on the right side of the figure. Radar positions and the coastline of Taiwan are also given. Frontal position is indicated by the heavy dashed line.

TAMEX front were as high as  $19 \text{ ms}^{-1}$ . Studies in the mid-latitudes by Browning and Harrold (1970) and Hobbs *et al.* (1980) showed most of the fronts to move in excess of  $10 \text{ ms}^{-1}$ .

### 3.2 RHI Analysis

Figures 24–26 are Range Height Indicator (RHI) scans from the NCAR CP-4 radar taken before (Figs. 24 and 25, at 1100 LST) and after frontal passage (Fig. 26, at 1258 LST). In all of these figures, the reflectivity field is at the top and the velocity field is at the bottom. The shade scales that indicate the values in the figures are located below each of the reflectivity and velocity plots. The range rings are at every 10 km.

The depth of the front is 1.57 km. Figure 24 is taken along the  $10^\circ$  azimuth. Toward the left side of the reflectivity plot, reflectivities of 36 dBZ are observed at 4.75 km height. This is called the brightband, and it is an indicator of the melting ( $0^\circ$ ) level. The velocity pattern clearly depicts the front. The leading edge of the front is 16.5 km from the radar, as indicated by the negative velocity values. Note the radar's location is at the left edge of the plots, and negative velocities represent flow towards the radar, while positive values denote flow away from the radar. The front, and the corresponding cold air associated with it, are seen as a shallow wedge of negative velocities underneath the positive velocity pattern in the center and right side of the figure. The maximum radial velocity in this cold wedge is  $15 \text{ ms}^{-1}$ . Above the front, the maximum radial velocity is  $16 \text{ ms}^{-1}$ , at 4.3 km

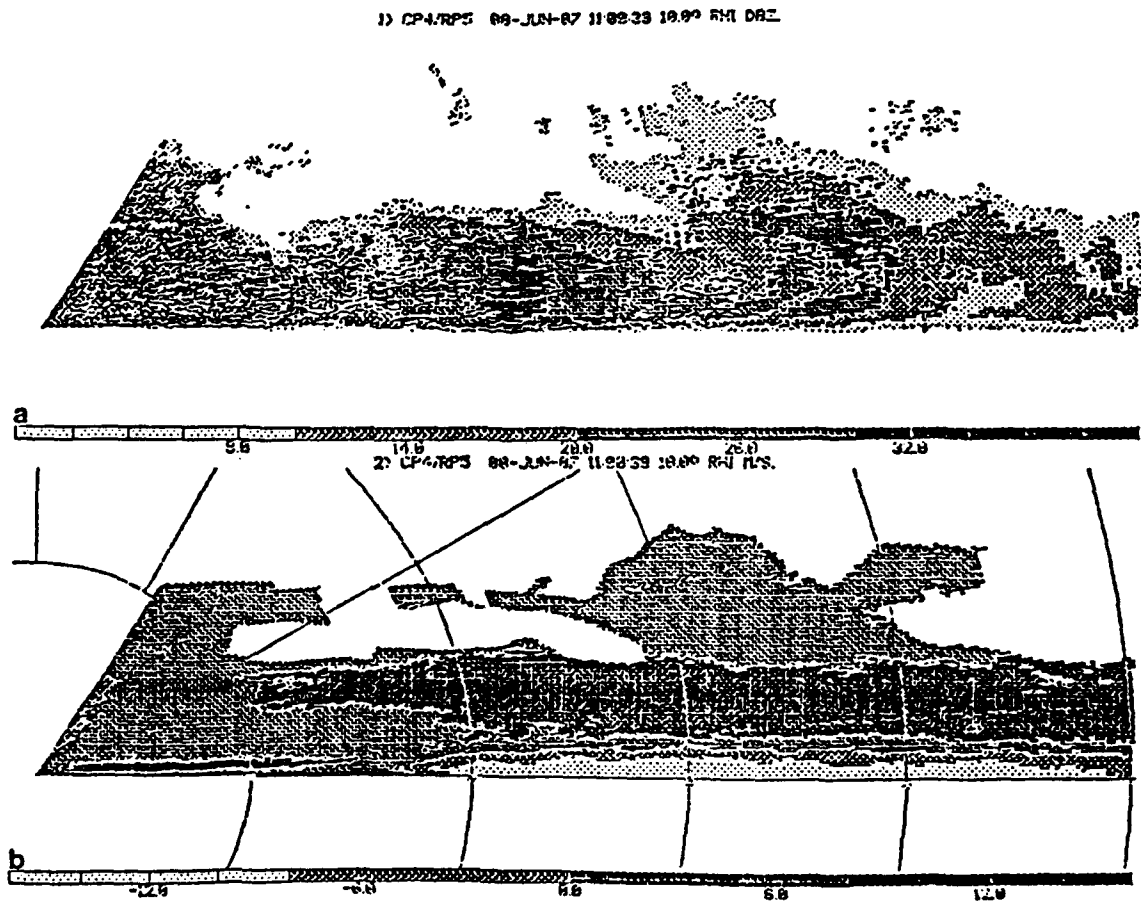


**Fig. 24.** RHI scan of reflectivity and radial velocity from the NCAR CP-4. (a) is reflectivity and (b) is radial velocity, both at 10 degrees azimuth at 110039 LST. Scales are given at the bottom of each figure.

1) CP4/RP5 00-JUN-87 11:01:35 39.97 RHI DBZ

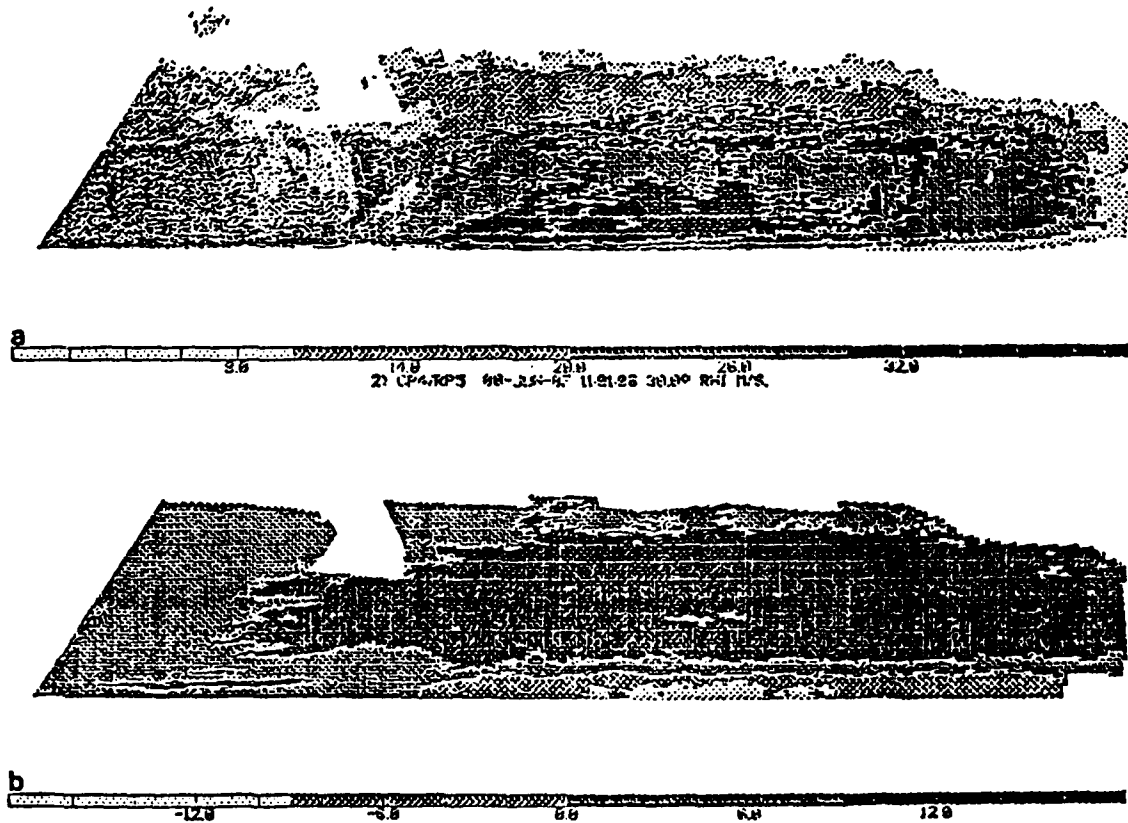


Fig. 25. RHI scan of reflectivity and radial velocity from the NCAR CP-4. (a) is reflectivity and (b) radial velocity for 30 degrees azimuth and 110108 LST. Range marks on the velocity display are in increments of 10 km. Scales are given at the bottom of each figure.

height. At the leading edge of the front, the reflectivity pattern indicates that a precipitation appears to be forming, as reflectivities greater than 30 dBZ are seen. A few kilometers behind the leading edge of the front, a well-developed core of 34 dBZ is seen at the 1.8 km height. To the right (toward the rear of the front) the echo weakens. This agrees with the findings of Houze (1977) who stated that new cells form at the leading edge of a line and mature cells move toward the rear of the echo pattern, where they dissipate. Between 20 and 30 km range, the echoes (greater than 20 dBZ) appear to curve toward the radar with decreasing height. This is caused by precipitation falling through a flow regime that is initially away from the radar into a flow regime towards the radar.

Figure 25 is taken along the 30° azimuth at 1100 LST. The reflectivity bright-band is clearly evident. There are several cores (32 dBZ or greater) behind the front. At lower heights, these cores merge into one echo. It is the upward extending sections of greater than 32 dBZ, separated by reflectivities of less than 32 dBZ, that indicate that this is a multicelled system. Again, the cells appear to form at the leading edge of the front, increase in intensity just behind the leading edge of the front, and then weaken as they move toward the rear. In Fig. 25, the front is 17.5 km from the radar, and as in Fig. 24 the maximum velocities seen are  $15 \text{ ms}^{-1}$  toward the radar, and  $16 \text{ ms}^{-1}$  away from the radar. In both Figs. 24 and 25 the maximum velocity are also behind the most intense and/or largest reflectivity cores.

The RHI scan at 1258 LST is depicted in Fig. 26. By this time the front has moved south of the NCAR CP-4 radar, and the orientation (at  $210^\circ$ ) of the figure is reversed from the previous RHI scans. The view is from behind the front toward the leading edge, which is almost 40 km from the radar. In this figure, small cells form at the leading edge of the front, and grow toward the rear of the front. It is also observed in Fig. 26 that the precipitation trajectories curve as they approach the ground. The maximum horizontal wind speed toward the radar  $16 \text{ ms}^{-1}$  is the same the maximum behind the front (flow away from the radar). The very leading edge of the front is nearly vertical in Fig. 26. Given this time and figure orientation, this blunt front coincides with island elevations greater than 1.0 km in height. In Figs. 24 and 25, the front is over water or island elevations less than 1.0 km in height. In these figures, the leading edge of the front is slightly tilted. Whenever the front was over water or island terrain elevations of less than 1.0 km the leading edge of the front had a slight slope. When the front's leading edge was in an area where the elevations exceeded 1.0 km it appeared nearly vertical.

### 3.3 VAD Analysis

The Velocity Azimuth Display (VAD) analysis used data from the NCAR CP-4 radar for times from 1052 LST to 1329 LST. All analyses used an antenna elevation of  $1.8^\circ$ . Slant ranges of 5.0 km, 10.1 km, 19.8 km, and 29.9 km were examined, although not all of these ranges were examined at each time. The VAD circles were designed so that the VAD circle did not cut through the front. Products

1) CP4/RP5 68-JUN-87 12:58:38 210.00 RHI DBZ

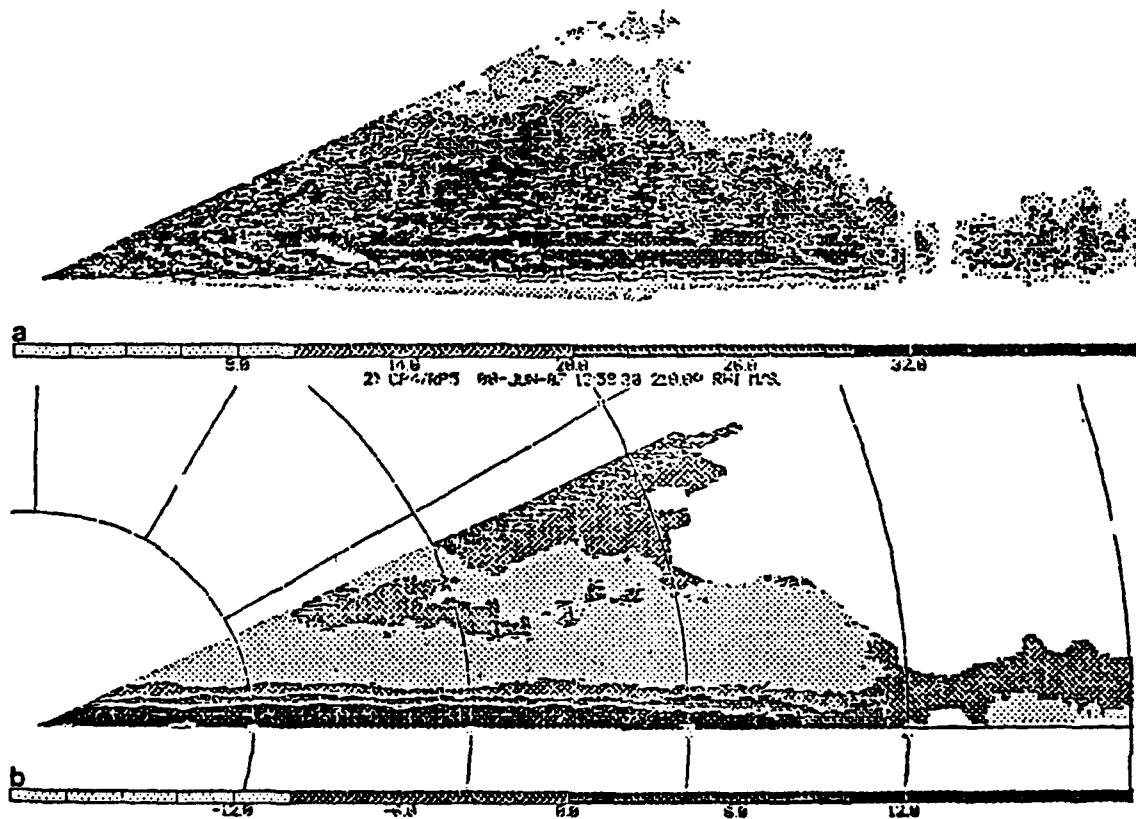


**Fig. 26.** RHI scans of reflectivity and radial velocity. Radar is NCAR CP-4. (a) is reflectivity and (b) is radial velocity, both at 210 degrees azimuth at 125830 LST. Scales are given at the bottom of each figure. Range marks on the velocity display are in increments of 10 km.

from this type of analysis include wind direction and speed, convergence, stretching (dilatation) and shearing deformation. Prior to discussion of the VAD results, a brief overview of these deformations is given.

In the lower atmosphere, values of dilatation and wind shear are typically of the order  $10^{-4}$ – $10^{-5} \text{ s}^{-1}$ . Larger values are often found with strong winds and/or smaller scales. Correspondingly, larger scales and/or light winds may decrease typical values by an order of magnitude. A stretching deformation field has two characteristic axes, one toward which the streamlines converge asymptotically (the axis of dilatation) and one from which the streamlines diverge asymptotically (the axis of contraction). Positive values of deformation give the X axis as the axis of dilatation, and Y as the axis of contraction. If the deformation value is negative the axes are reversed. In a pure deformation field a parcel of air is stretched along the axis of dilatation and compressed along the axis of contraction. The shearing deformation field resembles the stretching deformation field, except that the axes of shearing deformation are rotated with respect to those of stretching deformation. If the shearing value is positive then shear axes are  $45^\circ$  to the left of the axes of stretching deformation. If the shear value is negative the axes are  $45^\circ$  to the right. The air parcels are distorted through the wind field differences in shear. These two types of deformation are combined into the total deformation, which is located around one set of deformation axes (See Appendix D). Deformation is a primary factor in frontogenesis. To a first approximation, frontogenesis occurs when the

angle between the axis of dilatation and potential isotherms is less than  $45^\circ$ . If the angle is greater than  $45^\circ$ , then frontolysis occurs.

The VAD analysis at 1052 LST is given by Figs. 27a-d. The VAD observations are given by Fig. 27a. In all of the VAD plots, observed velocities are represented by crosses, the mean and first harmonic are drawn with a heavy line, and the thin line represents the mean plus the first and second harmonics. The value of deformation is  $3.7 \times 10^{-4} \text{ s}^{-1}$  at an angle of  $-56^\circ$ . For all times, the deformation was the greatest for the 5.0 km distance. This is partly due to the effects of the scale, as mentioned previously. Data from the 10.1 km VAD circle (Fig. 27b) give a reduced deformation of  $3.9 \times 10^{-5} \text{ s}^{-1}$ . When the VAD circle is expanded to 19.8 km (note: all VAD distances are slant range measurements) the deformation increases (compared to 10.1 km) to a value of  $1.2 \times 10^{-5} \text{ s}^{-1}$ . At this time, weak divergence ( $0.3 \times 10^{-4} \approx 1.7 \times 10^{-4} \text{ s}^{-1}$ ) is found in the 5.0 km, 10.1 km and 19.8 km VAD circles, and weak convergence ( $1.5 \times 10^{-5} \text{ s}^{-1}$ ) is found in the 29.9 km VAD circle. 40 minutes later, at 1132 LST, the wind field as seen by the VAD analysis changed drastically. The wind shifted nearly  $180^\circ$ . VAD circles show strong convergence ( $2.4 \times 10^{-4} \approx 10^{-3} \text{ s}^{-1}$ ) and deformation ( $8.7 \times 10^{-4} \approx 1.8 \times 10^{-3} \text{ s}^{-1}$ ). All these indicate that the front had just passed the radar site.



*Fig. 27a. PPI scans of reflectivity (left) and velocity (right) from the NCAR CP-4 at 1052. Elevation angle is 1.8°. Scales are given at the bottom of each figure.*

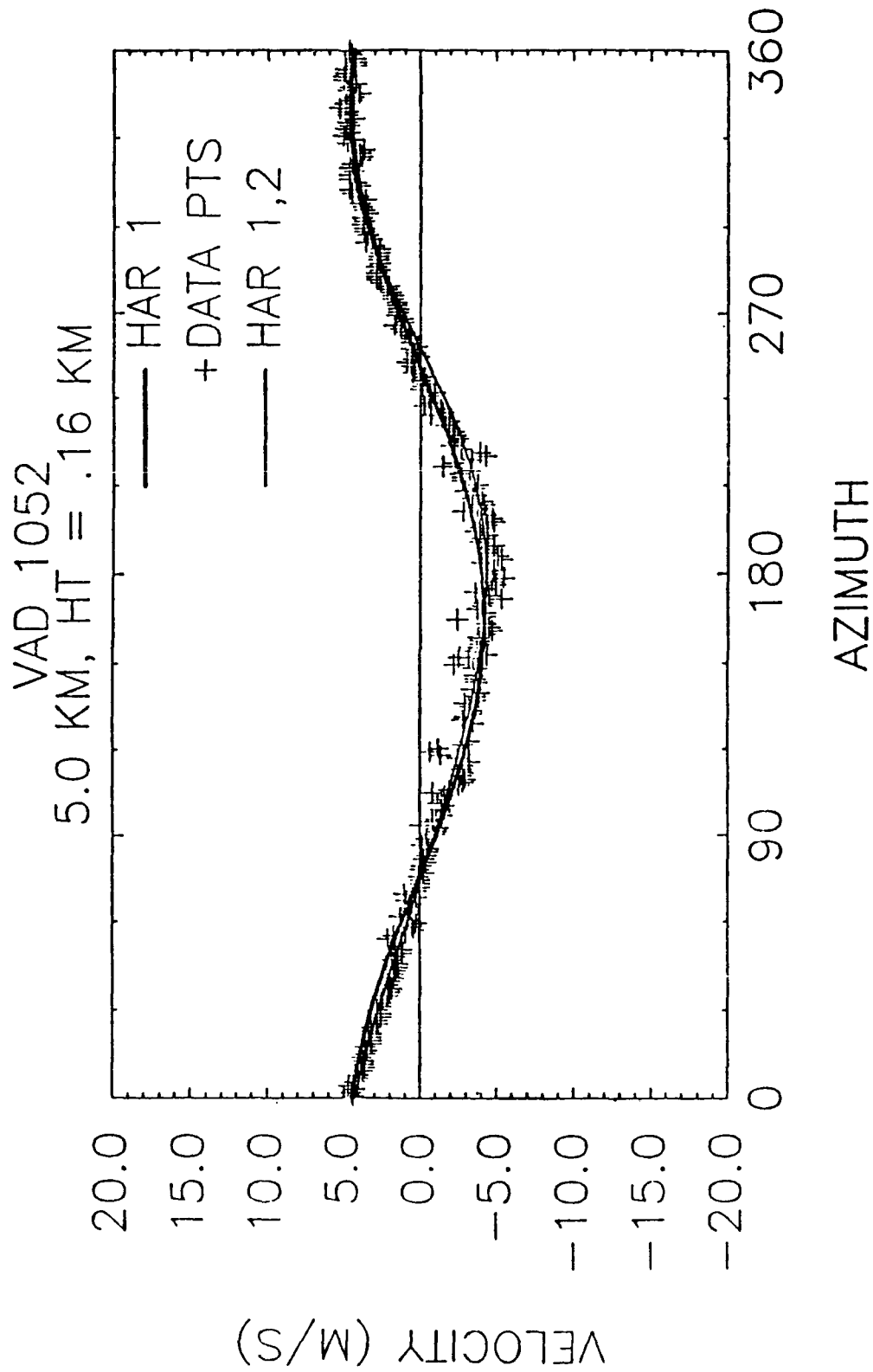


Fig. 27b. VAD at 1052. Range is 5.0 km. Raw velocity values are given by the crosses, first harmonic by the heavy line, and the first and second harmonics together are given by the thin line.

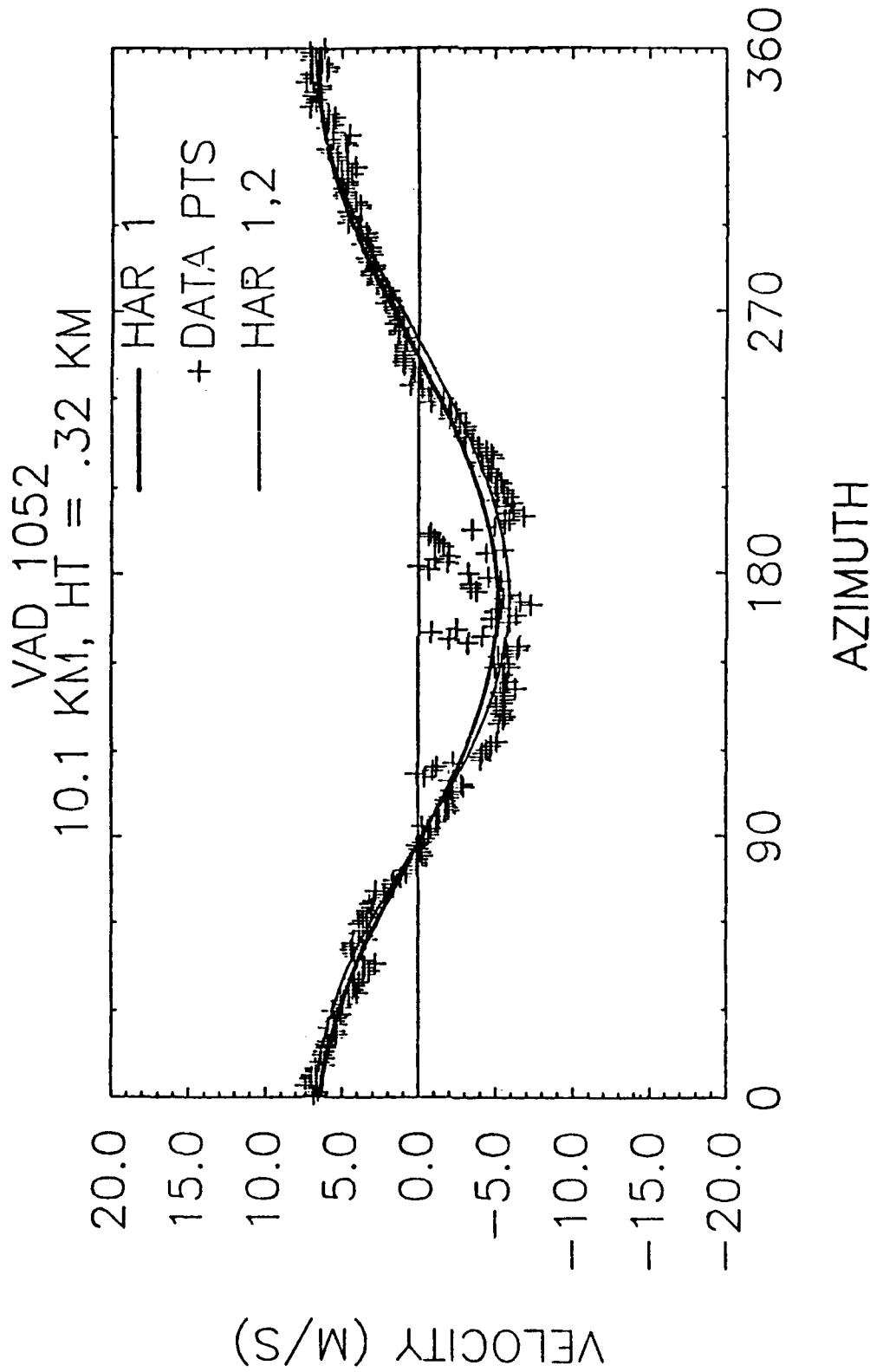


Fig. 27c. VAD at 1052. Range is 10.1 km. Raw velocity values are given by the crosses, first harmonic by the heavy line, and the first and second harmonics together are given by the thin line.

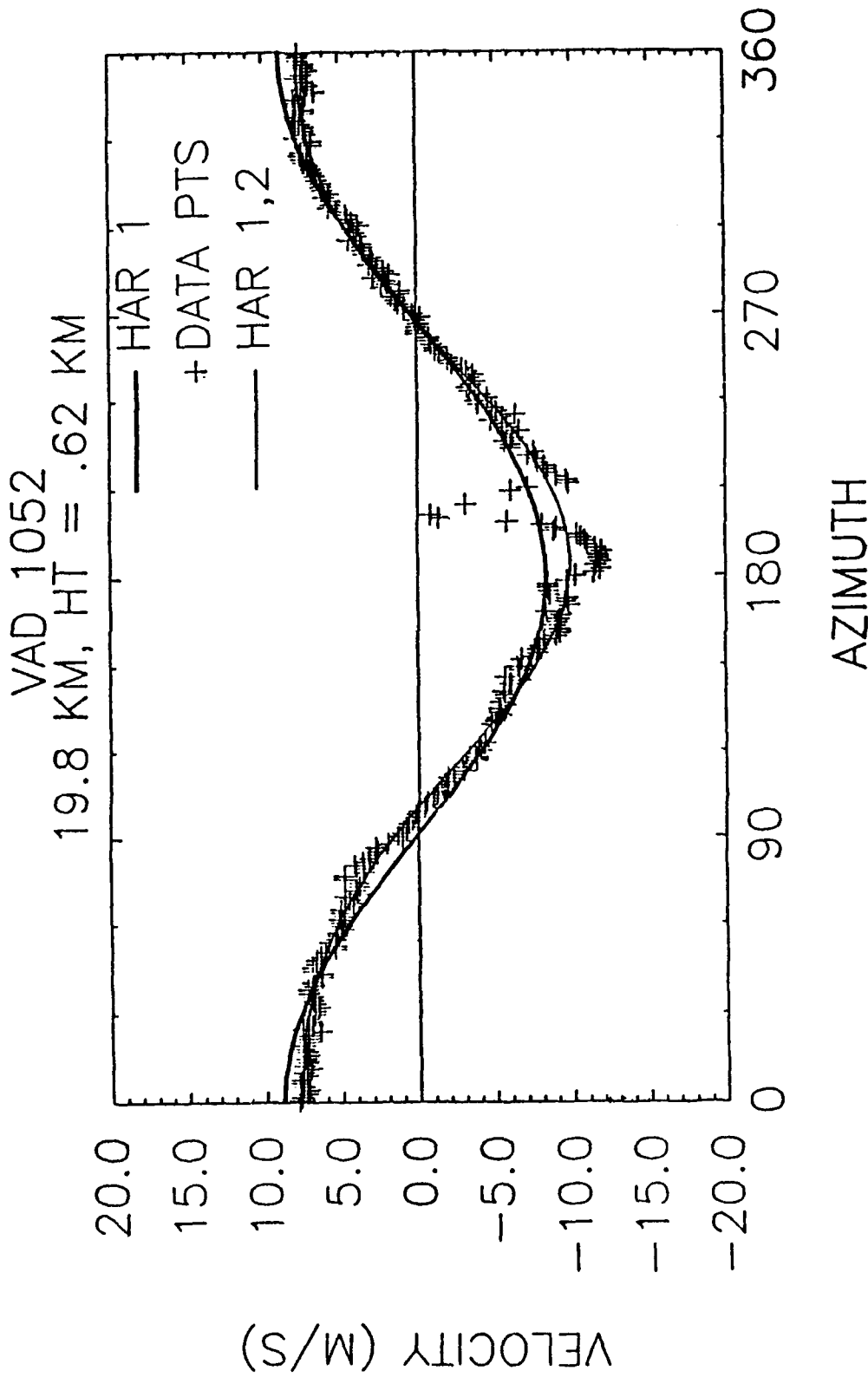


Fig. 27d. VAD at 1052. Range is 19.8 km. Raw velocity values are given by the crosses, first harmonic by the heavy line, and the first and second harmonics together are given by the thin line.

In Fig. 28a, the radar image for 1152 LST is given. All VAD circles still show convergence, but the magnitude is smaller than 20 minutes ago ( $2.6 \times 10^{-4} \approx 4.2 \times 10^{-4} \text{ s}^{-1}$ ). Deformation is also weaker ( $8.2 \times 10^{-4} \approx 1.2 \times 10^{-3} \text{ s}^{-1}$ ).

The radar image and VAD analysis at 1230 LST are depicted in Figs. 29a-d. The VAD circles were done at 5.0 km, 10.1 km, 19.8 km (Figs. 29b, 29c, and 29d, respectively). Similar wind fields were found at 1249 LST, which is depicted by Fig. 30a (the radar image), and Figs. 30b-d (the VAD circles). The VAD circles at 5.0, 10.1 and 19.8 km still show convergence, but the VAD circle at 29.9 km now shows very weak divergence ( $6.0 \times 10^{-8} \text{ s}^{-1}$ ) which would grow to  $2.5 \times 10^{-6}$  at 1329 LST. It was observed that in these VAD circles, the values obtained, with the given scale, are analogous to those found by Saucier (1965).



*Fig. 28a. PPI scans of reflectivity (left) and velocity (right) from the NCAR CP-4 at 1152. Elevation angle is  $1.8^\circ$ . Scales are given at the bottom of each figure.*

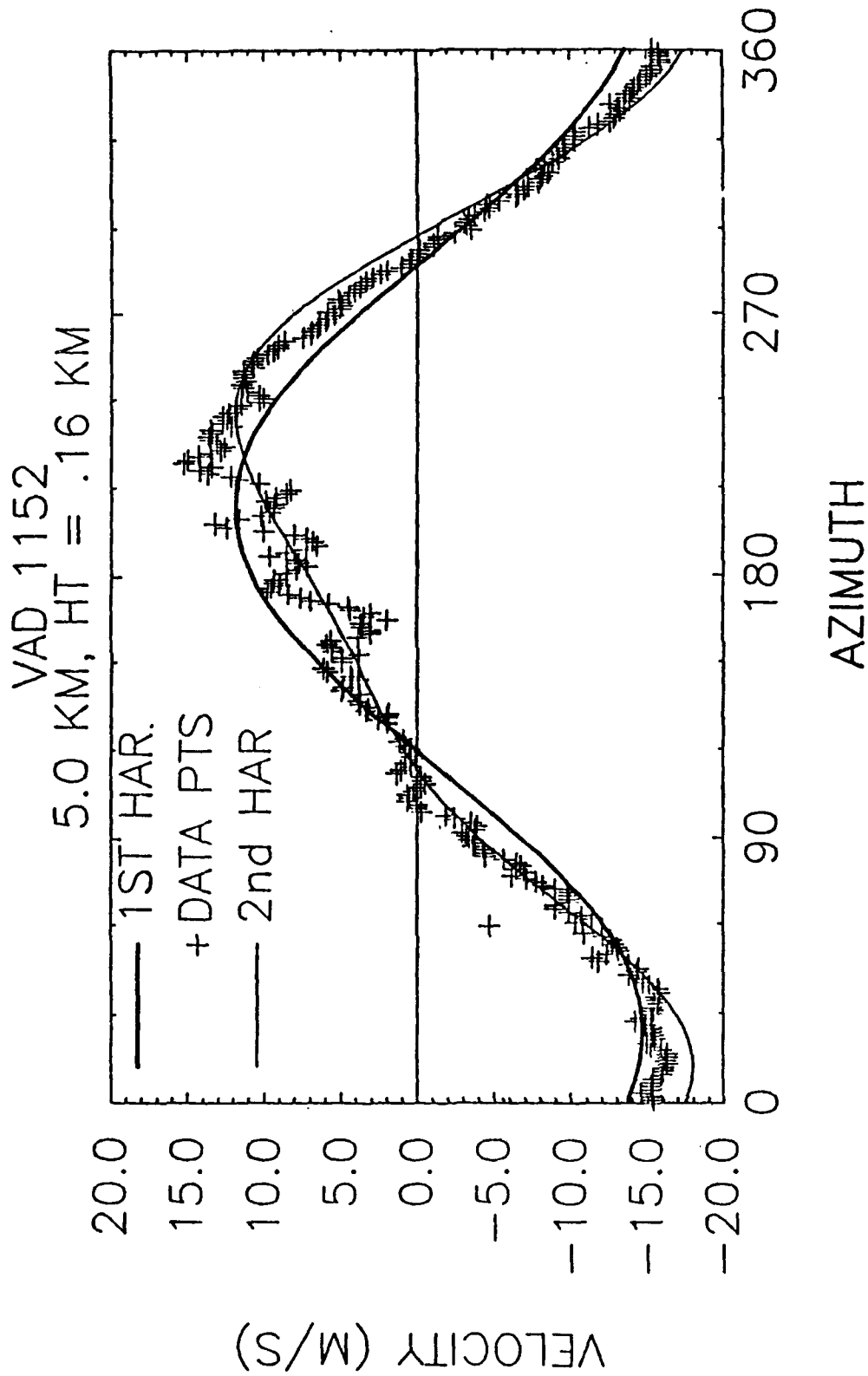


Fig. 28b. VAD at 1152. Range is 5.0 km. Raw velocity values are given by the crosses, first harmonic by the heavy line, and the first and second harmonics together are given by the thin line.



*Fig. 29a. PPI scans of reflectivity (left) and velocity (right) from the NCAR CP-4 at 1230. Elevation angle is  $1.8^\circ$ . Scales are given at the bottom of each figure.*

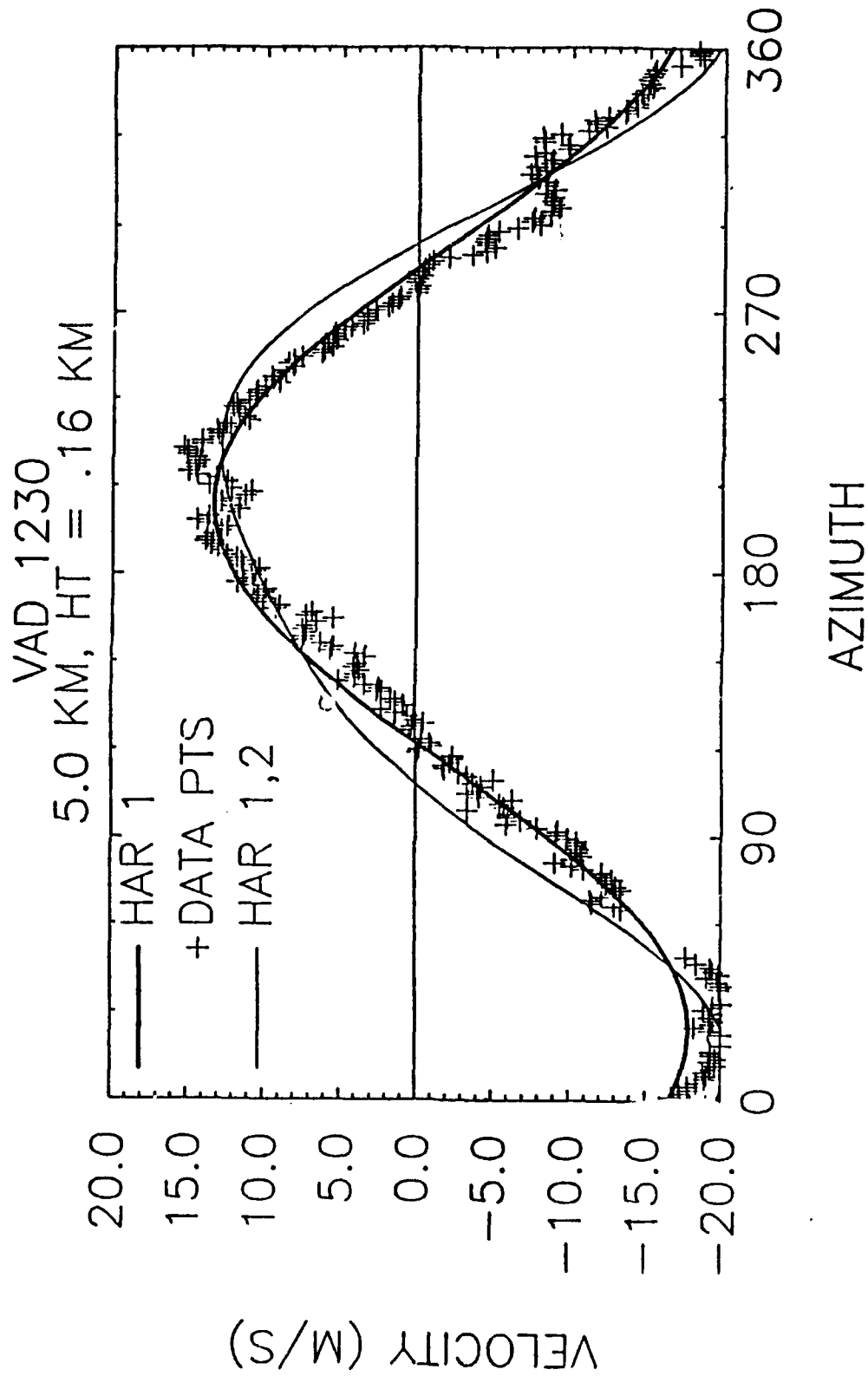


Fig. 29b. VAD at 1230. Range is 5.0 km. Raw velocity values are given by the crosses, first harmonic by the heavy line, and the first and second harmonics together are given by the thin line.

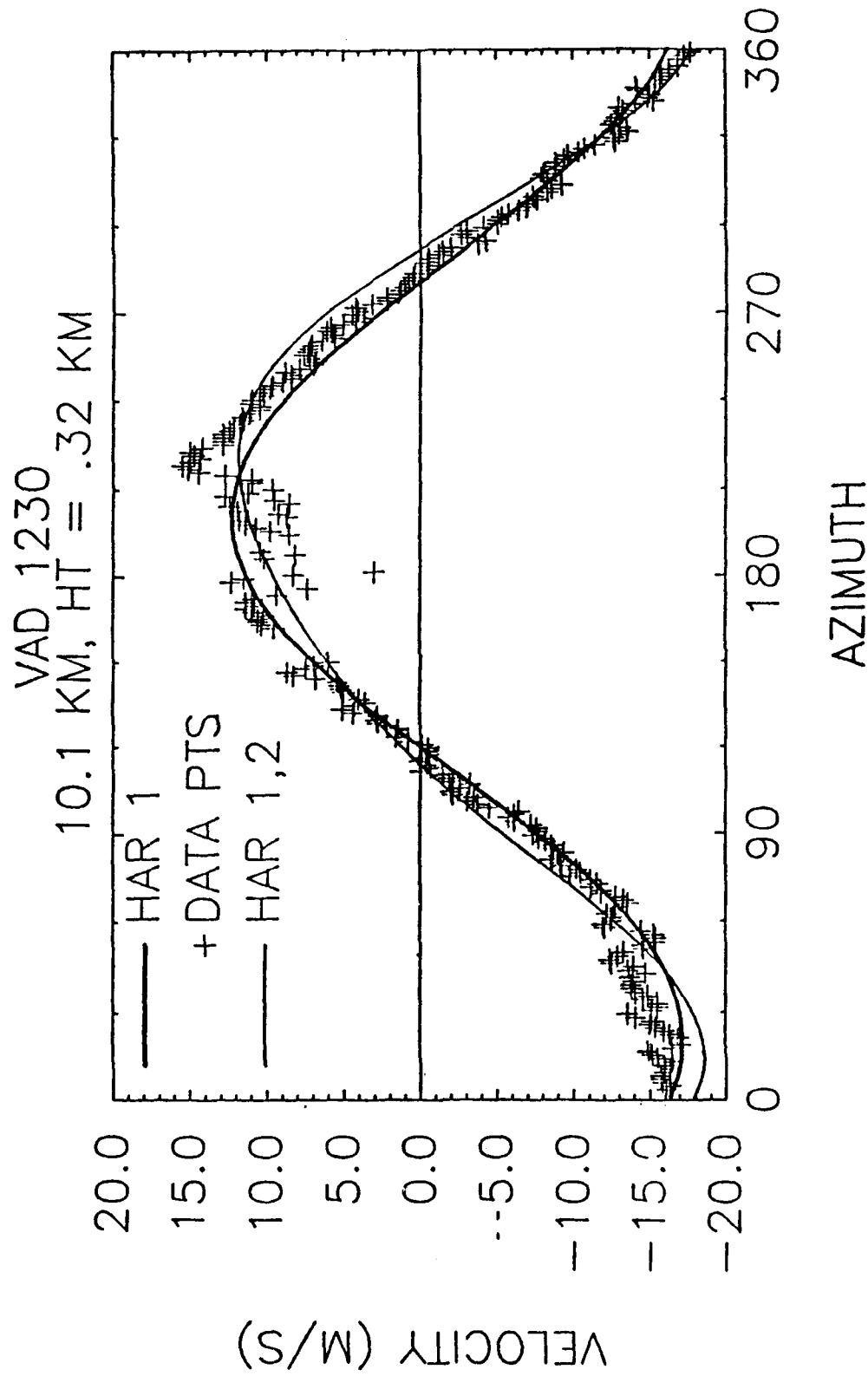


Fig. 29c. VAD at 1230. Range is 10.1 km. Raw velocity values are given by the crosses, first harmonic by the heavy line, and the first and second harmonics together are given by the thin line.

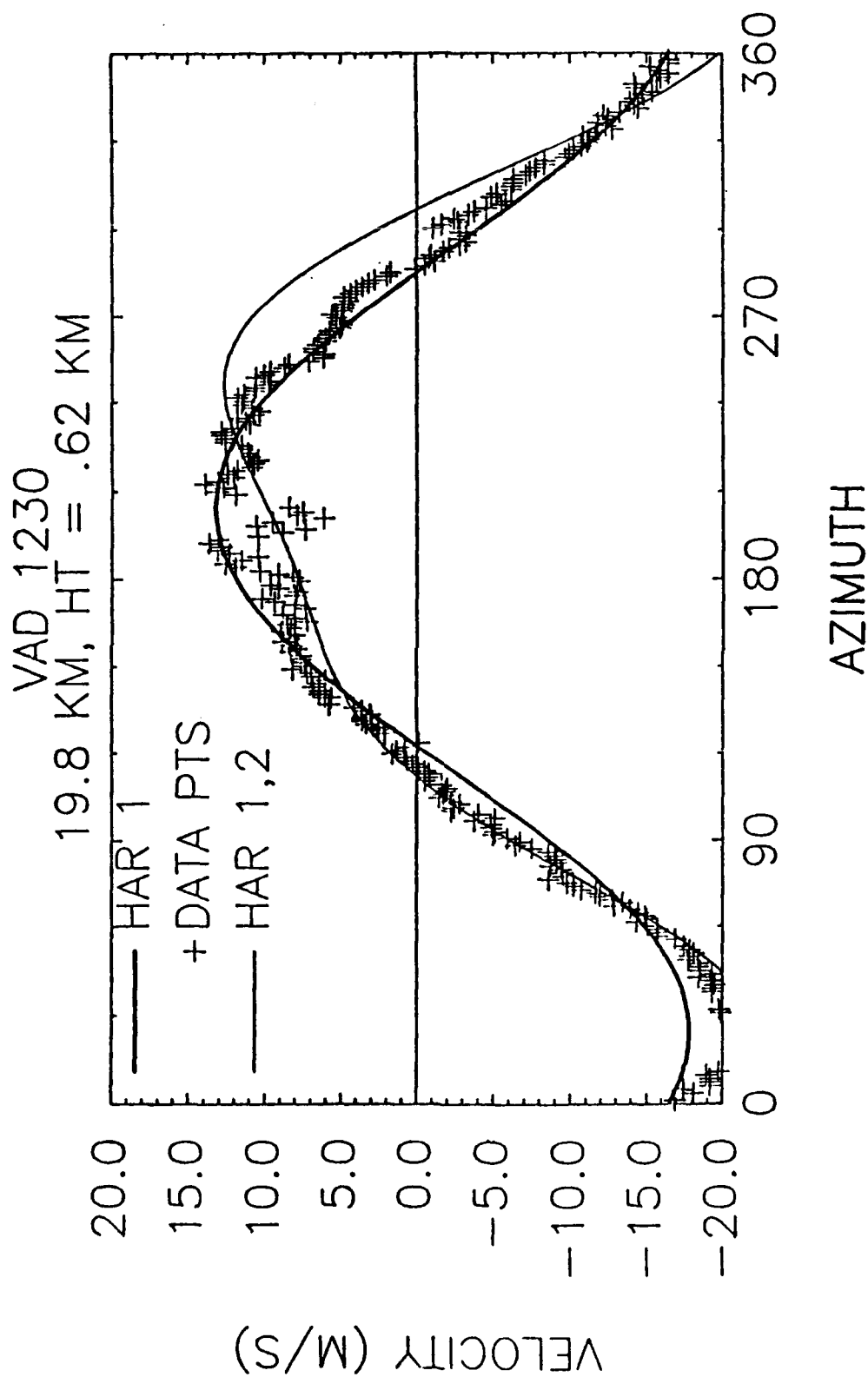


Fig. 29d. VAD at 1230. Range is 19.8 km. Raw velocity values are given by the crosses, first harmonic by the heavy line, and the first and second harmonics together are given by the thin line.



*Fig. 30a. PPI scans of reflectivity (left) and velocity (right) from the NCAR CP-4 at 1249. Elevation angle is 1.8°. Scales are given at the bottom of each figure.*

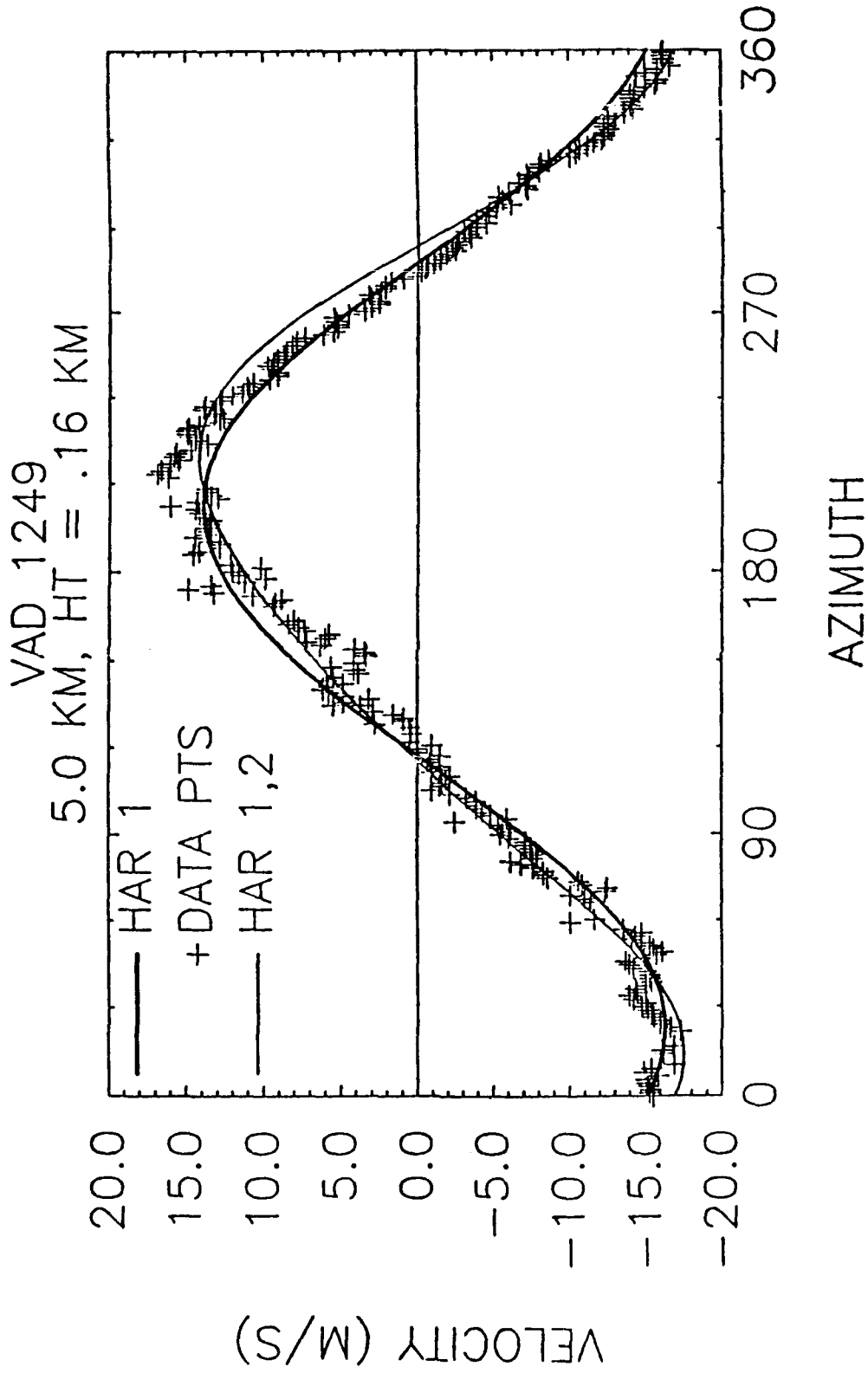


Fig. 90b. VAD at 1249. Range is 5.0 km. Raw velocity values are given by the crosses, first harmonic by the heavy line, and the first and second harmonics together are given by the thin line.

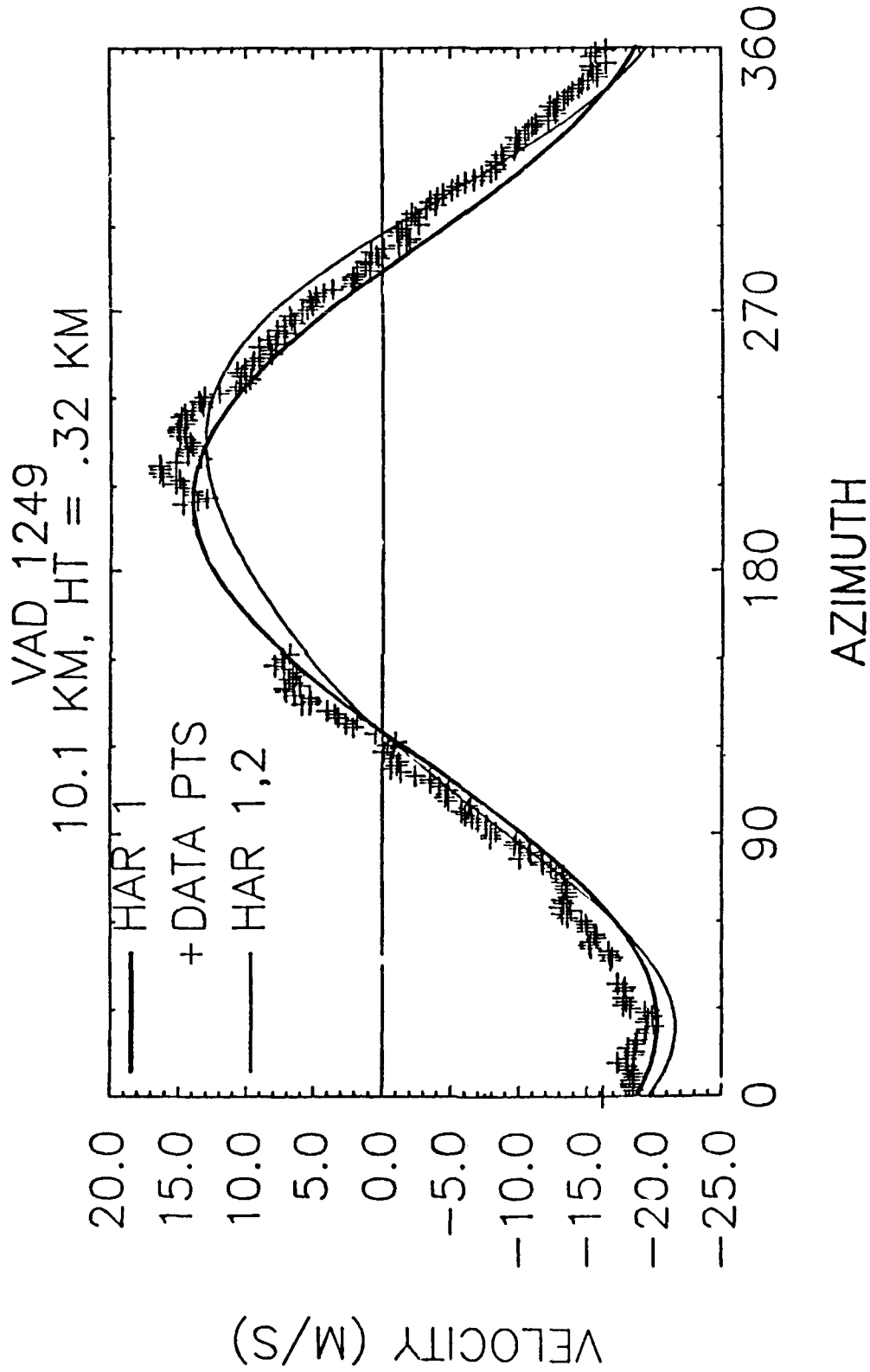


Fig. 30c. VAD at 1249. Range is 10.1 km. Raw velocity values are given by the crosses, first harmonic by the heavy line, and the first and second harmonics together are given by the thin line.

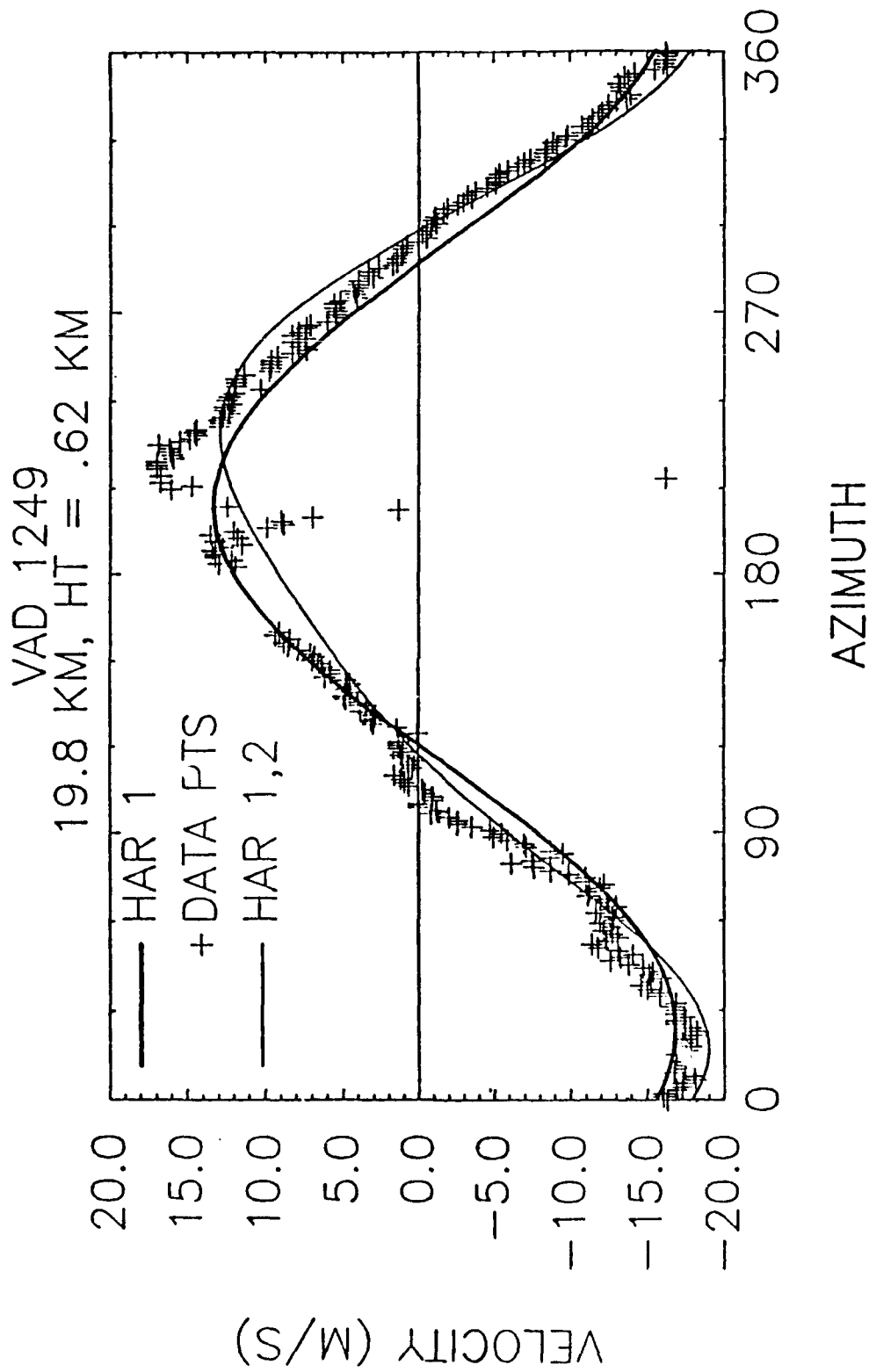
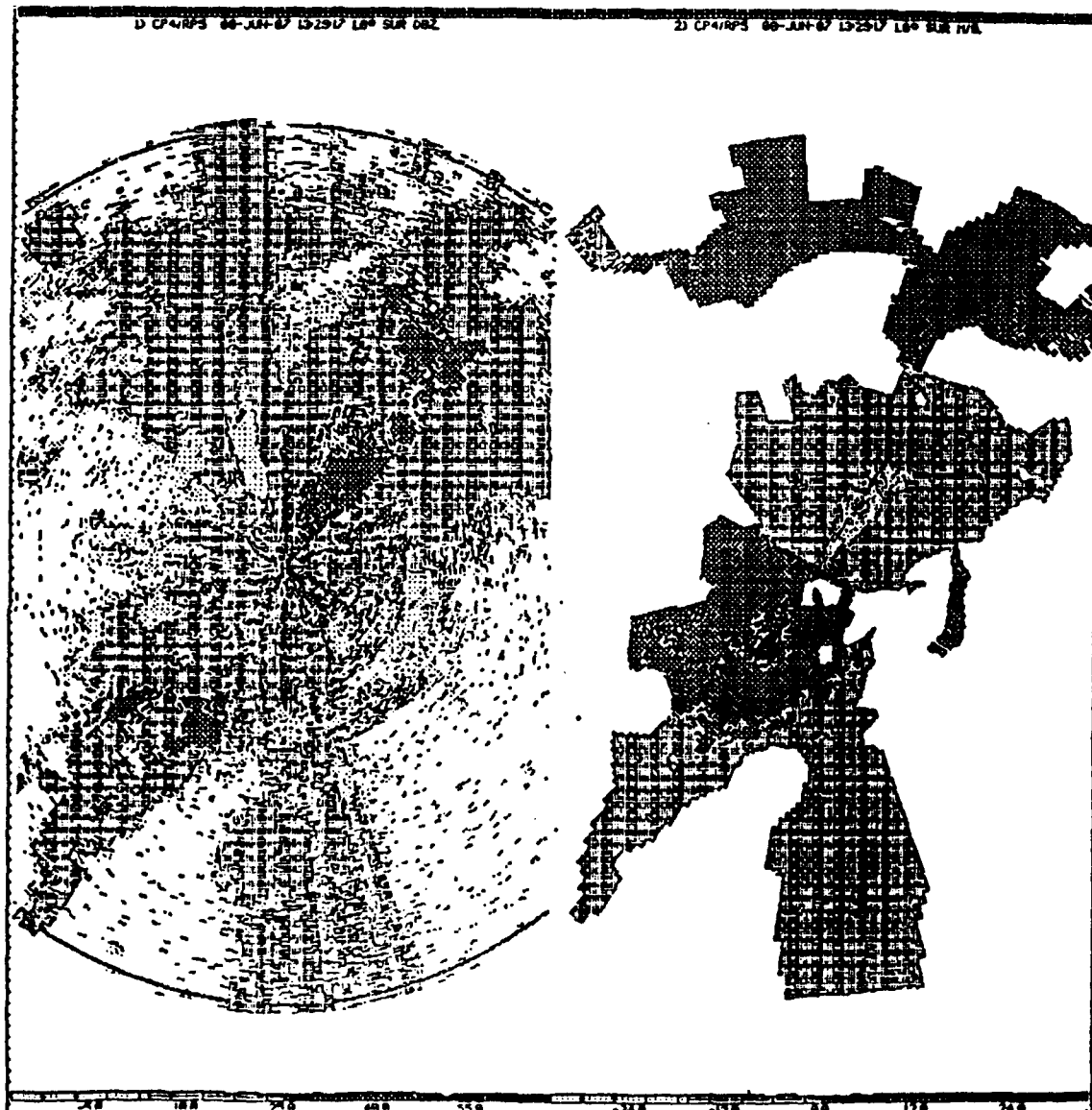
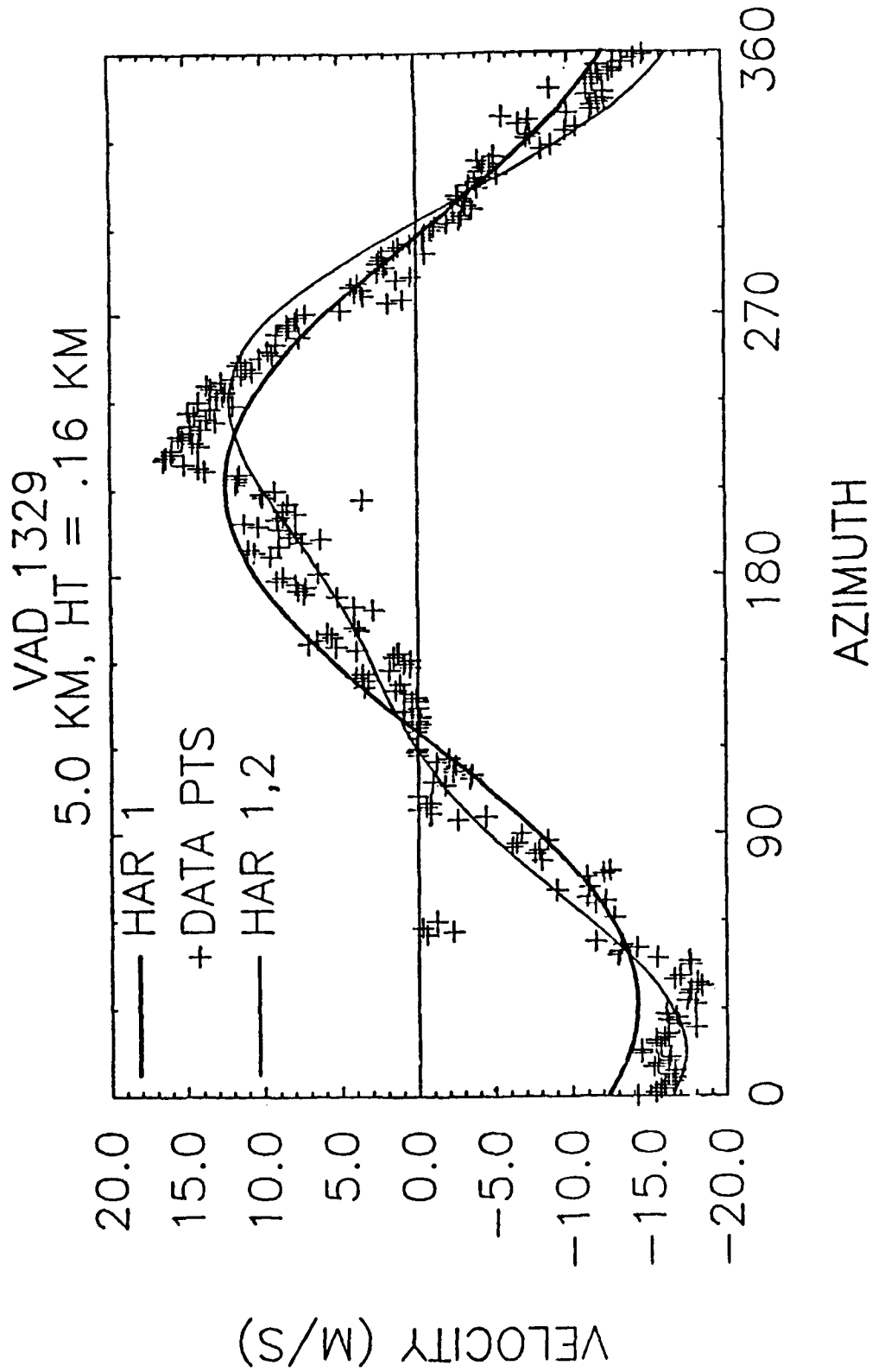


Fig. 30d. VAD at 1249. Range is 19.8 km. Raw velocity values are given by the crosses, first harmonic by the heavy line, and the first and second harmonics together are given by the thin line.



*Fig. 31a. PPI scans of reflectivity (left) and velocity (right) from the NCAR CP-4 at 1329. Elevation angle is 1.8°. Scales are given at the bottom of each figure.*



*Fig. 91b. VAD at 1329. Range is 5.0 km. Raw velocity values are given by the crosses, first harmonic by the heavy line, and the first and second harmonics together are given by the thin line.*

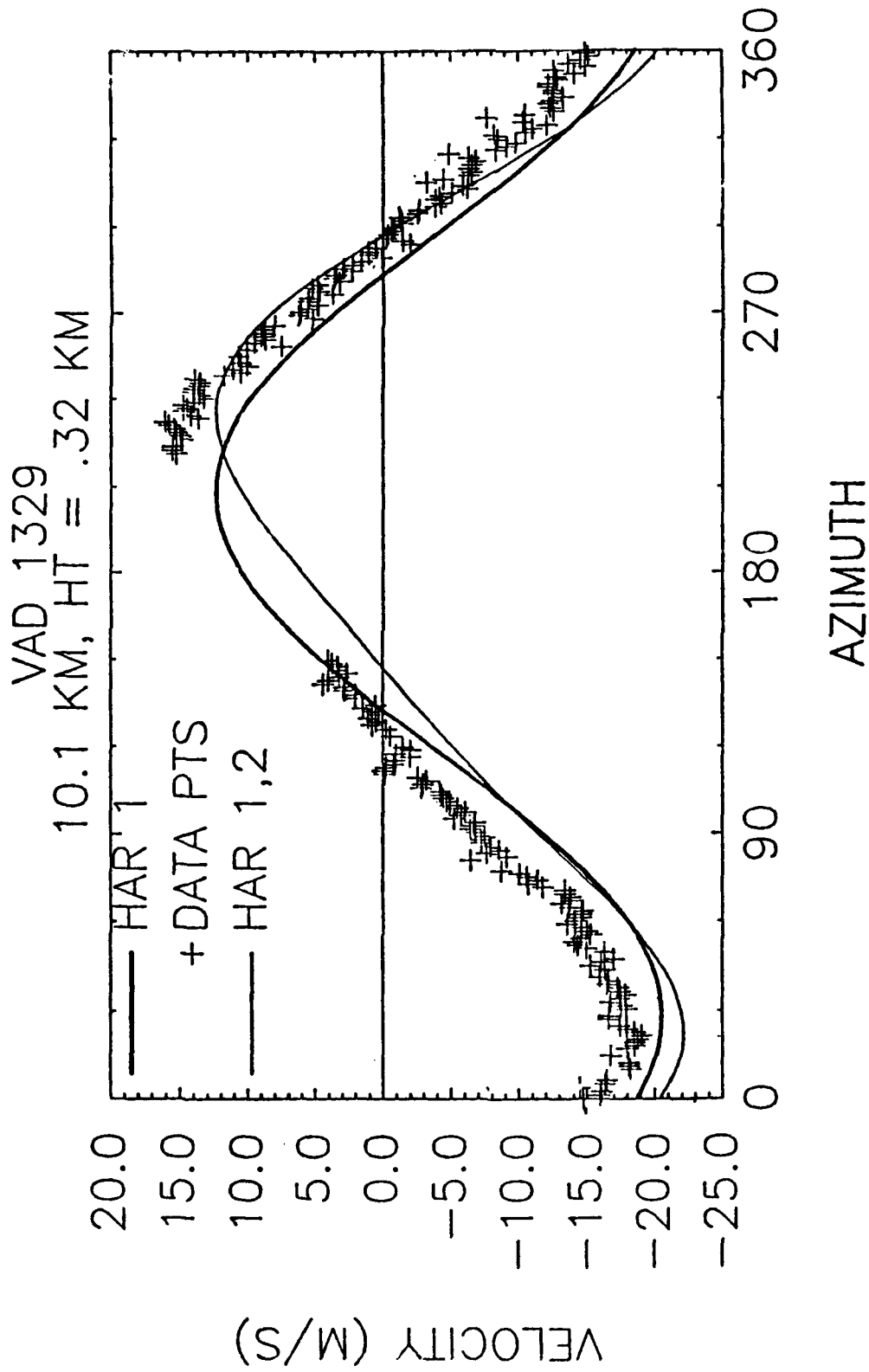


Fig. 91c. VAD at 1329. Range is 10.1 km. Raw velocity values are given by the crosses, first harmonic by the heavy line, and the first and second harmonics together are given by the thin line.

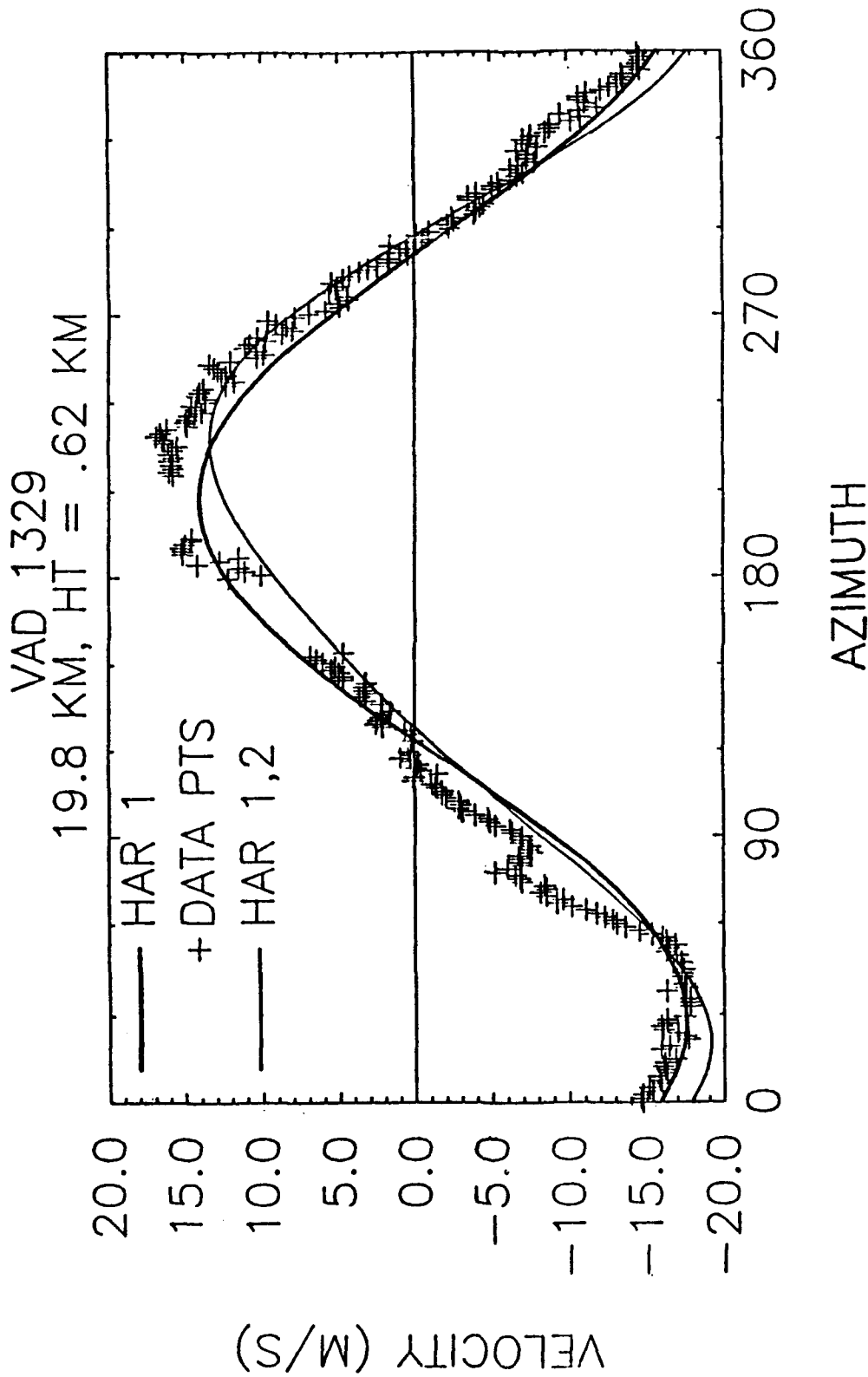


Fig. 31d. VAD at 1329. Range is 19.8 km. Raw velocity values are given by the crosses, first harmonic by the heavy line, and the first and second harmonics together are given by the thin line.

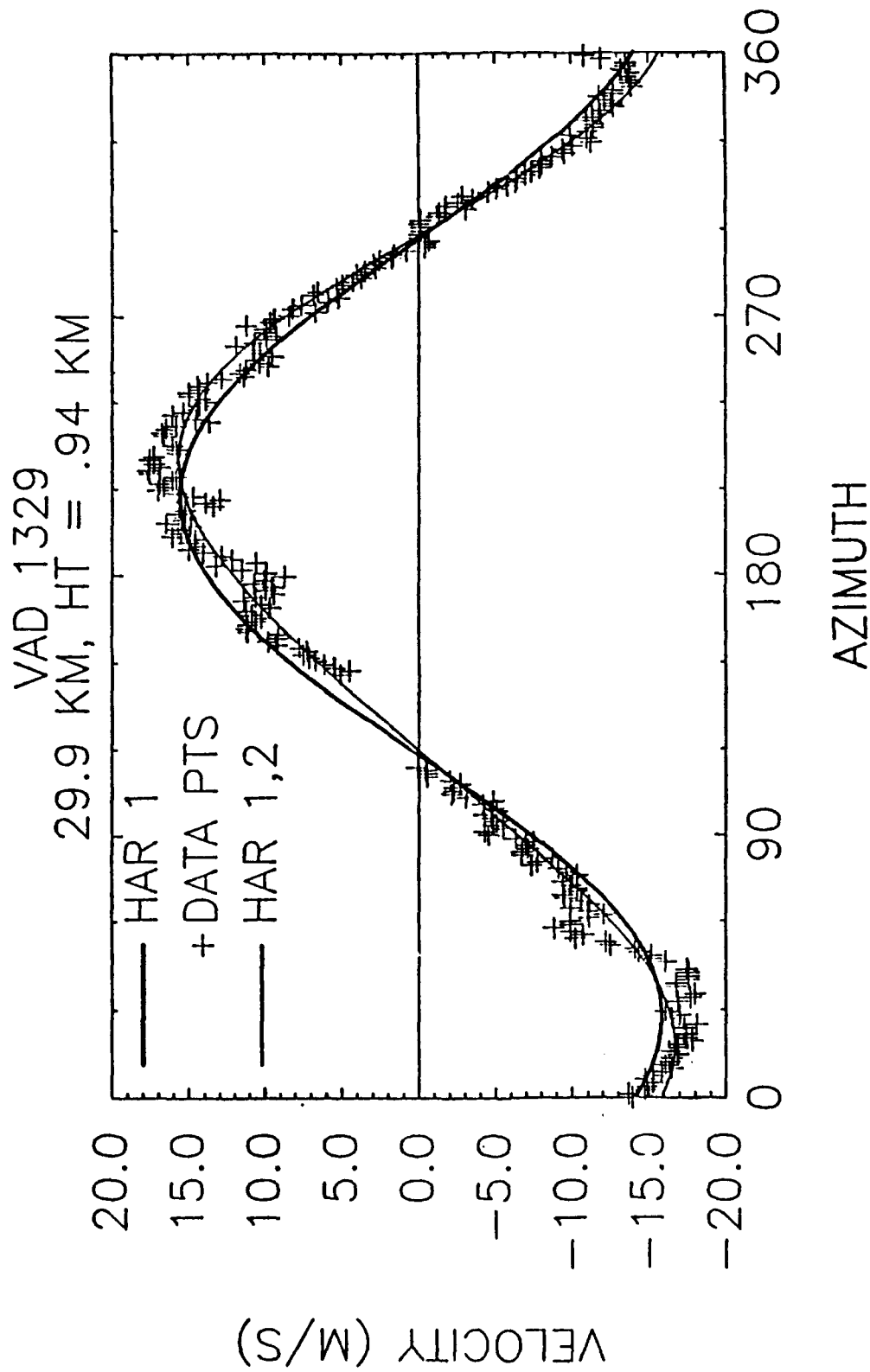


Fig. 31e. VAD at 1329. Range is 29.9 km. Raw velocity values are given by the crosses, first harmonic by the heavy line, and the first and second harmonics together are given by the thin line.

## Chapter 4

### Conclusions

#### 4.1 Conclusions

This study focuses on a Doppler radar analysis of a June 8, 1986 frontal system from Intensive Operating Period (IOP) #8 of the Taiwan Area Mesoscale Experiment (TAMEX). Data collected from two Doppler radars was used for the analysis. One radar was the National Center for Atmospheric Research (NCAR) CP-4 radar, located at a site known as Waipu Beach. The other Doppler radar, the National Oceanic Atmospheric Administration (NOAA) TOGA radar, was located at the CCK Air Force Base, just west of Taichung, approximately 45 km south of the NCAR radar. Analysis was done from 0820 LST to 1409 LST as the front approached and passed through the radar network. Two types of synthesis were performed with the data set. Dual-Doppler analysis was performed extending over an eight hour period, while Velocity Azimuth Displays (VAD) (single Doppler analysis) was performed for times when the front was in the vicinity of the NCAR radar. Also several vertical cross-sections through the front were examined.

The first set of radar echoes entered the analysis domain at 0820 LST. These echoes were observed in the southwestern portion of the analysis domain and they moved toward the northeast at approximately  $12 \text{ ms}^{-1}$ , driven by the synoptic scale

southwesterly winds and the sharpening mesoscale ridge as analyzed by Trier *et al.* (1989). At 1052 LST, the front was north of the analysis domain. The front was first observed in the 1132 LST analysis. It was diagnosed as an anafont. It propagated south, moving more rapidly over water (up to approximately  $12 \text{ ms}^{-1}$ ) than over land. Further, when the front moved over the island, it became virtually stationary. This position of the front was approximately co-located with the area of the island where the elevations exceeded 1.0 km. Thus, it appears that the higher island elevations served to block the front. This concept led to further examination of the front. In the dual-Doppler analyses, the front was only distinguishable for levels below 1.0 km level. This was verified in both the cross-sections of the dual-Doppler analysis and in the RHI scans taken through the front. Vertical depth of the front was estimated at 1.57 km. During the time the front traveled through the radar grid, the echo pattern occasionally showed a "T" pattern in which the front would be the cross of the "T". The stem of the "T" was formed by confluence between the mesoscale ridging and the synoptic scale trough. An intense echo was observed at the intersection of the "T", at what was referred to as the "triple point". This was at the intersection of the front and the ridge-trough confluence line.

Examination of the echoes and their cores revealed that several cells were always present. Since these cells were not always in the same place, it is suggested that the cells are relatively intense and have short lifetimes. Over the low elevations and the water, the cells were observed to increase in size with height. The maximum

areal extent was reached at the 2.0 km height. Above this, the cores decreased in size, with the noted exception of an occasional abrupt increase in expanse at the 5.0 km height. This was caused by radar brightbanding effects, and verified by the NCAR RHI scans, where the the freezing level was approximated at the 4.75 km height. For cells over the elevations greater than 1.0 km, the echoes followed the same height to size pattern, except these echoes reached maximum expanse at the 4.0 km level. Thus, it is observed that the echoes reached their maximum size approximately 2.0 km above ground level. On the average, the echoes were most often observed to reach maximum height between the 6.0 km and 7.0 km height.

VAD analysis revealed that prior to frontal passage, deformation favorable to frontogenesis was observed. Further, the deformation after the front passage was of a frontolytic condition. The winds ahead of the front were southerly, less than  $10.0 \text{ ms}^{-1}$  and veered with height, indicating warm air advection. Winds behind the front were northeasterly and had an approximate speed of  $17 \text{ ms}^{-1}$ . Prior to frontal passage, weak convergence was observed. After the front passes, the VAD circles revealed general divergence.

It was observed that the echoes associated with the front formed at the leading edge and moved towards the rear as they matured. This agrees with previous studies in both the tropics and in the mid-latitudes.

## REFERENCES

- Barry, R., and R. Chorley, 1982: Atmosphere, weather, and climate. Methuen and Co., London, 166-167.
- Bergeron, T., 1954: The problem of tropical hurricanes. *Quart. J. Meteor. Soc.*, **80**, 131-164.
- Bluestein, H. and E. Berry, 1982: The formation of severe thunderstorms at the intersection of a dryline and a front: The role of frontogenesis. *Preprints of the Twelfth Radar Conf.*, 597-602.
- Browning, K., and T. Harrold, 1970: Air motion and precipitation growth at a cold front. *Quart J. R. Met. Soc.*, **96**, 369-389.
- Browning, K., and R. Wexler, 1968: The determination of kinematic wind field properties using Doppler Radar. *J. Appl. Meteor.*, **7**, 105-113.
- Carbone, R. and R. Serafin, 1979: A Winter Squall line. Part II: Kinematic Structure Deduced from Triple Doppler Radar Observations. *Preprints of the Nineteenth Radar Conf*, A.M.S., Miami, 9-16.
- Chen, G.T.J., and C.C. Yu, 1988: Study of low-level jet and extremely heavy rainfall over northern Taiwan in the *Mon. Wea. Rev.*, **116**, 884-891.
- Cressman, G.P., 1959: An operational objective analysis system. *Mon. Wea. Rev.*, **87**, 367-374.
- Cunning, J., 1978: TAMEX Daily Operations Summary, NCAR/TN-305+STR, Colorado, 361 pp.
- Foote, G.B. and P.S. du Toit, 1969: Terminal velocity of raindrops aloft. *J. Appl. Meteor.*, **8**, 249-253.
- Hane, C, 1986: Extratropical squall lines and rainbands. *Mesoscale Meteorology and Forecasting*, P. Ray editor, A.M.S., 359-389

- Hobbs, P., T. Matejka, P. Herzegh, J. Locatelli, and R. Houze, 1980: The Mesoscale and Microscale Structure and Organizations of Clouds and Precipitation in Midlatitude Cyclones. I: A Case Study of a Cold Front *J. Atmos. Sci.*, **37**, 568-596.
- Houze, R. A., 1977: Structure and dynamics of a tropical squall line system. *Mon. Wea. Rev.*, **105**, 1540-1567.
- Houze, R. A., and C.P. Cheng, 1977: Radar Characteristics of Tropical Convection Observed During GATE: Mean Properties and Trends Over the Summer Season. *Mon. Wea. Rev.*, **105**, 964-980.
- James, P. K., and K.A. Browning, 1979: Mesoscale Structure of Line Convection at Surface Cold Fronts. *Quart. J. Roy. Meteor. Soc.*, **105**, 371-382.
- Joss, J. and D. Waldvogel, 1970: Raindrop size distribution and Doppler velocities. *Preprints of the Fourteenth Radar Conf*, A.M.S., Tuscon, 153-156.
- Kessinger, C. and H. Bluestein, 1979: The role of deformation at the dryline/front intersection. *Preprints of the Eleventh Radar Conf.*, 91-95.
- Kessler, E. and R. Wexler, 1959: Observations of a Cold Front, 1 October 1958. *Bull. Amer. Meteor. Soc.*, **41**, 253-257.
- Leary, C. and Houze, R. A., 1979: The Structure and Evolution of Convection in a Tropical Cloud Cluster. *J. Atmos. Sci.*, **36**, 437-457.
- Lhermitte, R., and D. Atlas, 1961: Precipitation motion by pulse Doppler. *Preprints of the Ninth Radar Conf.*, 213-223.
- Matejka, T. and Houze, R. A., 1978: Doppler Radar Measurements of the Airflow Within a Mesoscale Cold-Frontal Rainband. *Preprints of the Eighteenth Radar Conf*, A.M.S., Atlanta, 17-22.
- Moore, J. and M. Heggli, 1979: A Winter Squall line. Part I: The Meso-Synoptic Scale Structure *Preprints of the Nineteenth Radar Conf*, A.M.S., Miami, 4-9.
- Newton, C., 1950: Structure and mechanism of the prefrontal squall line. *J. Meteor.*, **7**, 210-222.
- Newton, C., and H. Newton, 1959: Dynamical interactions between large convective clouds and environment with vertical shear. *J. Meteor.*, **16**, 483-496.

- Newton, C., and J. Fankhauser, 1964: On the movements of convective storms, with emphasis on size discrimination in relation to water budget requirements. *J. Appl. Meteor.*, **3**, 651-668.
- Parsons, D., C. Mohr, and T. Gal-Chen, 1987: A severe frontal rainband. Part III: Derived thermodynamic structure. *J. Atmos. Sci.*, **44**, 1615-1631.
- Pedgley, D., 1962: *A meso-synoptic analysis of the thunderstorms on 28 August, 1958*. Geophysical Memoirs No. 106, 14, 74 pp.
- Rabin, R., and D. Zrnic 1980: Subsynoptic-scale vertical wind revealed by dual Doppler radar and VAD analysis. *J. Atmos. Sci.*, **37**, 644-654.
- Ray, P., 1988: Convective dynamics. To appear in *Radar Meteorology*, D. Atlas, Editor, A.M.S., Boston.
- Ray, P., C. Ziegler, W. Bumgarner, and R. Serafin, 1980: Single and multiple Doppler observations of tornadic storms. *Mon. Wea. Rev.*, **108**, 1607-1625.
- Rotunno, R., J. Klemp, and M. Weisman, 1988: A theory for strong, long-lived squall lines. *J. Atmos. Sci.*, **40**, 238-247
- Saucier, W., 1965: *The Principles of Meteorological Analysis*. Chicago Press, Chicago, 438 pp.
- Smull, B., and R. Houze, 1985: A mid-latitude squall line with a trailing region of stratiform rain: Radar and satellite observations. *Mon. Wea. Rev.*, **113**, 117-133.
- Smull, B., and R. Houze, 1987: Dual-Doppler radar analysis of a mid-latitude squall line with a trailing region of stratiform rain. *J. Atmos. Sci.*, **44**, 2128-2148.
- Trier, S., D. Parsons, and T. Matejka, 1989: An observational and numerical study of a subtropical cold front during TAMEX. *Preprints of the Twenty-fourth Radar Conf*, Amer. Meteor. Soc., Tallahassee, 561-564.
- Wang, S.T., 1986: Observational analysis of the interaction between fronts and the orography in Taiwan during the late winter monsoon season. *Proceedings International Conference on Monsoon and Mesoscale Meteorology*, Amer. Meteor. Soc. and Met. Soc. R.O.C., 123-135.

## Appendix A

### Dual-Doppler Radar Synthesis

The synthesis uses two radars in the solution. The dependent variables desired are the components of the wind motion,  $u$ ,  $v$ , and  $w$ . The equation that describes the radar observed velocity is:

$$u(x - x_i) + v(y - y_i) + W(z - z_i) = R_i V_i \quad \text{for } i = 1, 2 \quad . \quad (A1)$$

Here the subscript  $i$  denotes the number of the radars. The point  $(x_i, y_i, z_i)$  denotes the location of the  $i^{\text{th}}$  radar and the point  $(x, y, z)$  is the grid point location. For a given point,  $V_i$  is the measured radial velocity.  $R_i$  is a measure of the range from the radar described by

$$R_i = \left[ (x - x_i)^2 + (y - y_i)^2 + (z - z_i)^2 \right]^{\frac{1}{2}} \quad . \quad (A2)$$

In Eq. A1,  $W$  is the hydrometeor fall speed containing the vertical velocity,  $w$ , and the particle terminal fall speed,  $V_t$ . Thus,  $W$  is described by the equation

$$W = w + V_t \quad . \quad (A3)$$

At this point the unknown variables are  $u$ ,  $v$ ,  $w$ ,  $W$  and  $V_t$ . To reduce the number of unknown variables to obtain a unique solution to these equations, a value

for  $V_t$  is found. This terminal fall speed is found using the Joss and Waldvogel (1970) and the Foote and du Toit (1969) relationships. Foote and du Toit (1969) determined fall speeds using density of the atmosphere. As density increases closer to the ground the fall speed of hydrometer decreases. Joss and Waldvogel (1970) used reflectivity to find the terminal velocity. The higher the value of reflectivity, the higher the value of the terminal velocity. This relation is modified by the Foote and du Toit (1969) density relationship. The relationship between terminal velocity below the 4 km msl levels and reflectivity is expressed

$$V_t = -2.6(Z_e)^{.107} e^{(.4\kappa z)} \quad , \quad (4)$$

where  $Z_e$  is the effective reflectivity factor,  $\kappa$  is the negative of logarithmic rate of change of density with height  $\text{km}^{-1}$ ,  $z$  is the height above mean sea level (in km) at the grid point. Between 4 and 10 km, the relationship for  $V_t$  becomes

$$V_t = -2.6(Z_e)^{.107} e^{(.4\kappa z)} \left[ \frac{(10 - z)}{6} - \frac{(z - 4)}{3} \right] \quad . \quad (A5)$$

Above the 10 km level a value of  $-2 \text{ ms}^{-1}$  is used (See Figure A1).

The boundary condition value of zero for  $w$  is specified at the storm top. The value for  $W$  can be calculated using Eq. A3. Equation 1 is now solved for the remaining unknowns  $u$  and  $v$ , in terms of  $W$ . At radar #1,  $i = 1$ , and Eq. 1 becomes

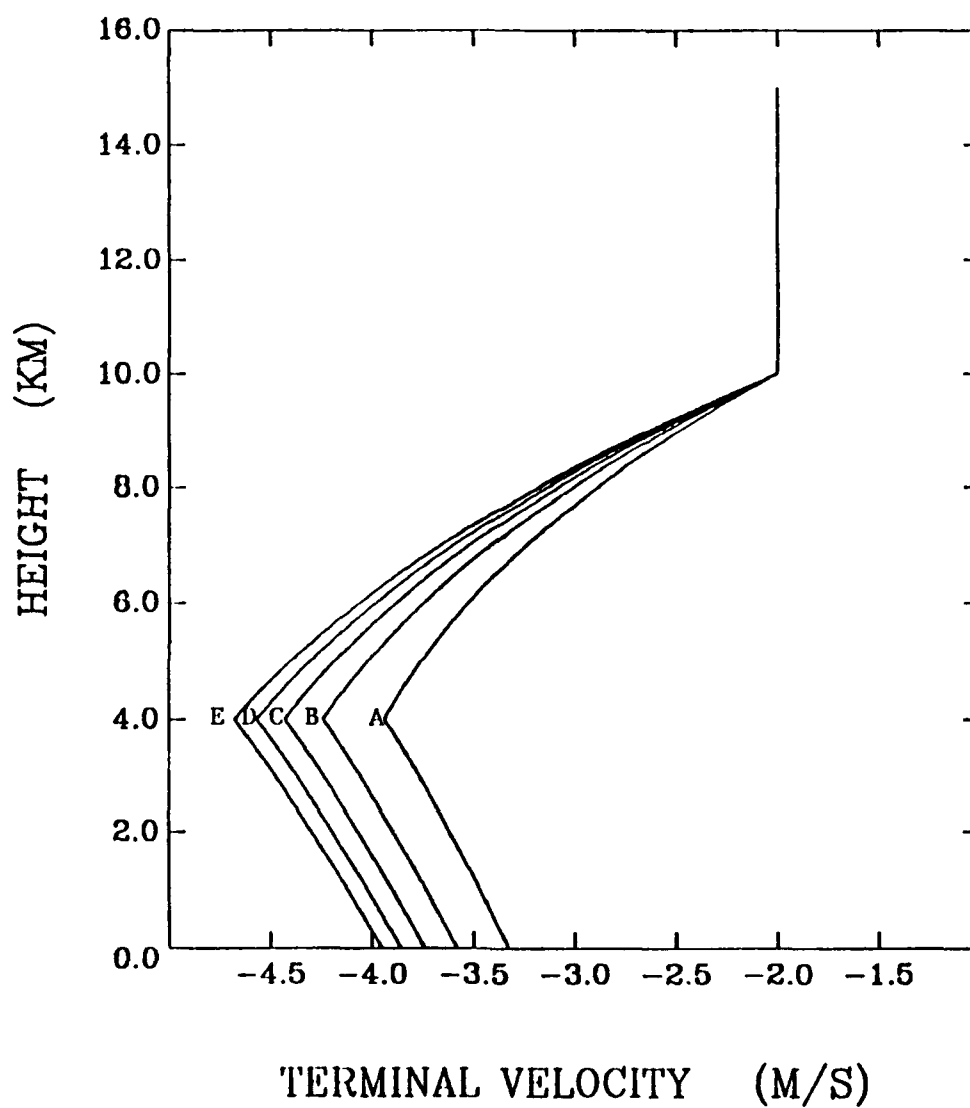


*Fig. A1. Terminal velocities from the adjusted Joss and Waldvogel (1970) equations. Plotted lines are done for: (A) 10 dBZ, (B) 20 dBZ, (C) 30 dBZ, (D) 40 dBZ, and (E) 50 dBZ. Negative velocities denote downward speed. All plots have a value of  $-2 \text{ ms}^{-1}$  above the 10 km height level.*

$$u(x - x_1) + v(y - y_1) + W(z - z_1) = R_1 V_1 \quad . \quad (A6)$$

Correspondingly, for radar #2, Eq. 1 is

$$u(x - x_2) + v(y - y_2) + W(z - z_2) = R_2 V_2 \quad . \quad (A7)$$

Now Eqs. A5 and A6 are solved for  $u$  by multiplying Eq. 5 by  $(y - y_2)$  and Eq. 6 by  $(y - y_1)$ . This gives

$$u(x - x_1)(y - y_2) + v(y - y_1)(y - y_2) + W(z - z_1)(y - y_2) = R_1 V_1(y - y_2) \quad , \quad (A7)$$

and

$$u(x - x_2)(y - y_1) + v(y - y_2)(y - y_1) + W(z - z_2)(y - y_1) = R_2 V_2(y - y_1) \quad . \quad (A8)$$

Then Eq. A8 is subtracted from Eq. A7, eliminating the  $v$ .

$$\begin{aligned} u[(x - x_1)(y - y_2) - (x - x_2)(y - y_1)] &= R_1 V_1(y - y_2) - R_2 V_2(y - y_1) \\ &\quad - W[(z - z_1)(y - y_2) - (z - z_2)(y - y_1)] \end{aligned} \quad (A9)$$

Thus,

$$u = \frac{R_1 V_1(y - y_2) - R_2 V_2(y - y_1) - W[(z - z_1)(y - y_2) - (z - z_2)(y - y_1)]}{(x - x_1)(y - y_2) - (x - x_2)(y - y_1)} \quad . \quad (A10)$$

Correspondingly, an equation for  $v$  can be derived, and is given by

$$v = \frac{R_2 V_2(x - x_1) - R_1 V_1(x - x_1) - W[(z - z_2)(x - x_1) - (z - z_1)(x - x_2)]}{(x - x_2)(y - y_1) - (x - x_1)(y - y_2)} \quad (A11)$$

Given a value for  $W$ , from Eq. A3, the values of  $u$  and  $v$  are found using Eqs. A10 and A11. Next, a new vertical velocity  $w$  can be found from the anelastic continuity equation

$$\frac{\partial u}{\partial x} + \frac{\partial v}{\partial y} + \frac{\partial w}{\partial z} - \kappa w = 0 \quad (A12)$$

The newly determined value of  $w$  is put back into Eq. A3, and a new value of  $W$  is determined. The iterative process continues until convergence of the solution is obtained. After convergence has been obtained, the value of  $w$  in the layer calculated is used as a boundary condition for calculating the next lowest layer. This process is repeated from the storm top to the surface in order to evaluate the entire storm volume.

## Appendix B

Variationally adjusted values of  $u$ ,  $v$ , and  $w$  are frequently used to provide a more accurate representation of the true wind field. This is done using the integrated horizontal divergence as a strong constraint. This means that the difference in the upper and lower boundary condition is specified (Ray *et al.*, 1980). The deviations between the new values and the observed values of the horizontal winds will be a minimum. If these deviations are normally distributed, a functional can be written as

$$E[u, v, w] = \int_y \int_x \alpha^2 (u - u^o)^2 + \beta^2 (v - v^o)^2 + \left[ \lambda \left[ \int_z \left( \frac{\partial u}{\partial x} + \frac{\partial v}{\partial y} \right) dz + C \right] \right] dx dy \quad (B1)$$

The variables  $u$  and  $v$  are the adjusted components of motion; the variables  $u^o$  and  $v^o$  are the observed horizontal components of motion. The variables  $\alpha^2$  and  $\beta^2$  are weights which are inversely proportional to the error variances in  $u$  and  $v$  respectively. Thus,  $\alpha^2 = \frac{1}{2\sigma_u^2}$ . Error variance is a measure of the differences between the estimates and the true values of  $u$  and  $v$ . Clearly, a large variance value will yield a small weight value. In the integrand's last term, which is the vertically integrated horizontal divergence,  $\lambda$  is the Lagrange multiplier. It is the value of  $\lambda$  that we will determine in order to variationally adjust  $u$ ,  $v$ , and to compute  $w$ .

The integrand of the functional,  $I$ , is next used in a general set of Euler-Lagrange equations. The set of Euler-Lagrange equations yield three equations and three unknowns. These unknowns will be  $\lambda$ ,  $u$ , and  $v$ . This gives us a set of Euler-Lagrange equations given by

$$-\frac{\partial}{\partial x} \frac{\partial I}{\partial \left( \frac{\partial u}{\partial x} \right)} + \frac{\partial I}{\partial u} = 0 \quad , \quad (B2)$$

$$-\frac{\partial}{\partial y} \frac{\partial I}{\partial \left( \frac{\partial v}{\partial y} \right)} + \frac{\partial I}{\partial v} = 0 \quad , \quad (B3)$$

$$\frac{\partial I}{\partial \lambda} = 0 \quad . \quad (B4)$$

These equations are solved, giving respectively

$$-\frac{\partial \lambda}{\partial x} + 2\alpha^2(u - u^o) = 0 \quad , \quad (B5)$$

$$-\frac{\partial \lambda}{\partial y} + 2\beta^2(v - v^o) = 0 \quad , \quad (B6)$$

$$\int_0^{z_1} \left( \frac{\partial u}{\partial x} + \frac{\partial v}{\partial y} \right) dz + C = 0 \quad . \quad (B7)$$

Next, B5 and B6 are solved for  $u$ , and  $v$  giving

$$u = u^o + \frac{1}{2\alpha^2} \frac{\partial \lambda}{\partial x} \quad , \quad (B7)$$

and

$$v = v^o + \frac{1}{2\beta^2} \frac{\partial \lambda}{\partial y} \quad . \quad (B11)$$

These values of  $u$ ,  $v$ , can now be substituted into Eq. B7, yielding an elliptic partial differenced equation which now has only one variable,  $\lambda$ .

$$\begin{aligned} \int_0^{z_T} \left[ \frac{\partial}{\partial x} \left( \frac{1}{2\alpha^2} \frac{\partial \lambda}{\partial x} \right) + \frac{\partial}{\partial y} \left( \frac{1}{2\beta^2} \frac{\partial \lambda}{\partial y} \right) \right] dz \\ = - \int_0^{z_T} \left( \frac{\partial u^0}{\partial x} + \frac{\partial v^0}{\partial y} \right) dz + C \end{aligned} \quad (B12)$$

From Eq. B12 a value of  $\lambda$  is determined. This can then be used in Eqs. B10, B11, and B12, to get the adjusted values for  $u$ ,  $v$ ,. These adjusted values will now satisfy the divergence equation.

## Appendix C

### Uncertainty in Wind Field Estimates

From Appendix A, the  $u$ ,  $v$ , and  $w$  components of the wind motion are given by the equations

$$u = \frac{R_1 V_1 (y - y_2) - R_2 V_2 (y - y_1) - W[(z - z_1)(y - y_2) - (z - z_2)(y - y_1)]}{(x - x_1)(y - y_2) - (x - x_2)(y - y_1)}, \quad (C1)$$

$$v = \frac{R_2 V_2 (x - x_1) - R_1 V_1 (x - x_2) - W[(z - z_2)(x - x_1) - (z - z_1)(x - x_2)]}{(x - x_2)(y - y_1) - (x - x_1)(y - y_2)}, \quad (C2)$$

$$\frac{\partial u}{\partial x} + \frac{\partial v}{\partial y} + \frac{\partial w}{\partial z} - \kappa w = 0 \quad . \quad (C3)$$

Here  $x$ ,  $y$ , and  $z$  represent the position of grid points, and the subscripted variables ( $x_1$ ,  $y_1$ ,  $z_1$ , and  $x_2$ ,  $y_2$ ,  $z_2$ ) are the radars' coordinates. The variance, ( $\sigma^2$ ), of a dependent variable measures the expected difference between a sample and the true value of that variable. The error variance of  $u$ ,  $v$ , and  $w$  are calculated at each grid point. In Eqs. C1, C2, and C3, the measurements of  $V_1$ ,  $V_2$ , and  $W$  are assumed independent. Thus, in calculating error variances, the covariances can be ignored (Ray, 1980). The error variances for  $u$ ,  $v$ ,  $w$ ,  $W$ ,  $V_1$ , and  $V_2$  are given by

$$\sigma_u^2 = \sum_{n=1}^N \frac{(u_n - u)^2}{N - 1}, \quad (C4)$$

$$\sigma_v^2 = \sum_{n=1}^N \frac{(v_n - v)^2}{N-1}, \quad (C5)$$

$$\sigma_w^2 = \sum_{n=1}^N \frac{(w_n - w)^2}{N-1}, \quad (C6)$$

$$\sigma_W^2 = \sum_{n=1}^N \frac{(W_n - W)^2}{N-1}, \quad (C7)$$

$$\sigma_{V_1}^2 = \sum_{n=1}^N \frac{(V_{1n} - V_1)^2}{N-1}, \quad (C8)$$

$$\sigma_{V_2}^2 = \sum_{n=1}^N \frac{(V_{2n} - V_2)^2}{N-1}. \quad (C9)$$

First examine the  $u$  component equation. Since  $V_1$ ,  $V_2$ , and  $W$  are independent, only the derivation of the first term need be examined in this equation, as the mathematical process applied will give the corresponding results for the other terms, as well as the  $v$  component equation. The first term of the  $u$  component is given in Eq. C1 as

$$u = \frac{R_1 V_1 (y - y_2)}{(x - x_1)(y - y_2) - (x - x_2)(y - y_1)}. \quad (C10)$$

Now the error variance for this term is found:

$$\sum_{n=1}^N \frac{(u_n - u)^2}{N-1} = \sum_{n=1}^N \frac{[R_1 V_{1n} (y - y_2) - R_1 V_1 (y - y_2)]^2}{[(x - x_1)(y - y_2) - (x - x_2)(y - y_1)]^2 (N-1)}. \quad (C11)$$

Equation C11 can be rewritten in the form of

$$\sigma_u^2 = \frac{[R_1 (y - y_2)]^2 \left[ \sum_{n=1}^N \frac{(V_{1n} - V_1)^2}{N-1} \right]}{[(x - x_1)(y - y_2) - (x - x_2)(y - y_1)]^2}, \quad (C12)$$

which is the same as

$$\sigma_u^2 = \frac{[R_1(y - y_2)]^2(\sigma_{V_1}^2)}{[(x - x_1)(y - y_2) - (x - x_2)(y - y_1)]^2} \quad (C13)$$

This is the expression for the error variance for the first term of  $u$ , applying this method to the rest of Eq. C1 gives the error variance of  $u$  as

$$\begin{aligned} \sigma_u^2 = & \frac{[R_1(y - y_2)]^2(\sigma_{V_1}^2) + [R_2(y - y_1)]^2(\sigma_{V_2}^2)}{[(x - x_1)(y - y_2) - (x - x_2)(y - y_1)]^2} \\ & + \frac{\{[(z - z_2)(y - y_1) - (z - z_1)(y - y_2)]^2\}(\sigma_W^2)}{[(x - x_1)(y - y_2) - (x - x_2)(y - y_1)]^2} \end{aligned} \quad (C14)$$

Correspondingly, the equation for the error variance in  $v$  is given by

$$\begin{aligned} \sigma_v^2 = & \frac{[R_2(x - x_2)]^2(\sigma_{V_2}^2) + [R_1(x - x_1)]^2(\sigma_{V_1}^2)}{[(x - x_2)(y - y_1) - (x - x_1)(y - y_2)]^2} \\ & + \frac{\{[(z - z_2)(x - x_1) - (z - z_1)(x - x_2)]^2\}(\sigma_W^2)}{[(x - x_2)(y - y_1) - (x - x_1)(y - y_2)]^2} \end{aligned} \quad (C15)$$

The vertical velocity variance is found by taking Eq. C3 (the anelastic continuity equation) and expressing it in finite difference form. In this form, the centered finite differences are used in the horizontal (with two grid spaces) and the vertical (with one grid space). The horizontal velocities are at level  $k$ . Since we are integrating downward the value of  $w$  at the top of the layer of integration must be known as  $(k + \frac{1}{2})$ . Equation C3 becomes

$$\frac{\Delta u}{2\Delta x} + \frac{\Delta v}{2\Delta y} + \frac{w_{k+\frac{1}{2}} - w_{k-\frac{1}{2}}}{\Delta z} - \kappa \left( \frac{w_{k+\frac{1}{2}} - w_{k-\frac{1}{2}}}{2} \right) = 0 \quad (C16)$$

Solving this for  $w_{k-\frac{1}{2}}$  gives

$$w_{k-\frac{1}{2}} = w_{k+\frac{1}{2}} \left( \frac{\frac{1}{\Delta z} - \frac{\kappa}{2}}{\frac{1}{\Delta z} + \frac{\kappa}{2}} \right) + \frac{\left( \frac{\Delta u}{2\Delta x} + \frac{\Delta v}{2\Delta y} \right)}{\left( \frac{1}{\Delta z} + \frac{\kappa}{2} \right)} \quad (C17)$$

The value for  $w_k$  is defined by

$$w_k = \frac{w_{k+\frac{1}{2}} + w_{k-\frac{1}{2}}}{2} \quad (C18)$$

Next, Eq. C17 is substituted into Eq. C18, and this expression is simplified to

$$w_k = \frac{1}{2} \left\{ w_{k+\frac{1}{2}} \left[ 1 + \left( \frac{\frac{1}{\Delta z} - \frac{\kappa}{2}}{\frac{1}{\Delta z} + \frac{\kappa}{2}} \right) \right] \right\} + \frac{\Delta u}{2 \left( \frac{2\Delta x}{\Delta z} + \kappa \Delta x \right)} + \frac{\Delta v}{2 \left( \frac{2\Delta y}{\Delta z} + \kappa \Delta y \right)} \quad (C19)$$

Repeating the above error variance methodology on Eq. C19 we get

$$\sigma_{w_k}^2 = \frac{1}{4} \left[ 1 + \left( \frac{\frac{1}{\Delta z} - \frac{\kappa}{2}}{\frac{1}{\Delta z} + \frac{\kappa}{2}} \right) \right]^2 (\sigma_{w_{k+\frac{1}{2}}})^2 + \frac{1}{2} \left[ \frac{\sigma_u^2}{\left( \frac{2\Delta x}{\Delta z} + \kappa \Delta x \right)^2} + \frac{\sigma_v^2}{\left( \frac{2\Delta y}{\Delta z} + \kappa \Delta y \right)^2} \right] \quad (C20)$$

## Appendix D

### VAD Analysis

Assume that a ground-based radar is located at the origin of a Polar coordinate system. The kinematic fields from the Fourier coefficients, based on the Velocity Azimuth Display (VAD) technique by Browning and Wexler (1968), are rederived using: the conventional definition of the azimuth angle ( $\theta$ ) in a clockwise manner (Browning and Wexler (1968) used counterclockwise); the convention of negative Doppler velocity ( $V_d$ ) as an indication of flow toward the radar; and the fact that the effects of the beam elevation ( $\phi$ , is a small angle) are negligible. Assuming a uniform wind field, Doppler velocity is defined by

$$V_d = V_x \cos \phi \sin \theta + V_y \cos \phi \cos \theta \quad . \quad (D1)$$

Here,  $V_x$  is positive towards the east and  $V_y$  is positive towards the north. The velocity components  $V_x$  and  $V_y$  can be expressed in terms of their value at the center of the scanned circle (subscript 0) and mean linear velocity (overbarred variables) by

$$V_x = V_{x0} + \frac{\overline{\partial V_x}}{\partial x} x + \frac{\overline{\partial V_x}}{\partial y} y \quad , \quad (D2)$$

$$V_y = V_{y0} + \frac{\overline{\partial V_y}}{\partial x} x + \frac{\overline{\partial V_y}}{\partial y} y \quad . \quad (D3)$$

Putting Eqs. D2 and D3 into Eq. D1, using  $x = r\sin\theta$  and  $y = r\cos\theta$ , where ( $r$ ) is the range, gives

$$\begin{aligned} V_d = & V_{x0}\cos\phi + r\cos\phi\frac{\partial\overline{V_x}}{\partial x}\sin^2\theta + r\cos\phi\frac{\partial\overline{V_x}}{\partial y}\cos\theta\sin\theta \\ & + V_{y0}\cos\phi + r\cos\phi\frac{\partial\overline{V_y}}{\partial x}\cos^2\theta + r\cos\phi\frac{\partial\overline{V_y}}{\partial y}\cos\theta\sin\theta \quad . \end{aligned} \quad (D4)$$

Using several trigonometric identities:  $\cos^2\theta = \frac{1}{2}(1 + \cos 2\theta)$ ,  $\sin^2\theta = \frac{1}{2}(1 - \cos 2\theta)$ , and  $\cos\theta\sin\theta = \frac{1}{2}\sin 2\theta$ , Eq. D4 becomes

$$\begin{aligned} V_d = & \frac{r}{2}\cos\phi\left(\frac{\partial\overline{V_x}}{\partial x} + \frac{\partial\overline{V_y}}{\partial y}\right) + V_{x0}\cos\phi\sin\theta + V_{y0}\cos\phi\cos\theta \\ & + \frac{r}{2}\cos\phi\left(\frac{\partial\overline{V_x}}{\partial y} + \frac{\partial\overline{V_y}}{\partial x}\right)\sin 2\theta - \frac{r}{2}\cos\phi\left(\frac{\partial\overline{V_x}}{\partial x} - \frac{\partial\overline{V_y}}{\partial y}\right)\cos 2\theta \quad . \end{aligned} \quad (D5)$$

Equation D5 can be put into a Fourier series of the form

$$V_d = \frac{1}{2}a_0 + \sum_{n=1}^{\infty} (a_n\cos n\theta + b_n\sin n\theta) \quad . \quad (D6)$$

This gives the non-zero Fourier coefficients of

$$a_0 = r\cos\phi\left(\frac{\partial\overline{V_x}}{\partial x} + \frac{\partial\overline{V_y}}{\partial y}\right), \quad (D7)$$

$$a_1 = V_{y0}\cos\phi, \quad (D8)$$

$$b_1 = V_{x0}\cos\phi, \quad (D9)$$

$$a_2 = -\frac{1}{2}r\cos\phi\left(\frac{\partial\overline{V_x}}{\partial x} - \frac{\partial\overline{V_y}}{\partial y}\right), \quad (D10)$$

$$b_2 = \frac{1}{2}r\cos\phi\left(\frac{\partial\overline{V_x}}{\partial y} + \frac{\partial\overline{V_y}}{\partial x}\right). \quad (D11)$$

The two-dimensional horizontal divergence, stretching deformation, and shearing deformation are, respectively, given by the terms

$$\left(\frac{\partial\overline{V_x}}{\partial x} + \frac{\partial\overline{V_y}}{\partial y}\right), \left(\frac{\partial\overline{V_x}}{\partial x} - \frac{\partial\overline{V_y}}{\partial y}\right), \left(\frac{\partial\overline{V_x}}{\partial y} + \frac{\partial\overline{V_y}}{\partial x}\right) \quad .$$

Thus, we can obtain the kinematic properties of the wind from

$$\left(\frac{\partial\overline{V_x}}{\partial x} + \frac{\partial\overline{V_y}}{\partial y}\right) = \frac{a_0}{r\cos\phi} \quad , \quad (D12)$$

$$|V| = \frac{(a_1^2 + b_1^2)^{\frac{1}{2}}}{\cos\phi} \quad , \quad (D13)$$

$$\left(\frac{\partial\overline{V_x}}{\partial x} - \frac{\partial\overline{V_y}}{\partial y}\right) = -\frac{2a_2}{r\cos\phi} \quad , \quad (D14)$$

$$\left(\frac{\partial\overline{V_x}}{\partial y} + \frac{\partial\overline{V_y}}{\partial x}\right) = \frac{2b_2}{r\cos\phi} \quad . \quad (D15)$$

Neither of the deformations gives individually the desired total rate and sense of the deformation in the motion unless one of the quantities is equal to zero. To derive the full value from this concept, the two types of deformation are combined to give the resultant direction of elongation (which is along the axis of dilatation) and the net rate of deformation (DEF) (Saucier, 1965). First, the angle ( $\alpha$ ) between the axis of dilatation and the initial X axis is calculated using

$$\tan 2\alpha = \frac{\frac{\partial \overline{V_x}}{\partial y} + \frac{\partial \overline{V_y}}{\partial x}}{\frac{\partial \overline{V_x}}{\partial x} - \frac{\partial \overline{V_y}}{\partial y}} = -\frac{b_2}{a_2} \quad . \quad (D16)$$

If both of the deformations are of the same sign, the axis of dilatation is rotated counterclockwise through the angle  $\alpha$ . Once this angle has been determined the magnitude of the total deformation (DEF) can be obtained from

$$\begin{aligned} \text{DEF} &= \left( \frac{\partial \overline{V_x}}{\partial x} - \frac{\partial \overline{V_y}}{\partial y} \right) \sec 2\alpha \\ &= \left( \frac{\partial \overline{V_x}}{\partial y} + \frac{\partial \overline{V_y}}{\partial x} \right) \csc 2\alpha \quad . \end{aligned} \quad (D17)$$

Further explanation of these terms is found in Chapter 3.